annual progress report

2008

VEHICLE TECHNOLOGIES PROGRAM

ANNUAL PROGRESS REPORT FOR THE ADVANCED POWER ELECTRONICS AND ELECTRIC MACHINERY TECHNOLOGY AREA

U.S. Department of Energy
Energy Efficiency and Renewable Energy
Bringing you a prosperous future where energy is clean, abundant, reliable, and affordable

U.S. Department of Energy
FreedomCAR and Vehicle Technologies, EE-2G
1000 Independence Avenue, S.W.
Washington, D.C. 20585-0121

FY 2008

Annual Progress Report for the Advanced Power Electronics and Electric Machinery Technology Area

Submitted to:

Energy Efficiency and Renewable Energy
Vehicle Technologies Program

Susan A. Rogers, Technology Development Manager

January 2009

Contents

Page

Acronyms and Abbreviations

3D	3-dimensional
AEEMS	axially excited electromagnetic synchronous
AlN	aluminum nitride
APEEM	Advanced Power Electronics and Electric Machines
APF	active power filter
BCD	bipolar CMOS-DMOS
BeO	beryllium oxide
CMOS	complementary metal–oxide semiconductor
CPLD	complex programmable logic device
CSI	current source inverter
CVT	continuously variable transmission
DBC	direct-bonded copper
DMOS	double-diffused metal-oxide semiconductor
DOE	Department of Energy
DSP	digital signal processing
ECVT	electronically-controlled continuously variable transmission
EETT	Electrical and Electronics Technical Team
ESR	equivalent series resistance
EV	electric vehicle
FEA	finite element analysis
FreedomCAR	derived from “Freedom” and “Cooperative Automotive Research”
FSCW	fractional-slot concentrated windings
FUDS	Federal Urban Driving Schedule
HEV	hybrid electric vehicle
IC	integrated circuit
ICE	internal combustion engine
IGBT	insulated gate bipolar transistor
INV/CONV	inverter/converter
IPM	interior permanent magnet
JFET	junction field effect transistor
MG	motor/generator
MOSFET	metal-oxide semiconductor field-effect transistor
NMOS	negative-channel metal-oxide semiconductor

OEM	original equipment manufacturer
ORNL	Oak Ridge National Laboratory
PCB	printed circuit board
PCU	power converter unit
PHEV	plug-in hybrid electric vehicle
PM	permanent magnet
PMOS	positive-channel metal-oxide semiconductor
PWM	pulse-width modification
SiC	silicon carbide
SOI	silicon-on-insulator
SR	set/reset
TC	temperature coefficient
THD	total harmonic distortion
VSATT	Vehicle Systems Analysis Technical Team
VSI	voltage source inverter
VTP	Vehicle Technologies Program
WBG	wide-bandgap
WEG	water–ethylene glycol
ZSIN	zero-sequence impedance networks

1. Introduction

The objective of the Advanced Power Electronics and Electric Machines (APEEM) activity is to develop technologies compatible with the high-volume manufacturing of motors, inverters, and DC/DC converters that will enable the automotive industry to achieve the goal by 2020 of an electric propulsion system with a 15-year life capable of delivering at least 55 kW for 18 seconds and 30 kW continuous at a system cost of $8/kW peak.

In order to make the electric propulsion system practical and affordable, the cost must be reduced by about 80%, the specific power must be increased by about 50%, the power density increased by about 55%, and the efficiency increased by about 10%.

Researchers supporting the Advanced Power Electronics and Electric Machines R&D activity continued to make significant progress in meeting these challenges during FY 2008.

In FY08 the APEEM motor activity concentrated on reducing cost via reductions in manufacturing costs, improvements in motor efficiency, elimination of the need for permanent magnets, and integrating the motor and generator functionality into a single machine.

The amorphous core assessment concluded that the high cost of the amorphous material and its unavailability in forms needed for electric motor cores does not allow it to meet the cost targets. Even though significant decreases in core losses are experienced the low saturation flux limits the ability of the material to meet the performance requirements.

Analysis of the concentrated windings approach indicated that in addition to anticipated manufacturing cost benefits the motor design offered reduced torque ripple and higher efficiency because of reduced copper losses. However, the motor had difficulty meeting the power requirements of the US06 driving cycle without modification of the gear set.

The uncluttered CVT design was modeled and the machine delivered a 30% increase in torque with a weight increase (compared to the baseline motor) of only 15%. In addition, the efficacy of the 3-dimensional torque path was confirmed.

Design development of the axially excited motor concept indicated that with the unique rotor configuration developed by ORNL a feasible design emerged that yielded a specific power of 1 kW/kg with a power density of 5 kW/L. This confirmed that it may be possible to achieve PM like performance from a PM-less motor.

The power electronics activity concentrated on topology activities that incorporated multiple functionality into a single unit and reduced the need for bulk capacitance, PE options for dealing with ripple currents, packaging concepts that enabled the use of silicon power devices with high-temperature coolants, and high-temperature devices.

Fulfilling the PEEM Program Joule milestone a 55 kW current source inverter prototype was designed, constructed, and successfully tested. The prototype reduced the capacitor requirement from 2000 μF to 195 μF and achieved a voltage boost of 3.45. The output voltage total harmonic distortion was less than 12.55.

A prototype 55 kW plug-in traction drive inverter with a charging capability of 20 kW was designed, fabricated, and tested. The efficiency attained was in the 92 to 97% range. Total harmonic distortion of the ac current was less than 10%.

A 30 kW continuous, 55 kW peak buck/boost dc-dc converter was designed, assembled, and tested. Efficiencies were in the 97 to 98% range. The power density of the unit was 17.8 kW/L and the specific power was 8.5 kW/kg. A second generation silicon-on-insulator, high-temperature gate drive chip was developed and successfully tested.

A number of developmental wide bandgap power devices were obtained from industry and tested to determine their performance characteristics over a temperature range from room temperature to 250°C. In addition, a novel integrated motor/inverter packaging concept was developed that takes advantage of the high-temperature capabilities of wide bandgap devices.

Designs for an active power filter using power electronics devices to replace the dc bulk capacitor were evaluated.

Designs were identified that directly cool the substrate in the inverter. Analysis indicated that silicon power devices can be cooled in a reliable manner with 105C water ethylene glycol (WEG) coolant. Compatibility of the substrate material with the WEG was initiated.

In addition to the PEEM development efforts benchmarking of the Toyota Lexus LS600H PEEM system was completed.

In order to achieve FreedomCAR goals for cost, power density and lifetime, significant advancements in the thermal management of both power electronics and motors for the electric propulsion system must be achieved. Excessive heat can degrade the performance, life, and reliability of power electronic components. The development of advanced thermal control technologies is critical to nearly all viable technology pathways that result in successful achievement of FreedomCar technical targets.

An objective and consistent material thermal interface material database has been established at NREL. The materials tested include greases, PCMs, filler pads, graphite, indium, thermoplastics, and carbon nanotubes. Overall, about 40 materials spanning the classes of materials mentioned above were tested. Some high-thermal performance greases and PCMs were identified.

Thermal testing of a Semikron inverter with baseline elliptical pin-fins and with NREL's jet-impingement heat exchanger was completed. The thermal resistance of the jet-impingement design was 31% lower compared to baseline elliptical fin-pins.
Temperature distributions of electronic devices were also more uniform. This superior performance becomes significant at higher power levels with the use of engine coolant.

NREL researchers fabricated and tested two air-cooled test articles with excellent agreement in performance between numerical predictions and test results. Heat flux levels up to 180 W/cm2 were achieved while keeping the surface temperature below 130°C.

A technique was developed for characterizing vehicle drive profiles and power electronics thermal duty cycles in the frequency domain. The methodology enables additional analysis, including rapid transient simulation in the frequency domain and comparison to power semiconductor package frequency response characteristics.

A parametric finite element mode was created for material and package size design studies for power semiconductor packages. The modeling methodology enables optimization and sensitivity studies across multiple design factors.

The multiple avenues of research described here are helping the FreedomCAR team understand the tradeoffs between alternative approaches to thermal control of power electronics and making significant progress to meeting the goals and objectives of the FreedomCAR program.

2. Thermal Management Systems

2.1 Direct-Cooled Power Electronics Substrate

Principal Investigator: Randy H. Wiles
Oak Ridge National Laboratory
National Transportation Research Center
2360 Cherahala Boulevard
Knoxville, TN 37932
Voice: 865-946-1319; Fax: 865-946-1262; E-mail: zhr@ornl.gov

DOE Technology Development Manager: Susan A. Rogers
Voice: 202-586-8997; Fax: 202-586-1600; E-mail: Susan.Rogers@ee.doe.gov

ORNL Program Manager: Mitch Olszewski
Voice: 865-946-1350; Fax: 865-946-1262; E-mail: olszewskim@ornl.gov

---

Objectives

- Develop and model an innovative power electronics mounting structure (direct-bonded copper [DBC] substrate) for an inverter that is directly cooled by water-ethylene glycol (WEG), thus eliminating the conventional heat sink and associated heat flow path.
- Reduce the size and weight of the heat sink for power electronics used in hybrid electric and plug-in hybrid electric vehicles (HEVs and PHEVs, respectively).
- Determine the feasibility of a design that directly cools the DBC, preferably using a 105°C coolant temperature.
- Develop mechanical and thermal models of an inverter substrate to predict performance.
- Research manufacturing capabilities and methods that will support the substrate designs.

Approach

- Determine the optimum ceramic materials for maximum heat transfer and minimum cost.
- Evaluate candidate materials and processing methods for a direct-cooled power electronics substrate.
- Select chip sets that will meet the inverter power requirement.
- Establish design parameters for computer models:
  - — determine appropriate thermal load for 3-dimensional simulations
  - — justify the number of chips to use for specific designs
  - — create metrics for a successful design
- Perform finite-element analysis (FEA) to optimize heat transfer characteristics of the assembly.

Major Accomplishments

- Design parameters established.
- Thermal FEA completed on five substrate designs.
- Mechanical stress FEA completed on the two preferred designs.
- Commercial processing methods identified and evaluated.

Future Direction

- Fabrication of preferred design(s).
- Laboratory testing to validate performance relative to modeling results.
- Complete designs based on laboratory results and integrate substrate into inverter package.

Technical Discussion

As consumer interest grows in HEVs and PHEVs, manufacturers are challenged to offer these technologies at reduced costs. The automotive manufacturer's goal is to reduce the price of these vehicles relative to the cost of traditional internal combustion engine (ICE) –powered vehicles. The thermal management of the power electronic systems that must be implemented into these products constitutes a large cost to both manufacturers and consumers. Currently, HEVs utilize two cooling loops. One cooling loop is for the ICE, which operates at approximately 105°C, and a second coolant loop is for the power electronics modules, which operates near 70°C. One way to significantly reduce the cost to both manufacturers and consumers is to use a single coolant loop for both the ICE and power electronics using 105°C coolant as the primary means of heat dissipation.

The purpose of this research and development project is to design a direct-cooled power electronics substrate that would enable the automotive manufacturers to use 105°C coolant, thus eliminating the secondary coolant loop. Thermal performance and mechanical stress FEA were performed on design concepts to ensure they satisfied the design criteria for material strength and thermal heat dissipation. Surveys were also conducted of manufacturers' capabilities and methods that supported the substrate design and fabrication.

Information contained in this annual report serves as a general discussion of this research effort. For more detailed information, please refer to ORNL/TM-2008/112. This report is a "Limited Distribution" report and is classified for Official Use Only. It will be released to the general public after the Oak Ridge National Laboratory (ORNL) patent office publishes the patent for the technology.

Proposed Solution

To enable cooling of the inverter with 105°C WEG, alternative cooling strategies are under consideration. One involves positioning the 105°C coolant as close to the silicon insulated gate bipolar transistor (IGBT) and diode as possible through the use of a (electrically insulating) ceramic heat exchanger.

A uniquely shaped structure was developed that allows for a compact chip layout, provides excellent sealing surfaces, and adequate space to incorporate coolant channels. This structure was designed with highly thermally conductive materials and allows enough surface area for the switches to be sintered/soldered to the assembly. Utilizing a lower thermal-conductivity material, such as alumina, necessitates increasing the width of the structure. This is necessary for heat dissipation. In either case, the length of the entire ceramic structure was maintained at a minimum for volume considerations. This length provides enough surface area for the switches, wire bonds, electrical connections, and sealing surfaces. Issues associated with sealing the substrate were also a concern. The rounded ends of the structure will provide an excellent sealing surface, as opposed to the flat plate designs that are common in micro-channel research. Because of manufacturing restrictions and automotive manufacturer guidelines, typical thin, flat plate DBC substrates are not feasible for direct cooling. More cross-sectional area has to be created to incorporate flow channels to remove the heat.

Additional concepts under consideration incorporate an annular coolant channel into which a thermal enhancement material is placed. In any design case, the ceramic in the substrate would serve the same primary role as a ceramic in a conventional DBC; namely, it would be an electrical insulator. The

substrate would then be metalized with copper to facilitate bonding (e.g., soldering or sintering) to a silicon IGBT and diode.

Candidate Materials and Processing Methods for a Direct-Cooled Power Electronics Substrate

Ceramic materials were sought that combine electrical insulation (>109 ohm-cm), the potential to be chemically compatible with WEG, good thermal conductivity (>50 W/mK), modest tensile strength (>200 MPa), and minimum cost. Candidate materials are listed in the following table.

Table 1. Candidate ceramic materials for a direct-cooled power electronic substrate

Candidate ceramic	Electrical insulation	Thermal conductivity	Cost	Chemical compatibility with WEG
Aluminum oxide or alumina (Al_2O_3)	Excellent	Fair	Low	Probably good
Aluminum nitride (AlN)	Excellent	Excellent	High	Unknown
Silicon nitride (Si_3N_4)	Excellent	Fair to good	High	Unknown
High-resistivity polycrystalline silicon carbide (SiC)	Could be excellent	Good to excellent	Medium to high	Unknown
Beryllium oxide (BeO)	Excellent	Excellent	Medium	Unknown

Some of the candidate ceramic materials are documented [1, 2] as being unstable when in contact with moisture. To examine the mechanical stability of the ceramics in contact with WEG, a series of strength and fatigue tests were performed on aluminum nitride (AlN), aluminum oxide (Al_2O_3), silicon nitride (Si_3N_4), and silicon carbide (SiC) after they were immersed in and impinged with WEG. Preliminary indications are that each material had no dramatic decrease in strength from contact with WEG; however, scanning electron microscopy of ceramic surfaces subjected to WEG impingement for 590 hours shows that erosion is occurring, probably as a result of a chemical reaction between the AlN and WEG. Longer-term studies are continuing. Additionally, electrical resistivity tests were also completed on the ceramic candidates at 25, 200 and 325°C. The results from the electrical resistivity tests showed that each of the candidate ceramic materials maintained an electrical resistivity of between 10^{-9} and 10^{-12} Ω-cm, which is well within the range of insulating materials. Complete results of the testing are documented in ORNL/TM-2008/112.

Ceramic Processing Methods

Ceramic processing methods were identified that could be used to produce a direct-cooled DBC. The manufacturing techniques should combine two characteristics: they should be capable of producing small-scale features (e.g., hole diameters of 1 mm or 0.040 in. or less) in a structure up to 50 mm in length and be mature processes with the capability for large-scale manufacturing applicable to the automotive industry. Four identified ceramic processing methods described in the following sections are considered to be "green-state" fabrication techniques; that is, they are methods that form processed ceramic powder into some desired shape at or near ambient temperature. The following sections describe these current state-of-the-art processing methods that satisfy the fabrication requirements.

Dry Pressing

Dry pressing is one of the most traditional ceramic processing methods. Its advantages are that most ceramic manufacturers are adept at it, it is a mature technology, it is relatively inexpensive, and it is amenable for mass production. Dry pressing alone could not produce the ORNL concept structure, so manufacturers would need to perform green-state machining of the dry-pressed billet to achieve the unique shape and to incorporate the coolant channels. Green-state machining is attractive because conventional grinding and machining tools can be used, whereas (expensive) diamond tooling is required

for machining after a ceramic has been sintered. The disadvantage of this method is that the architecture can be limited by what can be accomplished during green-state machining. For example, very small thru-hole diameters (e.g., 1 mm or 0.040 in.) may be difficult to produce in the ceramic's green state and maintain through the sintering process.

Extrusion

Extrusion is another traditional ceramic processing method. Like dry pressing, its advantages are that many ceramic manufacturers are experienced with it; it is a mature technology; it is relatively inexpensive; and it is amenable for mass production. Like dry pressing, extrusion alone could not produce the ORNL concept structure. Green-state machining would be needed; therefore, fine-scale-features of the final architecture could be limited.

Injection Molding

Injection molding can produce high-precision ceramic parts (e.g., ± 25 μm = ± 0.001 in.) in small or large sizes. It can yield high production volumes (tens of thousands to millions), can be adapted to almost any design, and results in low labor and costs. Another advantage of injection molding is machining costs can often be minimized once die and tooling have been optimized. It avoids the limitations inherent to green-state machining of dry-pressed or extruded billets in that internal features are not limited by symmetry and can be very complex if desired. For example, a helical pattern can be incorporated in a coolant channel to better promote turbulent flow of the WEG.

Ceramatec Process

The Ceramatec process combines tape casting, laser machining of the green tapes, and lamination to produce ceramic components with complex internal channels. Fine tolerances can be achieved, and the process is mature and is under consideration for a wide range of ion transport membrane technologies. Large dimensions are achievable in two of the three dimensions. The mass production capability of this process is not as good as that of dry pressing, extrusion, or injection molding.

Numerous candidate ceramic manufacturers have been identified. All have large-scale ceramic manufacturing capabilities, presently have sizeable ceramic markets, and could satisfactorily manufacture the ORNL concept structure. All were contacted about the heat exchanger concept, and its manufacturability was discussed.

Chip Set Selection

The primary rating of a silicon device is its current-voltage (I-V) characteristics, which dictate how much current the device can conduct at the expense of the forward voltage drop. For IGBTs, these curves depend on the applied gate voltage and junction temperature. For diodes, the characteristic curves are temperature dependent. It was determined that a silicon device can conduct rated current up to its maximum rated junction temperature as long as the waste heat being produced is consistently removed. Because these architectures eliminate large thermal resistances, more heat can be removed. This additional heat removal allows the chip to conduct at the rated current up to its maximum junction temperature.

The IGBT selected for use in modeling was an Infineon Technologies "trench type" IGBT. This chip has a maximum voltage rating of 600 V and a maximum current rating of 200 A. It possesses low $V_{CE(sat)}$, low turn-off losses, short tail current, and a positive temperature coefficient allowing it to be easily paralleled. The diode selected for use was an Infineon Technologies fast-switching diode chip in EMCON 3-Technology. This chip has a maximum voltage rating of 600 V and a maximum current rating of 200 A. It

possesses soft, fast switching characteristics, a low reverse recovery charge, and a small temperature coefficient. Both devices have maximum temperature operating ranges of –40 to 175°C.

Establish Design Parameters for Finite Element Analysis on 3-Dimensional Models for Heat Transfer Optimization

Determine Appropriate Thermal Load for 3-Dimensional Models

In previous research and development efforts, two inverter ratings were used in thermal models: 55 kW peak and 30 kW continuous. A constant efficiency in the inverter over the entire operational range was also assumed in these previous efforts. Thus the thermal load could be determined for continuous and peak loading. However, these assumptions are not entirely valid. Data from ORNL's Semikron [3] testing (table below) show that waste heat magnitudes can approach maximum values while the output is below the peak power rating. This result is due to decreases in efficiencies based on running conditions.

Waste heat produced by Semikron inverter for different output powers

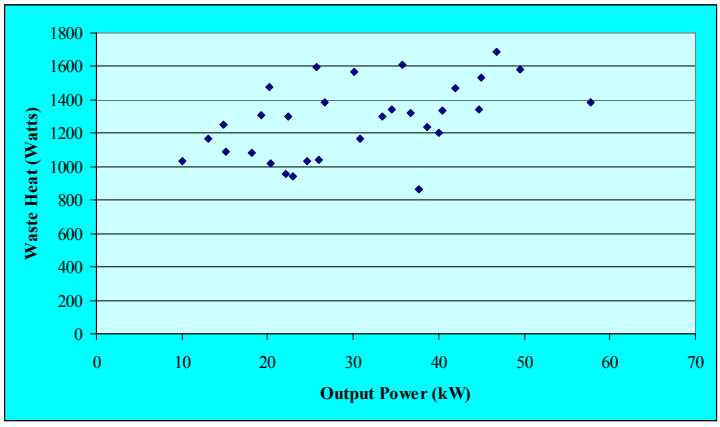

An approximate waste heat distribution for this architecture can be found using Semikron testing evaluation results and a maximum waste heat of 1,746 W. Assuming that the upper and lower leg of each phase will dissipate equal amounts of energy over an operational period, the heat loss per concept structure is 291 W. Each section will have two diodes and three or four IGBTs. It is assumed that the diode losses are about a third of the switch losses. This approximation is based on an application note from Semikron [4].

Using this ratio and four IGBTs per section implies that 75% of the loss will come from the switches and 25% from the diodes, or 54.6 W in losses per switch and 36.4 W in losses per diode. If three switches were used, the losses would be 72.75 W per switch and 36.4 W per diode. No attempt will be made to justify a continuous operating loss because of the efficiency dependency of the heat losses. Furthermore, using the maximum losses allows the design to be configured for the worst-case scenario. The design should then provide more than adequate cooling for transient power fluctuations and continuous load.

In this study, the heat load for the IGBT was varied to simulate the number of switches used for each half electrical phase. A minimum of three switches is required to achieve the current rating that is required for the inverter. Because the devices are being run on the upper end of their operational range, four switches may be used to spread the losses of the inverter out over a wider area and to add a margin of safety. The computer models will predict the maximum temperatures to determine if the selected chip population is a viable option.

Other Analysis Parameters

The fluid inlet velocity varied depending on flow channel size. Initial inlet velocity was consistent with a total inverter flow rate set at 2.5 gallons per minute (GPM). Each of the five designs should be able to pass a 1 mm particle through the flow channels; however, filtering of the coolant may be necessary; this will be determined during component testing. Fluid inlet temperatures were specified at 105°C. All other boundaries were modeled as thermally insulated. This assumption allows for a conservative design, and the actual thermal performance should result in lower junction and fluid temperatures because of other minor heat losses. The material properties used in the FEA modeling can be found in ORNL/TM-2008/112.

Determining the Thermal Performance Criteria

For a design to be considered successful, the thermal models must predict junction temperatures below 175°C and preferably below 150°C. Also, the coolant temperatures must be maintained below the boiling point of a 50/50 WEG mixture so that original equipment manufacturers (OEMs) do not have to alter system pressure ratings. Boiling points for 50/50 mixes of WEG for various system pressures can be found in ORNL/TM-2008/112. The coolant temperature performance criterion used in developing the models was limited to 130°C, which corresponds to 16 psig. As a consequence of concurrently satisfying these constraints and designing a practical direct-cooled ceramic substrate, five different substrate designs were ultimately considered.

Thermal FEA Results for 3-Dimensional Designs

Thermal Performance of Design 1

In Design 1, multiple flow channels are placed through the ceramic structure. They are equally spaced on a bolt circle that maintains a minimum distance of 0.050 in. between surfaces. The minimum distance is maintained to provide structural integrity and is based on ceramic manufacturing limitations.

When a load of 55 W per chip is applied, the maximum projected junction temperature is 141.7°C, and the maximum fluid temperature is 136.5°C for AlN. When Al_2O_3 is used, the projected junction temperature is 182.9ºC and the maximum fluid temperature is 163.0ºC. With SiC, the projected junction temperature is 144.7ºC and the maximum fluid temperature is 138.8ºC. If BeO is used, the projected junction temperature is 143.0ºC and the maximum fluid temperature is 137.5ºC. In each case using different ceramic materials, the maximum fluid temperature exceeds the boiling point with the load resulting from four switches. Therefore, no model needs to be run for the larger load that corresponds to three switches, as the increased load would increase both maximum junction temperature and fluid temperature.

Variations in the WEG mixture were investigated briefly to see if a temperature decrease would result from increasing the thermal conductivity of the solution. Solutions of 60/40 and 70/30 WEG were modeled. The maximum fluid temperatures did decrease but only by about a degree Celsius for each 10% reduction in ethylene glycol. Unfortunately, the boiling points also readjust for the new mix ratios. The boiling points also dropped by about a degree Celsius for each 10% reduction in ethylene glycol; thus the relative difference in maximum fluid temperature to allowable boiling points was constant. Therefore, no noticeable benefit is obtained from altering the fluid mixture from 50/50 WEG.

Thermal Performance of Design 2

Because Design 1 resulted in a maximum fluid temperature that exceeded the boiling point, other options were explored. In order to enhance the thermal conductivity of the fluid, a thermal enhancement material was added to the flow channels. The addition of a thermal enhancer into the flow channels provided a greater surface area within the flow channel to remove the waste heat more efficiently. The selected

material has a much higher structural integrity compared with other types of microstructures and provided a simple means of manufacturing.

The properties for the flow channel must be adjusted to reflect the addition of the thermal enhancement material. Also, the velocity of the inlet must be calculated for an effective area, because the thermal enhancement material blocks some of the inlet area. The material properties of the thermal enhancement material used in modeling the thermal data can be found in ORNL/TM-2008/112. Plug flow was assumed for the flow channels. This assumption is valid based on Darcy's Law for flow through porous media. In short, the thermal enhancement material prohibits boundary layer formation along the walls of the channel, which results in plug type flow.

The maximum fluid temperature is 122.7°C and the maximum projected junction is 129.3°C for AlN with an aluminum thermal enhancement material added to the flow channel and four switches. If BeO is used, the maximum junction temperature is 130.6ºC and the maximum fluid temperature is 123.1°C. When Al_2O_3 is used, the maximum junction temperature is 171.5°C and the maximum fluid temperature is 133.4°C. If SiC is used, the maximum junction temperature is 131.9°C and the maximum fluid temperature is 123.7°C. Results of the model containing an alternative thermal enhancement material in the flow channel can be found in ORNL/TM-2008/112.

The thermal enhancement material adds another benefit in that it can restrict bubble growth in the event of boiling. In an open channel design, bubbles can grow to the point of blocking flow. Furthermore, as a bubble develops on the wall, it creates a local hot spot which could be detrimental to a chip. The thermal enhancement material limits the bubble growth size. Thus if boiling were to occur, which the models do not predict, it could neither significantly block the flow nor create a large hot spot near the wall.

Thermal Performance of Design 3

Design 3 contains one coolant flow channel. This flow channel is filled with a thermal enhancement material. Using a total of four switches and a thermal enhancement material, the maximum junction temperature for AlN is 142.3°C and the maximum fluid temperature is 126.1°C. For BeO, the maximum junction temperature is 143.8°C and the maximum fluid temperature is 126.3°C. If Al_2O_3 is used, the maximum junction temperature is 224.4°C and the maximum fluid temperature is 127.9°C. If SiC is used, the maximum junction temperature is 145.9°C and the maximum fluid temperature is 126.4°C. For three switches using AlN, the temperatures remain within the performance criteria with a maximum junction of 147.9°C and a maximum fluid temperature of 125.6°C. Results of the model containing an alternative thermal enhancement material in the flow channel can be found in ORNL/TM-2008/112.

Thermal Performance of Design 4

After the previous designs for all materials were examined, it became obvious that it would be necessary to explore lower-cost options for the higher-thermal-conductivity materials (AlN, BeO, and SiC). Even though their thermal performance is far superior to that of Al_2O_3, substrates made of these materials would cost almost as much as the whole inverter at the current OEM's cost target. Additionally, concern was beginning to mount over the chemical compatibility of AlN with WEG (and therefore the potential for AlN erosion), lending a further rationale for considering Al_2O_3 because it is chemically inert against WEG.

In this geometry the minimum distance from the exterior of the ceramic shape to the flow channel can be smaller than in the previous models. This smaller distance is a result of an increase in local velocities created by the unique shape. In this design, the maximum chip temperature is 152°C and the maximum fluid temperature is below 125°C. Again, these temperatures satisfy the design temperature constraints. FEA results and probabilistic life design analyses showed that the maximum first-principles tensile

stresses from thermal loading were low and easily within the mechanical capability of the Al_2O_3 ceramic. The probability of survival analysis showed that 999,992 out of 1,000,000 ceramic structures (99.9992%) should sustain the imposed thermomechanical stresses without mechanical failure. Further optimization of this geometry could be explored to increase the probability of survival, but this model shows that an Al_2O_3 ceramic geometry is possible and actually quite viable.

This design also adds some other benefits. A common product with thermal enhancement material is a pipe with the enhancement material bonded onto the outer surface. In Design 4, this thermal enhancement subassembly could be pressed into a larger hole to form the annulus. The ends of the subassembly would have to be brazed closed to prevent a fluid bypass. However, the overall effect would reduce the weight of the substrate and should keep cost lower because less Al_2O_3 is needed to make the part than in a part with a solid core.

Thermal Performance of Design 5

To provide another design option with Al_2O_3, a multiple-flow channel design was explored. In this design process, the size of the flow channel filled with a thermal enhancement material, and the flow channel center location, were varied to determine an optimum design. In the final design iteration, the center of the hole was offset from the center of the chip to provide the coolest chip temperatures. The resulting temperatures proved that the offset dimension was critical for this design to meet the performance criteria.

The FEA ran on this model used a top silicon chip heat generation of 37 W to represent a diode and a side silicon chip heat generation of 55 W to represent an IGBT. The maximum chip temperature is 153°C and the maximum fluid temperature is below 125°C, and those meet the design temperature constraints. Again, these temperatures meet the maximum limits of the design parameters. FEA results and probabilistic life design analyses showed that the maximum first-principles tensile stresses from thermal loading were low and easily within the mechanical capability of the Al_2O_3 ceramic. The probability of survival analysis showed that 999,906 out of 1,000,000 ceramic structures (99.9906%) will sustain the imposed thermomechanical stresses without mechanical failure. Further optimization of this geometry could be explored to decrease the face-to-radius distance and increase the probability of survival, but this model shows that an Al_2O_3 ceramic geometry is possible and actually quite viable.

Design Results

Because of cost limitations, Designs 1–3 had to be modified in order to meet the design goals. These changes resulted in Designs 4 and 5, which show that 105°C coolant can be used with an Al_2O_3 substrate. These substrates will be joined by a manifold placed inside the capacitor. This design layout is similar to the refrigerant-cooled inverter researched by ORNL [5].

The capacitor(s) necessary to complete the inverter design dictates the overall volume of the direct-cooled power electronics substrate. Since this component has a larger volume than many of the other required components, volume reduction can be limited by the physical size of the capacitor. Based on capacitor designs obtained from the SBE, Inc., Power Ring Division, the preferred design in this research and development effort has a power density approaching 14 kW/L. However, this preferred design uses a ceramic substrate with a high-thermal-conductivity capability, which comes at a higher cost. If a lower-cost ceramic substrate is used, such as alumina, the cost is significantly reduced but the power density approaches 7.5 kW/L because of the size of the substrate necessary to spread the thermal load.

Cost Comparison

The direct-cooled power electronics substrate project is a totally new concept and therefore untried in industry. Costs can be quantified on conventional inverter architectures based on component purchase prices, material costs, and manufacturing assembly costs. The tangible expenses in this research effort are

material costs, fabrication costs for ceramic components, and estimated cost savings from the elimination of the conventional heat sink, the base plate/heat spreader, and the thermal interface material (TIM). Each of the ceramic fabrication costs is listed in the table below and is based on material and tooling costs per 100,000 pieces.

Table 2. Cost summary for ceramic materials considered in the fabrication of a direct-cooled power electronics substrate

Description	Material extrusion cost	Copper plating	Purchase price	Total cost per inverter
Aluminum nitride	$45.87	$3.12	$48.99	$293.94
Alumina	$2.97	$3.12	$6.09	$36.54
Silicon carbide	$30.25	$3.12	$33.37	$200.22
Beryllium oxide	$19.59	$3.12	$22.71	$136.26

If the ceramic of choice in the final inverter design were Al_2O_3, based on the information in the table above, the cost to produce the copper-plated ceramic substrate in a quantity of 100,000 units would be approximately $36.54. The savings from a conventional inverter, such as Semikron, would be $64.02 from just the elimination of the heat sink and the base plate. Additional savings would be realized by the elimination of the TIM, as well as a weight savings of ~3 kg per inverter in this research effort because the base plate and heat sink would not be required. These cost savings do not take into account the wire bonds or the cost of the IGBTs and diodes or the capacitor, since these costs are widely known for any inverter structure in mass production.

Design Matrix Summary

To help evaluate the effectiveness of each design, a performance matrix and weight system was developed. It contains the loads, thermal data, manufacturing variables and trade-offs, and cost. In addition, velocities were determined for each design that exceeded the performance criteria to determine how much flow increase would be required to meet the design intent. This increase in velocity was helpful in determining the preferred designs; however, an OEM recommended the volumetric flow rate be maintained at a maximum of 2.5 GPM. For a complete design matrix summary of each design, please refer to ORNL/TM-2008/112. Designs 4 and 5 meet the OEM's cost and performance targets.

Conclusion

This research effort concludes that directly cooling an Al_2O_3 ceramic substrate with 105°C coolant while maintaining silicon temperatures below their maximum operation temperature is viable. The shape of the substrate, the size and shape of the capacitor, the coolant flow channels, a thermal enhancement material placed within the flow channels, and the chip population on the substrate all play a key role. The unique shape of the designs discussed in this report were chosen because the required surface area could be obtained within the smallest package volume. Additionally, the unique structure of the shape is far easier to seal from the coolant than other types of planer structural shapes.

The addition of a thermal enhancement material into the flow channels provided a greater surface area within the flow channel to remove the waste heat more efficiently. This thermal enhancement material has a much higher structural integrity than other types of microstructures and provided a simple means of manufacture. FEA results were run using two types of thermal enhancement material; however, cost, availability, and environmental concerns due to manufacturability of the higher-thermal-conductivity material steered this research effort toward a more cost-effective approach.

The capacitor(s) necessary to complete the inverter design dictates the overall volume of the direct-cooled power electronics inverter. Since this component has a larger volume than many of the other required

components, volume reduction can be limited by its size. The preferred design in this research and development effort has a power density approaching 14 kW/L. However, this preferred design uses a ceramic substrate with a high-thermal-conductivity capability, which comes at a higher cost. If a lower-cost ceramic substrate is used, such as alumina, the cost is significantly reduced but the power density approaches 7.5 kilowatts kW/L as a result of the size of the substrate necessary to spread the thermal load.

Performance testing of Designs 4 and 5 will be performed to validate the FEA results. These designs meet the specified design criteria while providing a lower cost to the OEMs. Additionally, Designs 2 and 3 met the specified design criteria but at a higher cost. They could be constructed with three or four chips so long as the coolant system pressure is kept high enough to prevent boiling but low enough that the OEMs do not have to alter conventional radiator components. For initial bench testing in FY 2009, diodes will be used on Designs 4 and 5 to generate the waste heat needed to validate the modeling.

Publications

R. H. Wiles, C. W. Ayers, A. W. Wereszczak, and K. T. Lowe, *Direct Cooled Power Electronics Substrate,* ORNL/TM-2008/112, Oak Ridge National Laboratory, 2008.

Kirk T. Lowe and Rao V. Arimilli, "Application of Solution Mapping to Reduce Computational Time for Actively Cooled Power Electronics," in *Proceedings of the 4th Annual Comsol Conference*, in press.

References

1. Chung-Daw Young and Jeng-Gong Duh, "Corrosion of aluminum nitride substrates in acid, alkaline solutions and water," *Journal of Materials Science,* **30**(1), 185–195 (January 1, 1995).
2. S. Fukumoto, T. Hookabe, H. Tsubakino, "Hydrolysis behavior of aluminum nitride in various solutions," *Journal of Materials Science,* **35**(11), 2743–2748 (June 2000).
3. *Testing of the Semikron Validation AIPM Unit at the Oak Ridge National Laboratory – January 2005*, ORNL/TM-2005/44.
4. P. Salvati, F. Brucchi, and A. De Medici, "Sinusoidal inverter using SEMITOP® modules for electric vehicles applications," Application Note: SemiKron.
5. "Thermal control for inverters and motors," in *Annual Progress Report for the Advanced Power Electronics and Electric Machinery Program,* Oak Ridge National Laboratory, 2007.

Patents

Randy H. Wiles, Andrew A. Wereszczak, Curtis W. Ayers, and Kirk T. Lowe, "Direct Cooled Power Electronics Substrate," provisional patent number 61/037,129, March 17, 2008.

2.2 Characterization and Development of Advanced Heat Transfer Technologies

Principal Investigator: Thomas P. Abraham
National Renewable Energy Laboratory
1617 Cole Blvd.
Golden, CO 80401-3393
Voice: 303-275-3084; Fax: 303-275-4415; E-mail: thomas_abraham @nrel.gov

DOE Technology Development Manager: Susan A. Rogers
Voice: 202-586-8997; Fax: 202-586-1600; E-mail: Susan.Rogers@ee.doe.gov

NREL Task Leader: Kenneth Kelly
Voice: 303-275-4465; Fax: 303-275-4415; E-mail: kenneth_kelly@nrel.gov

---

Objectives

The key objective of this task is the characterization and development of advanced heat transfer technologies that would enable increased power density, lower cost materials, and the elimination of the secondary coolant loop. The uniqueness of this task is the development of candidate technologies for meeting all the three key targets (performance, cost, and reliability) of the U.S. Department of Energy (DOE) Vehicle Technologies Program's Power Electronics and Electric Machines (PEEM) program area.

- Reduce the thermal resistance to allow the use of higher temperature engine coolant at 105°C (today's coolant temperature for power electronics is 70°C) to cool the electronics, while keeping the temperature of silicon-based chips below the required temperature limits.
- Enabled by advanced thermal control (advanced cooling technologies in conjunction with novel packaging topologies), explore low-cost materials for cost-reduction.

Approach

Today's cooling methodology typically involves the use of a fin-based heat exchanger wherein the coolant enters at one end, absorbs heat from the dies (insulated gate bipolar transistors [IGBTs] and diodes) while traveling to the outlet, causing nonuniform temperature distribution across the IGBTs and the diodes. To meet the program dissipation target of 200-250 W/cm^2 and the reliability target (a life of 15 years), a more advanced thermal control is needed. For high dissipation levels, microchannel-based cooling is very promising. A microchannel-based heat sink optimized using first-order correlations was able to dissipate 500 W/cm^2 with a coolant-to-junction temperature rise of about 75°C [4]. A major drawback in the use of microchannels is that the higher pressure losses across the channels can quickly exceed the maximum pump capacity at these small dimensions. Cooling with a spray nozzle array achieved a dissipation rate of 165 W/cm^2, with a temperature rise of 22°C and a high pressure drop penalty of 40 psi [5]. Jet impingement cooling with microjets was able to dissipate 56 W/cm^2 with a temperature rise of 20°C and a high pressure drop of 24 psi [6].

For achieving dissipation rates in excess of 200 W/cm^2 with low pressure drops (well below 3 psi), NREL is developing next-generation cooling technology, which involves a combination of novel packaging topology and mesoscale jet impingement cooling in conjunction with surface enhancement. When used along with the double-sided cooling concept , this technology has the potential to extend dissipation rates with macroscale heat transfer to 400-500 W/cm^2, levels typically associated with microchannels. Thermal control that allows such high levels of dissipation would enable the use of low-cost materials, which typically have thermal disadvantages, like the low-temperature co-fired ceramic (LTCC) substrates.

Today's preferred substrate, aluminum nitride (AlN), is expensive. NREL is thus developing advanced thermal control that would enable AlN to be replaced with a low-cost substrate like alumina. The cold plate is another layer that presents a real opportunity for reductions both in cost and weight. The use of jet cooling may enable natural plastics to be used for the cold plate, thus making it cheaper and lighter.

Thermal control technologies should meet the key requirements for power electronics, such as target values for volume, cost, weight, and parasitic power. The key performance indicator for thermal control technologies is the maximum temperature limit apart from pressure drop. Simplicity, reliability, and a reduced number of components are also important objectives in the overall design of cooling systems. For cost reduction, low-cost materials are being explored that are enabled by a combination of advanced cooling technologies in conjunction with novel alternate packaging topologies, i.e., advanced thermal control. During the next fiscal year, efforts would focus on the development of low-cost power electronics (PE) thermal packaging while meeting the targets of performance and reliability.

NREL has collaborated with an inverter manufacturer, Semikron, within the framework of a cooperative research and development agreement (CRADA) to build a prototype of the heat exchanger based on the latest version of direct backside cooling design Partnering with Semikron allows the development and demonstration of the direct backside cooling concept as applied to a real-world inverter. It also helps to address questions about the reliability of the concept. The overall concept is not limited to the Semikron inverter; rather, it is applicable to any power conversion application. NREL has held discussions on this promising technology with the U.S. automotive industry and was successful in generating interest in this novel concept. Thermal testing was completed during FY 2008. Design iterations during previous fiscal years has led to the current design version, which is referred to in this report as Gen14. The pressure drop of Gen14 design is about half that of the Semikron baseline design with the elliptical pin-fins. Reduced pressure drop translates to a lower parasitic power, which means a smaller pump would be needed for dissipating the same level of heat. During the thermal testing, Gen14 provided lower and more uniform temperatures across all the IGBTs and the diodes when compared with the baseline design.

Developing this low-cost thermal solution—which meets the targets of performance, cost, and reliability—would help the U.S. automotive industry eliminate a separate cooling loop by allowing the use of general engine coolant at 105°C to cool the power electronics unit directly. It would also reduce the weight of the heat exchanger as a result of the eliminating the layers and enabling the use of lighter plastics for cold plates. This task would aid DOE in achieving one of its major targets—using a 105°C coolant inlet temperature for cooling power electronics.

Major Accomplishments

During the previous fiscal years, NREL developed a novel packaging topology based on direct backside cooling that eliminated several layers in the structure of IGBT packages to increase cooling effectiveness with a 105°C inlet coolant temperature [2, 3]. A state-of-the-art review of high-heat-flux cooling technologies identified direct backside cooling as a very promising technology for the near term [7]. NREL researchers were awarded a U.S. patent (number 7190581) during FY 2007 for this concept [10]. Simulations showed that it was possible to dissipate 90 W/cm^2 with a coolant-to-junction temperature rise of 21^{o}C . Thermal testing during the FY 2008 showed the dissipation level to be 92 W/cm^2 with the same temperature difference, providing confidence in the model's predictive capabilities. In comparison, Prius technology is able to dissipate at about 60 W/cm^2 with a temperature difference of about 50^{o}C [3].

Accomplishments during FY 2008

- Completed thermal testing of heat exchangers based on both baseline elliptical pin-fins and Gen14. The thermal resistance of Gen14 is 31% lower in comparison to that of the baseline elliptical fin-pins. Temperature distributions of devices were lower and more uniform with Gen14. This superior

performance becomes significant at higher power levels with the use of engine coolant. To meet the life target of 15 years, it is important that the dies operate cooler and that the temperature distribution is uniform.
- Verified that predictions with computational fluid dynamics (CFD)/thermal models were very close to the test data, providing confidence in the models' predictive capabilities.
- In response to a suggestion from Semikron, developed a concept based on baseplate cooling that was shown to be 30% better in comparison to the baseline elliptical pin-fin design.
- Demonstrated, through preliminary studies with thermal materials, that using advanced thermal control (advanced cooling technologies in conjunction with novel packaging topologies), it is possible to replace the traditional, expensive AlN substrate with low-cost alumina.
- Demonstrated that the direct backside cooling concept has the potential to reduce costs.

Future Direction

FY 2008 thermal testing validated the concept developed over the previous fiscal years. With the direct backside cooling concept providing an opportunity for cost reduction, one of the next steps is to realize its potential for cost reduction in a real-world inverter. We plan to make design changes to direct bonded copper (DBC) to take advantage of spreading physics at expected operating velocities. Today's trench IGBT technology allows a coolant-to-junction temperature rise of 45°C while planar IGBT technology allows 20 °C. With trench IGBT technology, using the extra parameter of surface enhancement along with improved spreading, it would be possible to increase the heat dissipation levels to 200-250 W/cm^2.

When used along with a double-sided cooling concept, NREL's cooling technology has the potential to extend the dissipation levels with macroscale heat transfer to 400-500 W/cm^2.

One of the key concerns is erosion/corrosion over time. One of the potential partners for addressing this real-world issue is the Corrosion Technology Laboratory at NASA's Kennedy Space Center. Another concern is the degradation of the DBC structure due to dynamic impacts from jets over time. We would be conducting dynamic impact tests over about 1000 cycles, taking an image with a scanning electron microscope (SEM)/X-ray and looking for possible degradation of the DBC.

Areas of Focus for FY 2009

Surface enhancement studies: Previous approaches to meeting the performance target came with a very high pressure drop penalty [5, 6]. This research activity aims to meet the performance target with low pressure drop (well below 3 psi). The key technology that would enable meeting the performance target without a high pressure penalty is surface enhancement. For example, for the Semikron inverter with 54 dies (36 IGBTs and 18 diodes), 54 jets is an optimal number with constraints such as the minimum velocity needed to obtain good heat transfer performance, a minimum jet diameter to prevent clogging, and uniformity in heat transfer performance. With 54 jets and a jet diameter of 1.5 mm, the heat transfer coefficient is about 18,500 W/(m^2.K), while the targeted value is about 50,000 W/(m^2.K). Extra levels of heat transfer would be obtained from surface enhancement with low pressure drops. Broad classes of surface enhancements to be explored are protrusions, coatings, and etching (micro/macro).

Low-cost PE thermal packaging: To achieve wider penetration into the vehicles market, cost is a key target for the DOE program. Low-cost materials would be identified using advanced cooling technologies in conjunction with novel packaging topologies. With industry inputs, researchers would identify shapes that enable "net-shape" processes. The geometrical shapes that enable "net-shape" processes eliminate the expensive step of machining.

Tools for Characterization and Development during FY 2009

Development of flow/thermal visualization capabilities: The use of liquid crystals as particle tracers has been demonstrated as a useful tool for the visualization of flow and temperature fields for a jet impinging on a hot target surface [8]. The impinging jet could be seeded with liquid crystals. Visualization with liquid crystals is expected to reveal more details of the flow/thermal fields as opposed to the traditional approach of measuring just global parameters like the heat transfer coefficient and the pressure drop.

Mesh-morphing-based optimization studies: Optimization tools based on mesh morphing are currently under development. Optimization studies would be performed with respect to the jet diameters, distance between the jets, number of jets, target distance, inlet/outlet regions, and other parameters. There would be a major focus to apply these optimization tools to real-world heat exchangers.

Efforts that Feed into Other Research Activities during FY 2009

Reliability studies: Even though direct backside cooling is very promising from the standpoint of heat transfer, long-term reliability is a concern. For the optimized design, reliability studies would be conducted. Reliability aspects would also be studied for low-cost topologies and materials. There is a separate task to address this key target.

Technologies and Tools for the Long Term

Two-phase cooling: The interest in weight reduction appears to be increasing in the automotive industry. Two-phase cooling technology is a candidate for meeting this target because of its enormous potential to enhance power density, thus making the system more compact and lighter. For an accurate modeling of boiling jet dynamics, a state-of-the-art mechanistic boiling model would be improved in conjunction with Fluent, a commercial CFD software.

Microchannels: For dissipation levels in excess of 300 W/cm^2, cooling technologies based on microchannels are candidates. Interest appears to be emerging in the automotive industry for applications with higher fluxes.

Electrical actuation: Even though microchannels have the potential to provide high heat fluxes with low thermal resistances, they typically come with a penalty i.e., high pressure drop. One possible alternative is to replace the mechanical pumps, which are optimized for use at macroscales, with micropumps that are more relevant for use at microscales.

Technical Discussion

Insulated gate bipolar transistors used as switches in power electronics are subjected to high thermal loads when heat (about 2500 W) is generated because of inefficiency. Lower and uniform die temperatures enable improved electric performance as well as the reliability of the IGBTs and the diodes. If the thermal resistance from the die to the coolant can be reduced, higher power densities can be achieved for the same level of cooling. Conversely, it also means that, with the same heat dissipation level, the die temperature can be lowered. It may be possible to have the IGBTs operate at high temperatures by using advanced materials like silicon carbide (Si-C). Today's industry standard, trench IGBTs allow die operating temperatures of 150°-175°C, while Si-C devices allow even higher die operating temperatures.

Figure 1 shows a cross-sectional view of a typical IGBT package. Most of the thermal resistance comes from the thermal grease because of its low thermal conductivity. Thermal greases are good from the standpoint of reliability, but they have very low thermal conductivities—in the range of 0.3 W/mK to 0.5 W/mK. The interface between the power module and the heat exchanger contributes about 40% to 50% of the total thermal resistance of the IGBT structure.

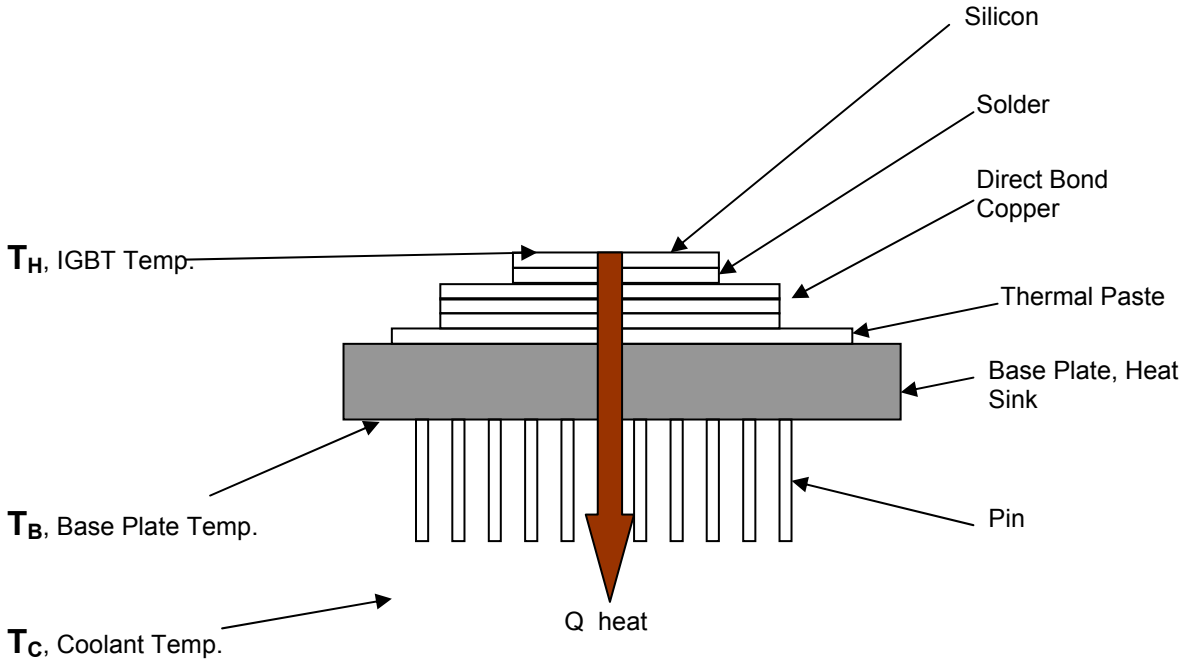

Fig. 1. Typical IGBT Structure with Different Layers and Heat Flow Path

An exploded detailed view of the Gen14 design is shown in Figure 2. The aluminum base plate, nozzle plate, and flow channel plate have been designed as individual components to reduce the cost of fabrication. Structural simulations during the previous fiscal years showed that the maximum stresses and deflections (for the design shown in Figure 3) to be compatible with Semikron's assembly process, which applies 3000 psi to the DBC during assembly.

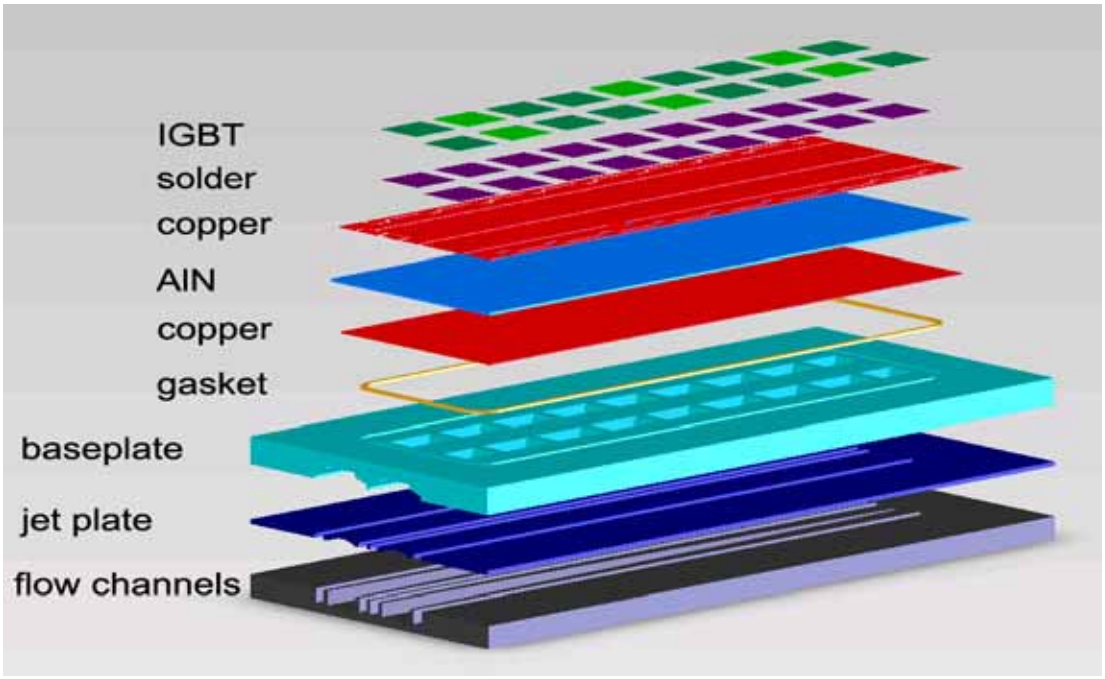

Fig. 2. Detailed View of Low-Thermal-Resistance IGBT Structure in Gen14 Design

CFD simulations from the previous fiscal year showed that, for the total flow rate of 10 lpm, flow rates across the individual jets are fairly uniform, with a variation of less than 8%. Researchers surmised that, once the outlet plenum fills up, a fairly constant outlet pressure develops that causes almost equal flow from the individual jets. Uniformity in flow and temperature across these nozzles is required to achieve temperature uniformity across all the dies.

Thermal Testing

A high-heat-flux test-loop facility developed by NREL is shown in Figure 4. It consists of a reservoir, pump, filter, mass flow meters, turbine flow meters, and valves for regulating flow rates. The loop is fully instrumented with pressure sensors, thermocouples for monitoring temperatures, and a data acquisition system controlled by LabView.

Fig. 3. Gen14 Design with Nozzle, Baseplate, and DBC

As noted earlier, it was shown during the previous fiscal year that the pressure drop for the Gen14 design is about half that of the baseline design. It is important to note that the baseline design has a single inlet/outlet, while the Gen14 design has two inlets/outlets. It appears that a significant amount of pressure drop is occurring near the inlet/outlet, which is the possible reason why the Gen14 design has a lower pressure drop.

For this milestone report, thermal test data only for a flow rate of 10 lpm would be presented, since the Gen14 design is optimized for 10 lpm. A forthcoming report would provide all the details of thermal testing along with the test data for all the power inputs (500 W and 1000 W) and flow rates (5, 10, and 15 lpm). The Semikron inverter was powered with ABC-1000. The ABC-1000 is a bidirectional, computer-controlled two-channel DC power processing system offering superior accuracy and flexibility. The ABC-1000 offers power up to 125 kW, with a voltage range of 8 to 420 VDC and a current range of ±1000ADC. As shown in Figure 4, the Semikron inverter, along with the heat exchangers, were insulated. Figure 5 provides a schematic for T-type thermocouple locations relative to the inverter. A total of four dies (two IGBTs and two diodes) per phase were instrumented, for a total of 12 instrumented dies for the

complete inverter. Since the inverter was shipped to us fully enclosed in the plastic cover, it was not possible to directly calibrate the thermocouples. We had control over inlet/outlet thermocouples. Inlet/outlet thermocouples were calibrated using a calibration bath. Along with these two calibrated thermocouples, the inverter with its 12 instrumented thermocouples was fully soaked in the environmental chamber at constant temperatures. The environmental chamber has a temperature range of -40^{o}C to 190^{o}C with humidity control, computer controllable and programmable, and has a data acquisition system that is isolated for accurate and safe high-voltage thermal and electrical measurements. Using the calibrated inlet/outlet thermocouples as references, we generated calibration curves for the 12 thermocouples.

While powering the IGBTs, we did not use gate electronics. The gate driver board was powered directly with 15 V. After the thermal testing with the baseline design was completed, the inverter was carefully disassembled from the heat exchanger and then reassembled onto the Gen14 design. This enabled us to use the same calibrated thermocouples for testing the Gen14 design. A liquid gasket was used for sealing. Using a liquid gasket aids in conducting testing without a detailed, robust gasket design. A better sealing design is recommended for use in a real-world inverter.

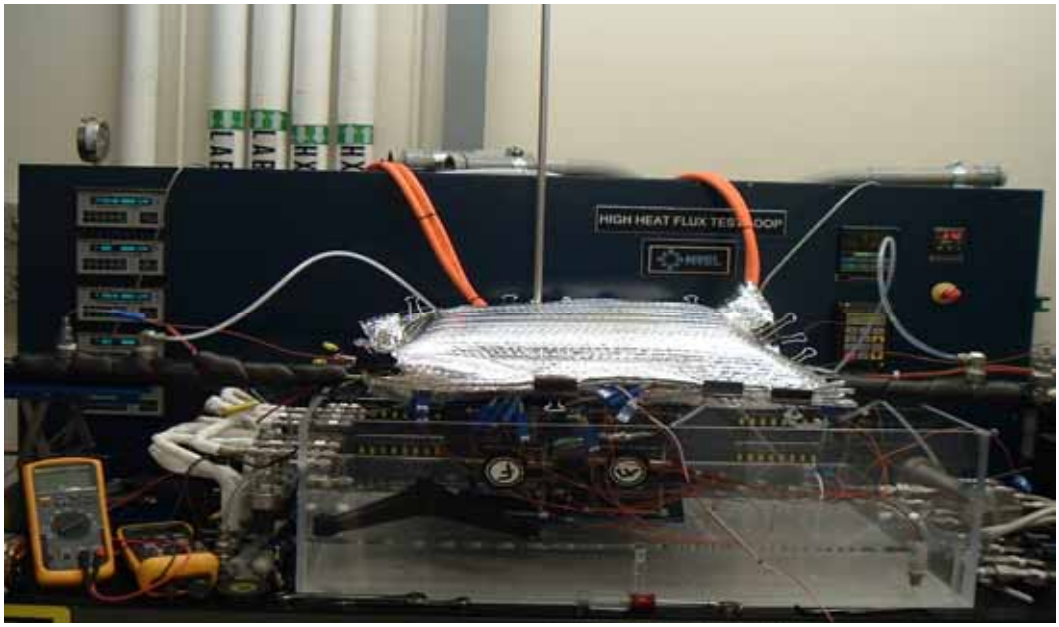

Fig. 4. High-Heat-Flux Test Facility Used for Thermal Tests

Figure 6 shows the thermal test data when all the IGBTs were powered with a total heat of about 1000 W for both the baseline and Gen14 designs at 10 lpm. Since the inverter is operating without any external load, IGBTs act as resistive loads, and the complete power input is dissipated as heat through the 36 IGBTs. As expected, for the baseline design, there is a linear gradient in temperature for both the powered IGBTs and unpowered diodes between the inlet and the outlet. For the Gen14 design, there is no such temperature gradient. Gen14 provides a more uniform coolant temperatures across all the IGBTs and the diodes in comparison to the baseline design. Also, both the IGBTs and the diodes were cooler for Gen14 when compared with the baseline design. This represents a marked improvement over the existing technology that sweeps coolant from one end to another— picking up heat along the way. Thermal resistance is computed as follows:

$$R_j = \frac{(T_j - T_c)}{Q} . \quad (1)$$

Here, R_j is the thermal resistance, T_j is the junction temperature, T_c is inlet coolant temperature, and Q is the heat input.

The measured thermal resistance from the junction to the coolant for Gen14 design is 31% lower in comparison to the baseline design. The peak die temperature among all the dies was used as the junction temperature. It is important to note that inverters are typically sized for peak temperatures and not the average. This level of improvement becomes very significant at higher power levels with the use of engine coolant. The variation of temperatures among the devices is an important parameter that could impact the reliability of the inverter modules. For the baseline design, the temperature difference between the IGBTs near the inlet and the one close to the outlet is given as follows:

$$delT = \frac{Q}{mC_p} . \quad (2)$$

Here, *delT* is the temperature difference between the IGBTs near the inlet and the outlet, Q is the heat input, m is the mass flow rate, and C_p is the specific heat of the coolant.

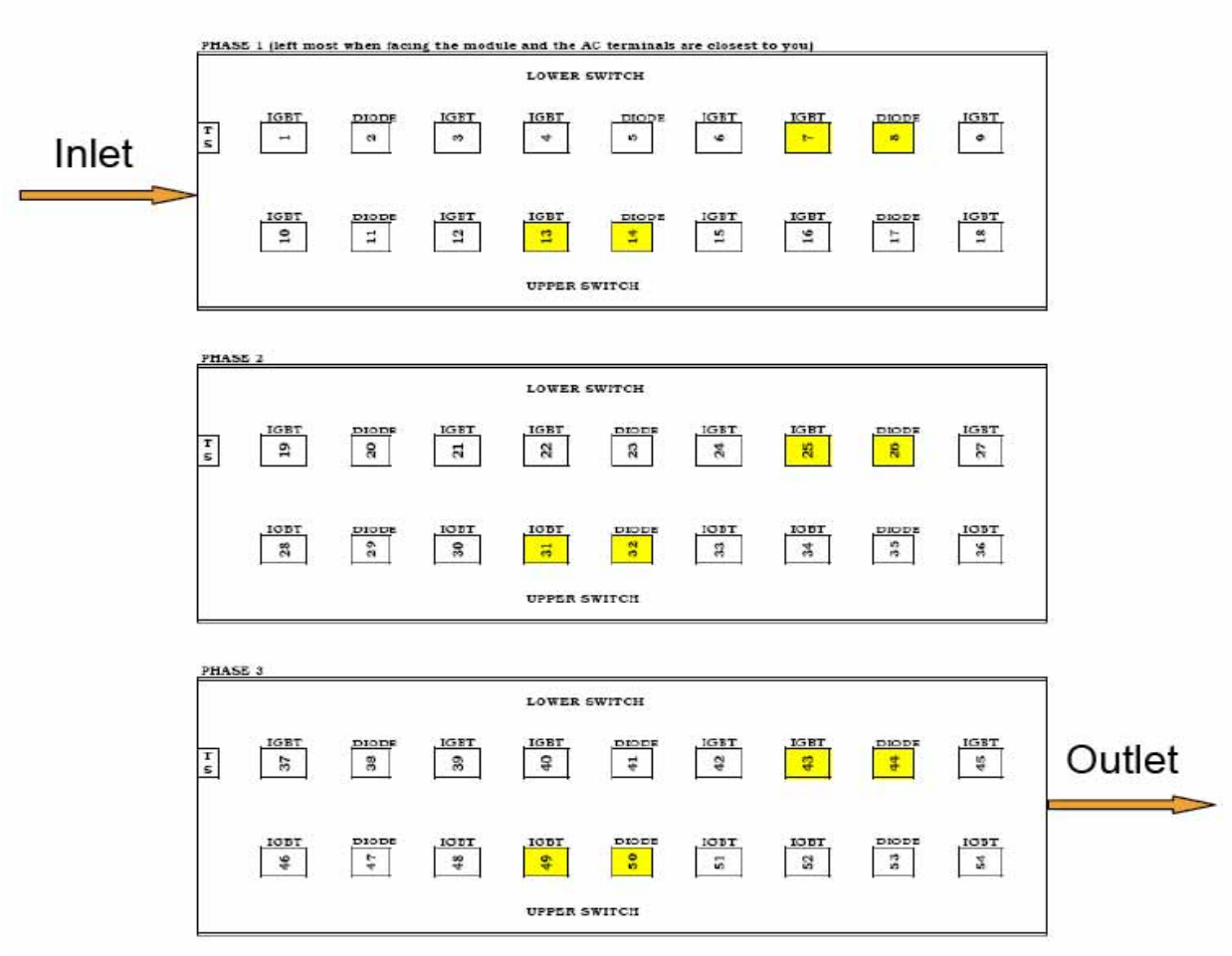

Fig. 5. Schematic of Thermocouples and their Locations Relative to the Inverter

For the baseline design, *delT* increases directly with high power levels and with the use of engine coolant. It is important to note that due to thermoelectrical interactions in the actual inverter, *delT* for the baseline design will be more than that given by Equation (2). For the Gen14 design, *delT* is expected to stay quite close to zero, even at higher power levels and with the use of engine coolant.

This means that the Gen14 design has IGBTs running not only cooler, but also more uniformly. The Gen14 design is expected to have exceptional performance in comparison to the baseline design when thermal reliability aspects become very critical with the use of high-temperature coolant. Figure 7 shows a similar trend, when all diodes are powered with 500 W at 10 lpm. The thermal resistance with Gen14 is 28% lower in comparison to that of the baseline design. In an actual operation, IGBTs run hotter when compared with the diodes. Hence, the improvement observed with IGBT powering is more relevant. Again, the temperature distribution between the diodes with the Gen14 design is more uniform that that of the baseline design.

Concept for 30% Performance Improvement – Baseplate Cooling

Based on a suggestion from Semikron, a CFD/thermal model of a baseplate cooling version was developed. In comparison to baseline design, a layer of cold plate is eliminated and the baseplate is cooled directly. The baseplate thickness used was 6.35 mm. The thickness of the thermal interface material (TIM) used was 21 microns. On the wetted surface of the baseplate, a surface enhancement factor of 3 was assumed. Figure 8 shows that direct cooling of the baseplate with surface area enhancement shows the potential to be 30% better in comparison to the baseline elliptical pin-fin design. In reality, the effective area available for heat removal would be less in comparison to the geometrical area. For this study, the TIM is used between the power module and the baseplate (specific to the Semikron inverter). This concept would be more promising in terms of thermal performance for the topology in which the power module is soldered to the baseplate. With the integration of heat pipes, this concept is expected to extend the improvement in performance to 60%. The baseplate cooling concept is being actively pursued in industry.

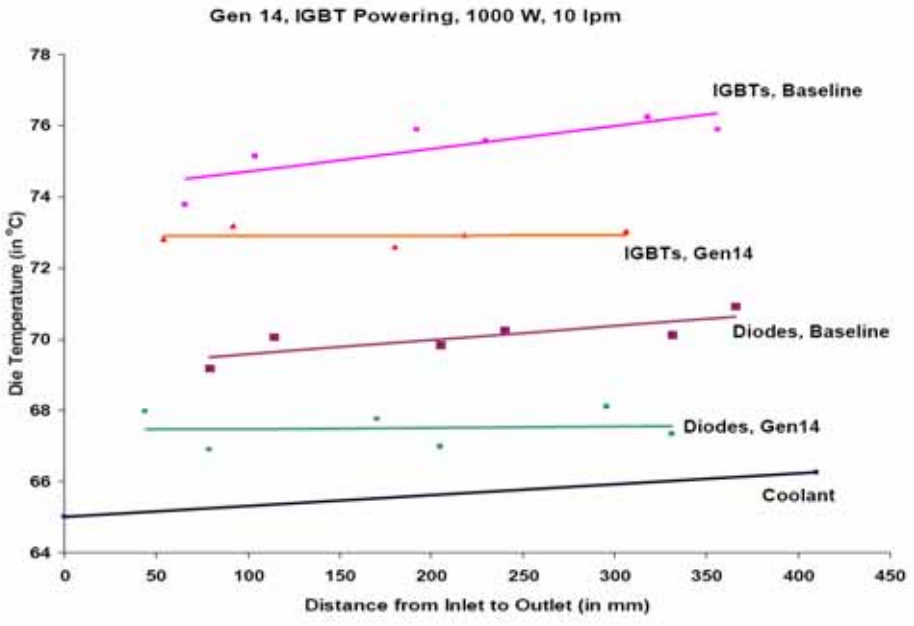

Fig. 6. Die Temperatures with IGBT Powering (1000 W, 10 lpm)

Jets Study

One of the concerns with the use of jets is localized cooling. A study was conducted to understand the effect of jet diameters on the distribution of the heat transfer coefficient. Jet diameters of 1.5 mm, 2 mm, and 3 mm were used. The inlet velocity was fixed at about 1.7 m/s. Figure 9 shows the distribution of the heat transfer coefficient in the radial direction. Distribution becomes more uniform when the diameters of jets increase, because the stagnation region at the point of impact gets smaller with increased jet diameters. This implies that, for package configurations that need fewer jets, larger diameter jets could be used for more uniform heat transfer distribution.

Materials Exploration Study for Cost Reduction

With cost as the key target, preliminary studies were conducted for identifying low-cost materials enabled by a combination of advanced cooling technologies in conjunction with novel alternative packaging topologies (advanced thermal control). Topologies used in the study are shown in Figure 10. Prius uses the Baseline Topology. The transitional topology, Topology 1, is very similar to the Baseline Topology but without pin-fins. In the case of Topology 2, the power module is soldered onto the base plate, which is cooled. This is the topology for the near term and is currently being pursued in industry. NREL is currently pursuing the next-generation topology based on direct backside cooling, Topology3. Studies showed that, enabled by advanced thermal control, it is possible to replace traditional, expensive AlN with low-cost alumina. The direct backside cooling concept (Topology 3) is shown to have the greatest potential for cost reduction. Key findings of the studies were presented at a recent conference [9]. A forthcoming report will contain the details of this effort.

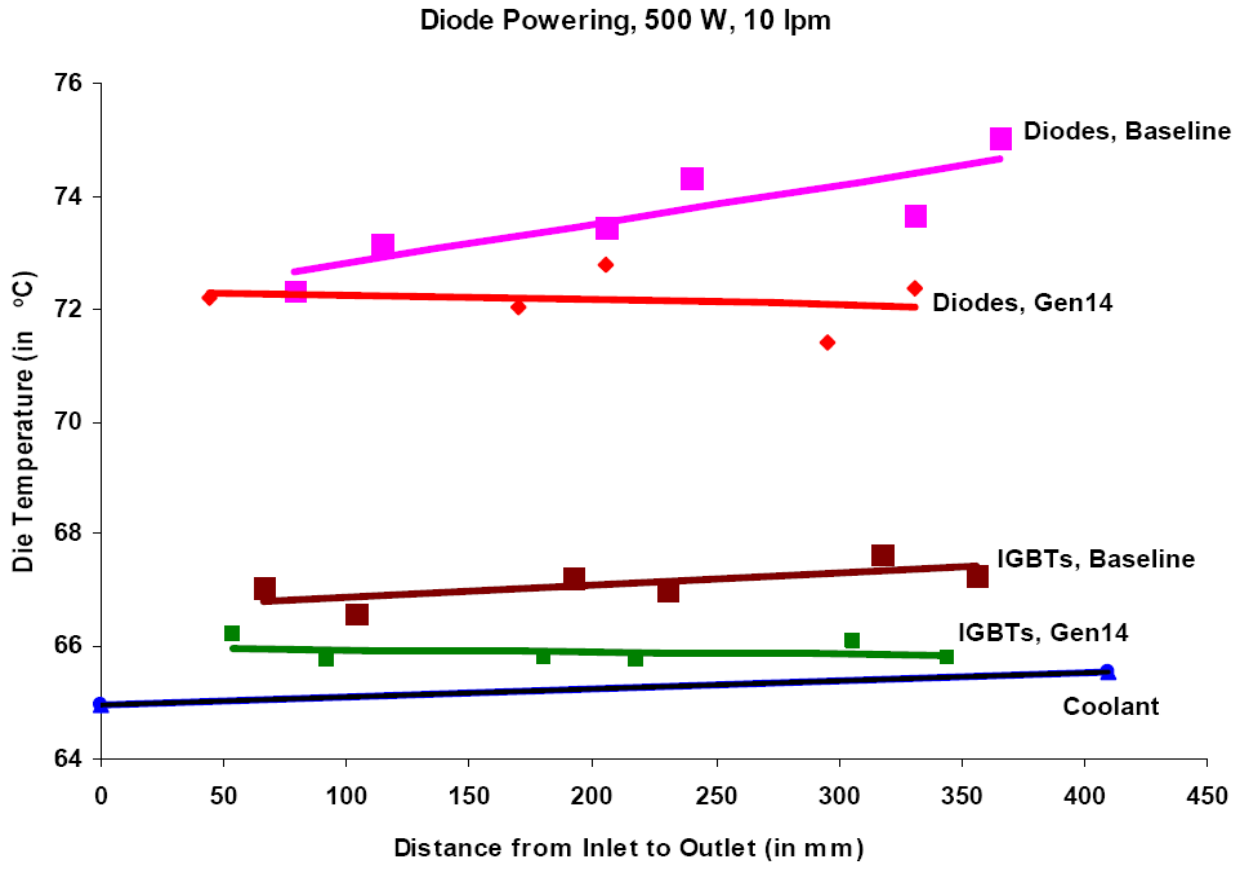

Fig. 7. Die Temperatures with Diode Powering (500 W, 10 lpm)

Conclusions

Thermal testing is completed for both the latest version of the direct backside cooling concept, Gen14, and the baseline design based on elliptical fin-pins. Gen14 provided lower and more uniform temperatures across all the IGBTs and diodes in comparison to the baseline design. The thermal resistance of Gen14 is 31% lower than that of the baseline design. This level of improvement would be very significant at higher power levels, especially with the use of engine coolant. During the testing, the dissipation rate with a coolant-to-junction temperature rise of 21°C is 92 W/cm^2, which is very close to the predicted performance, 90 W/cm^2. These values are for planar IGBT technology, which allows a temperature difference of about 20°C. With today's standard trench IGBT technology, which allows a temperature difference of 45°C, it would be possible to dissipate about 198 W/cm^2. With additional control parameters, like surface enhancement and improved spreading, it would be possible to reach the targeted dissipation levels of the DOE program of 200-250 W/cm^2. When this technology is used with the double-sided cooling concept, it has the potential to extend the dissipation rates with macroscale heat transfer to 400-500 W/cm^2, levels typically associated with microchannels. Preliminary studies with thermal materials indicate that using advanced thermal control (combination of advanced cooling technologies in conjunction with novel packaging topologies), it is possible to replace the traditional, expensive aluminum nitride (AlN) substrate with low-cost alumina. The direct backside cooling concept is shown to have the potential to reduce costs. For the next fiscal year, we plan to conduct detailed experimental/modeling studies for surface enhancement, optimize real-world heat exchangers with mesh-morphing-based optimization tools, and perform reliability studies. There would be a focused effort on the development of low-cost thermal packaging for a real inverter.

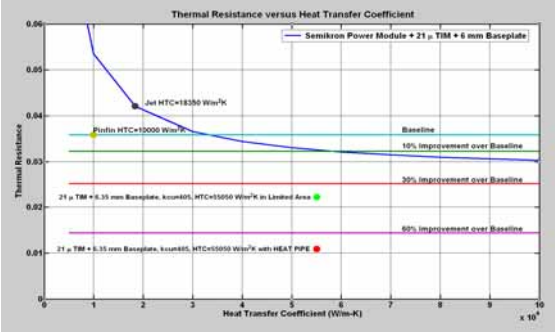

Fig. 8. Concept for 30% Performance Improvement over Baseline Design – Baseplate Cooling

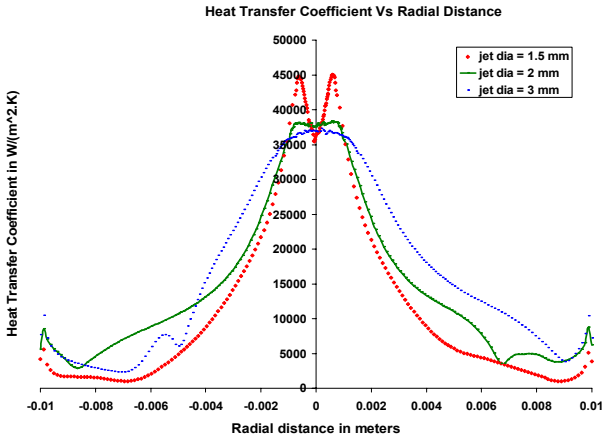

Fig. 9. Heat Transfer Coefficient Distribution Dependence on Jet Diameters

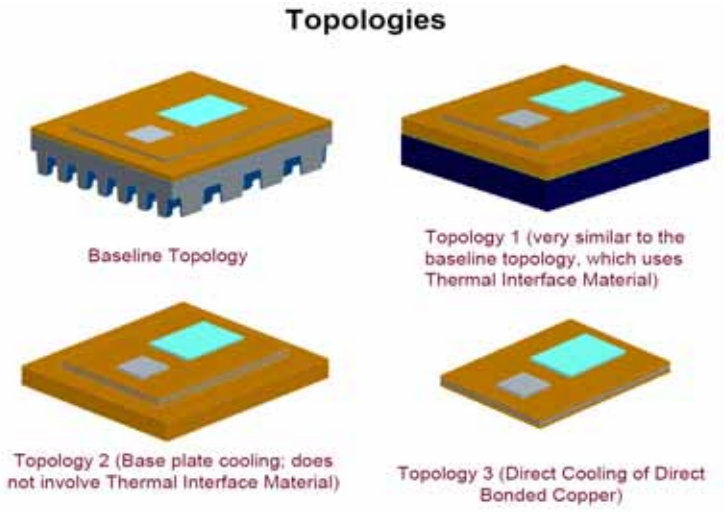

Fig. 10. Topologies Used in the Materials Exploration Study

References

1. T. Abraham, "Low Thermal Resistance IGBT Structure," NREL Technical/Milestone Report, 2007.
2. K Gawlik, "Low Thermal Resistance IGBT Structure," NREL Technical/Milestone Report, 2006.
3. D. Benhammou and V. Hassani, "Jet Impingement Experiment Study," NREL Technical/Milestone Report, 2005.
4. S.A. Solovitz, L.D. Stevanovic, and R.A. Beaupre, "Micro-channel Thermal Management of High Power Devices," IEEE, 2006.
5. L.J. Turek, D.P. Rini, B.A. Saarloos, and L.C. Chow, "Evaporative Spray Cooling of Power Electronics Using High Temperature Coolant," SemiTherm Conference, 2008.
6. A. Bhunia and C.-L. Chen, "Jet Impingement Cooling of an Inverter Module in the Harsh Environment of a Hybrid Vehicle," *Proceedings* of the 2005 ASME Summer Heat Transfer Conference, ASME, 2005.
7. B. Agostini, M. Fabbri, J. Thome, and B. Michel, "State of the Art of High Heat Flux Cooling Technologies," *Heat Transfer Engineering*, 28(4), 258-281, 2007.
8. S. Ashforth-Frost and U. Rudel, "Thermal and hydrodynamic visualization of a water jet impinging on a flat surface using microencapsulated liquid crystals," *International Journal of Fluid Dynamics*, Vol.7, 1-7, 2002.
9. T. Abraham, K. Kelly, K. Bennion, and A. Vlahinos, "Advanced Thermal Control Enabling Cost Reduction for Automotive Power Electronics," ANSYS Automotive Conference, Dearborn, MI, 2008.

Patents

1. V. Hassani, A. Vlahinos, and D. Bharathan, "Low Thermal Resistance Power Module Assembly," United States Patent Number 7190581, 2007.

2.3 Research and Development of Air Cooling Technology for Power Electronics Thermal Control

Principal Investigator: Desikan Bharathan
National Renewable Energy Laboratory
Center for Transportation Technologies and Systems
1617 Cole Boulevard MS 1633
Golden, CO 80401
Voice: 303-275-4613; Fax: 303-275-4415; E-mail:Desikan_Bharathan@nrel.gov

DOE Technology Development Manager: Susan A. Rogers
Voice: 202-586-8997; Fax: 202-586-1600; E-mail: Susan.Rogers@ee.doe.gov

NREL Task Leader: Ken Kelly
Voice: 303-275-4465; Fax: 303-275-4415; E-mail: Ken_Kelly@nrel.gov

---

Objectives

The overall objective of the thermal control activities is to develop advanced technologies and effective integrated thermal control systems aimed to meet DOE FreedomCAR program goals. These goals address key requirements for automotive power electronics such as target values for volumes, cost, and weight of various subcomponents. Another objective is to develop innovative cooling technologies suitable for automotive applications. The objective of the present research activity is to assess the potential for reducing the cost and complexity of cooling systems for power electronics using air. This study and assessment aim to quantify the relative merits of the use of air for cooling power electronic devices to achieve high-heat flux removal rates under steady-state and transient conditions, and the viability of air cooling from a thermal systems' perspective.

Approach

- Assess hardware options that may be available in the industry for varied air-cooling devices.
- Conduct system level analyses to identify areas of critical needs.
- Conduct computational analyses of fluid flow and heat transfer for promising devices and geometries.
- Fabricate and test prototype test articles and automotive-scale systems to validate design methods.
- Arrive at recommendations for future activities.

Major Accomplishments

- Characterized the potential for cooling with micro-channel geometries various fluids
- Developed simplified user-friendly software for quick assessment for various parameters
- Verified performance with computational fluid dynamic (CFD) analyses
- Identified air cooling heat exchanger geometries viable for use with automobiles
- Fabricated and tested two test articles with excellent agreement in performance between predictions and test results.

Future Direction

- Fabricate and test an automotive-scale air-cooled heat sink cooling an actual inverter (in collaboration with a supplier)

Technical Discussion

Current power-electronic modules are cooled with a dedicated water/glycol coolant loop operating at a nominal 70°C that eventually rejects heat to the ambient air using a radiator. An alternative technical pathway involves eliminating the separate cooling loop and/or using coolants at a high temperature (105°C). Both these approaches require advanced cooling methods to achieve high heat fluxes from the electronic chips.

Figure 1 shows a cross-sectional view of a die-mounted on a cold plate with the heat being removed by a coolant supplied to the bottom of the die. Various layers that impede the heat flow from the die to the cooling fluid are indicated. A major contributor to the overall thermal resistance turns out to be the thermal grease. However, the use of thermal grease is necessary to eliminate interlayer thermal stresses that result from differential thermal expansion between the layers.

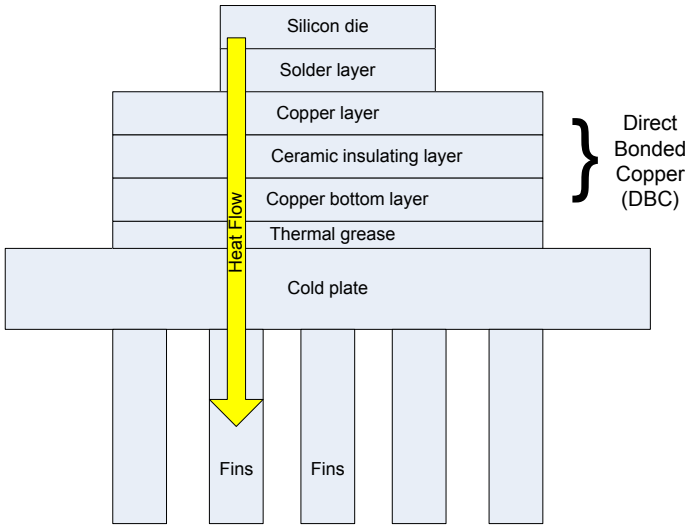

Fig. 1. Heat flux path and the various intervening layers

The next higher resistance usually comes from the heat exchanger rejecting heat to the cooling fluid. Ambient air is assumed to be available at a nominal 30°C for all the vehicle cooling strategies. Use of ambient air increases the overall temperature-driving potential available to reject heat from the chips. Air, as the cooling medium, is benign, nontoxic, and free when compared to many other fluids. Airflow is also amenable to be modulated in a transient manner to suit the needs the system, as the system load varies during operation.

The use of air on both sides of the silicon switches remains an attractive option. Use of air for cooling has many advantages. Air remains the ultimate heat sink for all heat rejection from an automobile. All the heat to be rejected, either directly or through the use of an intermediate coolant loop must end up in air. Direct use of air can eliminate many components of the cooling loop and the necessity for carrying a secondary coolant. Since the ambient air is at 30°C, air can be used to cool other components of the system, such as the capacitors. Capacitors with a central cavity are highly amenable to air cooling without exceeding limiting operating temperatures within their core.

Air cooling has many drawbacks as well. Air remains a poor heat transfer medium, with low thermal conductivity and low density. A fan or a blower must move the air stream to the required hot spots

requiring additional parasitic power loads. The coefficient of performance for such a system tends to be low.

Cooling with air may or may not meet requirements for current generation silicon-based devices that the temperatures at the chip be limited to 125°C maximum. Future technology changes, however, are expected to allow higher temperatures at the chip, with the trench IGBTs (Isolated Gated Bipolar Transistors) operating at 175°C, and Si-C devices operating at even higher temperatures. With these higher temperatures, air cooling becomes more practical.

To address many thermal control issues, NREL has undertaken a number of distinct areas of research and development. Multiple avenues of research are expected to result in significant advancement in thermal control of power electronics with a high degree of flexibility in design to meet the targeted goals and objectives of the FreedomCAR initiative. Progress made toward evaluating air cooling as a viable option for power electronic components in FY2008 under the FreedomCAR Program follow.

Initial assessment for air cooling focuses on a simple heat transfer that occurs on a single chip. We assume a chip heat-rejection area of nominal 1 cm^2 with the chip generating a heat load of 200 W. Air at ambient pressure and a temperature of 30°C is used to remove the heat.

Figure 2 shows a flow sheet for cooling with air developed using the commercially available software ASPEN. The chip shown as a block is maintained at a temperature of 125°C (using steam for purposes of the simulation).

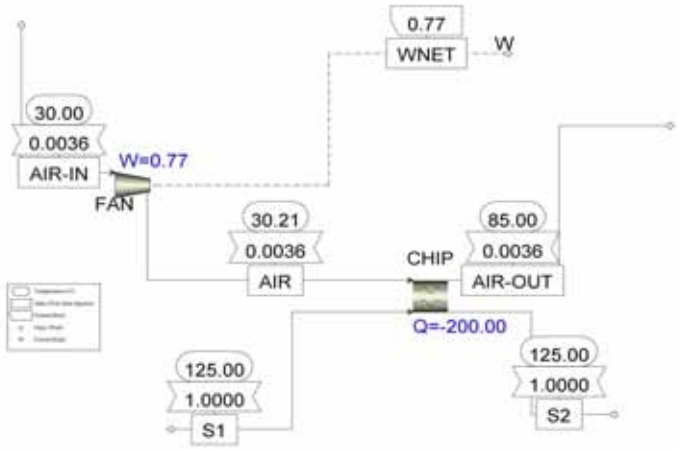

Fig. 2. Flow sheet for air cooling with a target chip held at 125°C, generating 200W heat load

Only key parameters are shown in this figure. The air approach temperature is fixed at 40°C below that of the target hot surface (a value typical for airflow applications). The fan operates with an efficiency of 56 %, once again typical for airflow.

We find that the airflow requirement per chip is about 3.6 g/s (or 2 ACFM—actual cubic feet per minute). The required UA product (the product of the heat-transfer coefficient and the available area for heat transfer) is 3.15 W/K.

Typical industrial airflow applications nominally achieve a heat transfer coefficient of about 40 W/m^2K. If we use this value, the required area is about 800 square centimeters. That is, the heat generated in the chip area of nominal 1 cm^2 must be spread out over an area, larger by a factor of 800. This can be accomplished through the use of fins or other means. We find, however, that nominal heat transfer coefficients fall well below the needs to accomplish the task at hand. To enhance the heat transfer coefficient and provide large area enhancements, we looked into micro-channel geometries.

Micro-channels have been shown to yield very high heat removal capability in many studies. Their attractiveness comes from being able to provide large surface areas in a relatively small volume. To maintain a low pressure drop through the micro-passages, fluid flow is generally limited to a laminar flow regime. Laminar flow heat transfer coefficients vary inversely with the passage hydraulic diameter. Maintaining low passage widths result in high heat transfer coefficients as well. For automotive applications, we compared air and liquid cooling approaches in the next section. While such comparisons have been reported for other applications, the requirements for automotive applications are unique and differ considerably from other applications.

Comparison of Air And Liquid Cooling

Consider a liquid cooling system for the power electronic components in an automobile. Figure 3 shows the liquid-cooling loop with the necessary components. The liquid cooling loop includes a filter, radiator and radiator fan, a liquid supply line, liquid distribution manifold, liquid return line, reservoir, and a liquid pump. The components may be a dedicated system to cool only the power electronic components (as in the case of those used in the Prius) or be part of the overall ICE cooling system. Note that every connection between the various components requires some form of clamping, or other hardware. As we note next, we find that the liquid cooling loop has many inter-connections and requires more components than the air-cooling system in general.

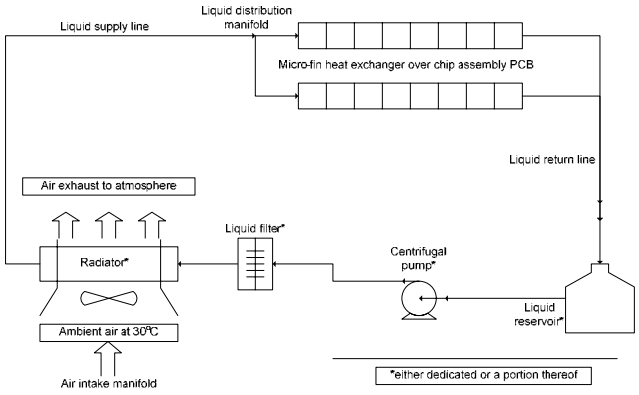

Fig. 3. Schematic Diagram of a Liquid-Cooling Loop

For comparison, figure 4 shows a typical arrangement for using air as the cooling fluid. Ambient air is drawn through an appropriate filter, then forced by a centrifugal fan, and distributed via manifolds over micro-channel heat exchangers located in close proximity to the heat sources. Heat is transmitted via highly conductive fins with high surface areas. Usually, a laminar air flow, established in the micro-channels adjacent to the fins, removes heat from the fins.

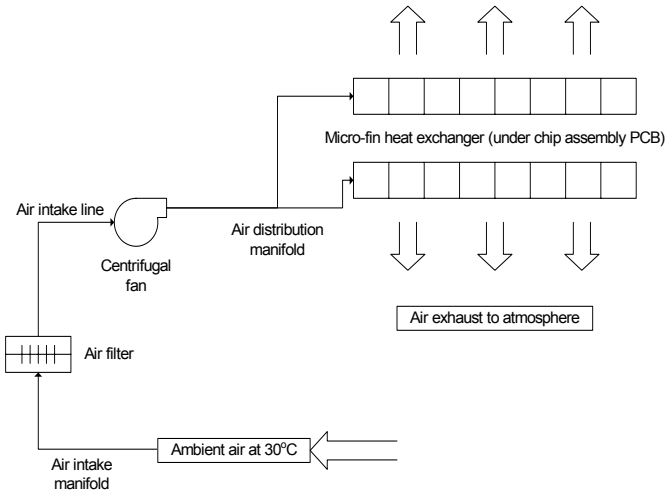

Fig. 4. Schematic Diagram for an Air-Cooled System

To carry out a direct comparison of the requirements of liquid vs. air cooling, we assumed an overall heat removal requirement of 3 kW from the power electronic components for an HEV. Additional assumptions are also made, as listed in Table 1. The approach temperatures, defined as the difference between the coolant outlet temperature and the maximum surface temperature, are typical values for air and liquid cooling.

Table 1. Assumptions for Comparing Air and Liquid Cooling

Quantity	Air Cooling	Liquid Cooling
Inlet temperature (^{o}C)	30	105
Approach temperature (^{o}C)	40	5
Mass flow rate (g/s)	54	50
Volume flow rate	94 (SCFM)	0.8 (gpm)
Configuration	Open loop	Closed loop

For this comparison, we used a liquid cooling temperature of 105^{o}C to be consistent with the FreedomCAR goals. Air ducts were made of polyethylene. Liquid hoses were standard automotive grade components. In both cases we used micro-finned heat exchangers mounted on the base plate of the electronic devices. Pump and fan efficiencies were taken to be typical 0.7. Detailed breakdowns of the components for each system allowed us to calculate various component masses, volumes, required parasitic power, and cost [Bharathan and Kelly, 2008]. Table 2 summarizes the results of this analysis.

Mass of the system is a key variable for automotive application. We find that the air-cooling system compares very favorably with the liquid-cooling system. Air-cooling system mass turned out to be one-half of that for the liquid cooling system. However, the air system is bulkier, occupying twice as much volume. Majority of the volume is related to the ducting necessary for handling air. Excess volumes are difficult to accommodate, especially in the cramped quarters under the hood of an automobile. The parasitic power for the air-cooling system is close to three times that for the liquid-cooling system, reflecting its lower coefficient of performance (COP). Parasitic power is the power it takes to run the cooling system. It is an important parameter in that parasitic power adds load to the ICE and impacts the fuel economy. Costs were calculated based on the raw material cost for the components and multiplying that cost by two to account for fabrication in large quantities.

Table 2. A Quantitative and Qualitative Comparison of Air-Cooling versus Liquid-Cooling Options

Quantity	Air Cooling	Liquid Cooling
System mass (kg)	1.4	3.8
Volume (cc)	7000	3800
Parasitic power (W)	80	28
Relative component and system fabricated costs ($)	48	78

The impact of parasitic power or the excess mass on the vehicle's gasoline usage, in terms of miles per gallon (mpg), is very small for both systems. Our evaluation showed that air-cooling systems may have additional benefits that are less tangible. These include a decreased number of components, increased reliability, ease of maintenance, and simplicity of design and installation. Based on these comparisons, we found that air cooling may provide a viable option for heat removal from power electronic systems in automotive systems. At present, cooling of the heat-generating chips from only one side is considered. With air cooling, the potential for cooling both sides of the chips will allow larger cooling loads and more compact and economic designs.

Micro-Channels

Micro-channels have been studied and many results are available in the literature. We followed the optimization method outlined by Muller and Frechette [2002] to identify proper geometry suitable for heat removal from electronic chips.

Figure 5 shows the details of the micro-channel as modeled. The fluid passage is denoted by a width, W, and the fin thickness by t. The fins with a height H, are mounted on a base plate of thickness t_b. Nominal values for the base plate width and length of 10 mm each are assumed for the model.

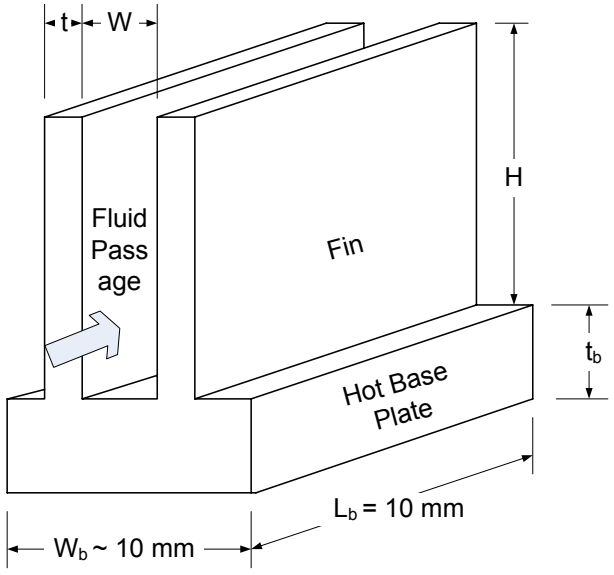

Fig. 5. Micro-fin array channel geometry

For laminar, incompressible flow, the Nusselt number (for uniform wall temperature) and the product fRe (where f is the friction factor and Re the Reynolds number) are simple functions of only the passage

aspect ratio, H/W. Given the geometry, this dependence allows us to calculate the Nusselt number and fRe product immediately. Further details of the calculations may be found in Muller and Frechette [2002].

As part of this project, we developed a "Micro-Channel Performance Estimator" program that provides a quick means to estimate micro-channel heat transfer with a variety of configurations and fluids. Specifically the aspect ratio of the channel, H/W can be varied from 50 to 1000 in increments of 50. The channel width, W, can be varied from 80 μm to 200 μm in steps of 10 μm. Choices of three fluids, namely, air, water, and ethylene glycol/water 50/50 mixture are available. Choices for fin and plate materials in the form of copper and aluminum are available. Base-plate thickness can be varied from 0.5 mm to 5 mm in steps of 0.5 mm.

Figure 6 shows the output page for the estimator program. The calculated results are listed on the top right with various parameters called out. The bottom half of the page provides the summary of the results in a graphical form. A required base-plate temperature is first selected, in the range of 125°C to 200°C (with steps of 25°C). The heat flux q (W/cm^2) and the parasitic power (W) are calculated and plotted along the left axis as functions of the fluid velocity (m/s) within the channel passage. The program goal of 200 W/m^2 heat flux at a base temperature of 125°C for silicon-based chips is indicated in the figure. A coefficient of performance (COP) for the device is evaluated as the ratio of heat removal rate to the parasitic power. COP is also plotted on the right-side axis as a function of the base plate temperature. COP values over 150 are not indicated in the figure, but are listed in the output window along with other variables. This program allows one to quickly evaluate the performance of micro-fin geometry for removing heat from hot spots in a printed circuit board.

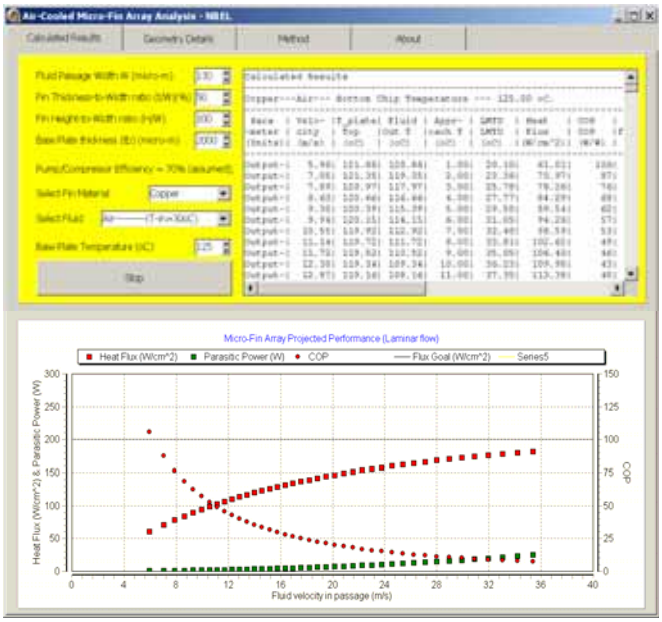

Fig. 6. Output page from the "Micro-Channel Performance Estimator" program

For air flow through the micro-fin channels, with copper as the fin material and base plate held at 125°C, we are able to achieve heat fluxes in the range of 60 W/cm^2 to 180 W/cm^2 over the selected range to parameters. With aluminum as the fin material, the range narrows down to 50 W/cm^2 to 150 W/cm^2. The COP ranges from about 12 to well over 150, with most values falling in the range of 50 to 100. For comparison, the flux values estimated for the electronic housing for Prius is around 60 W/cm^2 and that for Camry is 80 W/cm^2.

For a 50/50 ethylene glycol/water mix flow through the micro-fin channels, with copper as the fin material, and with the base plate held at 125°C, we achieve heat fluxes in the range of 60 W/m^2 to 160 W/m^2 over the selected range of parameters. With aluminum as the fin material, the range narrows to 45 W/m^2 to 120 W/m^2. The COP ranges well over 10,000, in most cases.

Despite the high COPs, liquid cooling comes with its own set of drawbacks. Primarily, the limitation to heat transfer in the use of glycol/mixture comes from its availability at only a high temperature of 105°C (as returned from the radiator). Also note that at high base-plate temperatures, the liquid can exit at higher temperatures. However, we need to maintain the system pressure high enough to keep the liquid from boiling.

The attached estimator program allows one to quickly estimate the achievable heat flux for a given set of parameters. The calculation method is simple, but not quite accurate in certain circumstances, as we shall discuss later.

The parasitic power for the micro-channel heat exchanger is a strong function of the channel flow length. By judiciously reducing the length of the channel, the parasitic power can be reduced substantially. This effect may have implications for the chip design. If the design permits, perhaps the chips can be rectangular strips rather than square in plan area. Or other features can be incorporated such that the hot spots appear in a long rectangular form. At present the channel length can at least be cut in half, by introducing the fluid centrally from above and allowing it to exit on two sides. Modeling such arrangement with computational fluid dynamics cuts the pressure drop by half, without significantly affecting the heat transfer.

We find that the air-cooling system compares very favorably with the liquid cooling system. Air cooling system mass turned out to be one-half of that for the liquid cooling system. However, the air system is bulkier, occupying more volume. The parasitic power for the air cooling system is close to three times that for the liquid system, reflecting its lower COP. However, the impact on the vehicle's gasoline usage, in terms of miles per gallon (MPG), for both systems is negligible. The air cooling system scores higher in less tangible areas, such as decreased number of components, increased reliability, ease of maintenance, and simplicity in design and installation.

Based on this set of comparisons, we find that air-cooling provides a viable option for heat removal from power electronic systems. Potential for cooling both sides of the heat-generating chips remains an even more attractive option.

Experimental efforts

Initial efforts to fabricate and test micro-fin air-cooled heat exchangers at NREL have been completed. Figure 7 shows a photograph of a test article fabricated at NREL for the tests. Thermal and flow performance data were obtained over a range of air flow rates in the laboratory. This test article was designed to cool a single chip of nominal 1-square centimeter area, generating fluxes up to 200 W/cm^2.

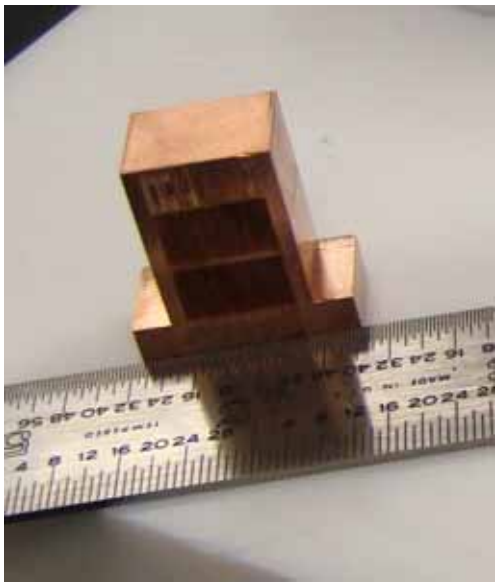

Fig. 7. Photograph of the air-cooled heat sink

Overall dimensions are indicated with a ruler placed adjacent to the air cooler in this picture. Experimental data on the obtained heat fluxes are shown in Figure 8. In this figure, the test article base temperature (in degrees Celsius) is plotted as a function of the heat flux imposed at the base of the heat sink. We covered a range fluxes up to 180 W/cm^2. Data for three different air flow rates are shown. At each airflow, the base temperature increases linearly with increasing imposed heat flux, as expected. Higher air flow rates yield lower base plate temperature. On account of the different layers on the chip, the chip temperature would be slightly higher than the base temperature indicated in this figure.

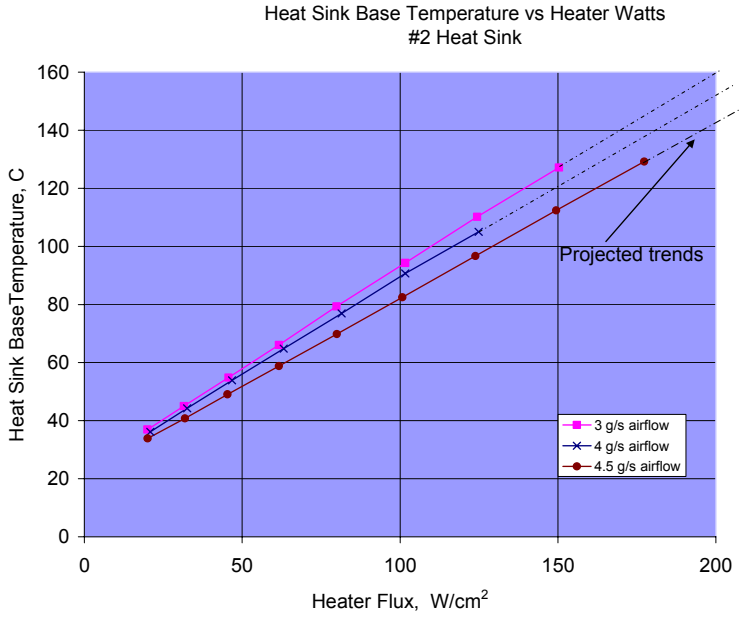

Fig. 8. Variation of base plate temperature as a function of heat flux, at varied air flow rates.

A second heat sink fabricated at the Illinois Institute of Technology is shown in Figure 9. Copper plates were etched to form the fins and spacers as shown in the photograph. Thermal tests revealed that this test article also behaved as predicted. Pressure loss data are discussed next.

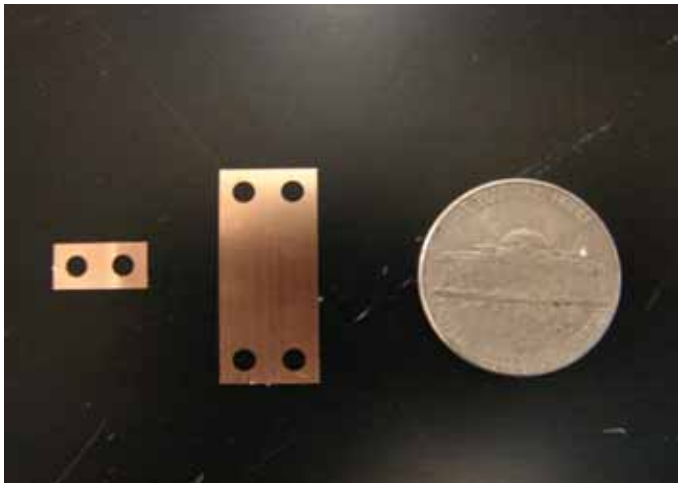

Fig. 9. Photograph of the spacer and fin for the test article fabricated at Illinois Institute of Technology

Pressure loss measurements for both these heat sinks were found to agree with model predictions quite well, as shown in Figure 10.

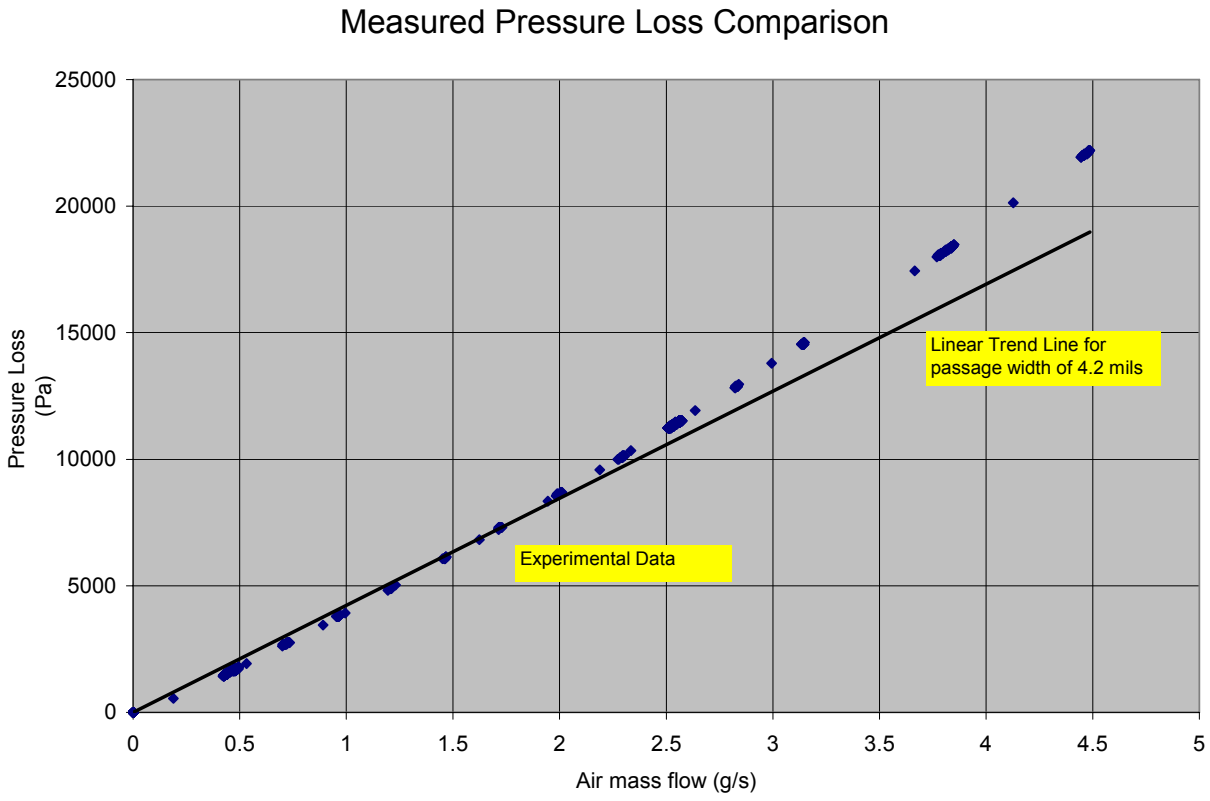

Fig. 10. Measured pressure loss for the heat sink versus air mass flow rate; comparison to predicted values are also shown.

Our experimental data validated that we can confidently design air-cooled heat sinks with a good certainty of performance for cooling power electronics.

Designs for an actual inverter

Figure 11 shows one concept as to how an air-cooled heat exchanger may be incorporated with the inverter design (as used by Semikron). The figure shows an exploded view. The heat exchanger fins fall directly below the high-heat generating switch mounted on a direct-bonded copper (DBC) board. Air is supplied from a side port of nominal 40-mm diameter. Air flows through the distribution manifold and enters the array of fins on both sides of the device. The bottom of the PCB is in intimate contact with the bottom plate of the heat exchanger. These two parts may be soldered together to achieve a low-resistance heat transfer path.

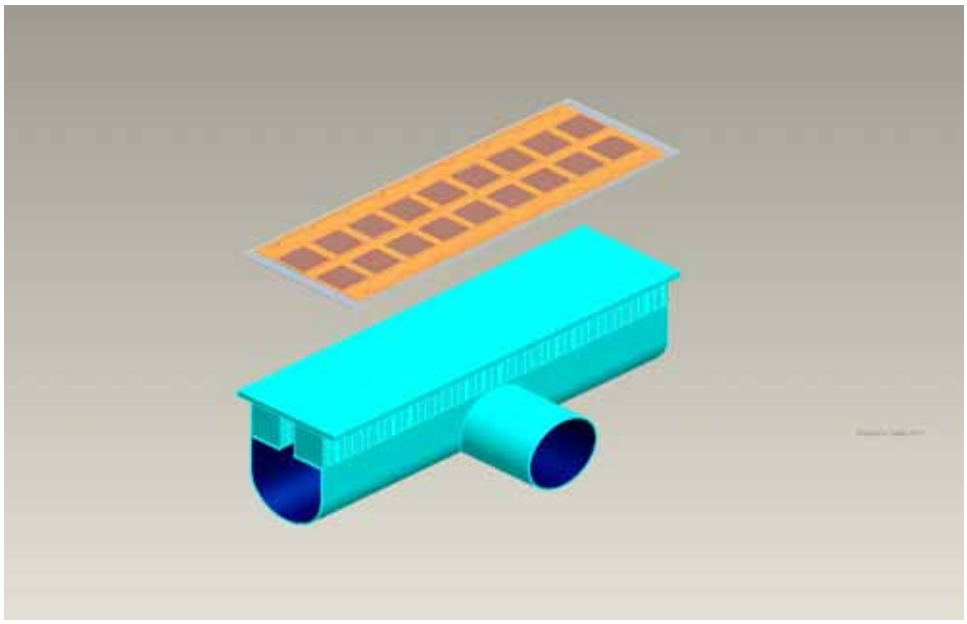

Fig. 11. Illustration indicating how air-cooled heat sinks can be accommodated for rows of electronic chips.

Computational fluid dynamics modeling results

We also conducted a variety of computational fluid dynamics (CFD) simulations for the air-cooled heat exchanger using Fluent. Detailed results of the CFD investigations were reported as part of the progress during FY 2007.

We found that air enters at its inlet temperature and begins heating up quickly as it contacts the fins. There appear large temperature gradients both in the stream-wise direction and perpendicular to it. Such variation is far from the assumptions used in our simplified model described earlier. Because of these gradients, we find that our performance estimator program over-predicts the heat flux by about 20%. At high air velocities, the stream-wise gradients lessen, and the perpendicular gradients increase.

On account of the cross flow, such gradients will prevail and simplified methods such as our estimator are likely to yield errors. We find that the simplified performance estimator over-predicts the heat flux as much as 20% routinely. Pressure drop and parasitic power compare favorably with Fluent CFD simulations, however. The value of the "estimator" program is that it provides very quick results that can lead to a design space that can be investigated in more detail to arrive at optimal designs for further development and testing.

Considering that the passage length is the key variable dictating pressure loss and parasitic power, attempts to reduce this passage length should be pursued in all designs for an air-cooled heat sink.

In Figure 12, variations of heat flux (in W/cm^2) as projected by the estimator program are plotted at constant COPs. Predicted data points are shown together with least-square fit straight lines to the data in this figure. Two values for COP are used, namely 25 and 50. The hottest temperature is varied from 125^{o}C (corresponding to today's silicon chips) to 200^{o}C (for a potential future chip material and fabrication technology). We find that the allowable heat flux increases linearly with increasing hottest temperature. The allowable heat flux is lower for the higher COP values. At the lower COP of 25, heat flux ranges from 100 to 240 W/cm^2. For the higher COP of 50, the flux range is from 140 to 270 W/cm^2.

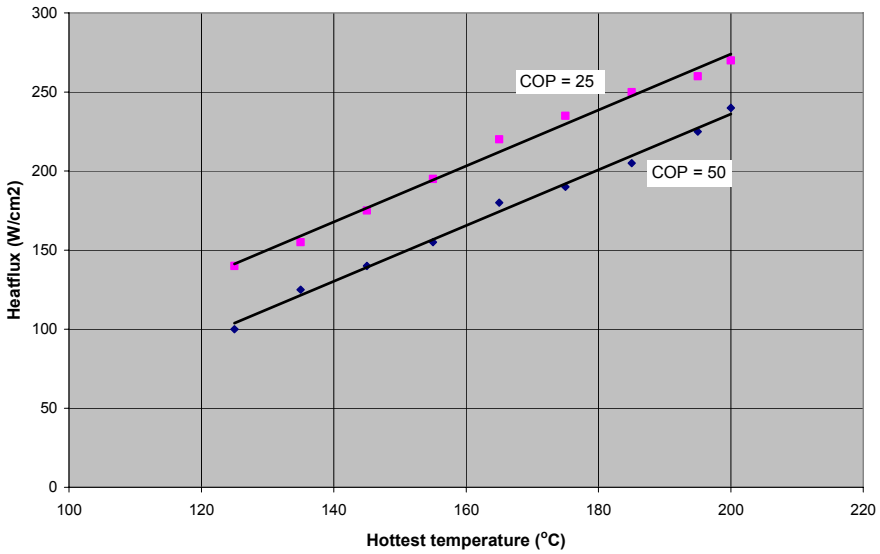

Fig. 12. Projected heat flux as functions of chip high temperature and overall COP

We find that parasitic power can be reduced significantly without losing heat flux removal capacity at the same air mass flow. Doubling the mass flow still yields a higher COP and a higher heat flux. Simple modifications can boost the performance of the micro-channel considerably. This example was shown as an illustration. Depending on the specific applications, key modifications to the geometry to maintain highly aerodynamic passages will result in further improvements in the overall performance of the micro-channel geometry.

Conclusion

Air cooling is very likely to meet the program goal for heat-flux removal at a rate of 200 W/cm^2 with relatively low cost and complexity. Air cooling also allows ready access to cool other components of the system, such as the capacitors.

While air cooling may not be appropriate for the current generation of silicon-based devices, it remains an attractive option for future devices that can operate at higher temperatures. Use of air helps avoid the need for a secondary cooling fluid in vehicles. Improving chip manufacturing technologies continue to push the envelope for the highest temperature environment that these chips may see during operation.

Air cooling remains a viable option for power electronics. Continued research in this area will result substantive progress in achieving the goals for this cooling technology. In the near future, we recommend fabricating and testing working inverters that use advanced air cooling for heat removal.

Publications

Bharathan, D. and Kelly, K., "An assessment of air cooling for use with automotive power electronics," a paper presented at the 2008 ITHERM conference, April 2008.

References

1. Cengel, Y.A., Introduction to thermodynamics and heat transfer, McGraw-Hill, New York, 1997.
2. Hans, J.C.; Dutta, S.; Ekkad, S., *Gas Turbine Heat Transfer and Cooling Technology*, Taylor and Francis, 2001.
3. Incropera, F.P., *Introduction to heat transfer*, Wiley, New York, 1996.
4. Marques, C. and Kelly, K.W., "Fabrication and Performance of a Pin Fin Micro Heat Exchanger," *J. Heat Transfer*, v126, pp 434-444, June 2004.
5. Muller, N and Frechete, L.G., "Optimization and design guidelines for high flux micro-channel heat sinks for liquid and gaseous single-phase flow," *Inter Society Conference on Thermal Phenomena*, IEEE paper 0-7803-7152-6/02.
6. Shen, J.R.; Wang, Z.; Ireland, P.T.; Jones, T.V.; Byerley, A.R. "Heat Transfer Enhancement Within a Turbine Blade Cooling Passage Using Ribs and Combinations of Ribs With Film Cooling Holes," *ASME J. of Turbomachinery*, v118, pp 428-434, 1996.

Patents

None

2.4 Project Title: Thermal Stress & Reliability for Advanced Power Electronics & Electric Machines

Principal Investigator: Michael P. O'Keefe
National Renewable Energy Laboratory
Center for Transportation Technologies and Systems
1617 Cole Boulevard MS 1633
Golden, CO 80401
Voice: 303-275-4268; Fax: 303-275-4415; E-mail:michael_okeefe@nrel.gov

DOE Technology Development Manager: Susan A. Rogers
Voice: 202-586-8997; Fax: 202-586-1600; E-mail: Susan.Rogers@ee.doe.gov

NREL Task Leader: Kenneth Kelly
Voice: 303-275-4465; Fax: 303-275-4415; E-mail: Kenneth_Kelly@nrel.gov

---

Objectives

The objective of this task is to develop and assemble a toolset to evaluate thermal stress and assess life implications for APEEM designs and technologies based on anticipated usage patterns. Predictive modeling tools, applied early in the development process can help guide R&D decisions, streamline time to market, and identify potential barriers to meeting life and reliability goals.

Approach

- meet with stakeholders, key constituents, and others to gain input and insight
- create an R&D plan and present to the EETT for review
- carry out the R&D plan
- technical approach:
  - — choose a baseline cooling design and document metrics and boundary conditions
  - — choose cooling technologies for consideration on an equal basis with the baseline system
  - — analyze and understand the power electronics module usage pattern (i.e., duty cycle)
  - — evaluate thermal stress due to dynamic loads
  - — analyze and understand the reliability implications of thermal stresses using knowledge from the literature and experts
  - — focus on specific next-generation cost-effective designs being researched and developed under the DOE APEEM program area
  - — compare the thermal stresses in concept designs to existing technology and usage patterns
  - — use information on stress and reliability implications to improve APEEM designs

Major Accomplishments

- met with stakeholders, key constituents, and others on this topic
- created an R&D plan and presented it to the EETT for review
- summary of the thermal reliability R&D presented to DOE program manager [1]
- baseline cooling design and two alternates assessed under equivalent operation at steady state

Future Direction

- create a toolset for the prediction of thermal stresses on automotive power electronics
- apply the toolset to technologies being considered under the APEEM program
- modules to be created/ integrated as depicted in Figure 1:

- vehicle systems module (can use extant DOE simulation programs such as ADVISOR or PSAT)
- power electronics heat generation and loss prediction module
- load transformation module which transforms thermal loads to stress and fatigue damage
- a post processing module to analyze results

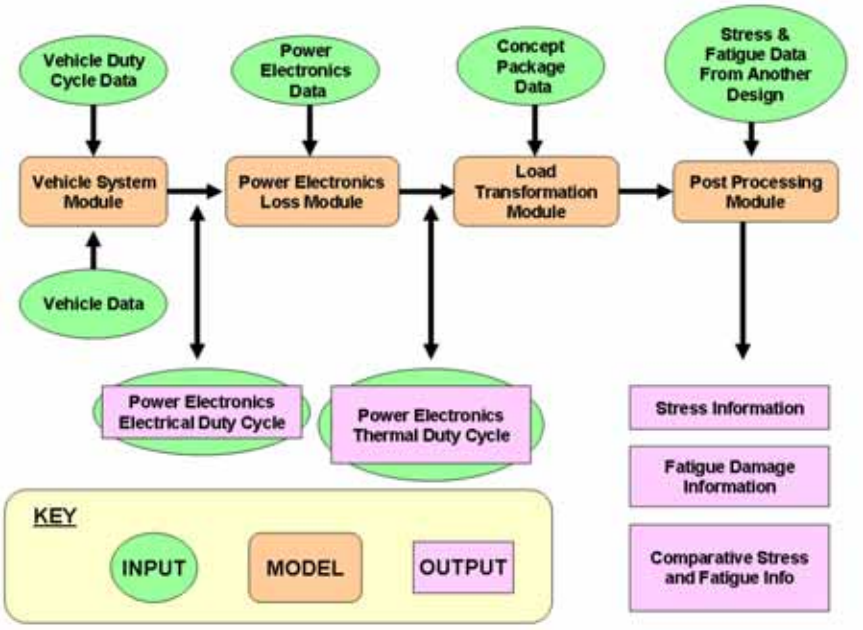

Fig. 1. Vision of a Toolset for Stress Prediction

Technical Discussion

As outlined in our previous report [1], three inverter topologies have been selected as candidates to use in developing and assembling our thermal stress and reliability analysis capability. The thermal stress and reliability implications of these packages are interesting in their own right as well. We intend to demonstrate the value of computer aided design and analysis related to thermal stress and reliability in the context of these three topologies.

The first topology is referred to as "direct backside cooling" and is a design developed here at NREL. The design minimizes thermal resistance and capacitance by eliminating as many layers as possible in the inverter package. The removal of non-critical package material enables jets of coolant to impinge directly on the backside of the DBC layer—very close to the heat generating solid state devices that comprise the inverter switch (IGBTs and diodes). This topology is depicted on the left hand-side of Figure 2. A second topology is a baseline pin-fin design. Pin-fin heat exchangers are in common use today. The baseline pin-fin heat sink topology is depicted on the far right of Figure 2. A third topology is composed of aspects from the first and second. This topology is jet impingement cooled but uses a baseplate to receive the benefits of heat spreading and additional thermal capacitance. This topology is shown in the middle of Figure 2.

The three topologies represent a good cross section from current technology to high-performance cooling. In order to compare these topologies, some care must be taken up front to put the pin-fin cooling and jet impingement cooling on a consistent basis. In order to put the topologies from Figure 2 on an equal basis, an analytical tool has been created based on fundamental heat transfer equations for pin-feat heat transfer and pressure drop. These equations are described in the following section. Performance for jet

impingement cooling is derived from NREL's extensive testing and CFD analysis of this technology [5, 6].

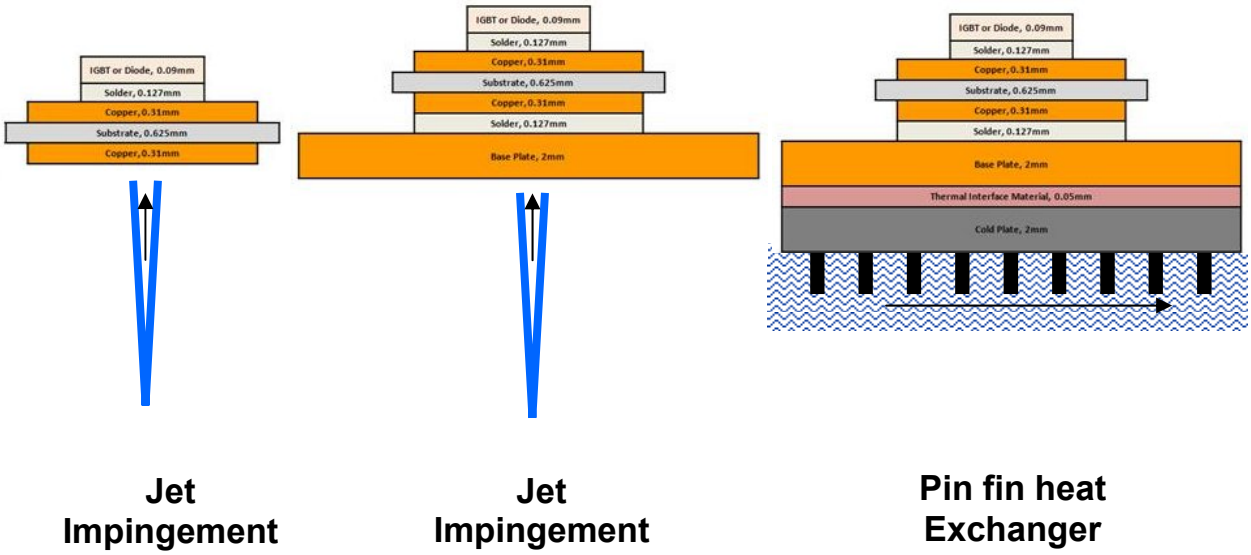

Fig. 2. Jet Impingement and Pin-fin Array Cooling Technologies Applied to Three Package Designs

Comparing Pin-Fin Heat Exchangers to Jet Impingement on and Equivalent Basis

When comparing two technologies with each other, it is important that the technologies be compared on a consistent basis. The thermal reliability project will develop and apply a methodology to assess life implications of APEEM designs and technologies based on anticipated device usage (i.e., duty-cycle). However, the APEEM designs must be put on a consistent basis if they are to be properly compared.

For cooling systems, one means for consistency is to compare thermal results at the same parasitic power. Parasitic power is the power required to move the coolant through the heat sink. Note that this parasitic power must be supplied from an external means such as a pump but it is not the same as the pumping power. The pumping power (i.e., the power required *by* the pump for the pump to function) will be larger than the parasitic power due to pump inefficiency. Parasitic power is defined as:

$$P_{loss} = \dot{V} \cdot \Delta p \qquad \text{Equation (1)}$$

In equation 1, P_{loss} is the parasitic power loss in units of power (for example, watts). The variable, $\dot{V}$, is the volumetric flow-rate of coolant in units of volume per time. Finally, Δp is the pressure drop through the heat exchanger.

When comparing inverter package designs, we are typically interested in determining the temperatures at the junction of the semiconductor switches and throughout the various layers of the power module. We would like to know how these temperatures vary spatially through the unit and temporally throughout the life of the unit over the typical usage patterns the power module would see in the field. In addition, we will be interested in determining the thermally induced stresses that arise between layers of the power module package due to differences in temperature. The ability to put the cooling technologies we're interested in on an equivalent basis is a necessary first step.

A MATLAB model was created using fundamental heat transfer equations for a pin-fin heat exchanger. The fundamental equations used in that model are presented here. We will begin with a focus on steady state heat transfer analysis though subsequent studies will be moving to dynamic temperature analysis.

For steady-state conditions, a simple thermal circuit can be constructed to represent the semiconductor switches and their corresponding heat-sink in a power module package. This is depicted in Figure 2.

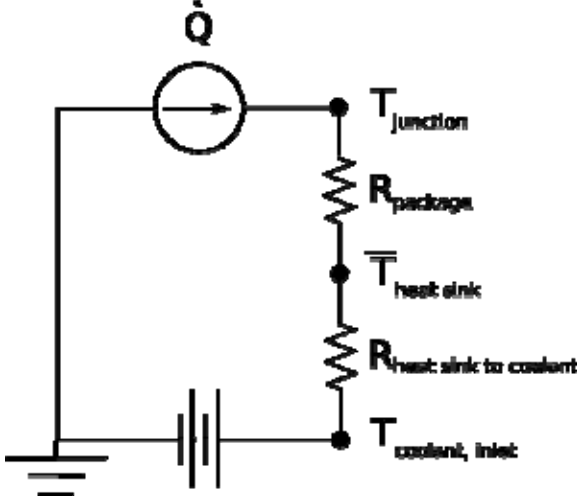

Fig. 3. Simple thermal circuit for stead-state heat transfer

In Figure 3, $\dot{Q}$ is the heat being generated by a semiconductor switch (assumed to consist of an IGBT and diode). The thermal circuit depicts the resistance to flow of heat from switch to coolant. The package resistance consists of the resistance to heat flow from the switch to the bottom of the heat sink. The temperature of the heat sink is taken as an average temperature. The second resistance in Figure 3 is defined as the resistance to heat flow from the heat sink to the coolant inlet. In the Figure, the remaining "voltage source" steps the temperature down from the coolant inlet temperature to absolute zero (depicted by ground).

For a dynamic temperature nodal network, it is important to model thermal capacitance. However, for a steady state system, thermal resistance is sufficient.

The first resistance shown in Figure 3 is the package thermal resistance and is a resistance to heat conduction. The thermal resistance of the package can be written as:

$$R_{conduction} = \sum_{L=1}^{N} \left(\frac{\Delta z_L}{k_L \cdot A_L} + R_{spreading,L} \right) \qquad \text{Equation (2)}$$

In equation 2, the thermal resistance of the package is composed of the 1D thermal resistance of the package layers plus a spreading resistance term which accounts for the fact that the problem is not 1D. In equation 2, Δz_L is the thickness of layer, L, where there are N layers numbered 1 to N. The term k_L is the thermal conductivity of layer L and A_L is the cross-sectional area of layer L.

The second resistance term in Figure 2 is a resistance to heat convection though it can incorporate aspects of the heat sink such as fin efficiency where applicable. In general, the thermal resistance from heat sink to coolant will decrease as the parasitic power used to move coolant through the heat sink increases

(though as we shall see, this is not always the case). The equivalent thermal resistance to convection can be expressed as:

$$R_{convection} = \frac{1}{U \cdot A_{\text{footprint}}} \qquad \text{Equation (3)}$$

In equation 3, U is termed the heat transfer coefficient. The term A is taken to be the 2D projected "footprint" of the heat sink in contact with the coolant. This area represented by $A_{footprint}$ does not take into account area enhancement. Instead, the effect of area enhancement is captured through augmentation of the equivalent heat transfer coefficient, U. The terms U and $A_{footprint}$ are defined such that the following is true:

$$\begin{aligned} \dot{Q} &= U \cdot A_{\text{footprint}} \cdot \left(\overline{T}_{\text{S}} - T_{\text{I}}\right) \\ &= \dot{m} \cdot c_p \cdot \left(T_{\text{O}} - T_{\text{I}}\right) \\ &= \dot{m} \cdot c_p \cdot \varepsilon \cdot \left(\overline{T}_{\text{S}} - T_{\text{I}}\right) \end{aligned} \qquad \text{Equation (4)}$$

Equation 4 yields the working definition for effective heat transfer coefficient, U. The coolant inlet temperature, T_I, is typically known and the average temperature of the heat sink, $\overline{T_S}$, can be estimated or measured. Note that the average temperature of the heat sink is measured at the base of any fin structure where the fin attaches to the heat sink proper. The "footprint" area of the heat sink is the length times the width of the area of the heat sink in contact with the cooling fluid. Note that this "footprint" area is literally length times width and does not include area enhancement. Equation 4 also reveals that the heat transferred by the heat sink must be equal to the heat picked up by the coolant. This is defined in terms of the mass flow-rate ($\dot{m}$) times the specific heat (c_p) times the difference between outlet and inlet temperature ($T_O - T_I$). To relate the transferred heat back to the average heat sink temperature, we can use the definition of heat exchanger effectiveness. Heat exchanger effectiveness, ε, is defined as the actual heat transfer divided by the maximum possible heat transfer which, for a single coolant flow, simplifies to the following: $\left(T_O - T_I\right)/\left(\overline{T_S} - T_I\right)$.

Effective heat transfer coefficient is thus defined by requiring equation 4 to equal the total heat transferred from the switch (assuming adiabatic[1] boundary conditions in all locations save the path from switch to coolant). Defining the convective heat transfer coefficient in this way allows us to compare heat transfer coefficients on a consistent basis. Furthermore, this is a very convenient definition since all of the parameters in equation 4 can be measured or estimated to determine U.

Our first task is to compare how the heat transfer coefficient for each technology varies with pressure drop and flow rate. First, let's consider pressure drop for the pin-fin technology.

Pin-Fin Pressure Drop

The pressure drop through a circular pin-fin array is given by the following set of equations [3, 4].

$$S_T = \frac{D_T}{D}, S_S = \frac{D_S}{D}, S_D = \frac{D_D}{D} \qquad \text{Equation (5)}$$

[1] Note: for this study, adiabatic boundary conditions are assumed. However, for future studies we will examine the impact of radiative and convective boundary conditions as these may be significant in automotive under-hood environments.

In the equation above, S_T is the dimensionless pin-pitch in the transverse direction which is perpendicular to the flow direction (i.e., width-wise across the flow channel). The variable D is the diameter of the pins. Similarly, S_S and S_D are the streamwise and diagonal dimensionless pin pitches defined in terms of the streamwise pin pitch, D_S, and diagonal pin pitch, D_D, divided by the pin diameter, D. The diagonal pin pitch and it's dimensionless counterpart are only defined for staggered pin arrays. The definitions of D_T, D_S, and D_D can be seen in Figure 4. Circular pins are assumed.

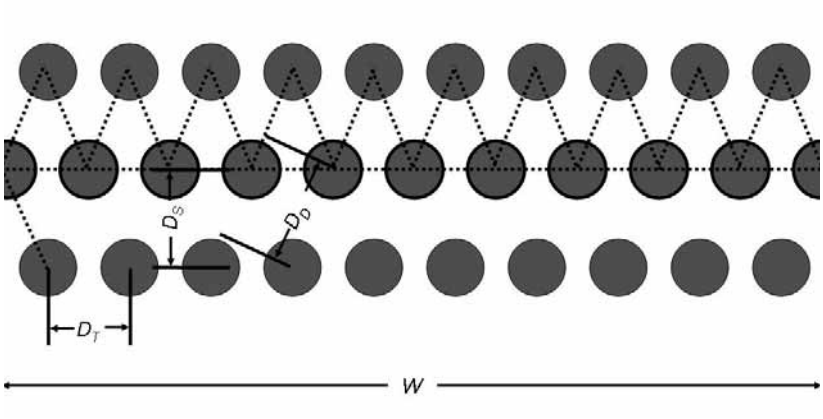

Fig. 4. Pin-fin Array for a Staggered Configuration (looking downward on the pins)

A key parameter in determining the pressure drop is the Reynolds number as determined using the maximum speed through the pin-fin array. This maximum speed can be calculated from the approach speed to the pin-fin array as follows. For an inline configuration (i.e., pins are directly behind each other in the flow path as opposed to staggered):

$$u_{\max} = \frac{S_T}{S_T - 1} \cdot u_{app} \qquad \text{Equation (6)}$$

In the equation above, u_{app} is the approach speed of the fluid entering the pin-fin array. U_{max} is the maximum fluid speed through the pin-fin array (e.g., m/s).

For a staggered configuration:

$$S_D = \sqrt{S_S^{\,2} + \left(\frac{S_T}{2}\right)^2} \qquad \text{Equation (7)}$$

$$u_{\max} = \max\left(\frac{S_T \cdot u_{app}}{S_T - 1}\ ,\ \frac{S_T \cdot u_{app}}{2 \cdot (S_D - 1)}\right) \qquad \text{Equation (8)}$$

Equation 7 defines the diagonal pin-pitch in terms of the streamwise dimensionless pin pitch (S_S) and the transverse dimensionless pin pitch (S_T). Equations 5-8 are defined and derived from the geometry of the pin-fin array and based on simple flow constriction calculations conserving the mass of fluid flowing through each opening between pins. Once the maximum speed is known, the Reynolds number can be calculated.

$$\mathrm{Re}_{\max} = \frac{u_{\max} \cdot D}{\nu} \qquad \text{Equation (9)}$$

The symbol v is the kinematic viscosity. Re_{max} is the maximum Reynolds number which determines the flow regime.

For inline pins, an equivalent friction factor can be determined as follows:

$$f = f_{inline} = \left(0.044 + \frac{0.08 \cdot S_S}{\left(S_T - 1\right)^{0.43 + \frac{1.13}{S_S}}} \right) \cdot \mathrm{Re}_{\max}^{-0.15} \qquad \text{Equation (10)}$$

For staggered pins (i.e., each row of pins is offset), the equivalent friction factor is given by:

$$f = f_{staggered} = \left(0.25 + \frac{0.118}{\left(S_T - 1\right)^{1.08}} \right) \cdot \mathrm{Re}_{\max}^{-0.16} \qquad \text{Equation (11)}$$

Given the friction factor, f, the pressure drop through the pin-fin array can be obtained:

$$\Delta p_{\text{pinfin}} = 4 \cdot f \cdot N_S \cdot \left(\frac{\mu_{wall}}{\mu_{bulk}} \right)^{0.14} \cdot \frac{1}{2} \cdot \rho \cdot u_{\max}^2 \qquad \text{Equation (12)}$$

The symbol N_S is the number of pins in the streamwise direction. Density of the coolant is given by ρ. The absolute (dynamic) viscosity is given by μ where the subscripts "wall" and "bulk" indicate that absolute viscosity as measured either at the wall temperature or at the bulk coolant temperature. Equation 12 yields the pressure drop for a pin-fin array. Pressure drop from jet impingement cooling is currently being estimated using empirical data from NREL experiments. However, we are considering the development of a parametric model for jet impingement similar to what is being presented here for the pin-fins.

The pressure drop as predicted by the analytical model is compared to the pressure drop from an experimental dataset for pin-fins as well as pressure drop for jet impingement cooling in a configuration using 54 jets and having a similar form factor and footprint as the pin-fin array. The 54-jet array uses 1.5 mm diameter nozzles. For more information on jet impingement cooling, please see [5-6]. These results are shown in Figure 5.

Lines of constant parasitic power are drawn upon Figure 5. The intersection of the parasitic power lines across two configurations can be used to determine the flow rates for an equivalent parasitic power. There are a few caveats with Figure 5. Although the analytical pin-fin model has been set up as close as possible to the test configuration, there are some differences. The two main differences are that the test model uses elliptical pin fins as opposed to circular pin-fins in the analytical design. Second, the test configuration corresponds to a commercial inverter design. The commercial design introduces additional pressure drops into the flow stream from, for example, the presence of non-pin-fin support structures in the flow. Despite these caveats, we show reasonable agreement between analytical prediction of pressure drop for pin-fins and experimental data for both pin-fin and jet impingement from laboratory experiment.

Data for the pin-fin configuration is given in Table 1.

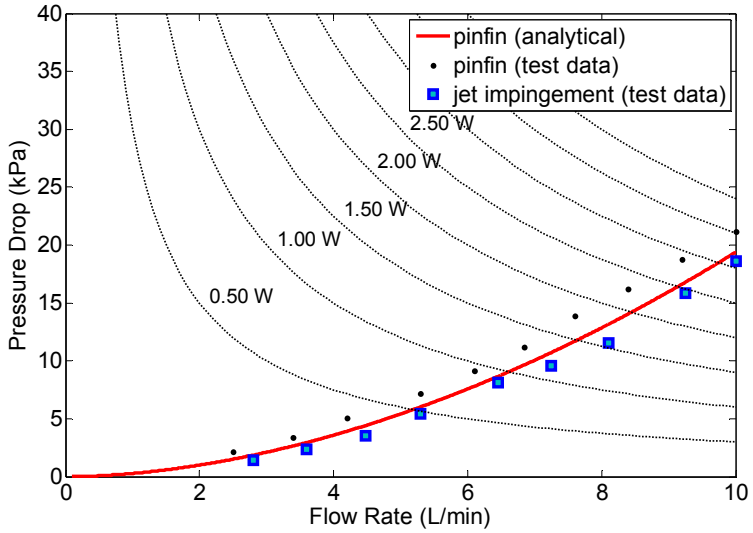

Fig. 5. Pressure Drop for a Pin-Fin Heat Exchanger compared with Jet Impingement Cooling

Pin-Fin Heat Transfer Performance

For thermal performance, we need to determine the Nusselt number which depends upon the value of the Reynolds number at the maximum flow speed and the Prandtl number (a temperature dependent property of the fluid). For an inline configuration, the Nusselt number is as follows:

$$Nu_{inline} = \begin{cases} if\ \ 1 \le \mathrm{Re}_{\max} < 100\ \ then\ \ 0.9 \cdot \mathrm{Re}_{\max}^{0.4} \cdot \mathrm{Pr}^{0.36} \cdot \left(\dfrac{\mathrm{Pr}}{\mathrm{Pr}_w}\right)^{0.25} \\ if\ \ 100 \le \mathrm{Re}_{\max} < 1000\ \ then\ 0.52 \cdot \mathrm{Re}_{\max}^{0.5} \cdot \mathrm{Pr}^{0.36} \cdot \left(\dfrac{\mathrm{Pr}}{\mathrm{Pr}_w}\right)^{0.25} \\ if\ \ 1000 \le \mathrm{Re}_{\max} < 2E5\ \ then\ 0.27 \cdot \mathrm{Re}_{\max}^{0.63} \cdot \mathrm{Pr}^{0.36} \cdot \left(\dfrac{\mathrm{Pr}}{\mathrm{Pr}_w}\right)^{0.25} \end{cases} \qquad \text{Equation (13)}$$

Similarly, the Nusselt number for a staggered pin-fin configuration is:

$$Nu_{staggered} = \begin{cases} if\ \ 1 \le \mathrm{Re}_{\max} < 500\ \ then\ \ 1.04 \cdot \mathrm{Re}_{\max}^{0.4} \cdot \mathrm{Pr}^{0.36} \cdot \left(\dfrac{\mathrm{Pr}}{\mathrm{Pr}_w}\right)^{0.25} \\ if\ \ 500 \le \mathrm{Re}_{\max} < 1000\ \ then\ 0.71 \cdot \mathrm{Re}_{\max}^{0.5} \cdot \mathrm{Pr}^{0.36} \cdot \left(\dfrac{\mathrm{Pr}}{\mathrm{Pr}_w}\right)^{0.25} \\ if\ \ 1000 \le \mathrm{Re}_{\max} < 2E5\ and\ \left(\dfrac{S_T}{S_S}\right) < 2.0\ then\ 0.35 \cdot \left(\dfrac{S_T}{S_S}\right)^{0.2} \cdot \mathrm{Re}_{\max}^{0.6} \cdot \mathrm{Pr}^{0.36} \cdot \left(\dfrac{\mathrm{Pr}}{\mathrm{Pr}_w}\right)^{0.25} \end{cases} \qquad \text{Equation (14)}$$

Table 1. Data for Pin-Fin Configuration

Property	Value
Number of Pins Streamwise (N_S)	66
Number of Pins Transverse (N_T)	8
Pin Height (mm)	7
Pin Diameter (mm) [hydraulic diameter]	2.68
Dimensionless Pin Pitch Transverse (S_T)	1.91
Dimensionless Pin Pitch Streamwise (S_L)	1.98
Coolant	Water
Inlet Coolant Temperature (^oC)	30
Coolant Flowrate (L/min)	1 to 10
Coolant Properties at 30 ^oC	
Density (kg/m^3)	996.8
Kinematic Viscosity (m^2/s)	8.04E-7
Absolute (Dynamic) Viscosity (N.s/m^2)	8.01E-4
Specific Heat (J/kg.K)	4178.4
Thermal Conductivity (W/m.K)	0.617
Prandtl Number	5.43
Coolant Properties at 35 ^oC	
Density (kg/m^3)	993.8
Kinematic Viscosity (m^2/s)	7.27E-7
Absolute (Dynamic) Viscosity (N.s/m^2)	7.22E-4
Specific Heat (J/kg.K)	4178.0
Thermal Conductivity (W/m.K)	0.625
Prandtl Number	4.83

For a pin-fin array, part of the flow is in direct contact with the bottom of the heat sink and heat is transferred similar to flow over a flat plate. For these conditions, the Reynolds number is:

$$\mathrm{Re}_{\max,plate} = \frac{u_{\max} \cdot L_S}{\nu} \qquad \text{Equation (15)}$$

In the above equation, L_S is the length of the pin-fin array in the streamwise direction. The variable v is the kinematic viscosity of the fluid. The corresponding Nusselt number is:

$$Nu = 0.664 \cdot \mathrm{Re}_{\max,plate}^{0.5} \cdot \mathrm{Pr}^{1/3} \qquad \text{Equation (16)}$$

The heat transfer coefficient based on the log-mean temperature difference is immediately available. The log mean temperature difference is given as [7]:

$$\Delta T_{lm} = \frac{\left(\overline{T_S} - T_I\right) - \left(\overline{T_S} - T_O\right)}{\ln\left(\frac{\overline{T_S} - T_I}{\overline{T_S} - T_O}\right)} \qquad \text{Equation (17)}$$

In the above equation, $\overline{T_S}$ is the average temperature of the heat sink, T_O is the outlet coolant temperature, T_I is the inlet coolant temperature, and ΔT_{lm} is the log mean temperature difference. Using this temperature, the heat transfer coefficient is given as:

$$h_{lmtd,pin-fin} = \frac{Nu \cdot k_{fluid}}{D}$$ Equation (18)

Similarly, for the flat plate, the heat transfer coefficient referenced to the log mean temperature difference is:

$$h_{lmtd,plate} = \frac{Nu \cdot k_{fluid}}{L_S}$$ Equation (19)

Note that $h_{lmtd,pin\text{-}fin}$ is the local heat transfer coefficient at the pin-fins as related to the log-mean temperature difference. However, to determine the actual heat transfer rejected from the fins, we must take into account the fact that the fins are not at a constant temperature. In fact, the further that we go down the length of a pin-fin, the more the temperature drops. Thus, the ability to transfer heat erodes with distance along pin length. This degradation in heat transfer can be accounted for using fin efficiency. Fin efficiency is given by the following relation:

$$m = \sqrt{\frac{4 \cdot h_{lmtd,pin-fin}}{k_{fin} \cdot D}}$$ Equation (20)

$$\eta_{fin} = \frac{\tanh(m \cdot H)}{m \cdot H}$$ Equation (21)

In the above equation, k_{fin} is the thermal conductivity of the pin-fin material. To transfer from log-mean temperature difference to $\left(\overline{T_S} - T_I\right)$, the temperatures we specified in Equation 2, we can use the effectiveness-NTU method [6]:

$$NTU = \frac{\left(h_{lmtd,plate} \cdot A_{plate} + h_{lmtd,pin-fin} \cdot A_{pin-fin} \cdot \eta_{fin}\right)}{\dot{m} \cdot c_p}$$ Equation (22)

In the equation above, NTU is the number of transfer units, $h_{lmtd,pin\text{-}fin}$ is the heat transfer coefficient at the pin-fins based on log-mean temperature difference, A_{pins} is the surface area of the pins (not including the tops), $h_{lmtd,plate}$ is the heat transfer coefficient based on log-mean temperature difference at the plate, A_{plate} is the area of the heat transmitting surface in contact with the fluid minus the pin-fin area, $\dot{m}_c$ is the mass flow rate of the coolant, and c_p is the specific heat of the coolant. The heat exchanger effectiveness can be calculated from the NTU for the case of a single coolant and heat sink as follows:

$$\varepsilon = \frac{\dot{Q}}{\dot{Q}_{\max}} = 1 - \exp(-NTU) = \frac{\left(T_{\text{coolant, outlet}} - T_{\text{inlet,coolant}}\right)}{\left(\overline{T}_{\text{heat sink}} - T_{\text{inlet,coolant}}\right)}$$ Equation (23)

The effective heat transfer coefficient referenced to the 2D projected area of the heat-sink, U_{eff}, can be expressed in terms of the temperature difference from heat sink to inlet coolant using the effectiveness as follows:

$$U_{eff} = \frac{\left(h_{lmtd,plate} \cdot A_{plate} + h_{lmtd,pin-fin} \cdot A_{pin-fin} \cdot \eta_{fin}\right) \cdot \varepsilon}{A_{2D}} \qquad \text{Equation (24)}$$

Often, the term $(UA)_{eff}$ in and of itself is valuable. This term is defined as follows:

$$(UA)_{eff} = \left(h_{lmtd,plate} \cdot A_{plate} + h_{lmtd,pin-fin} \cdot A_{pin-fin} \cdot \eta_{fin}\right) \cdot \varepsilon \qquad \text{Equation (25)}$$

Comparison of Pin-Fin Heat Exchanger to Pin-Fin Array

Based on Equation 25, a comparison can be made between the performance of a pin-fin heat exchanger and jet impingement cooling for the same parasitic power rates. This is shown in Figure 6 based on $(UA)_{eff}$ by parasitic power. The configuration presented here is the same as that from Table 1. Jet impingement cooling shows a 50% to 100% improvement in heat transfer for the same parasitic power.

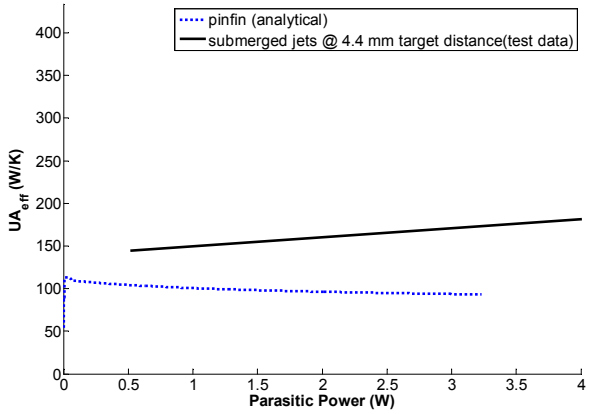

Fig. 6. $(UA)_{eff}$ as a function of flow rate for jets and pin-fins

A couple of notes regarding Figure 6 follow. Data for the pin-fin heat exchanger is determined from the analytical model based on the equations presented above. The heat transfer potential for the jet impingement cooling is estimated for a 54 jet array based on single jet experiments. The effective area of heat transfer for jet impingement is much smaller than the actual footprint (length times width of the cooling channel) of the heat sink. Thus, the "active heat transfer area" for the jet cooling is smaller than for the pin-fin case. Despite this, jets show a positive benefit to overall UA_{eff}. Because the majority of jet cooling occurs over a smaller amount of area, jets have potential to reduce the footprint of the inverter while transferring nearly the same amount of heat. This is not the case for the pin-fin heat exchanger where the heat transferred would be reduced in proportion to the decrease in heat sink footprint.

Another area that should be investigated is the use of flat fins for heat exchangers. Pin-fins appear ideal at providing significant heat transfer at low flow rates. However, as seen in Figure 6, as the flow rate, and thus parasitic power, increase, the performance actually begins to degrade. We currently do not have test data to validate this trend. However, we believe the reduction in UA_{eff} can be explained by corresponding reductions in fin efficiency and heat exchanger effectiveness at larger flow-rates. Flat or traditional fins do not impede the flow as much as pin-fins and thus may be able to transfer more heat at higher flow rates

with a lower parasitic power. Further investigation is necessary. Along similar lines, the analytical model should be extended to address elliptical pin-fins as well as circular pin-fins.

Figure 7 depicts the heat exchanger technologies we would like to include in future versions of the analytical heat sink model. They include flat fins such as found in the Toyota Camry power module heat sink, elliptical fins such as those found in Semikron technology, and jet impingement such as used in direct backside cooling.

To enhance jet impingement cooling, our team will also be investigating the use of surface enhancement to increase the effective area in contact with the jet.

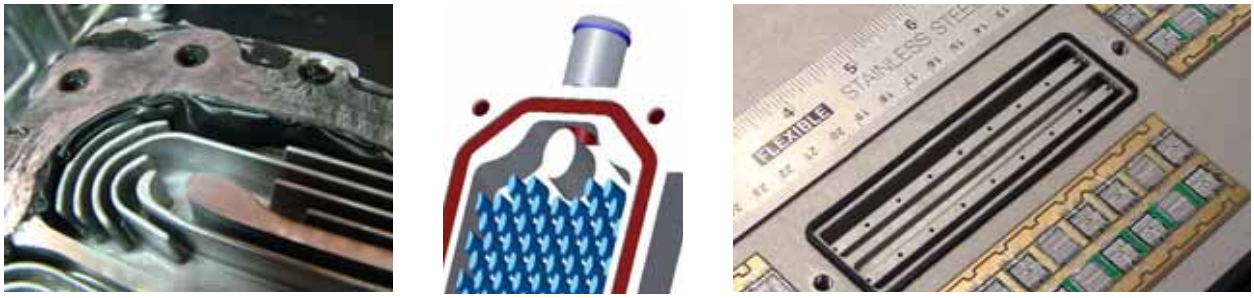

Fig. 7. (a) Flat fins used in Toyota Camry Hybrid heat sink (b) Elliptical Pin-fin design for Semikron heat-sink (c) Jet impingement cooling array

Conclusion

In conclusion, three topologies have been selected to analyze while developing and assembling the modeling capability for thermal stress and reliability analysis: a direct backside cooling configuration, a baseline pin-fin configuration, and a design that uses jet impingement upon a baseplate (refer to Figure 2). A necessary first step in examining these three topologies which use different cooling methods was to put all of the cooling methodologies on an equivalent basis. Equivalency was defined based on parasitic power – the power required to move coolant through a heat sink (equal to the pressure drop times the flow rate). Although test data was available for jet-impingement cooling, an analytical model was assembled based on fundamental heat transfer equations to predict the heat transfer performance of a pin-fin array. When put on an equivalent basis, jet impingement cooling data extrapolated to a 54-jet array the same size as the pin-fin array shows 50% to 100% more heat transfer capability than pin-fins at equivalent parasitic power. Further work is needed to compare both of these systems to other heat sink technologies such as flat fins and elliptical pin fins. Furthermore, we intend to investigate the use of surface enhancement to increase jet impingement cooling effectiveness. One potential feature of jet impingement cooling is the ability to reduce the "footprint" of the heat sink while transferring approximately the same amount of heat.

This report overviewed an analytical model that was used to compare pin-fin heat exchanger performance to jet-impingement performance on a consistent basis using parasitic power. The high level analytical model plays a good role as a design space exploration tool—capable of quickly running and estimating the performance of any pin-fin heat exchanger configuration. We would like to expand the number of these analytical models to include jet-impingement and flat fin configurations.

This work is a necessary first step in creating a larger reliability analysis toolkit for comparing different package designs and cooling technologies for both heat transfer performance as well as reliability on a consistent basis. Our next steps on the reliability task will be to perform detailed FEA analysis to include

thermal stresses of the three topologies using the work here to put their heat exchanger performance on a consistent basis.

Publications

O'Keefe, M. (July 2008). *Thermal Stress and Reliability for Advanced Power Electronics: Current Status and Future R&D Activities*. National Renewable Energy Laboratory Report NREL/MP-540-43565.

References

1. O'Keefe, M. (July 2008). *Thermal Stress and Reliability for Advanced Power Electronics: Current Status and Future R&D Activities*. National Renewable Energy Laboratory Report NREL/MP-540-43565.
2. Staunton, R., Ayers, C., Marlino, L., Chiasson, J., and Burress, T. (May 2006). "Evaluation of 2004 Toyota Prius Hybrid Electric Drive System". Oak Ridge National Laboratory Technical Report ORNL/TM-2006/423.
3. Kim, S. and Webb, R. (2006). "Analysis of Convective Thermal Resistance in Ducted Fan-Heat Sinks". *IEEE Transactions on Components and Packaging Technologies*.
4. Moores, K., Joshi, Y., and Schiroky, G. (June 2001). "Thermal Characterization of a Liquid Cooled AlSiC Base Plate with Integral Pin Fins". IEEE Transactions on Components and Packaging Technologies. Vol. 24. No 2. pp 213-219.
5. Narumanchi, S., Kelly, K., Mihalic, M., Gopalan, S., Hester, R., and Vlahinos, A. (2008). "Single-Phase Self-Oscillating Jets for Enhanced Heat Transfer". 24th IEEE SEMI-THERM Symposium.
6. Narumanchi, S., Bharathan, D., Hassani, V. (2005). "Comparison of Different Single-Phase Liquid Jet Impingement Cooling Configurations in the Context of Thermal Management in Power Electronics." Proceedings of the IPACK2005 ASME InterPACK 05. July 17-22, San Francisco, California, USA.
7. Incropera, F., De Witt, D. (1990). Fundamentals of Heat and Mass Transfer. Third Edition. John Wiley and Sons. New York. p. 426, 658-672.

2.5 Project Title: Power Electronics Thermal System Performance and Integration

Principal Investigator: Kevin Bennion
National Renewable Energy Laboratory
1617 Cole Blvd.
Golden, CO 80401-3393
Voice: 303-275-4447; Fax: 303-275-4415; E-mail:Kevin_Bennion@nrel.gov

DOE Technology Development Manager: Susan A. Rogers
Voice: 202-586-8997; Fax: 202-586-1600; E-mail: Susan.Rogers@ee.doe.gov

NREL Task Leader: Ken Kelly
Voice: 303-275-4465; Fax: 303-275-4415; E-mail: Kenneth_Kelly@nrel.gov

---

Objectives

Electric drive systems, which include electric machines and power electronics, are a key enabling technology for advanced vehicle propulsion systems that reduce the petroleum dependence of the transportation sector. To have significant effect, electric drive technologies must be economical in terms of cost, weight, and size while meeting performance and reliability expectations. The push to reduce the cost, weight, and size of critical electric drive components presents significant challenges related to thermal control and system integration. The integration of thermal control technologies with electric drive components must be done at a system level instead of being treated as an afterthought that is added at the end of the design process. This integrated systems approach requires a thorough understanding of the interactions between hardware design and thermal control technologies. This project will develop techniques to understand and improve the design of both hardware and thermal control into integrated systems. The end result will facilitate the integration of advanced power electronics thermal control technologies into commercially viable advanced automotive systems, including hybrid electric, plug-in hybrid electric, electric, and fuel cell vehicles.

Approach

The Power Electronics and Electric Machines (PEEM) program area in the DOE Vehicle Technologies Program is currently developing a suite of advanced thermal cooling technologies and performance data, including single-phase and two-phase jet impingement, air cooling, low thermal resistance insulated-gate bipolar transistor (IGBT) structures, improved thermal interface materials, and direct-cooled substrates. In order to evaluate, design, and develop thermal cooling systems that enable commercially viable products, a systems approach is required. A systems design approach focuses on two areas of the design. First, it looks at how the system is used to better match performance targets to actual use. Second, it looks at developing techniques to optimize the hardware design and thermal control techniques together to make most effective use of the design. As these system design techniques are developed, they will be used to support research in the PEEM program area. In addition, efforts will be made to review and implement the developed systems analysis techniques with industry through partnerships and collaborative arrangements. Working with industry will provide an understanding of technology trends and practical considerations for the implementation of technologies into viable automotive systems.

This year, researchers focused on the development of analytical capabilities and models to support the two areas of systems design previously mentioned. The efforts were focused on the following three topics, which are summarized in more detail in the technical discussion below:

1. Power Electronics Duty Cycle Characterization and Rapid Simulation
   - Develop the capability to obtain and characterize the thermal duty cycle of power semiconductor devices from vehicle drive cycles in the frequency domain.
   - Develop the capability to rapidly simulate the temperature response of power semiconductor devices in the frequency domain for optimization and reliability studies over vehicle drive cycles.
2. Inverter System Thermal Management
   - Develop a power electronics (PE) system model to investigate coolant temperature impacts on key supporting PE hardware.
   - Investigate the potential of dual cooling of PE systems.
3. Parametric FEA Model Development for Power Semiconductor Design Studies
   - Compare the frequency response of power semiconductor packages in terms of transient temperature cycling effects.
   - Develop the capability to study the impacts of package size and material properties in a parametric finite-element analysis (FEA) model of a semiconductor package, and apply it to various package configurations.
   - Investigate the potential of advanced double-sided cooling packages and options for advanced thermal control within an industry partnership.

Major Accomplishments

The key accomplishments for FY 2008 include the following:

- Developed a technique for characterizing vehicle drive profiles and PE thermal duty cycles in the frequency domain. The methodology enables additional analysis, including rapid transient simulation in the frequency domain and comparison to power semiconductor package frequency response characteristics.
- Developed an FEA parametric model and analysis techniques to characterize the transient behavior of power semiconductor package designs in the frequency domain. This technique enables qualitative comparison to frequency spectrum analysis of power semiconductor heat loads and rapid simulation of power semiconductor devices in the frequency domain.
- Created an FEA parametric model for material and package size design studies for power semiconductor packages. The modeling methodology enables optimization and sensitivity studies across multiple design factors.
- Established industry relationships to study the potential for double-sided cooling technologies.

Future Direction

The future direction of the thermal systems research through FY 2009 as it relates to power electronics includes the following:

1. Power Electronics Duty Cycle Characterization and Rapid Simulation
   - Apply developed techniques to characterize and compare thermal loading duty cycle across multiple advanced powertrain configurations consisting of hybrid electric, plug-in hybrid electric, electric, and fuel cell vehicles.
2. Inverter System Thermal Management
   - Compare power electronic cooling needs based on the operating environment across multiple advanced powertrain configurations consisting of hybrid electric, plug-in hybrid electric, electric, and fuel cell vehicles.
   - Investigate the potential for advanced thermal control to enable a lightweight PE system design.
3. Parametric FEA Model Development for Power Semiconductor Design Studies

- Experimentally validate the transient thermal response characteristics of power electronics package configurations.
- Perform modeling studies of advanced double-sided cooling packages to identify potential impacts on power electronics targets, and initiate hardware validation.

4. Continue to develop industry's involvement to improve our understanding of technology trends and practical considerations for the implementation of technologies into viable automotive systems.

Technical Discussion

As mentioned previously, the work for FY 2008 is grouped into the following main categories, which are explained in more detail in the following sections.

1. Power Electronics Duty Cycle Characterization and Rapid Simulation
2. Inverter System Thermal Management
3. Parametric FEA Model Development for Power Semiconductor Design Studies

Power Electronics Duty Cycle Characterization and Rapid Simulation

Thermal Duty Cycle Characterization

The transient nature of the thermal loading of the power electronics in HEV applications was shown in FY 2007 for the Toyota Prius hybrid traction drive inverter [1]. The "noisy" or highly variable nature of the thermal load makes it difficult to quickly understand and compare the impacts of drive profiles and vehicle configurations. The primary objective of the characterization of power semiconductor thermal duty cycles is not to capture the actual magnitude of the heat load but to analyze how the heat load varies over time. The actual heat load magnitude would depend on the vehicle type or application, but the duty cycle or variation over time is expected to be similar for comparable powertrain configurations. For this reason, in FY 2008 we developed a method for evaluating the thermal duty cycle in the frequency domain. The advantages include the following:

1. Promotes easier visual comparison of the thermal duty cycle.
2. Enables comparison to power semiconductor package frequency response characteristics.
3. Enables rapid model simulation in the frequency domain for linear lumped parameter models with constant coefficients.

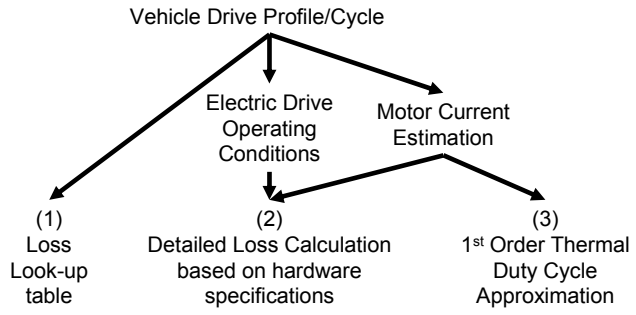

Fig. 1. Techniques for Determining Power Semiconductor Device Losses

The first step in characterizing the thermal duty cycle in the frequency domain is to determine the respective heat load as a function of time. Figure 1 highlights three methods for estimating the thermal duty cycle from losses within power semiconductor devices for traction drive applications. The first method utilizes measured device losses in tabulated form, which was used for the thermal duty cycle analysis in FY 2007 [1]. The disadvantages of this method include the availability of measurement data

and the allocation of the losses to the respective semiconductor devices. The second method involves detailed calculations based on the electric drive hardware and control techniques. The disadvantage of this method is the need for detailed data or parameter information related to the electric drive hardware and controls. While the first two methods are preferred for the heat load estimation, the required data is often unavailable early in the electric drive design, when component specifications are in development. For this reason, we proposed an alternate method for estimating the thermal duty cycle that is highlighted in Figure 1 as the third technique. With this technique, the transient thermal load is based only on the relative electric drive current. Since the heat load within the semiconductor device is highly dependent on the root-mean-square (rms) current of the electric drive, the variation in the rms current over the drive cycle approximates the variation in heat within the power semiconductors over the drive cycle. The actual magnitude of the losses can be adjusted to represent the desired magnitudes for the particular application or the approximate loading conditions between semiconductor devices (IGBTs and diodes) at a given operating point. While not a replacement for detailed loss data, the third method would allow for an initial analysis of transient heat loads on power semiconductor packages. This would support power semiconductor manufacturers and researchers interested in evaluating the transient effects of alternative power semiconductor packaging designs.

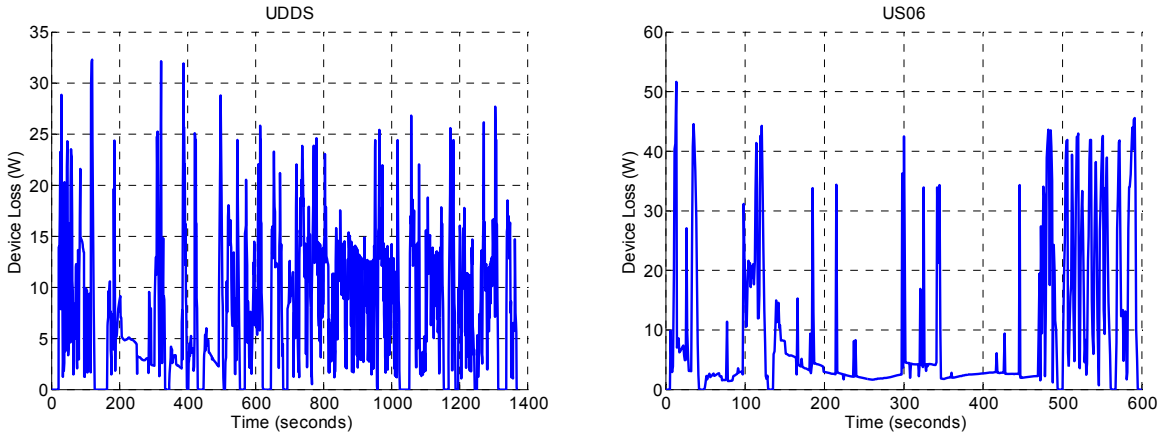

Fig. 2. Thermal Duty Cycle – Time Domain

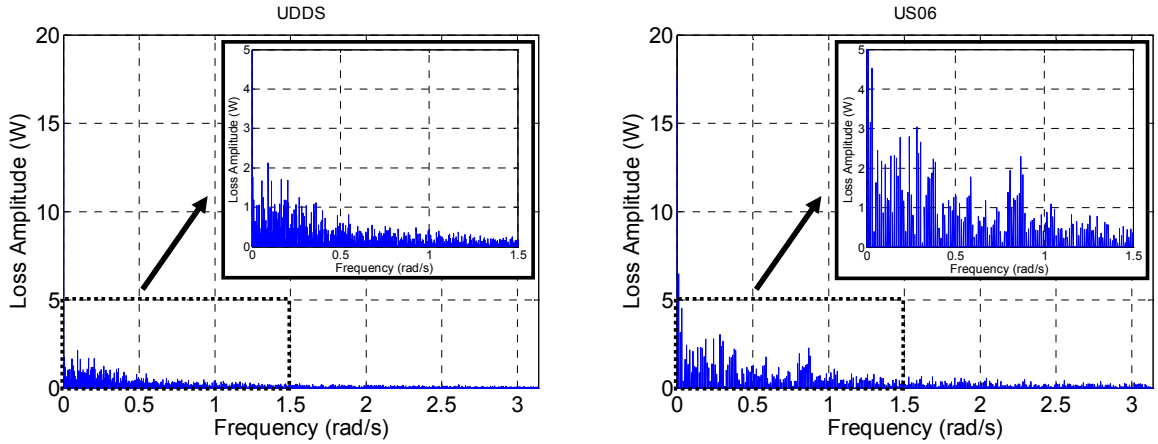

Note: Displayed FFT assumes cycle driven continuously (can construct other periodic data).

Fig. 3. Thermal Duty Cycle – Frequency Domain

The primary objective in FY 2008 included the development of the analysis tools and a demonstration comparing the thermal duty cycle of vehicle drive profiles in the frequency domain. Figures 2 and 3

illustrate how converting the time domain thermal loads into the frequency domain through a discrete Fourier transform [2, 3] enables an easier comparison of loading conditions from vehicle drive cycles. One is able to see not only an increase in the magnitude of the losses, but also higher loss magnitudes at higher frequencies, which impact the thermal stresses from power cycling. The highest frequency displayed in Figure 3 is limited by the sample rate of the vehicle drive cycles. For example, the data shown in Figure 3 correspond to a vehicle drive profile with a sample time of one second. This corresponds to a Nyquist frequency of 0.5 Hz or 3.14 rad/s.

Future work related to this project will extend this analysis to multiple drive cycles and powertrain configurations. In addition, a thorough comparison of the three highlighted methods for determining the power semiconductor losses is required. The significance of the proposed technique is that it enables a visual comparison of thermal duty cycles, and it supports additional systems analysis techniques discussed below. These techniques include rapid thermal simulation of power semiconductor packages in the frequency domain [3] and comparison to the frequency response of power semiconductor packages.

Rapid Thermal Model

A rapid or fast transient thermal model enables quick simulation of temperature over longer periods of time, such as those seen in vehicle drive cycles. The ability to take a temperature response for FEA simulations and build a lumped parameter network model was initiated in FY 2007. Simulations of the lumped parameter model in the time domain run significantly faster than detailed FEA models; however, the time to simulate long or multiple drive cycles can still be significant, depending on the required time step used for the solution. Instead of using the thermal load in the time domain as the input to the model, an alternative approach is to calculate the temperature response of the model using the thermal heat load in the frequency domain [3]. The temperature response is determined in the frequency domain by determining the transfer function of the linear lumped parameter model with constant coefficients. The output temperature response can then be converted to the time domain. Figure 4 compares the temperature response for each method for a hypothetical input heat load. As the graph shows, the results are the same, but the calculations in the frequency domain require significantly less computation time.

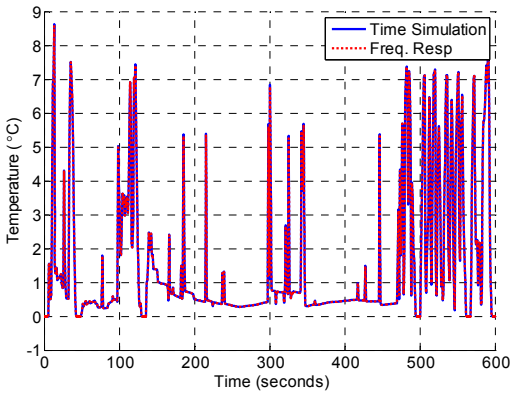

Fig. 4. Comparison of Time Domain and Frequency Domain Temperature Response Calculations

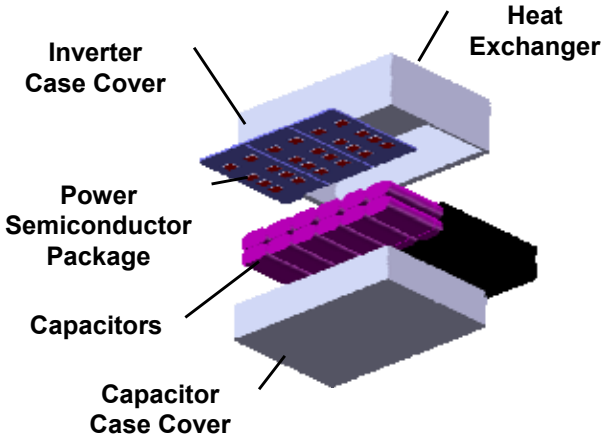

Fig. 5. Diagram of Inverter System Thermal Analysis Components (Exploded View)

The primary advantage of this rapid thermal simulation technique is the potential to evaluate system performance under transient loading conditions, as seen in actual drive cycles. The technique could provide a faster method for performing package optimization and reliability studies based on temperature fluctuation from power cycling.

Inverter System Thermal Management

In addition to evaluating the thermal control of power electronics at the power semiconductor package level, we developed a parametric finite-element model for thermal control of power electronics at the module level, including the key supporting components shown in Figure 5. Current hybrid electric vehicles often use a separate liquid coolant loop for the hybrid drive system, which includes the power electronics, because of the need for a lower temperature coolant loop than what is currently available on vehicles. In an effort to reduce system cost, there is interest in developing power electronics systems that are integrated into existing coolant loops within the vehicle. This could include the engine coolant loop for an internal combustion engine or the liquid coolant loop for a fuel cell. In either case, the coolant temperature could approach 105°C. As the coolant temperature increases in the heat exchanger, it not only impacts the cooling of the power semiconductor devices, but it also impacts supporting electronics such as the capacitors [4]. For this reason, it is important to look at the impact of alternative cooling designs on the entire system. In FY 2008, a preliminary investigation into the impact of coolant temperature on the PE system was performed. We looked at the impacts of coolant temperature, heat exchanger performance, and capacitor cooling on the capacitor temperature profile. The parameters used for the sensitivity analysis are listed in Table 1.

Table 1. Inverter System Sensitivity Parameters

Factors	Units	Levels
Heat Input – Power Semiconductor Losses	[W]	1500
Vertical Wall Effective Convection Coefficient	[W/m^2-°C]	5
Vertical Wall Ambient Air Temperature	[°C]	125
Capacitor Case Bottom Effective Convection Coefficient	[W/m^2-°C]	4 : 100
Capacitor Case Bottom Air Temperature	[°C]	125 : 40
PE Heat Exchanger Effective Convection Coefficient	[W/m^2-°C]	7,000 : 20,000
PE Coolant Temperature	[°C]	70 : 105

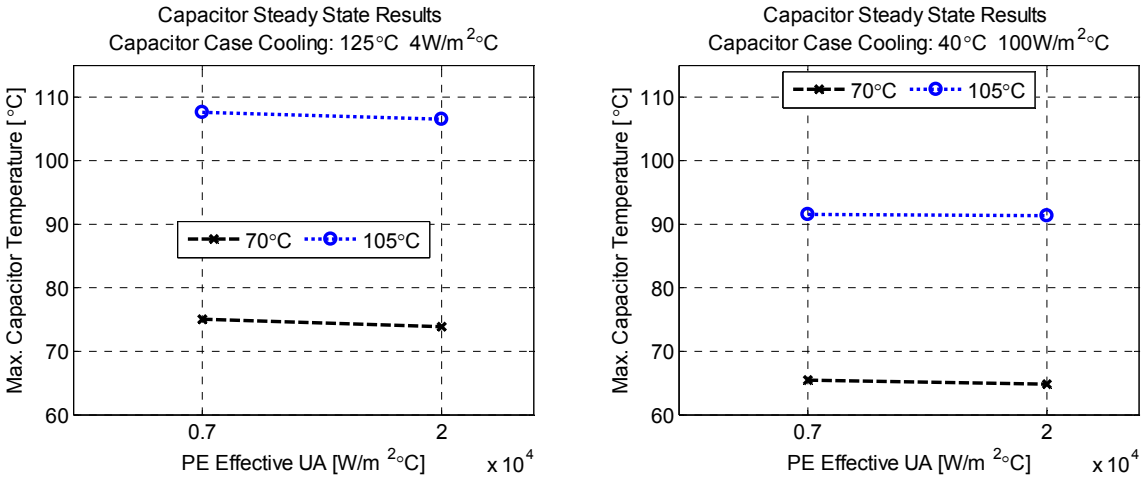

Fig. 6. Impact of PE Coolant Temperature and PE Heat Exchanger Performance on a Passively Cooled (left) and Actively Cooled (right) Capacitor

Figure 6 highlights the impact of the heat exchanger fluid temperature (70°C-105°C), capacitor cooling, and heat exchanger performance on the maximum capacitor temperature. As seen in the figure, the heat exchanger performance does not have a significant impact on the capacitor temperature in the steady state. In the steady-state condition, the capacitors approach the surrounding case temperature, which

approaches the coolant temperature for a thermally conductive case. However, the initial analysis shows that limited air cooling of the capacitor case with ambient air at 40°C has the potential to lower the capacitor operation temperature and allow the use of high-temperature coolant for the power semiconductors. For example, a small fan could be used to flow outside ambient air through the power electronics box and capacitors. This dual coolant approach would use an existing high-temperature liquid coolant loop for the power semiconductor devices, and a second air cooling loop for the supporting electronics. Future work will look at how alternative cooling techniques and vehicle operating environments impact the thermal design and weight of the power electronics system.

Parametric FEA Model Development for Power Semiconductor Design Studies

Package Transient Thermal Response Characterization

For power semiconductor thermal resistance, significant attention is placed on steady-state performance. However, the transient thermal impedance has a significant impact on package reliability because of the transient nature of vehicle drive profiles. This year we proposed a method for comparing transient thermal impedance based on the frequency response of the power semiconductor package, as shown in Figure 7. The process links the thermal duty cycle load in the frequency domain, as discussed previously, to the frequency response of the package. This method not only enables rapid simulation in the frequency domain based on the frequency spectrum of the thermal duty cycle, but it also enables quick qualitative comparisons based on the breakpoint or cutoff frequency of the frequency response.

To demonstrate the process, we evaluated the frequency responses of three power electronics package designs. Figure 8 highlights the main package layers, while Figure 9 shows each of the three configurations used in the analysis. The heat sink configuration is the standard power semiconductor package with a thermal interface material (TIM) between the baseplate and heat sink. The baseplate configuration removes the heat sink and TIM layers, and the baseplate is cooled directly. This is done to reduce the steady-state thermal resistance of the package. Finally, the direct-bond copper (DBC) configuration takes the removal of layers a step further. It removes the baseplate and the respective solder attachment, and the DBC is cooled directly.

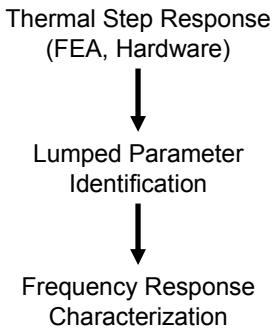

Fig. 7. Frequency response analysis process.

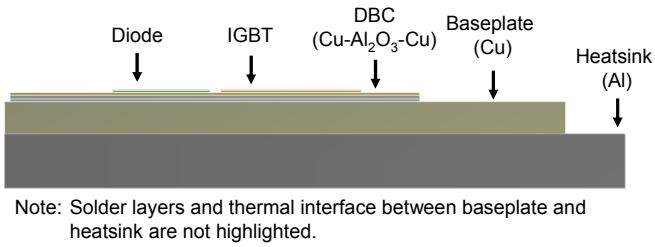

Fig. 8. General power semiconductor package.

Figure 10 compares the frequency response for each package assuming an isothermal boundary condition for the cooled surface. The breakpoint or cutoff frequency for each design is shown in the figure, and it is defined as the point where the thermal impedance drops by a ratio of -3 dB or 0.707 [5, 6] from the peak value. The output amplitude temperature is significantly attenuated at frequencies beyond the cutoff frequency. As expected, the DBC design has the lowest steady-state or low-frequency thermal impedance because of the removal of layers within the package. However, the reduced thermal mass of the DBC topology causes the cutoff frequency to increase by more than a factor of 10. The result is a system more vulnerable to the higher frequency dynamic loading conditions from vehicle drive cycles. For the drive cycles shown in Figure 3, the cutoff frequency for each of the packages is above the higher amplitude

frequencies shown in the frequency spectrum of Figure 3. From this initial analysis it would appear that the DBC package would not experience a significant increase in thermal stress due to power cycling from vehicle drive cycles. The heat sink topology does show some temperature attenuation beyond 0.5 rad/s, so some effect would potentially be seen in the other topologies for aggressive drive cycles, such as the US06 cycle shown in Figure 3. Also, this initial analysis does not look at other effects due to motor speed and switching frequency. Future work into FY 2009 will look to augment the technique through improved hardware validation and investigate how different cooling techniques could impact the transient thermal response. A thorough review of the loss estimation techniques is also required, along with the potential impact of higher frequency load sources.

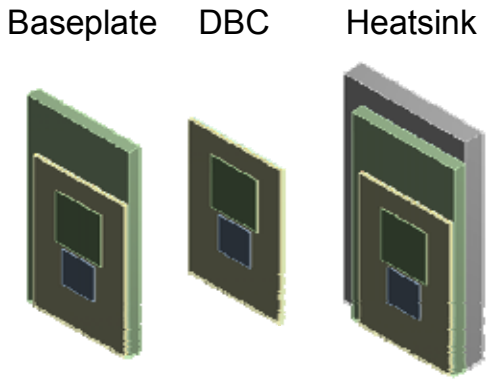

Fig. 9. Power Semiconductor Package Configurations

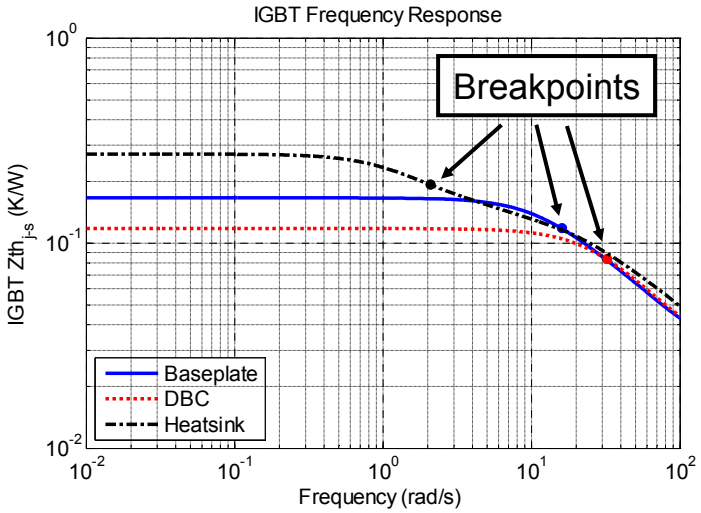

Fig. 10. Frequency Response of Power Semiconductor Packages

Power Semiconductor Package Design Study

In FY 2007, we developed an initial parametric FEA model to evaluate the sensitivity of different package designs to the coolant temperature and effective heat transfer coefficient in terms of the maximum heat flux through a power semiconductor package [7]. Other methods to improve thermal performance include using higher thermal conductivity materials and increasing the package size to apply the cooling to a larger surface area through thermal spreading, which will affect the size and cost of the system. For this reason, it is important to understand the interactions between package topology, material selection, package size, and cooling technologies. This year we added the capability to adjust material properties and package size. This new capability creates a modeling framework with the ability to simultaneously study the impacts of heat exchanger performance, material properties, and package geometry. This results in the ability to perform sensitivity and optimization studies to design the optimum power semiconductor package and cooling technologies for a desired application.

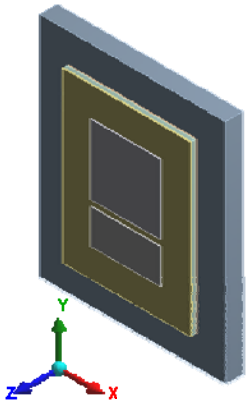

Fig. 11. General Package Construction and Coordinate System

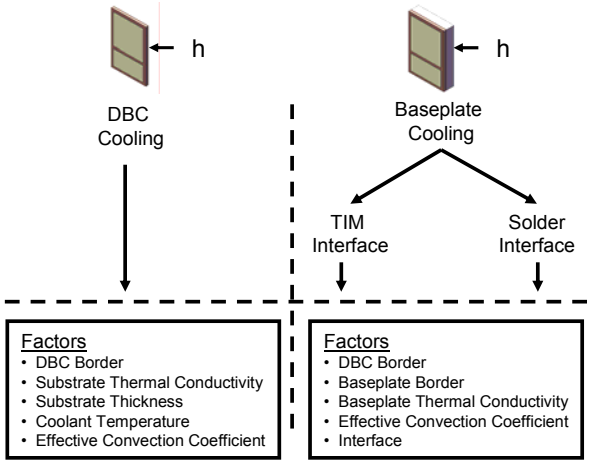

Fig. 12. Power Semiconductor Sensitivity Analysis Factors

To demonstrate the process, we modeled a generic power module package within ANSYS. The package is shown in Figure 11, and it consists of a single IGBT and diode device attached to a DBC substrate that is optionally attached to a baseplate or thermal spreader. Figure 11 also shows the modeling coordinate system to provide a reference for the design factors used in the sensitivity analysis. Two generic package topologies were selected, as shown in Figure 12. The DBC cooling design allowed direct cooling of the DBC, while the second topology included a baseplate that was attached to the DBC. The baseplate served as the heat exchanger surface in the second topology, which is commonly found in today's power semiconductor packages. Two methods for the baseplate attachment were considered. The first used conventional grease for the thermal interface material (TIM), and the second approach assumed a solder connection. The assumed contact resistances ($R_{t,c}$) are listed in Table 2 for the TIM and solder interfaces. The design factors or variables for each topology listed in Figure 12 are defined in Figure 13. Although the figure shows the convection cooling applied to the baseplate, for the DBC configuration the convection cooling was applied directly to the exposed surface on the bottom of the DBC.

Table 2. Thermal Contacts

	k [W/m-°C]	z [mm]	$R_{t,c}$ [mm^2-°C/W]
Silicon to DBC - Solder	32.4	0.13	3.92
DBC to Base - Solder	32.4	0.13	3.92
DBC to Base - TIM	1.0	0.10	100

Note: Dimensions are based on industry interactions and cited references [8-10].

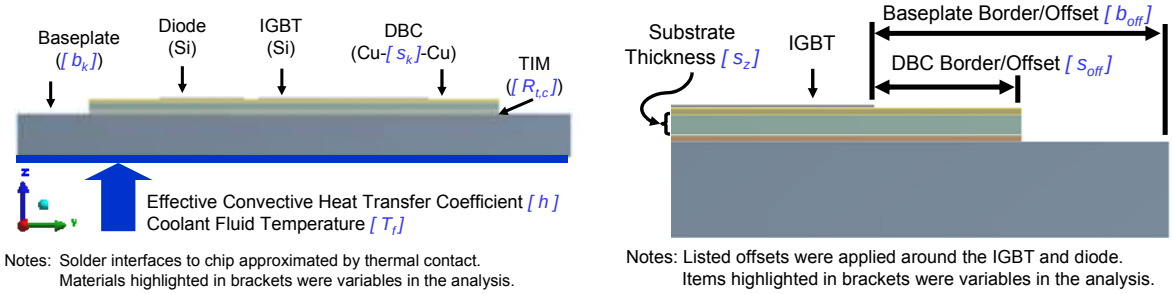

Fig. 13. Power Semiconductor Sensitivity Analysis Factors

Table 3. Layer Material and Geometry Summary

	k [W/m-°C]	x [mm]	y [mm]	z [mm]
IGBT	90	12	12	0.12
Diode	90	12	6	0.12
DBC-Copper	387.6	variable	variable	0.2
DBC-Substrate	variable : 170	variable	variable	variable : 0.64
DBC-Copper	387.6	variable	variable	0.2
Baseplate/Heat Exchanger	NA : variable	NA : variable	NA : variable	NA : 3

Notes: Dimensions are based on industry interactions and cited references [8-10].
Properties listed as (item1:item2) refer to the DBC and baseplate topologies, respectively.

A summary of the material properties and dimensions is provided in Table 3. The items listed as "variable" were changed in the model, depending on the design factors used in the sensitivity analysis. For example, while the IGBT and diode dimensions were fixed, the dimensions of other layers within the package were adjusted based on the desired values or levels for the design factors.

DBC Package Sensitivity Analysis

The first package configuration shown in Figure 12 is the DBC topology where cooling is applied directly to the backside of the DBC. The factors used for the sensitivity analysis and the selected levels are shown in Table 4. The thermal conductivity values for the substrate were selected to represent Al_2O_3 and AlN. The substrate thickness was adjusted based on the substrate material. Iterations utilizing Al_2O_3 or a thermal conductivity of 25 W/m-°C had a substrate thickness of 0.38 mm, while iterations using AlN had a substrate thickness of 0.64 mm [8-10].

Table 4. DBC Package Design Factors and Respective Levels

Factors	Description	Levels
s_{off}	Border between silicon and DBC or substrate	1.0, 2.47, 6.08, 15.0 [mm]
s_k	Thermal conductivity of substrate or ceramic layer	25, 170 [W/m-°C]
s_z	Substrate thickness	0.38, 0.64 [mm]
T_f	Temperature of cooling fluid	50, 70, 105 [°C]
h	Effective heat transfer coefficient	0.2, 1.4736, 10.8577, 80 [kW/m^2-°C]
Design Points:	96	

Figure 14 shows the effect of increasing the DBC size relative to the IGBT and diode. It highlights interactions between DBC size, convection coefficient, and substrate thermal conductivity. At low effective convective heat transfer coefficients (h), there is a continual improvement in performance as the DBC size (s_{off}) increases. However, at higher convective heat transfer coefficients, the rate of improvement decreases. This illustrates the impact that improved thermal control can have on DBC size. First, improvements in effective convective heat transfer coefficient enable improved thermal performance with smaller DBC areas. This impacts cost and size, which are critical for viable power electronics systems. Second, the optimum DBC size depends on the effective heat transfer coefficient. At a certain point, the cost or size impact of increasing the DBC surface area outweighs the potential improvement in thermal performance. This highlights the importance of understanding the relationships between package geometry and cooling technologies. In addition, the importance of matching material selection with thermal control is also highlighted. As shown in the graphs, the more aggressive cooling is better able to utilize higher thermal conductivity materials. The results show that material selection should be matched with cooling technologies to make the best use of materials having a higher thermal conductivity.

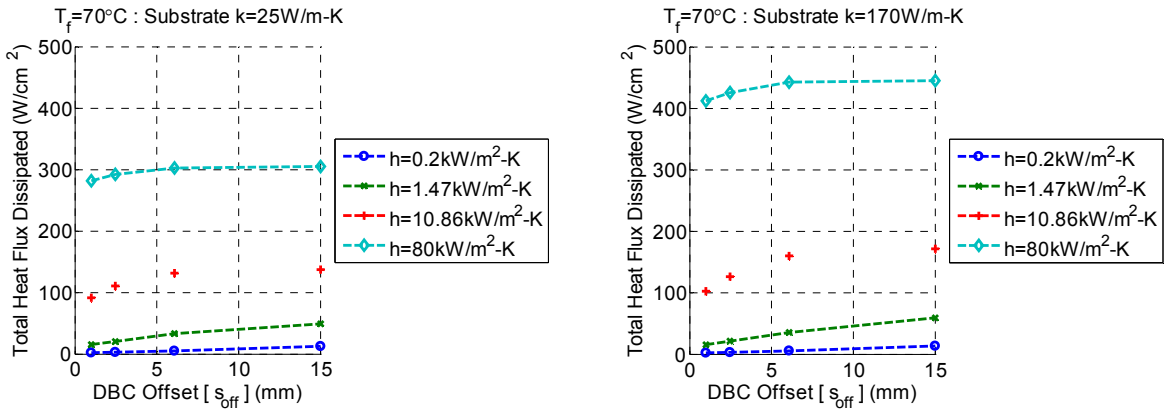

Fig. 14. Heat Flux vs. DBC Size and Substrate Thermal Conductivity for Multiple Effective Convective Heat Transfer Coefficients

Baseplate Sensitivity Analysis

The second package configuration shown in Figure 12 is the baseplate package. The baseplate acts as a heat spreader and heat exchanger. Two methods of attaching the baseplate to the DBC were modeled. The first model assumed a thermal grease TIM, and the second assumed a solder attachment. The factors used for the sensitivity analysis and the selected levels are shown in Table 5. The levels for the baseplate thermal conductivity were selected to represent a range of materials representing aluminum alloys, copper moly, AlSiC, copper, and heat pipes or vapor chambers. A discussion of the results is beyond the scope of this summary report (a technical report is planned for fiscal year 2009), but similar conclusions were seen as compared with the DBC topology. In general, the analysis highlights the need to understand the interactions at a systems level between package topology, material properties, package size, and cooling technologies to obtain an optimized solution for a particular application. This new modeling capability will support this need.

Table 5. Baseplate Package Design Factors and Respective Levels

Factors	Description	Levels
s_off	Border between silicon and DBC or substrate	1.0, 2.47, 6.08, 15.0 [mm]
b_off	Border between silicon and base layer or substrate	1.0, 2.47, 6.08, 15.0 [mm]
b_k	Thermal conductivity of base or heat exchanger layer	167, 190, 387.6, 5000, 25000 [W/m-°C]
h	Effective heat transfer coefficient	0.2, 1.4736, 10.8577, 80 [kW/m^2-°C]
Interface ($R_{t,c}$)	Contact resistance between DBC and baseplate	100, 3.92 [mm^2-°C/W]
Design Points:	400*	

* Removed design points with substrate larger than baseplate.

Investigation of Advanced Double-Sided Cooling Packages

As part of the work performed in FY 2007 [7], it was shown that double-sided cooling for power semiconductor devices could provide significant improvements in heat flux dissipation. For this reason, the development and integration of double-sided packaging with advanced thermal control technologies is seen as a key path to improving the power density of power electronics systems. During this year, we worked to develop a partnership with an industry partner (Delphi Corporation) that manufactures a power semiconductor package enabling double-sided cooling. This industry collaboration not only provides important feedback on technology trends and manufacturability, but it also provides opportunities to implement the developed systems analysis techniques in an industry setting. Future work will focus on

how advanced thermal control technologies developed as part of the PEEM program area can be integrated into double-sided cooling applications.

Conclusion

The objective of the thermal systems task is to facilitate the integration of advanced power electronic thermal control technologies into commercially viable advanced automotive systems. This requires understanding how the power electronics are used, how the environment in which they operate impacts thermal control, and how power semiconductor packaging and cooling impacts performance. Therefore, in FY 2008 we worked to develop methodologies and capabilities to meet these three needs.

A method was developed for comparing the thermal duty cycle on power semiconductor components in the frequency domain. This enables an easier comparison of different drive profiles and powertrain designs. One can see the impact on power semiconductor devices not only in terms of the magnitude of the losses, but also the frequency response, which impacts reliability of power semiconductor packages.

An initial investigation into how the power electronics operating environment and cooling techniques impact supporting components (capacitors) was performed at a power electronics systems level. It led to the development of an FEA power electronics system model, which will in turn lead to future work comparing how the operating environment of different powertrain designs could impact the power electronics system design and how existing vehicle coolants can be integrated into power electronics systems. The work will also lead to efforts to develop effective lightweight power electronics systems through improved thermal control.

Finally, improvements to parametric FEA models enable the ability to perform sensitivity studies for advanced thermal control technologies. This not only helps to provide design guidance but also helps to match packaging materials and thermal control technologies to obtain the most effective use of the selected materials and components. With collaboration from industry partners, we are applying the developed analysis techniques to investigate the potential of advanced packaging topologies, such as double-sided cooling, for power semiconductor packages.

References

1. M. O'Keefe, G. Albright, and K. Bennion, *Thermal Duty Cycles of Hybrid Electric Vehicle Power Electronic Components*, National Renewable Energy Laboratory Report No. TP-540-41829, 2007.
2. R. Figliola and D. Beasley, *Theory and Design for Mechanical Measurements* (2nd Edition), 1995.
3. J. Nelson, G., Venkataramanan, and M. EL-Refaie, "Fast Thermal Profiling of Power Semiconductor Devices Using Fourier Techniques," *IEEE Transactions on Industrial Electronics*, Vol. 53, No. 2, April 2006.
4. J. Hsu, R. Staunton, and M. Starke, *Barriers to the Application of High-Temperature Coolants in Hybrid Electric Vehicles*, Oak Ridge National Laboratory Report No. TM-2006/514, 2006.
5. W. Palm, Modeling, Analysis, and Control of Dynamic Systems (2nd Edition), 1999.
6. G. Franklin and J. Powell, *Feedback Control of Dynamic Systems* (3rd Edition), 1994.
7. M. O'Keefe and K. Bennion, "A Comparison of Hybrid Electric Vehicle Power Electronics Cooling Options," IEEE Vehicle Power and Propulsion Conference, September 9-12, 2007.
8. J. Miller, "Feasibility and Reliability of High-Temperature Power/Control Electronics for HEV's," prepared by Kevin Kennedy and Associates for Oak Ridge National Laboratory, June 21, 2004.
9. T. Laska, L. Lorenz, and A. Mauder, "The New IGBT Generation a Great Improvement Potential for Motor Drive Systems," IEEE Industry Applications Conference, Vol. 5, October 8-12, 2000.
10. Z. Khatir, "Real-Time Computation of Thermal Constraints in Multichip Power Electronic Devices," *IEEE Transactions on Components and Packaging Technologies*, Vol. 27, No. 2, June 2004.

2.6 Thermal interface materials for power electronics applications

Principal Investigator: Sreekant Narumanchi
National Renewable Energy Laboratory
MS 1633
1617 Cole Blvd
Golden, CO 80401-3393
Voice: 303-275-4062; Fax: 303-275-4415; E-mail: sreekant_narumanchi @nrel.gov

DOE Technology Development Manager: Susan A. Rogers
Voice: 202-586-8997; Fax: 202-586-1600; E-mail: Susan.Rogers@ee.doe.gov

NREL Task Leader: Kenneth Kelly
Voice: 303-275-4465; Fax: 303-275-4415; E-mail: kenneth_kelly@nrel.gov

---

Objectives

Thermal interface materials (TIMs) pose a major bottleneck to heat removal from the IGBT package. In a typical automotive IGBT package, the direct bond copper (DBC) layer is attached to the aluminum heat sink via a thermal grease, which has a thermal conductivity of 0.4 to 0.7 W/mK and is a major contributor to the thermal resistance in the package. An optimum TIM would help in dissipating higher heat fluxes, which in turn could enable reduced die size or fewer switching devices. Reducing the thermal resistance of the TIM can also help us achieve the FreedomCAR program goals of using glycol water at 105°C or even air cooling. All these would help reduce the cost, weight, and volume of power electronics, which is the main FreedomCAR goal.

A project was initiated in FY 2006 to thoroughly characterize the state-of-art conventional interface materials as well as novel materials and recommend a suitable candidate material for automotive power electronics applications. The specific objectives for FY 2008 were:

- Characterize the performance of materials such as greases, gels, phase change materials (PCMs), graphite, thermoplastics, filler pads and carbon nanotubes over temperature and pressure ranges characteristic of automotive applications.

Beyond FY 2008, the objectives include:

- Characterize the impact of thermal cycling on the thermal performance of the interface materials.
- Characterize the in-situ performance of these materials. Often, the package in-situ performance is not exactly the same as the material performance under more idealized conditions.

Approach

- NREL acquired and modified in-house a test stand to perform thermal resistance measurements over the automotive temperature (-40° to 150°C) and pressure ranges (20 to 150 psi). This test stand is based on the standard ASTM-D5470 steady-state test method for thermal resistance measurements. The apparatus allows us to measure the contact and bulk resistance of materials and also determine the thermal conductivity of materials. We performed consistent and objective characterization of thermal performance of interface materials.

Major Accomplishments

The following are the main accomplishments of this project in FY 2008:

- Thermal resistance measurements of a variety of interface materials were performed using the steady-state approach. This included a characterization of experimental uncertainty. Some samples were also acquired from NIST and the NREL experimental results matched favorably with the results reported by NIST using a guarded hot-plate, steady state approach for thermal resistance measurements.
- A significant objective and consistent material thermal performance database has been established. The materials tested include greases, PCMs, filler pads, graphite, indium, thermoplastics, and carbon nanotubes. Overall, about 40 materials spanning the classes of materials mentioned above were tested. Some high-thermal performance greases and PCMs were identified.
- We also tested a number of materials for other industry partners under work-for-others agreement or other DOE project funding.
- We had significant industry collaboration and interaction (automotive industry suppliers such as: UQM, Delphi, and Semikron; TIM manufacturers such as Parker Chomerics, Shinetsu, and Honeywell). The scope of collaboration included testing samples provided by industry partners, exchange of experimental results obtained via different test methods, and seeking information about the practical industry perspective on TIMs.
- Some of NREL's experimental results also influenced Delphi's choice of an appropriate material for use in their prototype inverter.

Future Direction

The following activities are planned for FY 2009 and beyond:

- In collaboration with industry, the performance of the best performing materials in a realistic package configuration will be characterized. The thermal resistance of the package/composite structure will be characterized based on the steady-state approach for thermal resistance measurements. A transient test methodology will also be explored. A transient thermal tester has been purchased and will soon be part of the in-house capabilities at NREL.
- We will conduct studies related to thermal cycling of the package with the TIM in place. The impact of thermal cycling on the thermal performance of the TIM will be characterized. This cycling will be performed over a temperature range of -40° to 150°C and after cycling, the thermal resistance of the package will be characterized on the NREL test stand. (both transient and steady-state). Aspects such as the impact of aging (long-term exposure of the package at an elevated temperature) on the thermal performance of these interface materials will also be explored. These studies will also be conducted in an environmental chamber. A mechanistic understanding of TIM degradation is currently lacking in the literature. An attempt will be made to propose models for degradation of TIMs.
- The results of all the studies related to thermal resistance and reliability will be actively disseminated to automotive power electronics industry in particular, as well as the broader electronics packaging community.
- A number of package configurations are appearing in the industry which eliminate the TIM altogether. A more extensive survey of industry trends and requirements will be performed in order to assess if TIMs will be required in the future.

Technical Discussion

Importance of Thermal Interface Materials and Challenges for Automotive Power Electronics

Figure 1 shows the different layers constituting a typical insulated gate bipolar transistor (IGBT) package in an inverter. The silicon die is soldered to the direct bond copper (DBC) layer, which is composed of an aluminum nitride layer sandwiched between two copper layers. This DBC layer is soldered to a copper baseplate, and the grease layer serves as the interface between the baseplate and the heat sink. This

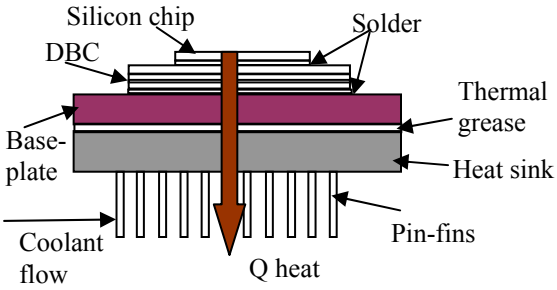

Fig. 1. Layers Constituting the IGBT Package in an Inverter (not to scale)

thermal grease can be up to 100 microns thick (bond-line thickness, or BLT) and, depending on the formulation, it has a thermal conductivity in the range of 0.4 to 5 W/mK. In an actual IGBT package, overall size, layout, and manufacturing process and assembly can cause the DBC substrate to have a camber of up to 100 microns, so the TIM is required to fill this gap, at least at certain points in the package. Grease is still predominantly used in IGBT packages in an inverter. This grease layer can contribute almost 40% to 50% of the total resistance of the layers in the package. Reducing the thermal resistance of the TIM can help us achieve the FreedomCAR program goals of using glycol water at 105°C or even air cooling. In most inverter configurations, a clamping mechanism is used to attach the package to the heat sink. This results in the TIM being subjected to a pressure of the order of 170 to 340 kPa.

To assess the impact of thermal resistance of the TIM, we performed a 3-D finite element analysis using ANSYS. The domain used for the 3-D simulations of the Toyota Prius inverter is shown in Figure 2. Figure 2(a) shows the actual Prius inverter [1]; Figure 2(b) shows the representation of the inverter in ANSYS; Figure 2(c) shows the simulation domain, which consists of 1 IGBT-diode pair; and Figure 2(d) gives some representative temperature contours in the simulation domain. Details of the simulations are provided in [2].

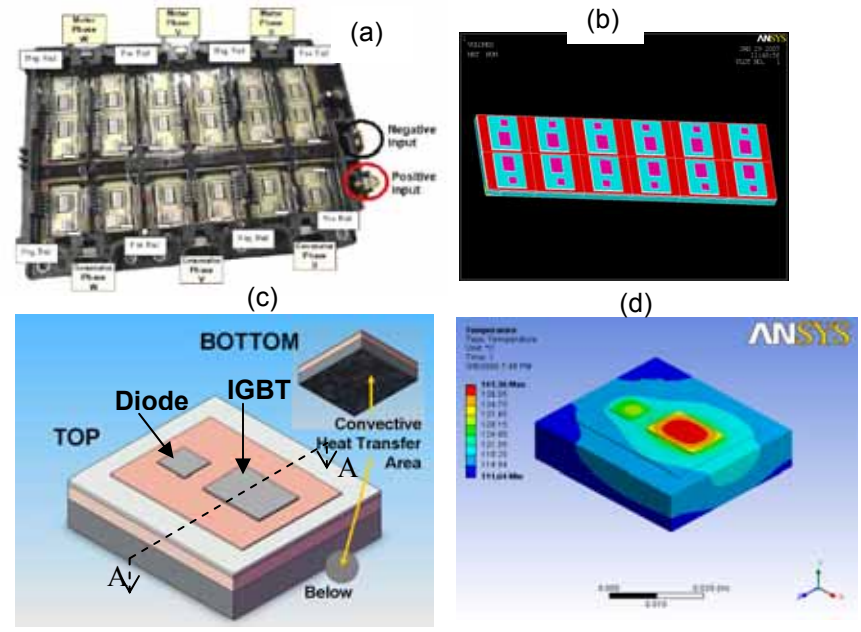

Fig. 2. (a) Prius Inverter [1], (b) Representation of the Prius Inverter in ANSYS, (c) Simulation Domain, (d) Sample Temperature Contours in the Simulation Domain

Figure 3 shows the impact of the TIM thermal resistance on the maximum die temperature. The baseline case shown corresponds to an average-performance grease, as measured at NREL. For the analysis, the grease thermal resistance was set at 100 mm^2K/W. The 5x TIM case corresponds to a TIM thermal resistance of 20 mm^2K/W (5 times lower than the baseline), the 10x TIM case corresponds to 10 mm^2K/W, while the 20x TIM corresponds to 5 mm^2K/W. Note that the thermal resistance values include the material bulk thermal resistance as well as the contact resistance. The numerical results for temperature are accurate (mesh-independent) to within 1%. Figure 3 shows that, for the baseline case, there is a significant temperature jump across the TIM (approximately 23°C). For the 5x TIM case, the temperature rise across the TIM is 7°C, for the 10x TIM case, the temperature rise is 4°C, while for the 20x TIM, the temperature rise is only 2°C. A smaller temperature rise across the TIM translates to a lower die temperature. This aids in achieving the FreedomCAR program goals of using 105°C glycol-water or air cooling. Interestingly, reducing the thermal resistance beyond 10x does not significantly change the maximum die temperature. This implies that, once the thermal resistance of the interface material is no longer the dominating resistance (< 4 mm^2K/W), it does not matter if its resistance is reduced further. It must be mentioned that these conclusions are dependent upon the package configuration. However, our analysis results for a different package also lead to the conclusion that the TIM stops being a thermal bottleneck below a resistance of 4 mm^2K/W. It is also worth noting that the baseline case corresponds to a TIM thermal resistance of 100 mm^2K/W. It is possible that this resistance could be even higher in an actual inverter, depending on the type and thickness of grease used.

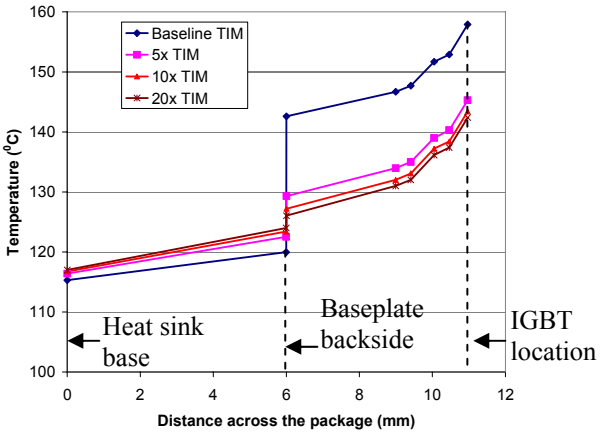

Fig. 3. Impact of TIM Thermal Conductivity on the Maximum Temperature in the Die

The total thermal resistance of an interface material is composed of the bulk resistance and the contact resistances. Accordingly, the thermal resistance of an interface material can be written as follows:

$$R = R_c + BLT/k_{TIM} , \quad (1)$$

where R_c is the contact resistance, BLT is the bond-line thickness of the interface material, and k_{TIM} is the bulk thermal conductivity of that material. A high thermal conductivity can reduce the bulk thermal resistance of the interface material, but the contact resistance must also be minimized. Contact resistance is an area that has received significant attention in the literature (e.g., [3-5]).

The focus here is on automotive power electronics cooling, but thermal interface materials also play a key role other microelectronics and high-power applications, as well [5]. The continual increase in cooling

demand for microprocessors has led to an increased focus on improving thermal interface materials. Significant advances have been made in the development of thermal greases/gels, phase-change materials (PCMs), solders, and carbon nanotubes (CNTs) as interface materials. Greases, gels, and PCMs are the most widely used, and their thermal performance has reached 10 mm^2K/W [5]. However, it should be noted that the BLT determines the performance to a significant extent. The high performance of greases/gels and PCMs is for thin BLT (less than 25 microns – which may not be practical for typical automotive power electronics applications). Recently, significant progress has been made in characterizing the performance of CNTs as TIMs [6, 7]. Carbon nanotubes yield a thermal resistance as low as 4 mm^2K/W [7] under certain conditions.

Despite the promising performance of some TIMs, a number of barriers have to be overcome before an advanced, high-performance TIM can be used in automotive power electronics. For example, some industry power electronics suppliers use lower-performance grease for ease of use, stability, or improved package in-situ performance. In the automotive industry, greases are still used predominantly as interface materials. Some problems with greases include pump-out during repeated thermal cycling, dry-out over time [5] (aging effects), and nonuniform application. One reason for their widespread use is that greases fill up the microscopic voids and cavities between mating surfaces very well. This results in a fairly low contact resistance (the first term on the right-hand side in Eq. (1)) at even moderate pressures (lower than 200 kPa). We elaborate on this aspect in a subsequent section. In addition to thermal performance, a TIM should have a long life, be reliable, account for manufacturing variations (e.g., camber in the package of the order of 100 microns), be easy to apply, and be inexpensive. In addition, it is often found that the in-situ performance of TIMs is different from the performance during material characterization through one of the several techniques prevailing in the literature. This also brings up the critical issue of the lack of a universally accepted standard for thermal resistance measurements. The ASTM D5470 approach [8] is the closest to being an accepted standard for thermal resistance measurements. However, it has its shortcomings and is not universally accepted.

The several aspects mentioned in the previous paragraphs form the motivation for our research. Typically, in the literature, results for different materials are reported with different techniques. Our intent is to report results for different materials with one single methodology (based on ASTM D5470) and create a consistent, objective database of the thermal performance of materials over different conditions. Our goal is also to understand all the parameters and mechanisms that affect the thermal performance of any TIM. Understanding in situ behavior and the reliability (e.g., impact of thermal cycling, "aging" effects) of TIMs are also important goals. Mechanistic understanding of the thermal degradation of TIMs is currently an open area of research [5]. The ultimate goal of our research is to fabricate/identify a low-thermal-resistance material that would be suitable for automotive power electronics applications. In the current report, we describe in detail the thermal performance of different thermal interface materials

Test Apparatus for Thermal Resistance Measurements

NREL acquired, tested, redesigned and improved a test stand, based on the ASTM D5470 test method [2, 8], for measuring thermal resistance. The intent of establishing the test stand was to characterize the thermal performance of novel as well as state-of-the-art thermal interface materials that are suitable for automotive applications and to develop an objective, consistent database. Figure 4 shows the test apparatus in the Electrical Systems Laboratory at NREL as well as details of the components of the test stand. The apparatus and the measurement procedures are described in detail in [2].

Experimental Uncertainty. The uncertainty in the thermal resistance measured from the steady-state test method was estimated by the method of Kline and McClintock [9]. The accuracy of this methodology is dependent upon the temperature and heat flow in the metering blocks being one-dimensional, as well as on the accuracy of the temperature measurement in the metering blocks. For most of the measurements, the discrepancy between the heat flux in the hot and cold metering blocks was less than 4%. The accuracy

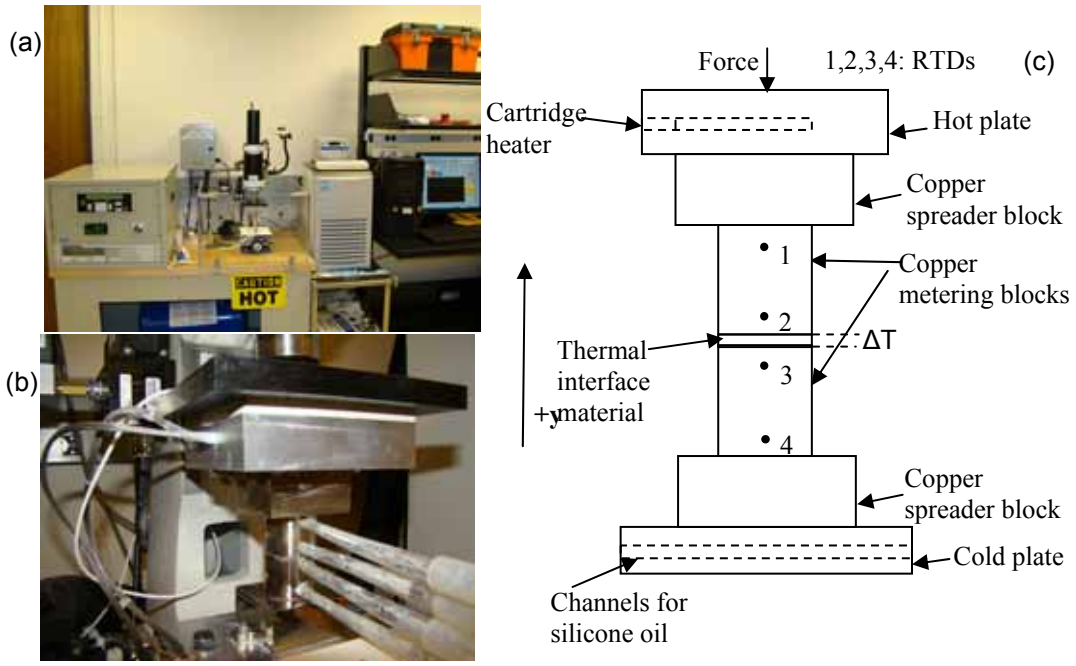

Fig. 4. Test Apparatus for Thermal Resistance Measurements; (a) Facility Setup at NREL, (b) the Apparatus, (c) Stack-up of the Different Layers

of the RTD probes, during the initial calibration, with respect to a NIST-traceable probe was within 0.04 K. Some drift in the accuracy is possible, but is difficult to estimate. The overall uncertainty in the resistance measurements is estimated to be ±10% (at 95% confidence levels). The repeatability of the experimental results was within ±4%. The uncertainty in the thickness of the polymeric interface materials imposed via glass spheres is about ±6%, which is the uncertainty in the diameter of the glass spheres.

Comparison with other techniques/test apparatus

Extensive numerical modeling was performed to understand and gain confidence in the experimental data obtained from the apparatus. The numerical predictions for temperature in the apparatus agree well with the experimental predictions. These comparisons are described in detail in [2]. In addition, comparisons have been made between the steady-state approach described here and the transient laser flash results in active collaboration with Delphi Corporation. Figure 5 presents the results for two PCMs – the Honeywell PCM45-G and Loctite Powerstrate Xtreme PS-X, and a thermoplastic Cookson Staystik 1172. The comparisons have been described in detail in [2]; the main conclusion is that the two techniques compare very favorably for PCMs, while for thermoplastics, the match is still reasonable given the uncertainties involved. These include differences in measurement methodology, substrates adjacent to the TIMs, as well as TIM preparation. In addition, experiments were also performed on a Yttria-stabilized Zirconia sample (9.1%) [10] obtained from NIST, Boulder. From the experiment at NREL, the thermal conductivity of the 3.0 mm thick sample at about 95°C average sample temperature is 2.4 W/mK. For the same sample, the thermal conductivity result obtained by Slifka et al. [10] with a guarded-hot plate approach is 2.2 W/mK for a sample temperature of 125°C. Hence, the result from the NREL experimental setup and the result of Slifka et al. [10] are well within the experimental uncertainty bars. These favorable comparisons provide confidence in the experimental predictions from the NREL test apparatus. Hence in the subsequent sections, we look at the experimental results for a wide variety of TIMs.

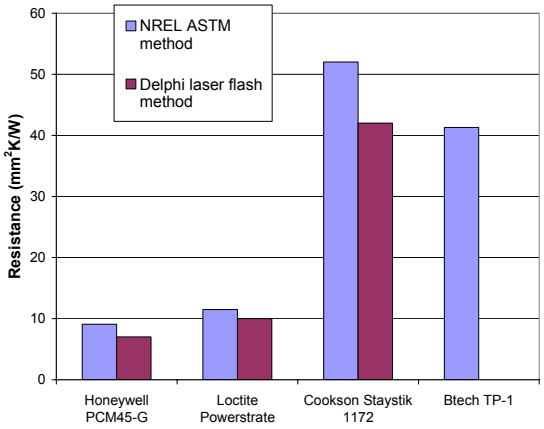

Fig. 5. Comparison Between NREL steady-state approach and the Delphi Laser Flash Method

Test results for polymeric TIMs

In this section, we discuss experimental results for various commercially available polymeric TIMs such as greases, gels and PCMs. Greases are predominantly used in the automotive industry despite well-known problems related to pump-out and dry-out. The intent here is to understand the mechanisms underlying the thermal performance of polymeric TIMs and also to create a consistent, objective database of the performance of these commercially available TIMs.

Since grease is still the most predominantly used interface material in the automotive power electronics industry, we performed experiments with some brands of commercially available thermal greases. Some of these greases (Aavid Thermalloy Thermalcote 251G, Wacker Silicone P12) are currently in use in automotive inverters. In addition, some experiments were also performed with gels and PCMs. These experiments were performed over a sample temperature range of 55° to 80°C, a thickness range of 25 to 150 microns, and an applied pressure of 170 kPa.

Figure 6 shows the thermal resistance as a function of TIM thickness at an average sample temperature of ~75°C. To maintain the thickness of the polymeric TIM layer, we used glass spheres acquired from Mo Sci Corporation. The volume of the glass spheres is a negligible fraction of the total volume of the grease in between the metering blocks. Figure 6 shows that, as the TIM thickness increases, the thermal resistance also increases linearly, as expected. For any given TIM thickness, the thermal resistance may also change as a function of temperature. The temperature dependent behavior will be discussed in a subsequent section. For any given TIM listed in Figure 6, the inverse of the slope of any linear curve gives the thermal conductivity of the material, and the y-intercept gives an estimate of the contact resistance. From a thermal perspective, the Shinetsu-X23-7783D-S, Dow Corning TC-5022, and 3M AHS1055M greases are high-performance materials. For a 25-micron thick layer of the 3M grease, the thermal resistance is 13.4 mm^2K/W. Even for a 150-micron thick layer, the thermal resistance is only about 41 mm^2K/W. In our study, we are exploring a TIM thickness range of 25 to 150 microns, because in actual packages, manufacturing constraints may cause unavoidable gaps of 100 to 150 microns.

Figure 7 shows contact resistances for the various TIMs for a BLT of 75 microns. Individual differences in the TIMs may be a result of how well they wet the surfaces and fill up the microscopic surface irregularities [5]. The Shinetsu-X23-7783D-S and 3M AHS1055M greases, and the Honeywell PCM45 phase change material have the lowest contact resistances (6~7 mm^2K/W). In fact, for all the TIMs in Figures 6 and 7, the contact resistances are in the range of 6 to 20 mm^2K/W. It is important to note that

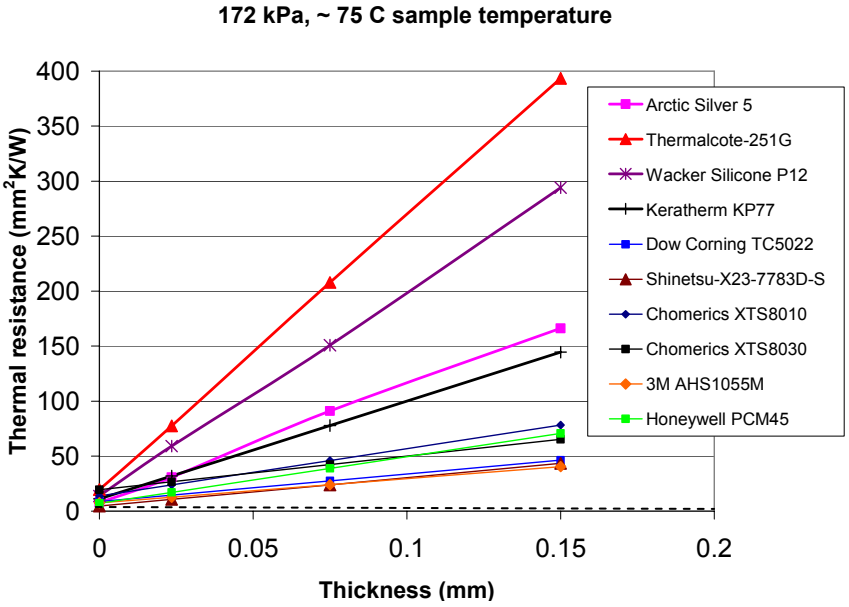

Fig.6. Thermal Resistance versus Thickness for Different Polymeric TIMs (Dashed Line: Target Value of 4 mm²K/W)

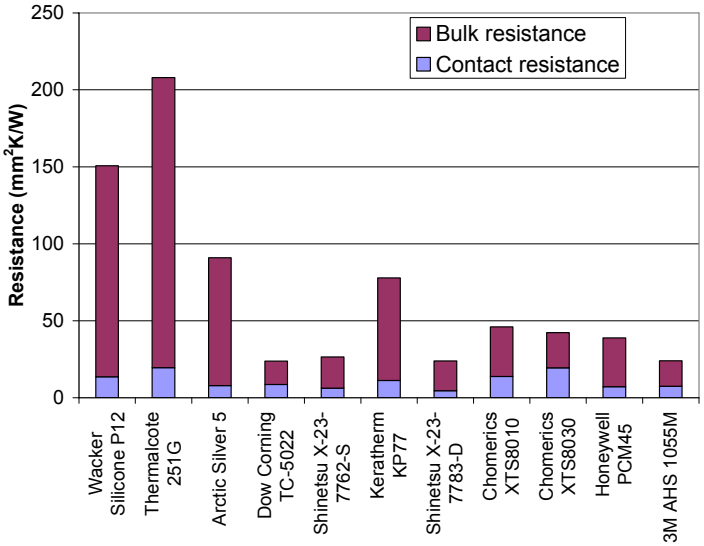

Fig.7. Contribution of Bulk and Contact Resistances for Various Polymeric TIMs with 75 microns BLT and Average Sample Temperature of ~75°C

for some of the TIMs at 75 microns BLT, the contact resistance is only a small fraction of the overall resistance (e.g. Thermalcote 251G – 8 to 10%), while for others the contact resistance is significant portion of the overall resistance [e.g. Shinetsu X23-7783D – 28 to 30 %)]. Though not presented here, the contact resistance of TIMs can be estimated theoretically [3-5]. It would be interesting to compare modeling results for contact resistance with the experimental results obtained here. Arguably, the contact resistance of greases is quite low, which may be one reason for their widespread use despite significant

drawbacks. Figure 6 shows that, as the BLT of the grease increases, the bulk resistance of the grease dominates over the contact resistance. The Chomerics XTS8010 gel has a high contact resistance (~ 19 mm^2K/W); however, because of semi-or-fully cross-linked structure, these materials are expected to be more reliable than conventional polymeric TIMs. We plan to explore aspects related to reliability in the near future.

Overall, the results in Figure 6 suggest that high-performance greases can yield resistances as low as 13 and 30 mm^2K/W, for a BLT of 25 and 100 microns, respectively. Our analysis indicates that the interface material completely stops being a bottleneck below a resistance of 4 mm^2K/W for a conventional IGBT package configuration. This is the reason why this number is indicated as a target in Figure 6. The results here suggest that, while the commercially available TIMs tested in this study can be used to obtain very good performance, none approaches 4 mm^2K/W for practical BLTs of the order of 75 microns. In addition, reliability is a concern with a majority of the polymeric TIMs. Aspects related to reliability include performance after thermal cycling (pump-out), aging effects (dry-out effects on viscosity, thermal performance), and uniform application.

The key to the good performance of the Shinetsu, Dow Corning and 3M greases seems to be a high content of very conductive particles and small amounts of proprietary solvent that enhances performance. However, due to the high loading of conducting particles, these greases are viscous. In addition, the Chomerics XTS8010 and 8030 gels are also very viscous. As a consequence, these materials are not as easy to work with as the Thermalcote 251G and Wacker Silicone P12 greases. The long-term behavior of a number of TIMs presented in Figure 6 is not well known. We plan to characterize aspects related to the reliability of the TIMs in the near future.

Impact of temperature on thermal resistance of polymeric TIMs

In the near future, trench IGBTs will soon be the norm. These trench IGBTs have a maximum temperature rating in the range of 150° to 175°C . Hence, it is important to characterize the performance of these materials at elevated temperatures of the order of 130°C. Hence, we performed experiments to characterize the performance of a few polymeric TIMs, such as Dow Corning and Shinetsu greases, and the Honeywell PCM45G over a temperature range from 20°C to 130°C. Figure 8 shows the results for the thermal resistance plotted as a function of the average sample temperature. For the cases where there is no thickness control, the pressure was maintained at 170 kPa. For all the materials, the thermal resistance increases as the temperature of the sample increases. In addition, after the high-temperature experiment, when the temperature is decreased and the low-temperature experiment is repeated, then the original low-temperature thermal resistance is almost recovered. The temperature effect is particularly pronounced for the 150 microns thick Shinetsu grease. For both the low-temperature and the high-temperature experiments, the temperatures in the hot and cold metering blocks (Figure 4(c)) are within 10°C of each other. This implies that varying thermal conductivity of the copper block is not likely to be an issue. This leads to the hypothesis that at higher temperature, the TIMs are not “wetting” the metering blocks as well as they do at lower temperature. Interestingly, it maybe possible that the different coefficient of thermal expansion of the TIMs and the metering blocks maybe a factor in determining the degree of wetting, and consequently, the thermal resistance of the TIMs. Figure 8 suggests that the impact of temperature on the thermal resistance can be as much as 40%. These results suggest closer examination of the impact of temperature on the in-situ thermal resistance in a package maybe worthwhile. In addition, a quantitative assessment of the impact of temperature on contact resistance is also warranted.

Test results for other materials

In addition to polymeric TIMs, we have also explored other materials such as thermoplastics, indium (metallic TIM), graphite, filler pads and carbon nanotubes. The results for a number of these materials are shown in Figure 5 and Figure 9. The average sample temperature in all these experiments is around 60°C.

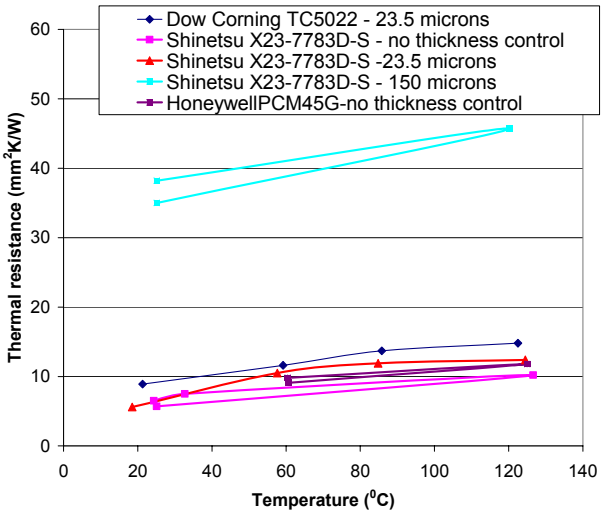

Fig. 8. Temperature-dependence of the Thermal Resistance of Polymeric TIMs

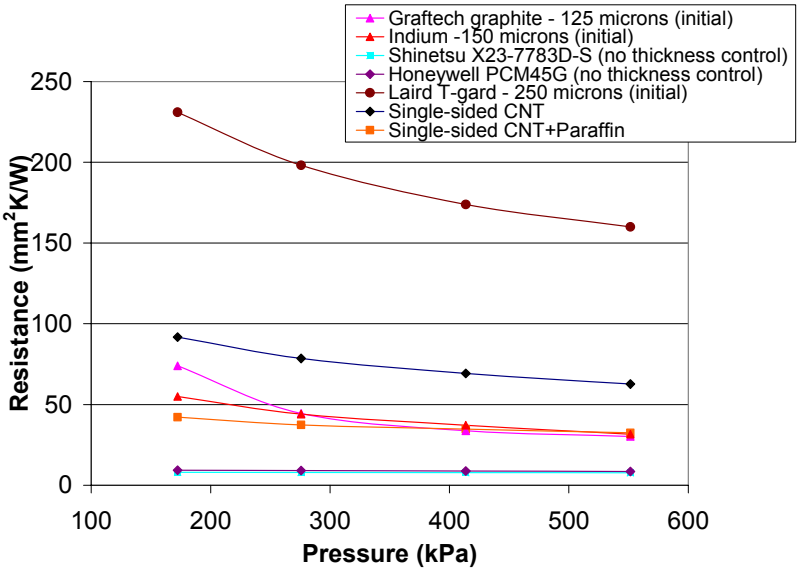

Fig. 9. Resistance versus Pressure Characteristics for Different TIMs

From the viewpoint of automotive power electronics, indium is not desirable as a TIM because it is electrically conducting and presents a danger of electrical short-circuiting. Its melting point is only 156°C, and in the event of temperature spike, it is likely to melt and pose the risk of short-circuiting in the package. For completeness, we present results for a 150 micron thick indium foil in Figure 9 as a function of pressure. The performance is rather modest, with a thermal resistance of 55 mm^2K/W at 172 kPa, and a resistance of 31.6 mm^2K/W at 552 kPa. It is interesting to observe the nearly flat resistance versus pressure curves for the Shinetsu X23-7783D-S and Honeywell PCM45G (Figure 9) polymeric TIMs. This clearly indicates the good wetting characteristics of these materials even at modest pressure. It is worth noting that there is no thickness control for both the Honeywell as well Shinetsu TIMs in Figure 9, there is no thickness control.

Filler pads are another class of TIMs which are used in electronics packages. The Laird T-gard filler pad does seem to be a very high resistance material (Figure 9) and not very suitable for use in electronics packages. The Fujipoly Sarcon X-30 pad at 172 kPa on the other hand has a thermal resistance of only 35 mm^2K/W.

The thermal resistance of graphite sheet from Graftech was also tested. The thermal resistance was approximately 30 mm^2K/W at 552 kPa (Figure 9). Also, at lower pressures, the thermal resistance results are not very stable indicating the surface contact characteristics of the graphite sheet is not very repeatable at low pressures.

The last class of materials presented in Figure 9 is carbon nanotubes grown/deposited on a copper substrate via plasma-enhanced chemical vapor deposition (PECVD). A copper substrate with CNTs grown on one side was obtained commercially. In the experiment, the CNTs touch one of the metering blocks. For the other interface, a PCM is used as the interface between copper substrate and the metering block. From the overall thermal resistance measurement, the resistance corresponding to the PCM and copper itself is subtracted out. This is analogous to the approach followed by Xu and Fisher [6]. An SEM image of the CNT growth on the copper substrate is shown in Figure 10. The CNT density is $10^9/cm^2$. The catalyst used is a 300 nm Chromium coating, and the multiwalled CNTs are 150-200 nm in diameter and 40 microns high. As shown in Figure 9, despite the CNT growth via PECVD, the thermal resistance is fairly high (~92 mm^2K/W) at 172 kPa, and is not close to the high-performance results reported in [7]. The key could well be the tri-catalyst configuration utilized in [7] for the CNT growth. We have also tested other samples of CNTs grown/sprayed on copper substrates, obtained from various sources, and the performance is similar to the single-sided CNT sample shown in Figure 9. These results suggest that good thermal performance from CNTs is obtained under very specific growth conditions and catalyst configurations. When paraffin wax is added to the CNT surface, the thermal resistance drops by almost 65 to 85% over the pressure range from 172 to 552 kPa – as shown in Figure 9. This suggests that with paraffin wax, the CNT-CNT contact as well as the CNT-metering block contact improves considerably - resulting in improved thermal performance. Overall, in regards to CNTs as TIMs, our measured performance has not matched up to best-reported results in the literature [7, 11]. In addition, while the theoretical potential for CNTs as TIMs is very high, many practical aspects have to be addressed before CNTs can be considered as TIMs in power electronics packages.

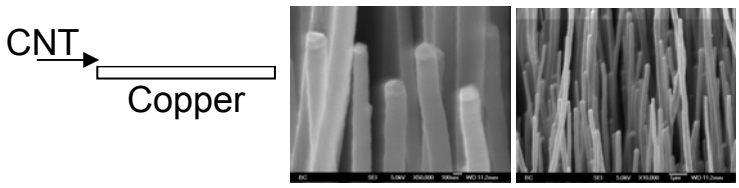

Fig. 10. SEM Images of CNT Growth on a Copper Substrate (Single-Sided CNT Sample)

Conclusions and Future Steps

Thermal interface materials pose a significant bottleneck to heat removal from the IGBT package. From a DOE Vehicle Technologies Program and automotive industry perspective, a reliable, cost-effective, and high-thermal-performance TIM can help to meet some program goals. These goals could include cooling with 105°C glycol-water, or even air cooling, and extracting maximum heat flux from the device, whether it be conventional silicon-based, trench IGBT or silicon-carbide-based, and keeping the maximum temperature within acceptable limits.

The experimental results from the steady-state-method-based apparatus at NREL were compared with alternate testing approaches such as the transient laser flash as well as the steady-state guarded hot-plate method. Reasonable match was found between the results obtained via the NREL apparatus and the other approaches. Experiments were performed with several polymeric TIMs, and their performance was characterized over a range of temperatures, pressures and BLTs. The Shinetsu, 3M and Dow Corning greases are superior in thermal performance over other polymeric TIMs that were tested. These results suggest that care has to be taken in choosing the type of TIM that is selected and the thickness of the TIM that is applied, since its impact on die temperatures is significant. Results also suggested that the contact resistance of polymeric TIMs is fairly low. The performance of other materials such as indium, graphite sheet, filler pads, and carbon nanotube samples obtained from various sources are inferior to the polymeric TIMs mentioned above. The results also indicated that none of the tested TIMs were able to go below a resistance of about 30 mm^2K/W at BLTs of 100 microns or greater. Practical inverter configurations are likely to require a TIM thickness of about 100 microns. Hence, a conservative goal would be to identify/fabricate a TIM that would have a thermal resistance of about 4 mm^2K/W at bond line thicknesses approaching 100 microns. It appears that from an automotive power electronics package viewpoint, there is no commercially available material that meets this target thermal performance.

For materials with promising thermal performance outlined in this study, we plan to characterize all aspects related to reliability in the automotive environment. These include the impacts of thermal cycling and elevated temperatures (~150°C) (aging) on the performance of the TIMs. We also plan to characterize the automotive power electronics package in-situ performance of the most promising TIMs.

Acknowledgments

The author would like to acknowledge the support provided by Susan Rogers, Technology Development Manager for Power Electronics and Electrical Machines, Vehicle Technologies Program, DOE Office of Energy Efficiency and Renewable Energy. The author also acknowledges helpful interactions with Gary Eesley at Delphi Corporation and the power electronics team at NREL.

References

1. R.H. Staunton, L.D. Marlino, J.N. Chiasson, and T.A. Burress, "Evaluation of 2004 Toyota Prius Hybrid Electric Drive System," Oak Ridge National Laboratory Technical Report, ORNL/TM-2006/423, 2006.
2. Narumanchi, S., Mihalic, M., Kelly, K., and Eesley, G., "Thermal Interface Materials for Power Electronics Applications", Proceedings of the ITherm Conference, Orlando, FL, pp. 395-404, May 28-31, 2008.
3. C.V. Madhusudana, *Thermal Contact Conductance*, New York: Springer-Verlag, 1996.
4. M.M. Yovanovich and E.E. Marotta, “Thermal Spreading and Contact Resistances," in *Heat Transfer Handbook,* A. Bejan and A.D. Kraus, Editors, Hoboken, NJ: John Wiley & Sons, pp. 261−395, 2003.
5. R. Prasher, “Thermal Interface Materials: Historical Perspective, Status and Future Directions,” in *Proceedings of the IEEE*, Vol. 94, No. 8, pp. 1571–1586, 2006.
6. Xu, J., and Fisher, T.S., "Enhancement of Thermal Interface Materials with Carbon Nanotube Arrays", *International Journal of Heat and Mass Transfer*, Vol. 49, pp. 1658-1666, 2006.
7. B.A. Cola, J. Xu, C. Cheng, X. Xu, T.S. Fisher, and H. Hu, "Photoacoustic Characterization of Carbon Nanotube Array Thermal Interfaces," *Journal of Applied Physics*, Vol. 101, No. 054313, 2007.
8. American Society for Testing and Materials, ASTM Standard D5470-01, 2005.
9. S.J. Kline and F.A. McClintock, “Describing Uncertainties in Single-sample Experiments,” *Mech. Eng.* (Am. Soc. Mech. Eng.), 75, pp. 3-8, 1953.
10. Slifka, A.J., Filla, B.J., and Stalick, J.K., "Thermal Conductivity of Two Compositions of Yttria-Stabilized Zirconia", *Thermal Conductivity*, Vol. 25, pp. 147-154, 1999.

11. T. Tong, Y. Zhao, L. Delzeit, A. Kashani, M. Meyyappan, and A. Majumdar, "Dense Vertically aligned multiwalled carbon nanotube arrays as thermal interface materials", *IEEE Transactions on Components and Packaging Technologies*, Vol. 30, No. 1, pp. 92-100, 2007.

3. Electric Machinery Research and Technology Development

3.1 Uncluttered Rotor PM Machine for a CVT Design

Principal Investigator: Donald J. Adams
Principal Technical Investigator: John S. Hsu
Oak Ridge National Laboratory
National Transportation Research Center
2360 Cherahala Boulevard
Knoxville, TN 37932
Voice: 865-946-1321; Fax: 865-946-1262; E-mail:adamsdj@ornl.gov

DOE Technology Development Manager: Susan A. Rogers
Voice: 202-586-8997; Fax: 202-586-1600; E-mail: Susan.Rogers@ee.doe.gov

ORNL Program Manager: Mitch Olszewski
Voice: 865-946-1350; Fax: 865-946-1262; E-mail: olszewskim@ornl.gov

---

Objectives

- Develop a new machine that combines the motor and generator/motor into one unit with the potential to be used as a continuously variable transmission (CVT), as well as other applications that require two electric machines. The expected advantages of this new machine are
  - Additional torque coupling between the two rotors for producing more wheel torque
  - The potential for a simpler, less costly CVT from combining a motor and generator into one machine with only a single permanent magnet (PM) rotor
  - Brushless design
  - Based on the uncluttered rotor principle, the concept can be extended for kinetic energy storage to reduce battery stress

Approach

Because the use of a secondary rotor working in conjunction with a PM rotor is a totally new technology, there is no previous experience that can be used for reference. The development process is an iterative process in determining the positive and negative aspects of various structural arrangements through both mechanical finite element analysis (FEA) and electromagnetic simulations. Numerous challenges associated with this technology and the process required to model, simulate, and derive results are to be addressed for complex 3-dimensional (3D) models.

The FY 2008 goal was to continue the modeling and simulation of the CVT, derive motor characteristics and parameters from the simulations, and perform a first order cost evaluation.

Major Accomplishments

In FY 2006 a proof-of-concept secondary rotor that had no rotating windings, and a wound core stator for exciting the secondary rotor, were fabricated. The brushless secondary rotor concept was validated through tests conducted on a prototype motor. The physics of the CVT machine were explained in the FY 2006 report.

In FY 2007, simulations were initially conducted for axial-gap and radial-gap approaches. The radial-gap machine was selected for detailed simulations. The simulation results further confirmed that the principle

of this new type of machine is workable; the torque of the PM rotor can be transferred directly to that of the secondary rotor, the stationary excitation core of the secondary rotor sees no rotational torque, and the axial force can be practically eliminated by an axially symmetrical arrangement.

In FY 2008 it became evident that modeling and verifiable simulation of such a complex electromagnetic machine is extremely difficult. The simulations require considerable computer power and time, resulting in slower progress on the work. This truly is a novel machine and to our knowledge no such simulation had been done before. Nevertheless, a design was demonstarted in simulations that resulted in a 30% effective power increase with only a 15% weight increase compared with the baseline machine (a Toyota Prius).

Future Direction

Because of budgetary constraints in FY 2008, a decision was made not to continue this particular project into FY 2009 as planned and not to build a prototype. Much was learned during this project about the behavior of complex electric machines and how to simulate and design such a machine with a significant 3D flux component. This knowledge and the tools developed during this project will be utilized in future projects, some of which have already been selected for funding in FY 2009.

This study proves that the uncluttered rotor concept can be used for the radial-gap electric machine structure. The axial-gap structure is somewhat easier to fit geometrically because it has more room available for the uncluttered rotor and its excitation. Moreover, this machine has a much wider impact than what is shown from the radial-gap model simulations, because the uncluttered rotor opens a door for new types of electric machines that require a brushless rotating armature. Such a machine can be used in numerous applications in addition to hybrid-electric-type automotive applications.

Technical Discussion

The old traditional brush-type electric machines, such as the commutator dc motor and the slip-ring synchronous machine, rely on brushes and/or slip rings to transfer the electric energy to rotating components without speed interference. For example, the brushes and slip rings of a wound field synchronous machine can deliver a dc current to the excitation field coil. Regardless of the rotor speed, the dc current going through the brushes would not be cluttered by the rotation frequency. This is quite different from using a wound stator that has the same number of poles as the wound rotor for energy transfer to the rotor. The frequency of the induced electromotive force in the wound rotor is linearly proportional to the speed of the rotor. The rotation frequency is cluttered into the rotor-induced voltage. The uncluttered rotor developed at Oak Ridge National Laboratory (ORNL) specifically solves this cluttering problem.

The uncluttered rotor concept opens a door for advanced brushless machine developments. The CVT in this study relies on the uncluttered rotor to transfer electric energy through the magnetic flux coupling that does not require a set of contacting slip rings and brushes. The uncluttered rotor can be viewed as a rotating stator (or armature) without brushes.

Besides the use of the uncluttered rotor for brushless energy transfer, the CVT of this investigation utilizes the counter torque of a rotating armature for torque amplification. This concept is explained through Fig. 1.

The upper sketch in Fig. 1 shows a traditional motor with a rotating rotor. A mechanical load is coupled to the shaft; the stator sees the same torque but in an opposite direction to the shaft torque. The stator frame must be bolted down to the floor; otherwise the stator would roll on the floor.

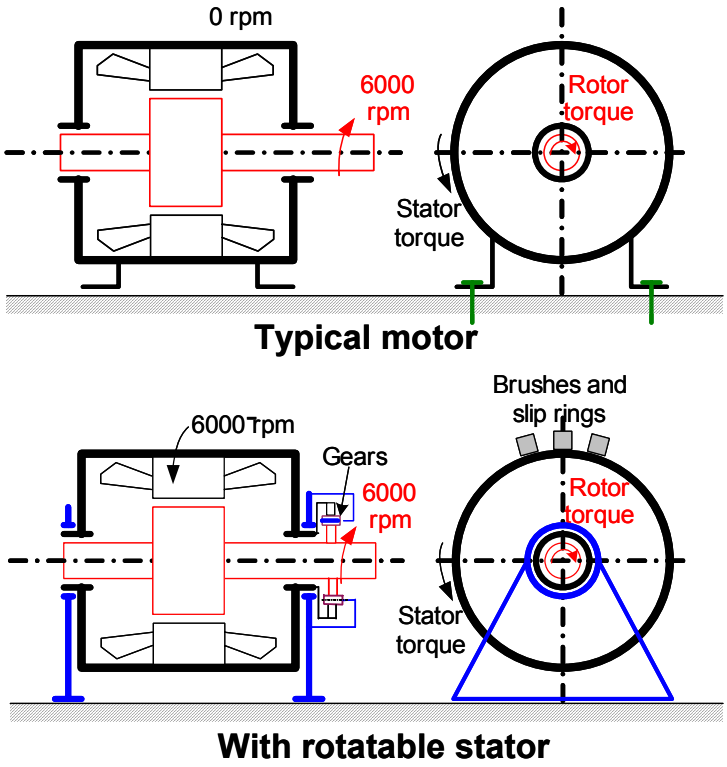

Fig. 1. Typical motor and a motor with rotatable stator.

The lower sketch in Fig. 1 shows that if the stator is allowed to rotate freely through the addition of more bearings and slip rings are used for energizing the stator windings, the stator will rotate in a direction opposite to the rotor. If a gear set is coupled between the stator and the rotor shaft, the direction of the stator torque will change and will be the same as the shaft rotating direction, resulting in the amplification of the shaft torque output. The amplification ratio depends on the gear ratio.

With this understanding of the uncluttered rotor for brushless energy feeding and the use of the rotating stator (or rotating armature, to be exact) for torque amplification, the ORNL CVT technique is discussed.

Figure 2 shows a sketch of the axial-gap CVT machine. As planetary gears are used in many leading hybrid vehicles, the sample CVT machine is connected to a planetary gear. The radial-gap CVT sketch used in the calculations for this report is not shown because it has export control restrictions.

Although some existing hybrid vehicles might use more than one set of planetary gears, Fig. 3 illustrates the operation principle with an example of one planetary gear set. If the uncluttered rotor is coupled to the sun gear that rotates in a given direction, then assuming the planetary gear is not rotating (i.e., the engine is not running), the ring gear will be driven to rotate in an opposite direction. The output torque of the ring gear can be increased according to the gear ratio when the sun gear runs faster than the ring gear. In our sample simulation, the ring gear is coupled to the PM rotor.

Inside the bore of the wound stator are the PM rotor, uncluttered rotor, and exciter coils. The interior PM (IPM) rotor interacts with the stator currents from its outer periphery and interacts with the uncluttered rotor from its inner periphery. The exciter core is stationary. Therefore, it does not see the centrifugal

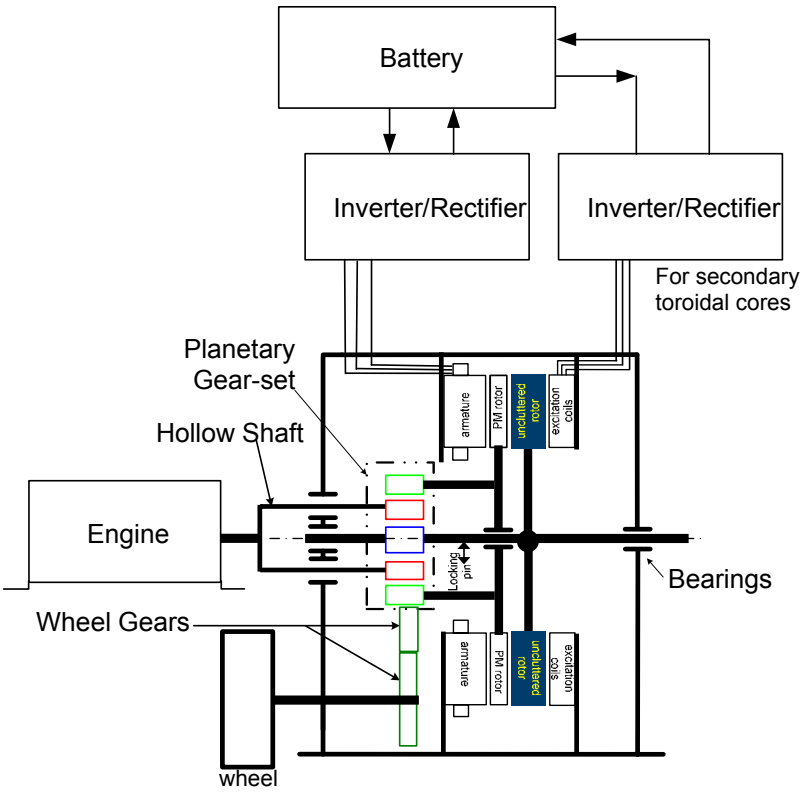

Fig. 2. Sketch of an axial-gap sample CVT machine in a vehicle.

force; higher-saturation-level, high-frequency compressed powder material should be investigated further for this application.

There are many possible designs for CVTs using the uncluttered rotor concept. The two major groups are the radial-gap and the axial-gap configurations. Because of the long computation time required for a 3D model, the computations in this study are focused on a radial-gap model to see what can be gained and to obtain scaling equations for other models with different dimensions.

Beginning with a baseline design for comparison purposes, a Prius IPM motor stator of 3.4-in. stator core length was used as a starting point for the study. It determines the dimensional boundary for this sample study. The rotor outer diameter of the Prius motor remained unchanged, but the rotor lamination slot configuration was changed for the CVT assembly. The center portion of the IPM rotor was modified to have an additional torque-producing air gap for the uncluttered rotor and to accommodate its stationary exciter core.

Unlike a 2D finite element simulation traditionally used in motor design, which takes only minutes to solve, a 3D model such as the sample CVT can take hours (or days) to solve one simulation. The simulations to adequately assess the operation of this concept were extremely computation- intensive and time-consuming.

The comparison of component weights between the Prius motor and the ORNL CVT machine is shown in Table 1. The ratio of total weights between the ORNL CVT machine and the baseline (Prius) motor is 94.8/82.5 = 1.149 = 1.15

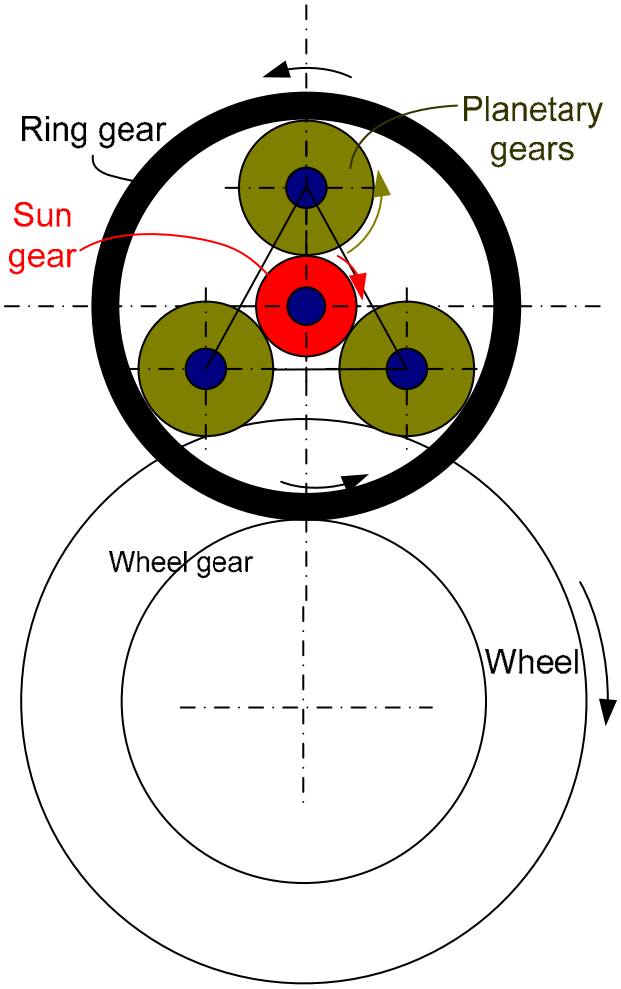

Fig. 3. Planetary gear in a hybrid vehicle.

Table 1. Comparison of component weights between baseline (Prius) and ORNL CVT machines

Components	Prius (lb)	ORNL CVT (lb)
Stator core	42.2	42.2
Stator copper	15.0	15.0
PM core	22.5	6.1
PM	2.8	2.6
Uncluttered rotor and excitation	0	28.9
Total	82.5	94.8

Uncluttered rotor torque estimation

The ratio of the uncluttered rotor torque from interacting with the PM rotor and the stator torque from interacting with the PM rotor can be derived from the law of physics; torque is the product of force and the torque arm length, and the force is derived from the product of current, turns, and conductor length.

$$\frac{(Uncluttered\ rotor\ torque)}{(Stator\ torque)} \approx \left(\frac{Number\ of\ equivalent\ exciter\ slots}{Number\ of\ stator\ slots}\right) \cdot \left(\frac{Excitor\ slot\ length}{Stator\ slot\ length}\right) \cdot \left(\frac{Exciter\ diameter}{Stator\ bore}\right) \tag{1}$$

Substituting the numbers into Eq. (1) gives the torque ratio of

$$\frac{(Uncluttered\ rotor\ torque)}{(Stator\ torque)} \approx \left(\frac{2}{48}\right) \cdot \left(\frac{11"}{3.4"}\right) \cdot \left(\frac{3.98}{6.375}\right) = 0.084 \tag{2}$$

When the stator produces 401 Nm of torque, with the same ampere-turns per equivalent exciter slot the uncluttered rotor produces

$$(Uncluttered\ rotortorque) \approx 0.084 \cdot 401Nm = 33.7Nm. \tag{3}$$

Equation (1) can be used as a coarse scaling tool for new configurations with different dimensions.

Figure 4 shows the plot of the 3D finite element uncluttered-rotor torque versus the phase angle of the phase-1 exciter coil; under the same number of exciter-slot ampere turns as that of the stator slot, the peak uncluttered rotor torque is –36.7 Nm. The 36.7 magnitude is not far away from the 33.7 Nm magnitude predicted by the coarse scaling Eq. (3).

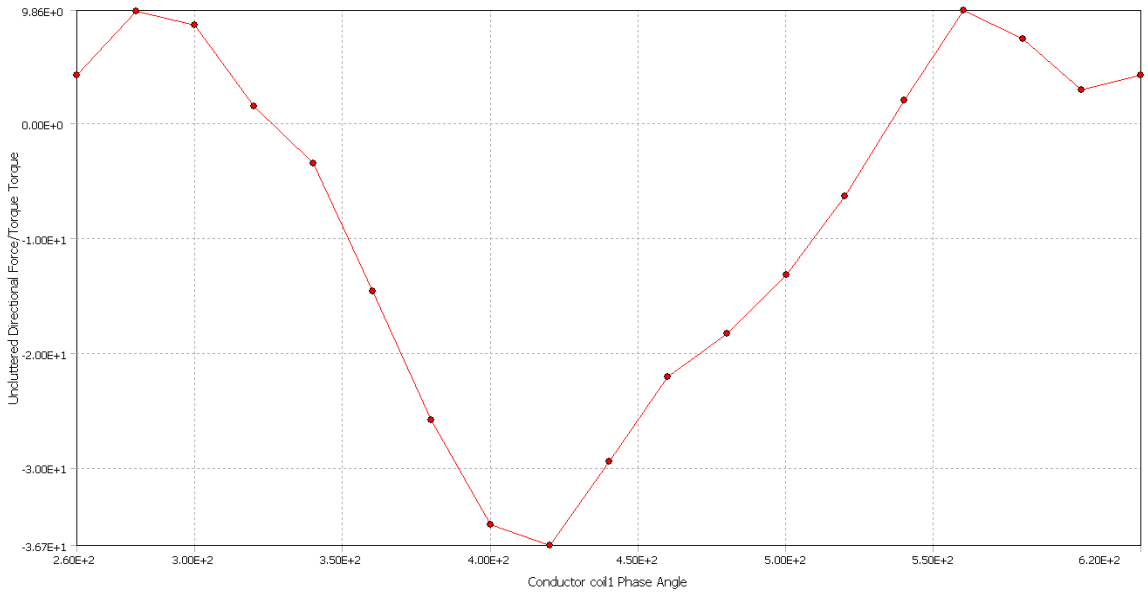

Fig. 4. Uncluttered rotor torque versus conductor coil-1 phase angle.

The peak torque produced by the interaction between the PM rotor and the wound stator core is 401 Nm, as shown in Fig. 5 for the torque versus conductor-a phase angle.

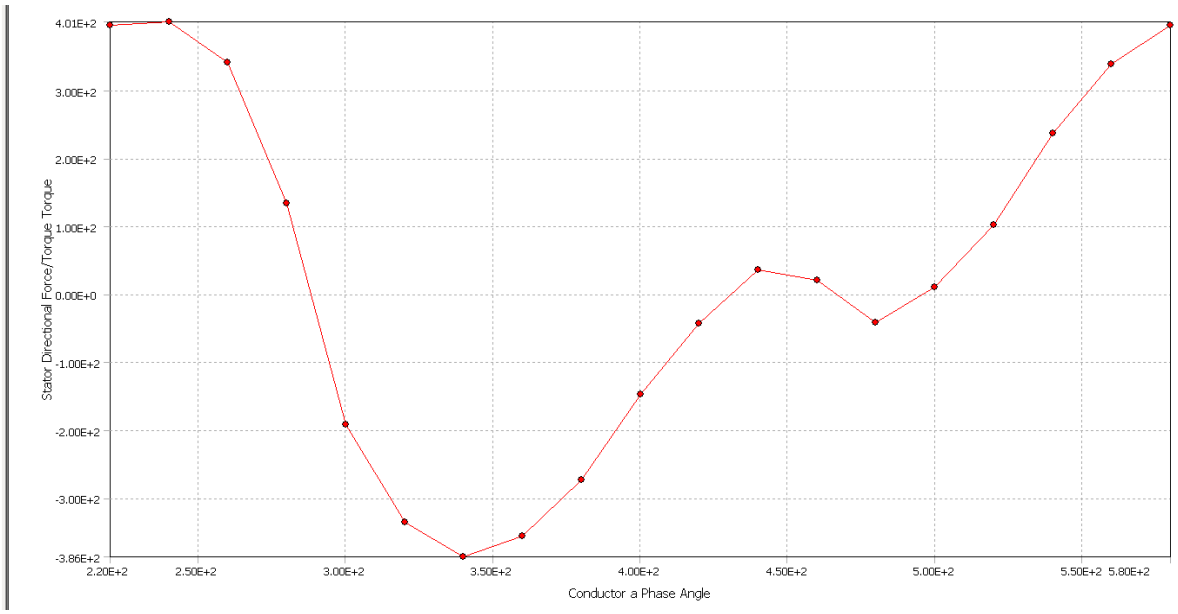

Fig. 5. Torque produced by stator wound core and PM rotor versus conductor-a phase angle.

Impacts of the uncluttered rotor torque on the CVT

The impact of the 36.7 Nm torque on the wheel torque from the CVT is quite remarkable. Assume the gear ratio between the ring gear and the sun gear equals the ratio of the permissible speed limits of the uncluttered rotor and the PM rotor. In our sample case, this ratio is (14,000 rpm/6,000 rpm) = 2.33. The additional torque to the wheel is the sum of the following torques:

1. The torque (36.7 Nm) produced by the interaction between the uncluttered rotor and the PM rotor.
2. The counter torque of the uncluttered rotor received from the PM rotor is a negative 36.7 Nm; this –36.7 Nm torque drives the sun gear and subsequently transfers to the ring gear and drives the wheel. Taking the gear ratio of 2.33 and the torque direction change into consideration, the effect to the wheel from this counter torque is 36.7 • 2.33=85.5Nm.
3. The total additional torque produced by both the torque of (1) and the effective counter torque of (2) is 36.7 + 85.5 = 122.2Nm.

The CVT power output as compared with that of the baseline (Prius) motor is (122.2 + 401) / 401 = 1.30. A 30% increase of torque (or power) is obtained.

Conclusions

- The 3D simulations confirm that the ORNL uncluttered-rotor CVT concept can be applied to a commercially available IPM machine.
- During simulations the center portion of the PM rotor of the IPM machine was modified to accommodate the uncluttered rotor and its excitation. The modified machine contour diameter and length were confined to the original IPM machine.
- At 287 A of root mean square phase current (or 406 A current amplitude), the stator gives 401 Nm maximum torque and the uncluttered rotor gives 36 Nm maximum torque.
- From the mechanical stress standpoint, the IPM rotor is allowed to run at 6,000 rpm while the uncluttered rotor with a smaller diameter is allowed to run up to 14,000 rpm.

- The uncluttered rotor can be used to drive the sun gear of the planetary gear set. Its 36 Nm torque is amplified to (14,000/6,000) • 36 = 84 Nm at the ring gear that drives the wheel.
- The machine power rating is thus increased to (401 + 36 + 84) / 401 = 1.30 times without increasing the overall contour size.
- As compared with the Prius motor, the ORNL CVT has a 30% torque (or rating) increase with a total weight increase of only 15%.
- This 30% power gain takes advantage of the high-speed capability of the small-diameter uncluttered rotor and the existing planetary gear for converting the counter torque of the uncluttered rotor to drive the wheel.
- The 30% power gain is produced by two exciter coils, compared with the 48 stator coils in the original IPM machine. Each of the two exciter coils has about the same ampere-turn rating as each of the 48 stator coils. The copper loss of the two exciter coils is about 2/48 = 4.2% of the 48 stator coils. From the copper loss standpoint, the machine has 4.2% additional copper loss to gain an additional 30% power output.
- The additional core loss has two contradicting factors. First, the loss per volume would be higher as a result of the higher speed of the uncluttered rotor. Second, the volumes of the exciter and uncluttered rotor are small. Special attention must be paid to the core loss reduction for the uncluttered rotor (e.g., using thin and low-loss laminations) and the exciter core (e.g., using low-loss compressed powder with 1.5 Tesla saturation-level materials). However, the core-loss reductions need to be further investigated.
- The scaling equations provide a tool for other machine configurations.
- This uncluttered rotor concept opens a door for various brushless electric machine improvements.
- A prototype machine has not yet been built. It should be the next step for further research on the uncluttered rotor concept.

Publications

J. Hsu, "Hybrid-secondary uncluttered induction (HSUI) machine," *IEEE Transactions on Energy Conversion* **16**(2), ITCNE4, (ISSN 0885-8969), 192–197 (June 2001).

J. Hsu, "Closure on hybrid-secondary-uncluttered induction (HSUI) machine," *IEEE Transactions on Energy Conversion* **17**(1), ITCNE4, (ISSN 0885-8969), 150 (March 2002).

References

1. J. Perahia, "Discussion of hybrid-secondary-uncluttered induction (HSUI) machine," *IEEE Transactions on Energy Conversion* 17(1), ITCNE4, (ISSN 0885-8969), 150 (March 2002).

Patents

1. John Hsu, "Hybrid Secondary Uncluttered Induction Machine," U.S. Patent No. 6,310,417, October 30, 2001.
2. John Hsu, "Simplified Hybrid-Secondary Uncluttered Machine and Method," U.S. Patent 6,891,301, May 10, 2005.
3. John Hsu, "Hybrid-Secondary Uncluttered Permanent Magnet Machine and Method," U.S. Patent 6,977,454, December 20, 2005.
4. John Hsu, "Electric Machine for Hybrid Motor Vehicle," U.S. Patent 7,270,203, September 18, 2007.
5. John Hsu, "Radial Gap Hybrid Secondary Uncluttered Permanent Magnet Electric Machines," Invention Disclosure 1934, May 7, 2007.

3.2 Axially Excited Electro-Magnetic Synchronous Motor

Principal Investigator: C. W. Ayers
Oak Ridge National Laboratory
National Transportation Research Center
2360 Cherahala Boulevard
Knoxville, TN 37932
Voice: 865-946-1342; Fax: 865-946-1262; E-mail: ayerscw @ornl.gov

DOE Technology Development Manager: Susan A. Rogers
Voice: 202-586-8997; Fax: 202-586-1600; E-mail: Susan.Rogers@ee.doe.gov

ORNL Program Manager: Mitch Olszewski
Voice: 865-946-1350; Fax: 865-946-1262; E-mail: olszewskim@ornl.gov

---

Objectives

- Produce a reasonably detailed design of an axially excited electromagnetic synchronous (AEEMS) motor, which is a synchronous high-torque motor using no permanent magnet (PM) material.
- Use finite element magnetics modeling to optimize the design in order to provide a reasonable estimate of size and weight.
- Determine the feasibility of the concept for lowering manufacturing costs owing to the rotor's simplicity and the lack of PM materials.
- Perform a cost analysis to determine if the concept results in a lower-cost machine compared with the Prius motor.

Approach

This project proposes a mechanical design for the rotor and axial excitation stator, expected to work in conjunction with a conventional radial-gap stator. The concept is called the AEEMS motor. This design focuses on a high-speed rotor capability, optimization of the flux paths for the magnetics in the axial stator and the rotor, and minimization of weight and added materials.

Magnetics finite element analysis (FEA) modeling was performed for the rotor and axially excited stator based on the mechanical design, and iterations between the two were performed throughout the design and modeling stages to improve the design. Evaluating the three-dimensional flux paths for this motor/rotor design was the main effort required for the magnetics modeling. The software used for this effort was ProEngineer Mechanica (mechanical and thermal FEA) and Ansys EMAG magnetics software (magnetic FEA).

Major Accomplishments

- The mechanical stator and rotor design has been completed to provide a basic model for the FEA of the magnetic performance of the motor. The design was based on a basic stator configuration and size such as is used in the Prius drive. A unique rotor configuration was developed along with axial excitation poles to magnetically excite the rotor.
- The stator design, which was originally believed to follow a conventional philosophy, evolved during the project and resulted in a different lamination structure that enhances the magnetic performance of the motor. The overall geometry of the stator is essentially the same, but the laminations are different.
- FEA modeling has been performed on the basic motor design, providing data that were fed back into the mechanical design.

- Multiple iterations were made in the rotor and stator designs, with FEA model results continually providing insight leading to mechanical changes and performance improvements.
- A feasible design has been shown with estimates of a specific power = 1 kW/kg and a volumetric power density = 5 kW/L.

Future Direction

This project combined technologies developed at ORNL utilizing brushless field excitation with a novel stator design from a FY 2007 project with the University of Wisconsin. Combining these technologies shows promise in moving toward the 2015 motor targets. This project accomplished the goal of ascertaining potential benefits from a motor using external field excitation without a PM rotor.

The decision has been made not to continue this specific project into FY 2009. In an effort to maximize resources, the lessons learned from this effort are being carried forward and consolidated into another FY 2009 project that involves similar concepts and builds upon this work.

Technical Discussion

This concept is a motor that is expected to be lower in cost than a PM motor, with a higher speed capability and higher power density. Rotor manufacturing will be simplified because no PM installation is required. Simplified manufacturing and changes in some materials produce the lower cost.

Inherent in this motor design is the natural ability to field weaken as speed increases as a result of the full control capability of the electromagnetic excitation coils used for rotor magnetization. Since the rotor can be naturally "weakened" as speed increases, core losses in the rotor will be much lower than in PM motors. This reduction in core losses in the rotor increases the efficiency of the inverter/motor system over the efficiency of a conventional inverter/PM motor system.

This design will produce a motor that provides traction motor functions for hybrid electric vehicles with a higher power density. Along with this performance improvement, a more robust and lower-cost motor design is expected. This design also has no dependence on rare earth materials/magnets with their associated cost, availability, temperature, and performance issues.

The design is based on a Prius-size core for convenience of comparison. The tradeoff between adding copper excitation coils and steel axial excitors and deleting the magnet material is estimated to result in a cost reduction. Total motor cost can be estimated based on comparisons with Prius and Camry motor construction. It is possible that some savings in manufacturing and assembly might occur in addition. Steel laminations for the stator can be made from radial subsections used to make up the whole circular stator core, instead of from one large circular stamping with a lot of waste area. The rotor is not expected to use laminations. The stator segments will be smaller and simpler and have more efficient punchings without the associated material losses inherent in single-piece circular punchings. See the Cost Analysis section of this report for cost comparison details.

The AEEMS motor concept uses a rotor that contains no PM material but provides magnetic flux paths axially excited by electromagnetic poles on the ends of the motor. To accomplish this excitation, axial excitors are required. These add iron and copper to the motor, adding weight and volume. These additions, though, are offset by removal of the expensive PM material from the design.

Figure 1 shows a cutaway of the motor concept with copper windings removed to allow the main components to be viewed. The rotor shaft and the trapezoidal blue components in the center make up the rotating portion of the motor. The large circular components wrapping around the motor are the axial excitors that provide magnetic flux in the rotor and flux communication to the stator. There is an axial air

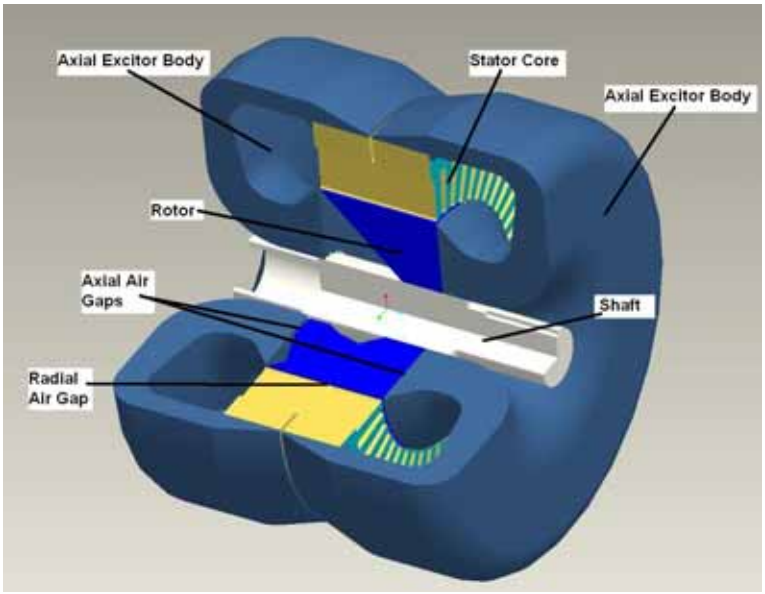

Fig. 1. AEEMS prototype design; 3D ProEngineer model used for FEA modeling.

gap between the flared axial excitor pole faces and the rotor axial face (a brushless design), and there is also the conventional radial air gap between the rotor circumference and the stator teeth.

Figure 2 is an exploded view showing the parts of the assembly opened up to provide more details of the design of the motor. The two rotor halves interleave together, and air gaps between all portions provide a magnetic break between the two sections. One rotor will have a positive flux orientation relative to the stator, and the other rotor half will have a negative flux relative to the stator. The axial excitors provide this flux with coils wound around the yoke adjacent to the shaft bearings. The two coils on opposite ends of the motor will have current flowing in opposite directions to provide the positive and negative rotor pole orientations.

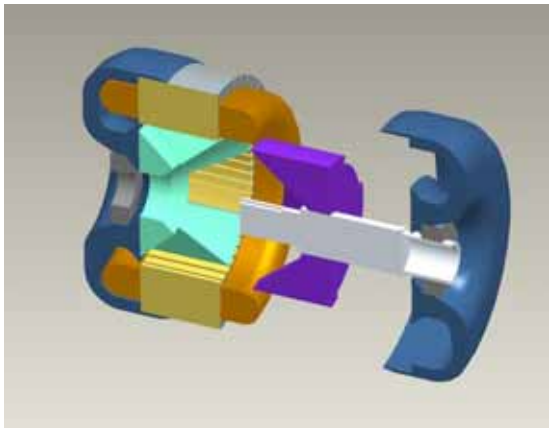

Fig. 2. Exploded view of the AEEMS motor showing subcomponents.

The stator design was originally intended to be a conventionally laminated stator with laminations similar to those in the Prius stator. During the development of the concept, it became clear that a different type of stator construction would be necessary. The new stator concept contains lamination punchings that are much simpler in shape and can be made with reduced punching waste. The simpler punchings come with a slightly more complex assembly requirement. This arrangement is required to promote magnetic flux in the correct directions in the stator, providing the lowest resistance to magnetic flux. The stator windings

are conventional, but the new arrangement of the laminations is required to handle the flux from the axial excitor magnetic field.

Note that in Fig. 3, the rectangular punchings are arranged to make up the new stator concept. In this prototype photo, the angle between segments is created by inserting an extra small tab of lamination in the yoke of the stack. A more developed prototype may use a wedge of lamination placed between the segments in the center of the yoke portion. This stator design essentially requires three different lengths of punchings, all the same width (essentially zero waste).

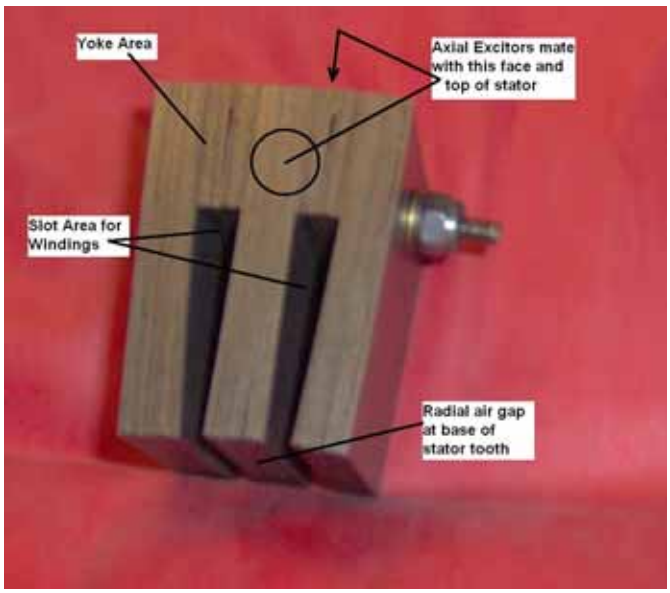

Fig. 3. Photo showing two slots of a prototype of the AEEMS stator lamination concept.

A ProEngineer model was made to show the construction with more of the detail that would probably be used in an actual prototype. The prototype in Fig. 3 was a quick demonstration model put together with simple pieces. Figure 4 shows a quarter section of the stator design from a ProEngineer model. This lamination arrangement allows magnetic flux to flow freely in the axial direction, allowing the axial excitation design to function.

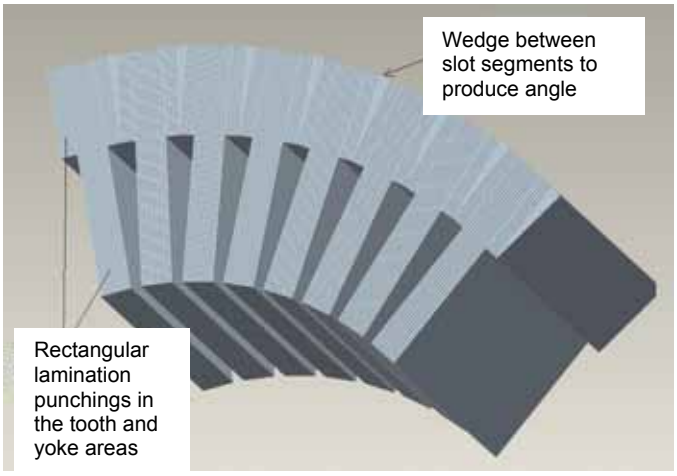

Fig. 4. Rectangular punching style stator construction for the AEEMS motor.
This concept requires a wedge-shaped piece between each stator segment.

Finite element analysis results

Ansys EMAG software was used to model the magnetic performance of the motor components. Small slices were first used, 22.5° segments, to speed up the solution time and aid in achieving a quick understanding of the basic magnetic behavior of the design. As the design became better understood magnetically, the model was made more complex, and eventually a 360° full model was used to perform the magnetic solutions. The full model results provided the direction for mechanical design changes.

Figure 5 contains a 90° segment from early in the development stage, showing how the magnetic flux lines behave in the material. At this stage, fundamental concepts were being explored; sources of leakage were being searched for and mitigated by changes in the mechanical design (such as the circumferential slot shown, which was determined to be unnecessary for flux control).

The colored arrows show flux line direction, and the yellow and red lines depict areas nearing flux saturation. These areas can then be modified to reduce the saturation tendency by placing material where it is needed or to remove material, and weight where it is *not* needed when flux density is very low.

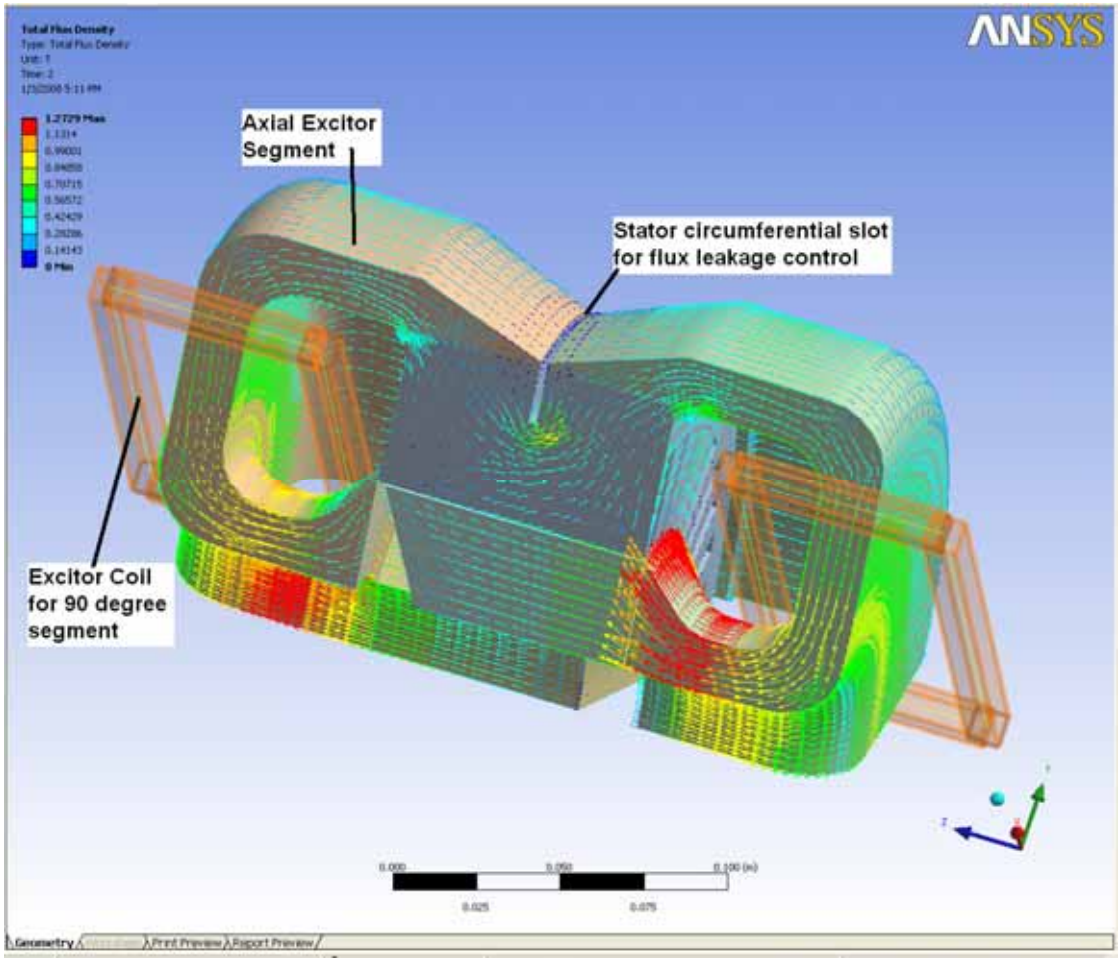

Fig. 5. A 90° model segment from ProEngineer software used with Ansys EMAG software to evaluate magnetic performance.

Figure 6 shows the view of flux lines in the full 360° motor model. The locked rotor torque estimated from this configuration was 235 N m. The motor design provides flux paths in the conventional 2-dimensional plane of the motor and in the third dimension parallel to the shaft. The design allows the

flux to go axially (i.e., out of the page) through the pole side faces, around through the excitor sections, and into the stator edge and outer circumference.

The design uses reluctance torque, combining a mix of two different reluctance paths— one in the plane of the motor and another in the axial direction. It is believed that these two separate paths can be further studied and developed to produce an even higher torque design in future work.

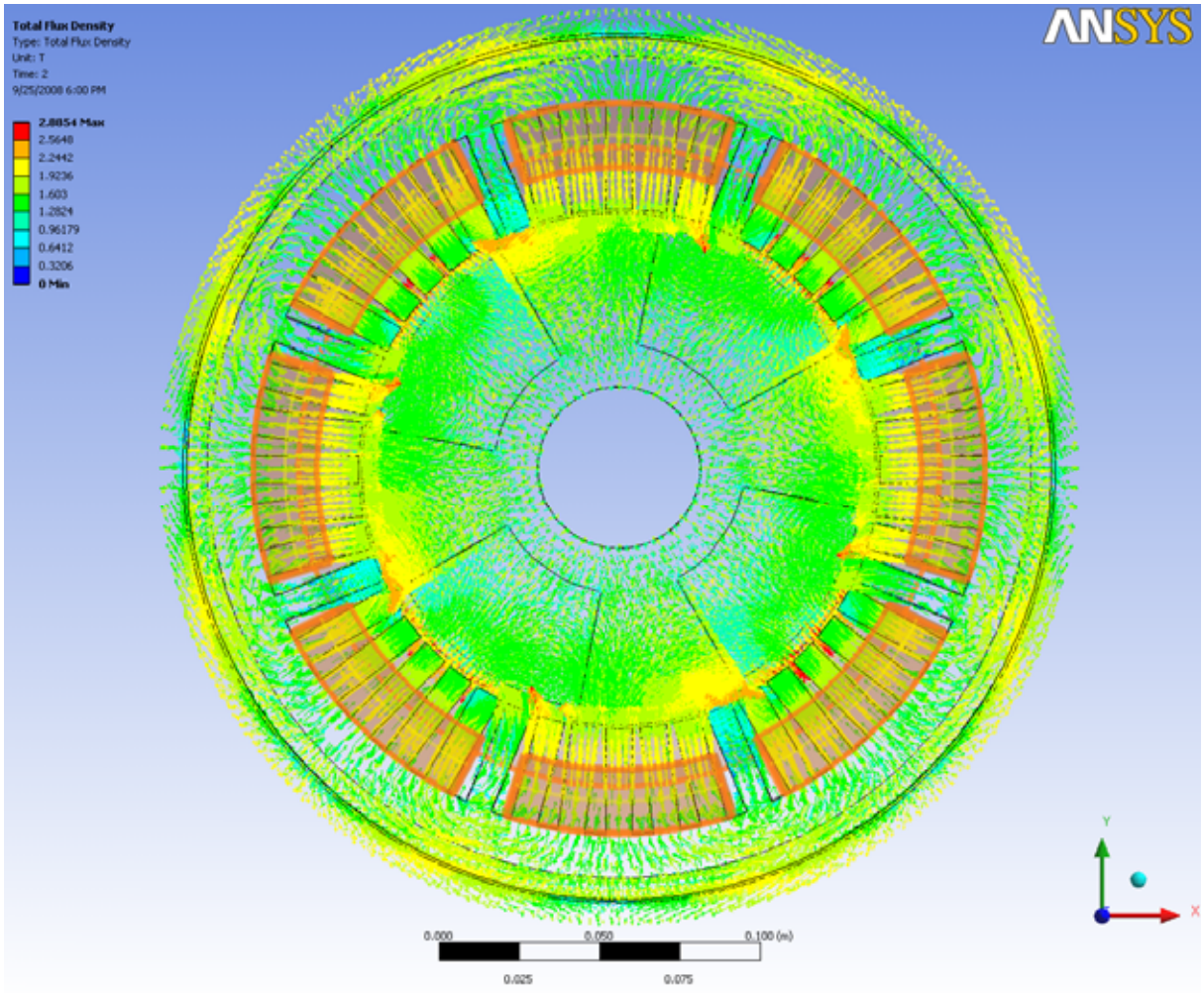

Fig. 6. Model results from Ansys EMAG for a 360° slice of the motor.

Figure 7 shows the 360° model from a side view (with one excitor removed), which gives an indication of the complexity of the 3-dimensional flux in this type of motor. Torque results from various EMAG solver runs are shown in the plot in Fig. 8. After a reasonable model was found with good torque performance, multiple runs were made while the rotor angle was changed to search for the best rotor position for peak torque. The peak torque was seen in a couple of very similar geometries in the "4/24 data" and the "Misc at tdc+57", shown in Fig. 8.

Some areas of leakage between rotor halves were reduced, and a configuration with increased radial air gap area was analyzed to produce the final improvements in the design so as to achieve 235 N m peak

torque. Note that this is the highest torque possible; further study is very likely to increase this number to even better torque levels. This value was determined to be a good stopping point for the feasibility study based on findings and budget.

The intent of the feasibility study has been met, with positive results.

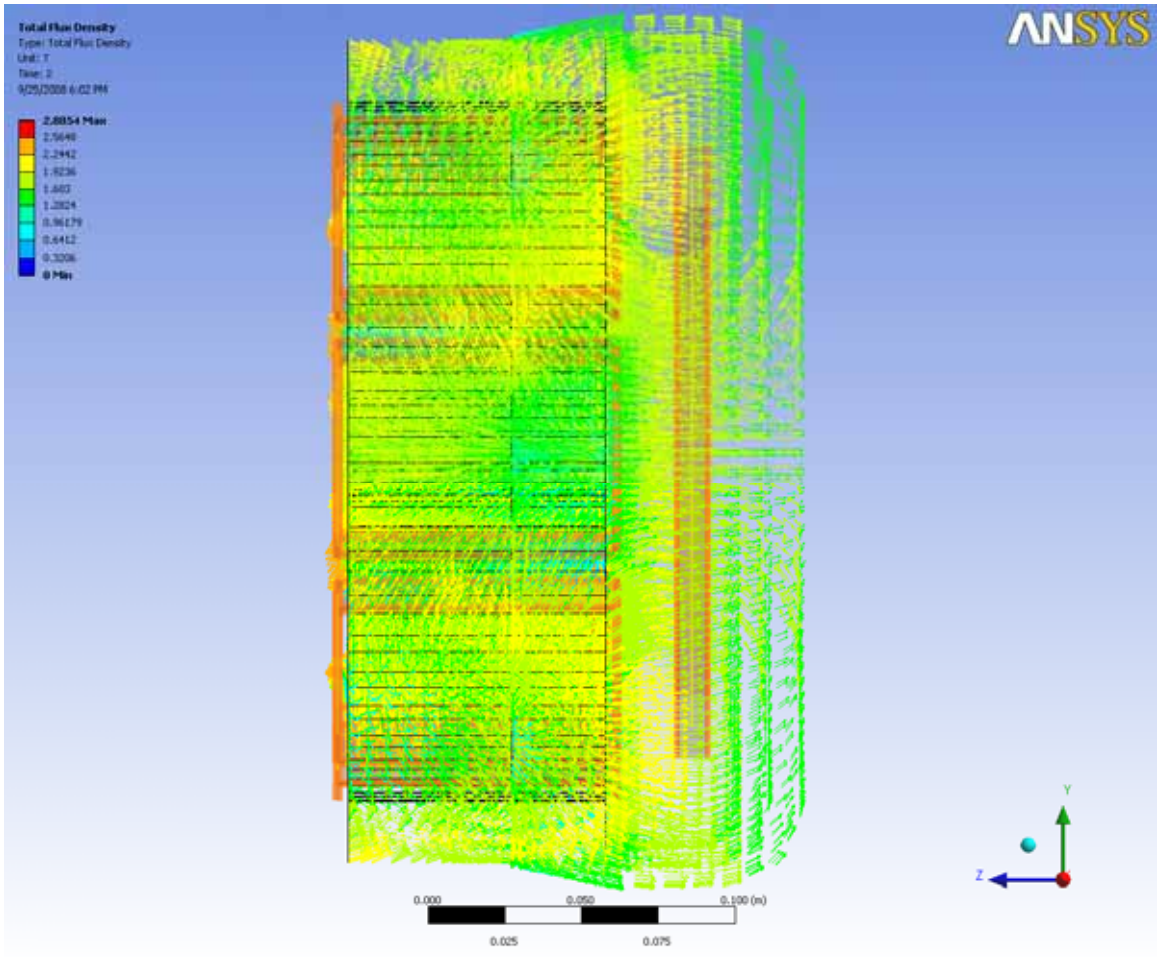

Fig. 7. Side view of the 360° EMAG model.

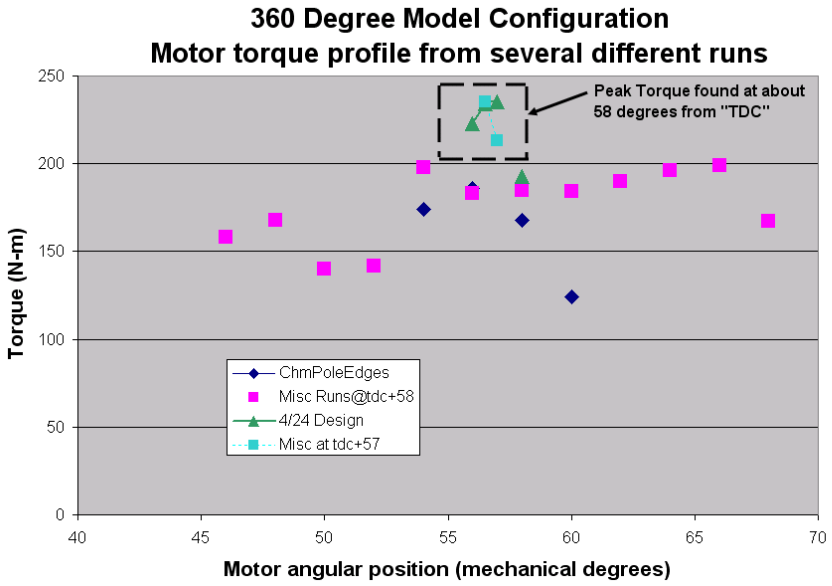

Fig. 8. Plot showing torque achieved with various motor geometries versus motor angular position.

Cost analysis comparison of this motor design with the Toyota Prius design

The approximate cost for finished neodymium iron magnets (simple rectangular shape) is about $60/kg (cost information furnished by Arnold Magnetics in August 2008).

Prius PM material volume is estimated to be V = 11 in^3. This was calculated from the Prius magnet cross-section dimensions and the lamination stack length of 3.29 in. Using this volume, the mass was calculated for the PM material:

$$\text{Mass of PM } (11\ in^3) \times (0.3\ lbm/in^3) = 3.3\ lbm \text{ (equals } 1.5\ kg)$$

Based on this calculation, the approximate cost of the PM in the Prius motor = 1.5 kg · $60/kg = $90.

Copper costs have changed rapidly during the past year, so a few sources were checked to estimate the present raw copper cost. As of about August 22, 2008, costs were as follows:

Wikipedia	$2.80 / lbm
New York Futures	$3.36 / lbm
AllBusiness.com	$3.50 / lbm → $7.70 / kg

The $49 cost estimate decrease is mainly due to the removal of PM material from the motor design. In addition to the estimation in Table 1, the dollar amount needs to be normalized to the projected power density of the AEEMS motor compared with the Prius power density.

Power estimates

AEEMS power is calculated to be 61.5 kW peak with an assumed base speed of 2,500 rpm (this number needs to be validated by further study). The volume of the model, created in ProEngineer Wildfire 3D

modeling software, was found to be 12.0 L. The mass (also from the ProEngineer software model) was found to be 63 kg.

Prius specific power:	1.1 kW/kg
Prius power density:	3.3 kW/liter
AEEMS specific power:	0.97 kW/kg
AEEMS power density:	5.1 kW/liter

The costs in Table 1 need to be normalized to the differences in specific power and power density found in the two motor designs. In other words, the cost reduction shown in Table 1 for the AEEMS motor needs to be lowered according to the lower specific power but increased in light of the higher power density.

Based on specific power:

$$\text{AEEMS cost} = \frac{0.97}{1.1} \times -\$49 = -\$43$$

Table 1. Material additions/subtractions from the Prius motor design

Item description	Added to	Subtracted from	Cost ($)
Stator iron	0	0	+ $ 0
Excitor iron	24.8 kg		$ 25
Excitor copper	2.1 kg		+ $ 16
Permanent magnet material			– $ 90
AEEMS cost compared with Prius		7.3 kg	– $ 49

Based on power density:

$$\text{AEEMS cost} = \frac{5.1}{3.3} \times -\$49 = -\$\ 75$$

Based on these numbers, the AEEMS estimated cost *reduction* relating to materials would be an average of $59.

Manufacturing cost considerations

The AEEMS stator lamination design provides for a very simple and cost-effective punching with essentially zero waste. This compares with the type of standard punching used in conventional motor stators, such as those in the Prius, which have a significant amount of unavoidable waste.

While the stator punchings may provide some amount of savings in manufacturing material, the difference in the AEEMS stator assembly procedure will probably show a small increase in effort that would offset the savings in lamination waste. The actual increase/decrease in cost for the stator construction will require further study.

Stator wiring will be fairly conventional, so stator wiring and assembly costs will be basically unchanged. The added magnetic excitors will require winding, but the windings will probably be done as a simple spun core and will be inexpensive to fabricate and install.

The rotor, by specific design, will have no PMs; therefore, the rotor fabrication and assembly will be very simple, with similar or slightly lower cost and effort compared with an induction motor. Any cost savings in this area are likely to offset the slight costs associated with the excitor winding and assembly.

Overall, at *this stage* of the concept study, the manufacturing costs seem to be approximately equal between a Prius or Camry comparison motor and the AEEMS concept design. No large differences are anticipated.

Conclusion

This feasibility study has shown that the AEEMS design can produce significant torque, up to 235 N m, for this size of stator and rotor (based on the 2004 Prius size). The information gained this year indicates the design is a feasible concept and could be further refined and made more complete with future work. A first-order cost analysis based on comparison with a known motor, the Prius PM traction motor, has shown that it may be possible to produce the AEEMS motor at slightly less cost. The important comparison is that this design is slightly lower in cost and requires no PM material, thus fulfilling a need for an alternative motor design in addition to common designs such as induction and PM motors.

The motor configuration studied in this year's effort shows these estimated results:

Locked rotor torque	235 N-m
Total mass	63 kg
Total swept volume	12 liter
Estimated power (base speed 2,500 rpm)	61 kW peak
Specific power	0.97 kW/kg
Volumetric power density	5.1 kW/liter

Further development is required to determine the potential efficiency, nominal base speed capability, and rotor speed capability of the motor.

3.3 Application of Concentrated Windings to Electric Motors without Surface-Mounted PMs

Co-Investigators: John W. McKeever and Pedro J. Otaduy
Oak Ridge National Laboratory
National Transportation Research Center
2360 Cherahala Boulevard
Knoxville, TN 37932
Voice: 865-946-1316; Fax: 865-946-1262; E-mail: mckeeverjw@ornl.gov

DOE Technology Development Manager: Susan A. Rogers
Voice: 202-586-8997; Fax: 202-586-1600; E-mail: Susan.Rogers@ee.doe.gov

ORNL Program Manager: Mitch Olszewski
Voice: 865-946-1350; Fax: 865-946-1262; E-mail: olszewskim@ornl.gov

---

Objectives

- To determine if electric motor configurations using interior permanent magnets (IPMs) can benefit from using fractional-slot concentrated windings (FSCW) instead of distributed windings in electric vehicle (EV) or hybrid electric vehicle (HEV) traction drives.

Approach

Task 1. Redesign a (computer model of a) commercially available baseline IPM motor by replacing distributed windings with concentrated windings.

- Four concentrated winding configurations with 8 poles were chosen because they were compatible with the baseline IPM, which had 8 magnets (4 pole pairs). The configurations, expressed as slots/poles, were 9/8, 12/8, 24/8, and 48/8; they have fundamental harmonic winding factors of 0.945, 0.866, 0.500, and 0.256, respectively.
- These configurations were modeled in SPEED and their performance parameters and torque ripple examined to determine if any of them had potential to be an HEV traction drive.

Task 2. Craft an algorithm that represents saturation in a lumped parameter model of an IPM motor with sufficient accuracy to provide insight into the effect of saturation on IPM motor performance.

- The purpose of this task was to provide insight about and quantify the effect of magnetic saturation on inductances, Lq and Ld, as the line current and motor speed change. Inductance relates the flux-links to current. Values of Lq and Ld change as the motor core becomes magnetically saturated during operation. Corrected values were needed to perform Task 4—a simulation of the motor traversing two standard driving schedules, the US06 and the Federal Urban Driving Schedule (FUDS)—to compute an average performance in terms of miles per gallon. The difficulty of creating a physics-based algorithm forced us to obtain our insight and inductance correction coefficients from SPEED's PC-BDC software, which applies finite element analysis (FEA) of the flux-links using its PC-FEA module as a function of speed and line current as the rotor turns. The ratio of the inductance computed by FEA to the inductance computed with saturation neglected defines the saturation correction coefficients used in Task 4.

- A script was written to obtain the saturation coefficient dependency on current and speed. The script queries the PC-BDC FEA software looping through ranges of motor speed, current, and control angle. The control angle delivering the maximum efficiency was used to select the parameters needed for use in Task 4.

Task 3. Complete a performance analysis of 55-kW IPM motors with concentrated windings to identify a configuration that can meet FreedomCAR targets.

- Analysis of the 9/8 IPM with concentrated windings was completed and compared with a baseline IPM model having distributed windings.

Task 4. Determine the average efficiency (in mpg) for the 9/8 IPM with concentrated windings as it traverses US06 and FUDS driving schedules and compare it with the average efficiency (in mpg) for the baseline 48/8 IPM with distributed windings.

- Resurrected and updated ORNL's driving schedule simulation program, which is on a LabVIEW platform.
- Coordinated the results from Task 2 to make them compatible for use in the simulation program.
- Completed simulations of the US06 and FUDS driving schedules using models of the 9/8 IPM with concentrated windings and the 48/8 IPM baseline with distributed windings as traction drives, and compared their performance.

Major Accomplishments

- Compared with the 12/8, 24/8, and 48/8 adjusted to have the same number of coils per phase, the 9/8 IPM with FSCW was the only configuration with acceptable torque ripple of 8% at base speed; consequently, it was selected for further analysis.
- Saturated inductance correction coefficient tables were calculated for the 9/8 IPM with concentrated windings and for the baseline 48/8 IPM with distributed windings in preparation for the simulation of these motor models traversing the US06 and FUDS. The simulation was conducted as Task 4 using ORNL's driving simulation program.
- Detailed modeling of the 9/8 IPM with concentrated windings showed that
  - The number of turns per coil for maximum power is 11, up by 3 from the number used to compare torque ripple among the 8-pole configurations with concentrated windings.
  - Torque ripple is half that of the baseline IPM with distributed windings.
  - The base speed is 5,800 rpm, 2.3 times higher than the 2,500 rpm base speed of the baseline IPM with distributed windings.
  - At base speed, the power delivered to the shaft is 12.8% higher than that delivered by the baseline IPM.
  - The torque versus rpm performance curve extends over 6 times base speed, allowing the motor to deliver significant power at high speeds, characteristic of motors with concentrated windings.
  - In spite of 4% more bridge flux leakage, the efficiency at base speed is over 98%, 11.6 percentage points higher than that of the baseline IPM, because better copper use reduced current density in the stator wires by a factor of 3, from 32 to 11 A/mm^2.
  - Although the current density diminishes as the speed increases to 18,500 and 33,460 rpm, the efficiency drops from 98 to 86%—about the same as the baseline IPM at its 2500 rpm base speed—because of increasing eddy current and hysteresis losses in the core.
  - Compared with the baseline IPM with distributed windings, the $/kW, kW/kg, kW/L, and efficiency of the 9/8 motor with concentrated windings are better at speeds up to 18,500 rpm; but this edge is lost because of a 10 kW reduction in shaft power between 18,500 and 33,460 rpm.

  - — Because concentrated windings make better use of copper, more copper was used; to offset the increased copper costs, the savings from simplified fabrication must be more than the 2% assumed in this study.
- Simulations of the US06 and FUDS cycles with the 9/8 IPM with concentrated windings and the baseline 48/8 IPM with distributed windings have been completed and show that the following:
  - — If the gear ratio were increased 1.25× above the base gear ratio, from 4.114 to 5.145, the baseline IPM with distributed windings could meet US06 and FUDS cycle requirements with a maximum of 51.4 mpg and 72.8 mpg, respectively.
  - — The US06 and FUDS requirements could be met by the 9/8 IPM with concentrated windings only after the gear ratio was increased 3.5× above the base gear ratio, from 4.114 to 14.399. This would achieve values of 50.13 mpg and 70.68 mpg, respectively, slightly below baseline values.
  - — To fully negotiate the US06 and FUDS cycles, the IPM with concentrated windings had to be operated at speeds of up to 33,460 rpm, which means that the rotor would have to be specially reinforced and might not be feasible for these dimensions.
  - — The gains in efficiency at base speed and half maximum speed for the 9/8 IPM with concentrated windings occur because of reduced copper losses but are overwhelmed by eddy current and hysteresis losses as the speed climbs to 33,460 rpm.
  - — Eddy current losses in the magnets, were not included in this study but should be included in future calculations.

Future Direction

No additional work is planned. However, results of this study suggest that motor modeling should include calculation of magnet losses and that 9-slot, 8-pole or other IPM configurations with concentrated windings should be designed in concert with standard driving schedules to meet their requirements at reasonable motor rotor speeds without inordinately increasing the gear ratio.

Technical Discussion

Early motor development began with concentrated windings but changed to distributed windings because they produced sinusoidal back-emfs (electromotive forces). Concentrated windings have reawakened research interest for several reasons, including increased fault tolerance at higher operating speeds, reduction of the end turns, improved packing of wires in the stator slots, and reduced fabrication costs. This project focused on simulating different interior PM motor configurations using concentrated windings to assess their performance benefits.

Four slot/pole configurations with concentrated windings compatible with the baseline IPM 8-pole rotor are 9/8, 12/8, 24/8, and 48/8 in order of reducing winding factor. The four were modeled for comparison to have 32–33 turns per phase so that the 9/8 had 11 turns/coil and 3 coils/phase, the 12/8 had 8 turns/coil and 4 coils/phase, the 24/8 had 4 turns/coil and 8 coils/phase, and the 48/8 had 4 turns/coil and 8 coils/phase. Figure 1 compares the torque ripple of these four configurations at base speed.

The torque fluctuation of the 9-slot and 12-slot stators are similar, but the torque ripple is 3.5 times greater for the 12-slot stator. The 24- and 48-slot stators deliver much lower torque at base speed. The torque ripple for the 9/8, 12/8, 24/8, and 48/8 is 8.5%, 27.4%, 52.3%, and 218%, respectively, showing that the 9/8 configuration is closest to the FreedomCAR target for torque. For this reason it was selected for more detailed analysis.

A script was written to calculate the motor model's characteristic values of flux links and inductance, Ld and Lq, using the finite element capability of SPEED's PC-BDC module, which accounts for magnetic saturation. Calculations were performed over three loops: for speeds of 1,000 to 18,500 rpm in steps of 2,500 rpm, for ISP (the current set point) values from 10 to 400 A in steps of 50 A, and for advance

control angles of 0 to 90 degrees in steps of 5°. An interesting feature of the 9/8 configuration is its ability to deliver power at speeds well above its base speed of 5,800 rpm. This is shown in Fig. 2, which summarizes the results obtained for torque, current, power, efficiency, and the advance angle that produces maximum efficiency between 1,000 and 18,500 rpm. Figures 3a and 3b show the values of Ld, Lq, psiMd (PM drive flux-links), and efficiency as a function of advance angle for currents limited by the two extreme current set point values of ISP = 10 and ISP = 400, respectively. Information from plots like those in Fig. 3 characterizes core saturation, which relates values of Ld, Lq, and psiMd to current in the stator. It was necessary to complete these calculations to prepare for Task 4, which is to simulate the motor operating as a traction drive traversing standardized driving schedules. Plots like those in Fig. 3 are then summarized as shown in Fig. 4, which is a plot of values Ld, Lq, and psiMd as a function of the stator's ampere-turns, a form that may now be used by ORNL's driving schedule simulation program.

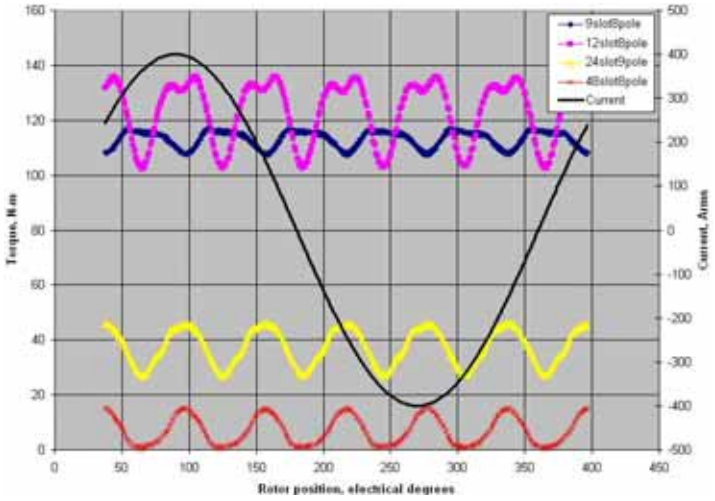

Fig. 1. Torque ripple for IPMs with 8-pole concentrated windings configured for 33 turns per phase.

The 9/8 configuration in Fig. 5 was initially ranged using smaller intervals of gamma in the computational loops of SPEED's PD-BDC (with the embedded PC-FEA module) to determine the number of turns per coil that would produce maximum shaft power. From Fig. 6, we see that the value of TC (turns per coil) should be 11 or 12. We chose TC=11.

The advance angle is the angle between the terminal voltage and the back-emf generated by the rotor, which coincides with the q-axis. To determine the base speed, the advance angle at which the motor delivers maximum power was determined first at each speed for which the corresponding torques and powers are shown in Fig. 7. The base speed, 5,800 rpm, was determined as the speed at which the torque starts to drop. The slope of the drop is much less than for the baseline IPM.

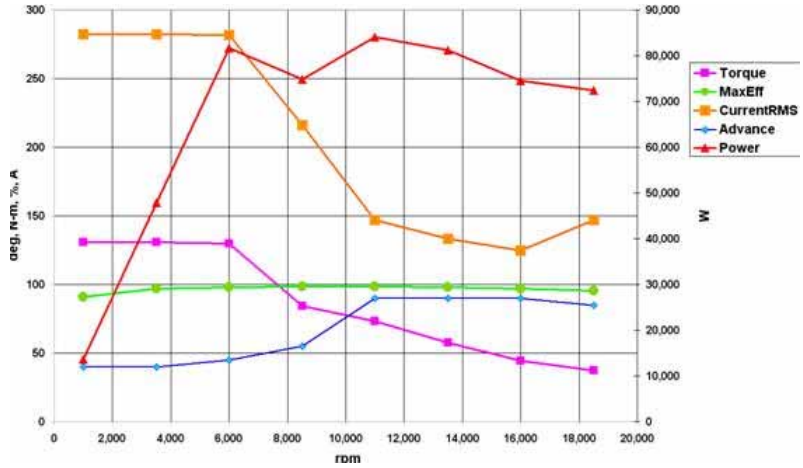

Fig. 2. Performance parameters to 18,500 rpm for 9-slot, 8-pole IPM with concentrated windings.

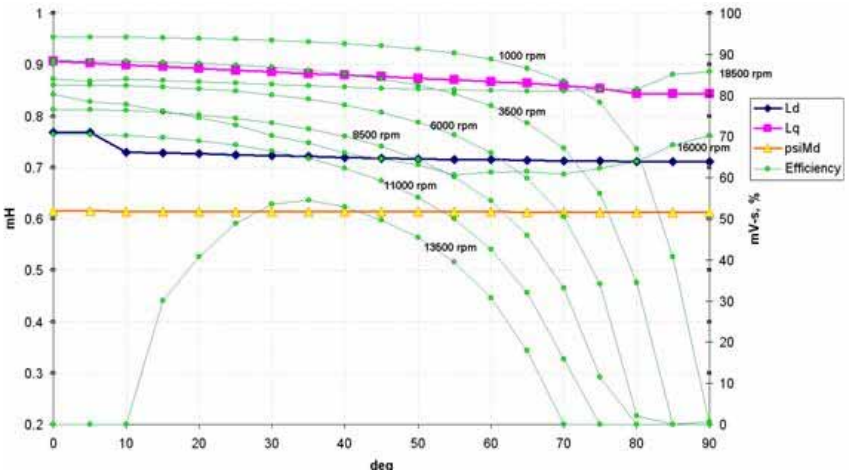

(a) Parameters as a function of advance angle for current controlled by a current set point, ISP=10.

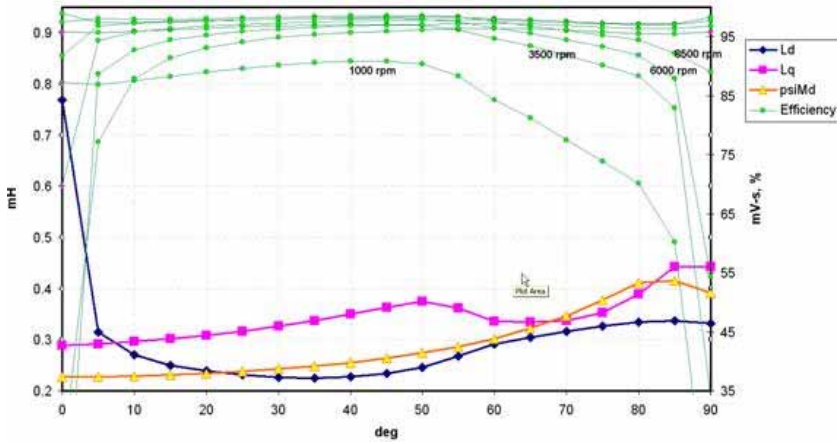

(b) Parameters as a function of advance angle for current controlled by a current set point, ISP=400.

Fig. 3. Lq, Ld, flux links (psi) as a function of advance angle for an unsaturated (ISP=10) and for a saturated (ISP=400) IPM core.

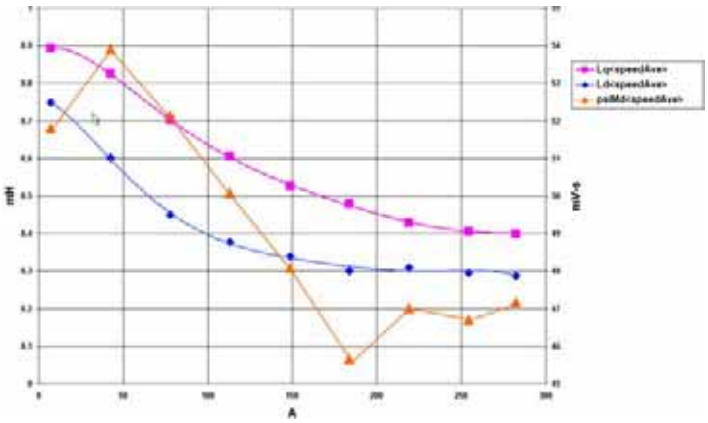

Fig. 4. Inductance and flux links showing the effect of core saturation in the 9-slot, 8-pole IPM.

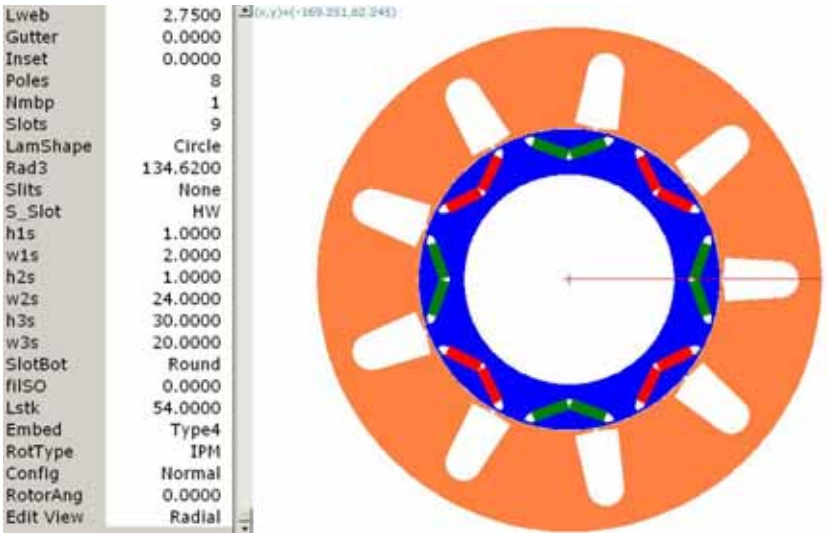

Fig. 5. Outline of IPM configuration with 9 slots and 8 poles.

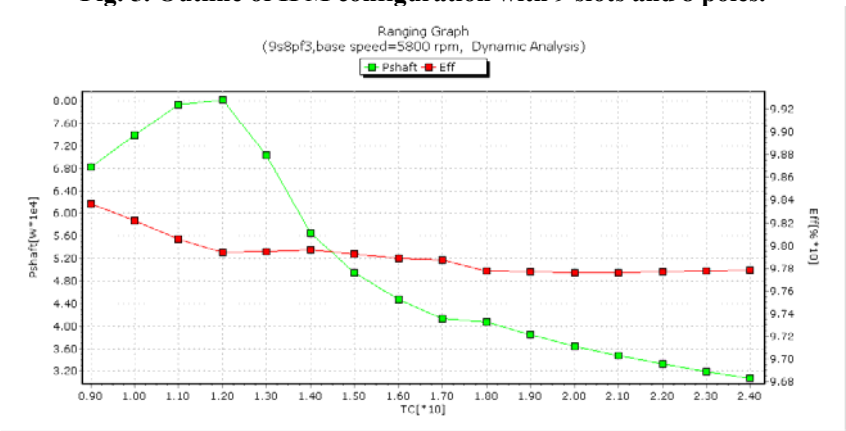

Fig. 6. Maximum shaft power is delivered when there are 11 or 12 turns per coil.

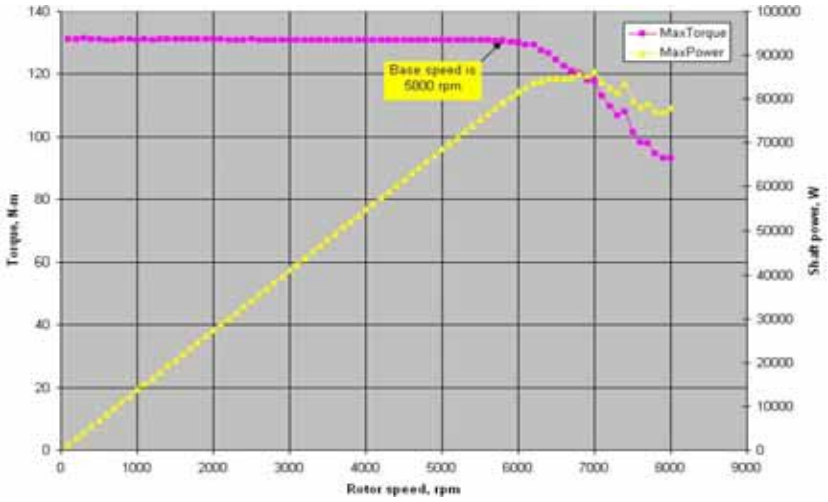

Fig. 7. Determination of base speed when torque begins to drop.

The template editor from SPEED's PC-BDC module shows the physical dimensions in Fig. 8.

Dimensions							
Config	Normal	RotType	IPM	Poles	8	Slots	9
Lstk	54.0000	Embed	Type4	LM	5.3100	S_Slot	HW
Rad3	134.6200	Rad1	80.1900	BetaM	120.0000	SD	14.0000
Stf	0.9700	Inset	0.0000	MagWid	38.4800	SO	2.0000
NOH	0.0000	Bridge	1.0000	SOang	20.0000	TWS	5.0000
RotorAng	0.0000	RadSH	56.3000	TGD	1.0000	Gap	0.7700
Ecc	0.0000	Polarity	Normal			Edges	Bridged
Windings							
Connex	Wye			Offset	3	TC	11
WdgType	Custom	PPATHS	1	Ext	0.0000	NSH	13
WireSpec	SFill	SFg	0.7000	XET	1.0000	InsThick	0.0364
Skew	0.0000					Liner	0.4000
Control							
RPM	5800.0000	Vs	450.0000	Drive	Sine	DCSource	Fixed DC
ISP	400.0000			Sw_Ctl	ISP_HB	°gamma	43.0000
HBA	32.0000	HBtype	Constant				
ChopType	Soft	FixfChop	ISChop12				
NumPoly	1						
PolyOffs	1						
Settings							
ISLA	64.0000	Tol	8.0000	Tol_ISLA	Auto	Cycles	0
EMFCalc	ToothFlux	eCalc	Auto	CalcVwfm	dPsi/dt	XRx	0.0000
CalcVer	cv9			eqRevert	false	RTorq	On
TorqCalc	Pos_Seq	TSMin	0.0000	TSMax	0.0000	mmBase	1000.0000

Basic design | Magnetics | Calc. Options | Thermal | Embedded FEA | Harmonics

Fig. 8. SPEED's PC-BDC template editor for the 9/8 IPM with concentrated windings.

Figure 9 is a flux density map that shows how the flux pattern differs between the 9/8 configuration with concentrated windings and the baseline 48/8 configuration with distributed windings. Note that while the baseline IPM has 4 axes of symmetry, the 9/8 IPM has only one.

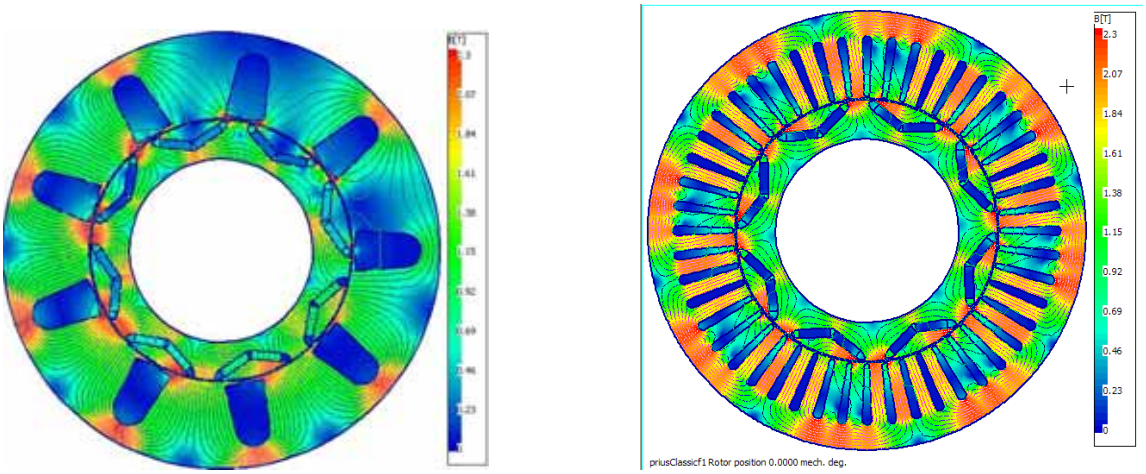

(a) 9/8 configuration with concentrated windings **(b) Baseline configuration with distributed windings**

Fig. 9. Flux density maps showing asymmetric flux linkages of the 9/8 motor during operation at 5,800 rpm compared with the axisymmetric flux linkages of a baseline motor.

Table 1 compares the motor weight and cost of the 9/8 IPM with concentrated windings against the baseline IPM with distributed windings. The assumption used in this study is that the savings permitted by simplifying fabrication is 2% of the manufacturing and miscellaneous cost. Costs and weights from Table 1, certain performance parameters from Table 2, and volumes of 6.07 L for the baseline IPM with distributed windings and 5.88 L for the 9/8 IPM with concentrated windings were used to calculate the targets in Table 3.

Table 1. Comparison of mass and cost of a baseline IPM having distributed windings with an IPM having concentrated windings.

Component or feature	Price ($/kg)	Baseline commercial IPM model with distributed windings (6.07 L volume)		9/8 IPM model with concentrated winding (5.88 L volume)	
		Mass (kg)	Cost ($)	Mass (kg)	Cost ($)
Sintered magnets	89.18	0.671	59.84	0.671	59.83
Rotor core laminations	3.07	3.391	10.41	3.391	10.41
Stator core lamination	2.91	11.411	33.21	11.577	33.69
Rotor shaft (75 mm)	3.97	5.718	22.70	5.718	22.70
Copper wires	7.34	5.230	38.39	6.031	44.27
0.22-in. thick Al housing	2.20	3.10	6.82	3.01	6.63
Manufacturing and misc.			40% of material cost 68.55		38% of material cost[1] 67.46
Total		29.52	239.92	30.40	244.99

[1] The 2% difference in manufacturing and miscellaneous costs is the savings assumed from simplified fabrication procedures (bobbin winding the stator segments followed by stator assembly).

Table 2. Comparison of performance parameters and FreedomCAR targets of a baseline IPM having distributed windings with an IPM having concentrated windings

	Baseline IPM with distributed windings at base speed, 2,500 rpm	9/8 IPM with concentrated windings at base speed, 5,800 rpm	9/8 IPM with concentrated windings at 18,500 rpm	9/8 IPM with concentrated windings at 33,460 rpm
Shaft power, kW%	70.46	79.50	72.40	62.78
Shaft torque, N-m	269.1	130.9	37.37	17.92
Efficiency, %	86.5	98.07	95.45	86.23
Shaft fluctuations, N-m	39.59	9.66	3.05	2.63
Mean FE torque, N-m	253.41	113.2	12.59	9.95
J, A/mm^2	32.44	10.72	5.55	4.53
Line current, A_{rms}	277.4	281.4	144.1	118.7
Id, A	-237.4	-191.0	-132.0	-114.1
Iq, A	143.5	206.6	57.8	32.8
Lq, mH	1.0775	.3578	.4343	.4343
Ld, mH	.6871	.2312	.3371	.3371
Copper loss, W	10886	1370	367	244
Core Loss, W	95	197	3080	9781
Bridge flux leakage, %	14.8	19.0	14.9	14.9

Table 3. Values corresponding to FreedomCAR targets

Quantity	Baseline IPM with distributed windings	9/8 IPM with concentrated windings at 5,800 rpm	9/8 IPM with concentrated windings at 18,500 rpm	9/8 IPM with concentrated windings at 33.460 rpm	Approximate 2015 targets
$/kW	3.41	3.08	3.08	3.90	7
kW/kg	2.39	2.62	2.38	2.06	1.3
kW/L	11.6	13.5	12.31	10.7	5
Efficiency, %	86.5	98.1	95.5	86.2	97
Torque ripple, %	15.6	8.5	24.2	26.4	5

The driving schedule simulation employs a vehicle model that computes the power needed at the vehicle's tires for it to follow a specified speed-versus-time profile. The performance of the IPM motor is modeled following the standard d-q transformation approach described in reference 1. The IPM motor uses the fundamental Ld and Lq inductances and magnet flux-linkages with their dependence on stator current shown in Fig. 4. These are determined with Version 8.0 of SPEED-FE employing a 2-dimensional finite element computation of saturation effects. At every time step, the model computes the voltage, electrical current, and advance control angle needed to meet the power demanded by the driving schedule.

The inverter model receives from the motor model a demand for power, voltage, current, and advance control angle and computes the power demand on the battery. The computed total power demand for the battery includes the losses in the cabling and battery. To facilitate comparison between the 9/8 IPM with concentrated windings and the baseline 48/8 IPM with distributed windings, it was assumed that the vehicles traveled over level ground without climatic wind and that the transmission losses, which occur between the motor's output axle and the tires, were zero. Figure 10 shows the chronological demand velocity of the vehicle for the US06 and FUDS schedules.

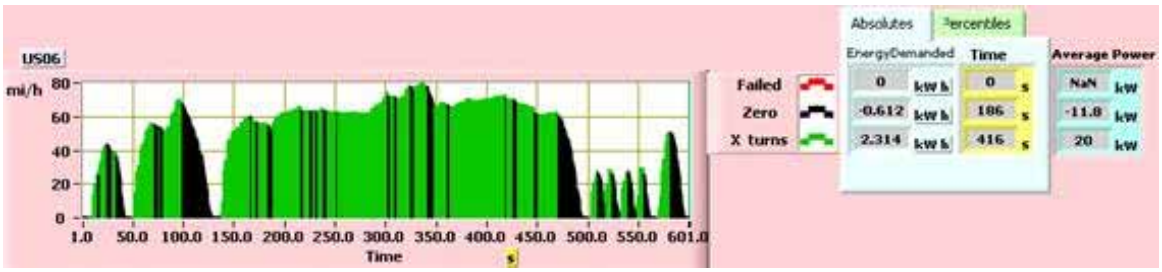

(a) US06 cycle

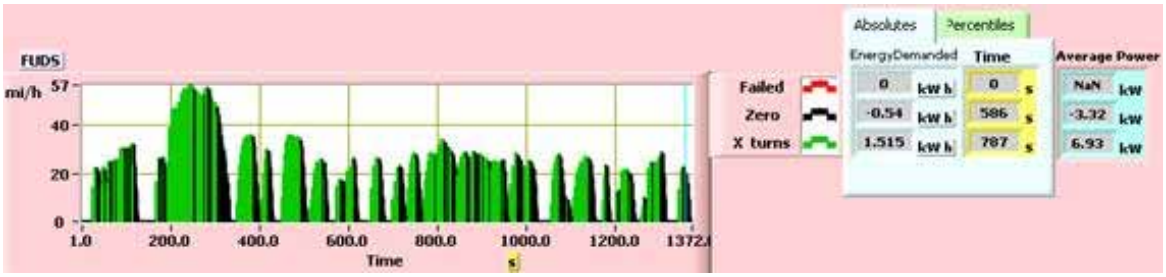

(b) FUDS cycle

Fig. 10. Vehicle demand velocity versus time for two standard driving schedules.

Considering that the tire diameter and vehicle velocity determine the rotational speed of the wheels, it is the task of the effective gear ratio between the wheels and the electric motor's rotor to operate the motor in its optimum speed range. For example, the baseline IPM with distributed windings can meet demands of the US06 and the FUDS cycle with a gear ratio of 4.114. The 9/8 IPM with concentrated windings with the same gear ratio fails to meet the power demand several times along the driving cycle, accumulating a deficit of 13.2% and 5.8% of the total energy demanded by the US06 and FUDS cycles, respectively. This may be remedied by increasing the gear ratio multiplier, defined as the total gear ratio divided by 4.114, which eliminates the energy deficiency and produces a valid mpg rating. As the gear ratio multiplier continues to increase, the mpg value passes through a maximum and again encounters a region with an energy deficiency. This means that there is a value for the gear ratio multiplier at which maximum mpg occurs.

Figure 11 is the simulation summary of the baseline IPM with distributed windings traversing the US06 and the FUDS cycles. Figure 12 is the simulation summary of the 9/8 IPM with concentrated windings traversing the US06 and the FUDS cycles. Table 4 summarizes the results of ORNL's US06 and FUDS driving simulations in which one traction drive model was a baseline 48/8 IPM with distributed windings and the other was the new FSCW 9/8 IPM.

Conclusion

At its base speed of 5,800 rpm, the 9/8 IPM with concentrated windings performs better than the baseline IPM with distributed windings. It has half the torque ripple and a third of the current density reflected in an eighth of the copper losses. It delivers 12.8% more power at an efficiency 11.6 percentage points higher. ORNL's driving schedule simulation program revealed that, in spite of its superior performance at base speed, it could not meet the power demands of the US06 driving schedule unless the gear ratio was multiplied by 3.5 to increase the effective gear ratio from 4.114 to 14.399. This increase requires the motor's rotor to operate at angular velocities of up to 33,460 rpm, which is unreasonably high. Further work is warranted to coordinate motor design with the required performance of IPM motors with concentrated windings.

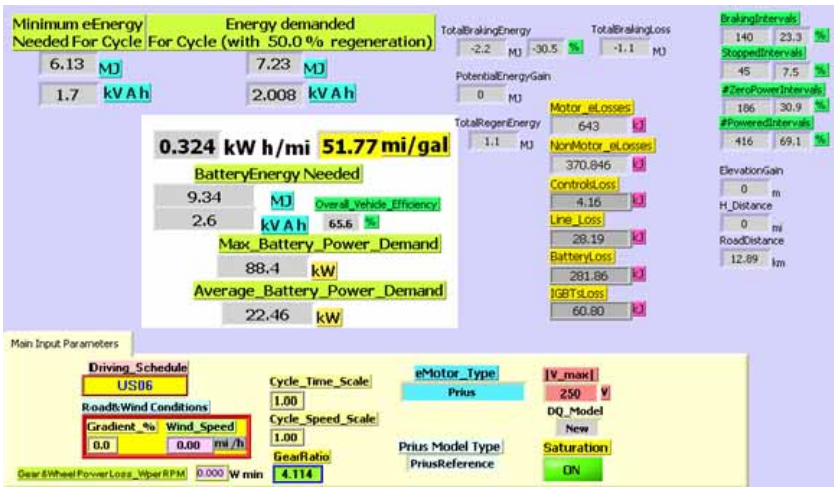

(a) US06 cycle

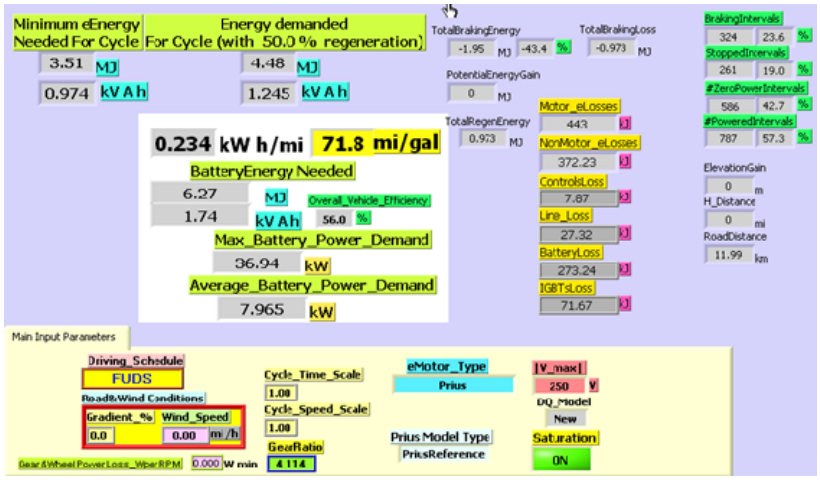

b) FUDS cycle

Fig. 11. Simulation summary of baseline IPM with distributed windings for two driving cycles.

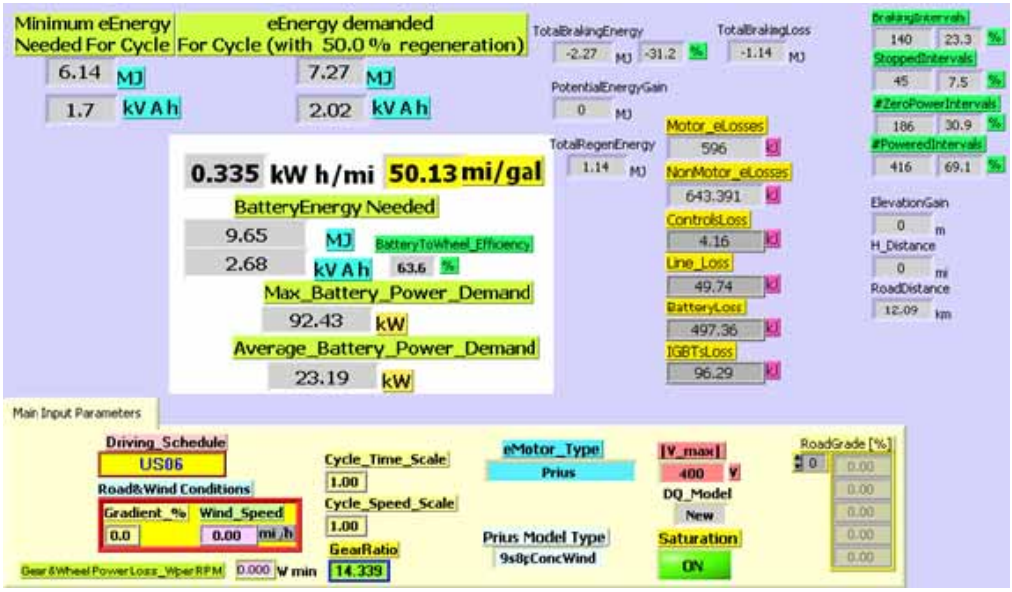

(a) US06 cycle

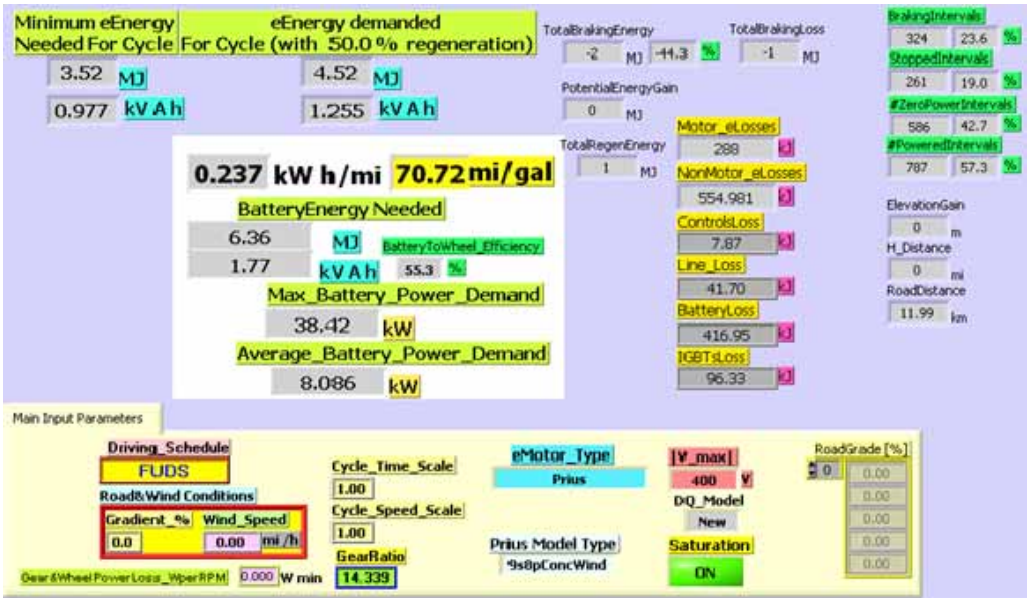

(b) FUDS cycle

Fig. 12. Simulation summary of 9/8 IPM with concentrated windings for two driving cycles.

Table 4. Summary of miles per gallon for baseline IPM with distributed windings and 9-slot, 8-pole IPM with concentrated windings traversing US06 and FUDS cycles

	Baseline 48/8 distributed windings				9/8 concentrated windings			
	US06 cycle		FUDS cycle		US06 cycle		FUDS cycle	
Reducing gear*	% energy deficiency during operation	Miles per gallon	% energy deficiency during operation	Miles per gallon	% energy deficiency during operation	Miles per gallon	% energy deficiency during operation	Miles per gallon
0.5×	2.23		0	61.89				
1×	0	51.77	0	71.80	13.2		5.86	
1.25×	0	51.40	0	72.34				
1.5×	4.7		0	71.93				
2×	29.5		5.6		2.14			61.93
3×					.0815			69.33
3.25×					.0244			
3.5×					0	50.13		70.68
4×					0	49.90		71.24
4.5×					0	49.33		71.19
6×					0	48.53		70.78

* The base gear ratio of the simulation is 4.114, which means that the motor's rotor rotates 4.114 times faster than the vehicles' wheels.

Reference

1. P. J. Otaduy, J. S. Hsu, and D. J. Adams, *Study of the Advantages of Internal Permanent Magnet Drive Motor with Selectable Windings for Hybrid Electric Vehicles*, ORNL/TM-2007/142, Oak Ridge National Laboratory, 2007.

3.4 Amorphous Core Material Evaluation

Principal Investigator: John W. McKeever
Oak Ridge National Laboratory
National Transportation Research Center
2360 Cherahala Boulevard
Knoxville, TN 37932
Voice: 865-946-1316 ; Fax: 865-946-1262; E-mail:mckeeverjw@ornl.gov

DOE Technology Development Manager: Susan A. Rogers
Voice: 202-586-8997; Fax: 202-586-1600; E-mail: Susan.Rogers@ee.doe.gov

ORNL Program Manager: Mitch Olszewski
Voice: 865-946-1350; Fax: 865-946-1262; E-mail: olszewskim@ornl.gov

---

Objectives

- Conduct a four-step evaluation of the potential for soft amorphous or nanocrystalline core materials to improve the efficiency of radial-gap interior permanent magnet (IPM) motors.
  - — Obtain the latest magnetization and loss data from vendors to use in motor simulation.
  - — Obtain cost data from vendors to compare with the cost of standard laminated M-19 core material.
  - — Determine feasibility of manufacturing bulk pieces of amorphous material sufficiently large to fabricate a stator and core for a 55-kW radial-gap IPM motor.
  - — Perform simulations comparing a baseline IPM motor having a standard M-19, 24 gauge 3% silicon steel laminated core with a motor having a core fabricated from 8-in. wide by 0.001-in. thick Metglas® 2605SA1 tape.
  - —

Approach

Task 1. Acquire latest material property data from vendor for motor performance simulations.

- Communications with experts such as Matthew Willard (Naval Research Laboratory) were made to acquire background data on amorphous (non-detectable crystal size) and nanocrystalline (crystal sizes below 0.1 μm) materials. Vendor representatives at Metglas®, Hitachi Metals, and AK Steel provided Metglas and M-19 loss and cost data.
- Magnetec was initially responsive but later became unwilling to communicate further because the company has no development of shredded powder cores and cannot make stacked laminations because of the brittleness of their material, which is advertised as Nanoperm®.
- Light Engineering, Inc., was contacted regarding one of its commercially available axial-gap motors made with Metglas to find out if it could meet the FreedomCAR cost target.

Task 2. Perform motor performance analyses.

- Loss data for Metglas were put in a form compatible with SPEED software for simulations of the performance of a baseline IPM that is similar to a commercially available IPM motor. Cost data for Metglas were obtained for comparison with cost data for M-19 silicon steel.
- Performance simulations of the baseline IPM with a Metglas core were compared with simulations of a baseline IPM with a standard M-19 silicon steel core.

Task 3. Perform cost impact analysis

- Representatives from Metglas and Hitachi discussed the feasibility of applying Powerlite® technology, which Hitachi uses to produce small amounts of material for use in chokes, to produce larger chunks of material for use in stator segments and rotors of radial-gap IPM motors.

Major Accomplishments

- Determined that the study should focus on amorphous Metglas rather than nanocrystalline Nanoperm, which is in reality Finemet. This proved to be a good choice because even though the Metglas flux density saturation was 0.4 T above that of Nanoperm, it was still not sufficiently high to deliver the required power at 2,500 rpm or 6,000 rpm.
- Obtained Metglas 2605SA1 loss data and reduced it to a form that could be used in SPEED software for motor simulations at 167 Hz (2,500 rpm) and 400 Hz (6,000 rpm).
- Determined the material cost of Metglas 2605SA1 is 4.5 times that of M-19 laminated silicon steel.
- Determined there is no known way to produce bulk pieces of Metglas 2605SA1 at reasonable cost for radial gap motor stators and rotors. Commercial axial-gap motors that can meet FreedomCAR targets except for cost are available from Light Engineering.
- Calculated and compared the performance of a baseline IPM with a standard M-19 core and the same motor with a Metglas 2605SA1 core. The comparison showed there is no gain in efficiency at 2,500 rpm or 6,000 rpm at maximum current.
- Detailed examination of the simulations showed the following.
  - The increased magnetic permeability of the Metglas led to a 2.2% increase in flux leaking through the bridge at 2,500 rpm and an increase of 0.4% at 6,000 rpm.
  - The reduced saturation flux density of Metglas (1.56 T) compared with the standard M-19 silicon laminates (2.2 T) prevented the Metglas motor from achieving sufficient flux linkages to deliver the amount of torque and power delivered by the M-19 motor.
  - Because of the lower saturation of the Metglas core, the additional copper losses overshadowed the reduction in eddy current losses leading to reduced efficiency

Future Direction

- Further work in this area is not planned.
- If further work were pursued, two significant areas would require development:
  - A major effort would be necessary to develop a way to produce bulk material from as-made 0.001 Metglas tape, such as weaving on a computerized loom.
  - A major effort would be necessary to develop an IPM that can deliver the required power at the saturation flux density of Metglas.

Technical Discussion

Willard of the Naval Research Laboratory sent a reference to a 1999 document (of which he was a co-author) that summarizes then-recent developments in the synthesis, structural characterization, properties, and technology applications related to amorphous and nanocrystalline soft magnetic materials [1]. ORNLs initial research path was to investigate the nanocrystalline material marketed by Magnetec as Nanoperm. Willard knew of only one commercially available nanocrystalline soft magnetic alloy, which is marketed under the names of Finemet by Hitachi Metals and Vitroperm® by Vacuumschemeltze. Its composition is Fe-Si-B-M-Nb-Cu, whereas the alloy Nanoperm has the composition Fe-Zr-B-Cu [2]. The Magnetec product Nanoperm has a composition like that of Finemet rather than like the alloy composition associated with Nanoperm.

Representatives from Metglas (which was acquired by Hitachi Metals) and from Hitachi Metals were helpful and were willing to discuss related technology by phone as well as email. Hitachi's chief engineer suggested that the nanocrystalline materials about which we were inquiring are unsuited for motor

applications because they are too brittle to handle and their saturation flux density is only 1.2 T. Instead, he recommended an amorphous Fe-based alloy, such as Metglas, which is more ductile and has a saturation flux density of 1.6 T. His recommendation and our comparison of the properties of Finemet and Metglas led to our decision to evaluate the Metglas alloy 2605SA1.

Vendor loss data for Metglas 2506SA1 (from an Electric Motor Education and Research Foundation CD containing the third edition of *Lamination Steels*) were put into a form compatible with SPEED software for a comparative IPM motor performance simulation using a standard M-19 core and a Metglas core. These loss data were submitted to a nonlinear least squares fit using the form of the Steinmetz equation for eddy current loss and hysteresis loss,

$$P_{loss} = C_h f B_{Peak}^{a+bB_{peak}} + C_e f^2 B_{Peak}^2 \quad . \tag{1}$$

The parameters from the fit for loss in W/lb were, $C_h = 0.0010316$, a = 1.4712, b= –0.21237, and $C_e = 1.36585 \times 10^{-6}$. The first three parameters were entered as calculated in the SPEED database for Metglas. The last parameter was entered into the SPEED database as $C_{el} = C_e/(2\pi^2) = 6.919 \times 10^{-8}$ to be compatible with the database form of the eddy losses. The fit provided loss values in W/lb within about 1% at 400 Hz and 6% at1000 Hz. The upper limit for this study was 400 Hz..

The efficiency of a baseline IPM motor with a laminated M-19, 24 gauge silicon steel core was compared with the efficiency when the core was replaced by Metglas 2605SA1. The efficiency curve as a function of line current is shown in Fig. 1. The surprising result—that there was no gain at 2500 rpm until the line current was below 100 A, even though Metglas reduced core losses by a factor of 25—suggested that other properties were impacting the performance. Figure 2 compares the magnetization curves for laminated M-19, 24 gauge silicon steel and for Metglas 2605SA1 on a small scale to emphasize the crossover at 3000 A-turns/m, and compares the 1.56 T saturation of the Metglas with the 2.2 T saturation of M-19. Saturation of the magnetic flux density in the motor with a Metglas core prevented the motor from delivering the power available to the motor with the M-19 core (Fig. 3).

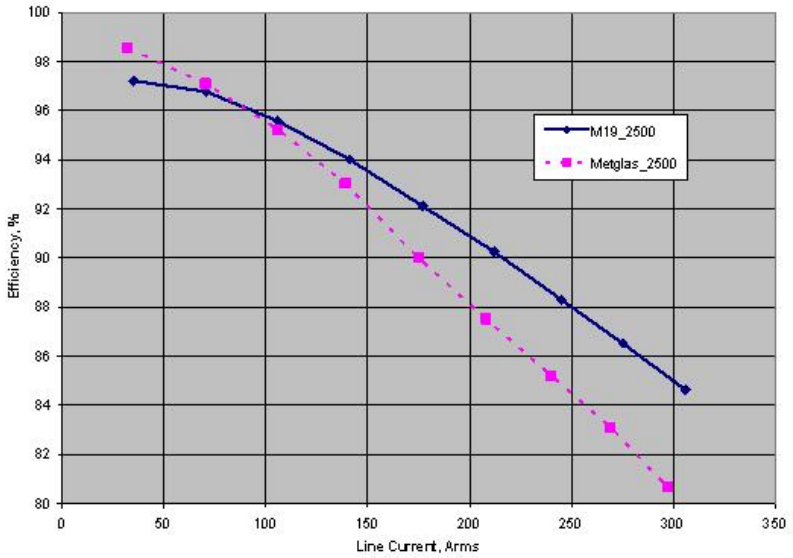

Fig. 1. Efficiency of baseline IPM with M-19 and Metglas 2605SA1 at 2500 RPM.

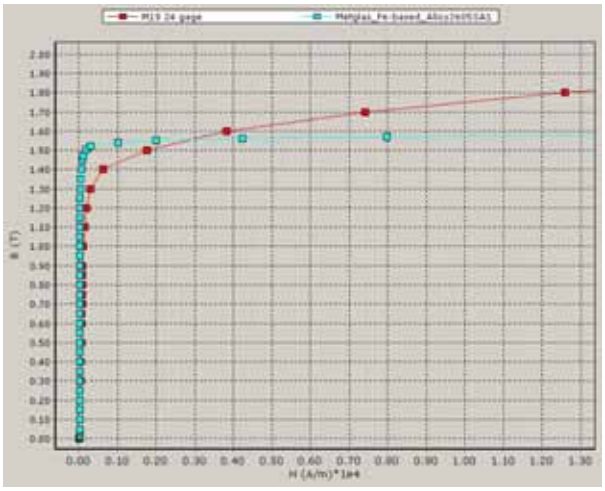

Fig. 2. Magnetization curves of laminated M-19, 24 gauge silicon steel and Metglas 2605SA1.

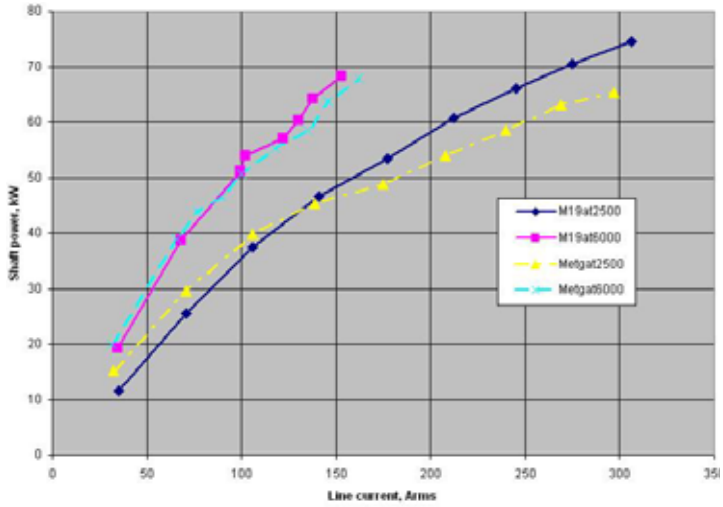

Fig. 3. Shaft power curves of laminated M-19, 24 gauge silicon steel and Metglas 2605SA1.

Increased power delivery from the motor with an M-19 core is enabled by its ability to support more flux linkages. This is illustrated by the more intense orange and red areas for M-19 in Fig. 4a compared with the same regions for Metglas in Fig. 4b. By setting the B(T) scale so that yellow appears at saturation (2.2 T for M-19 and 1.56 T for Metglas), Fig. 5b shows that during operation, the Metglas core is saturated over a much larger region than the M-19 core (Fig 5a). Larger copper losses in the motor with the Metglas core (Fig. 6) were responsible for canceling the benefits of reduced eddy current losses. The increased copper losses were the result of increased field weakening current, Id, which produces no torque but adds to the total current. The increased Id resulted because the saturated saliency ratio for Metglas is below that for M-19 (Fig. 7); and as the direct and quadrature currents, Id and Iq, readjust to produce maximum power, Id must increase more for Metglas to compensate for the reduced saliency ratio. This is shown in Eq. (2).

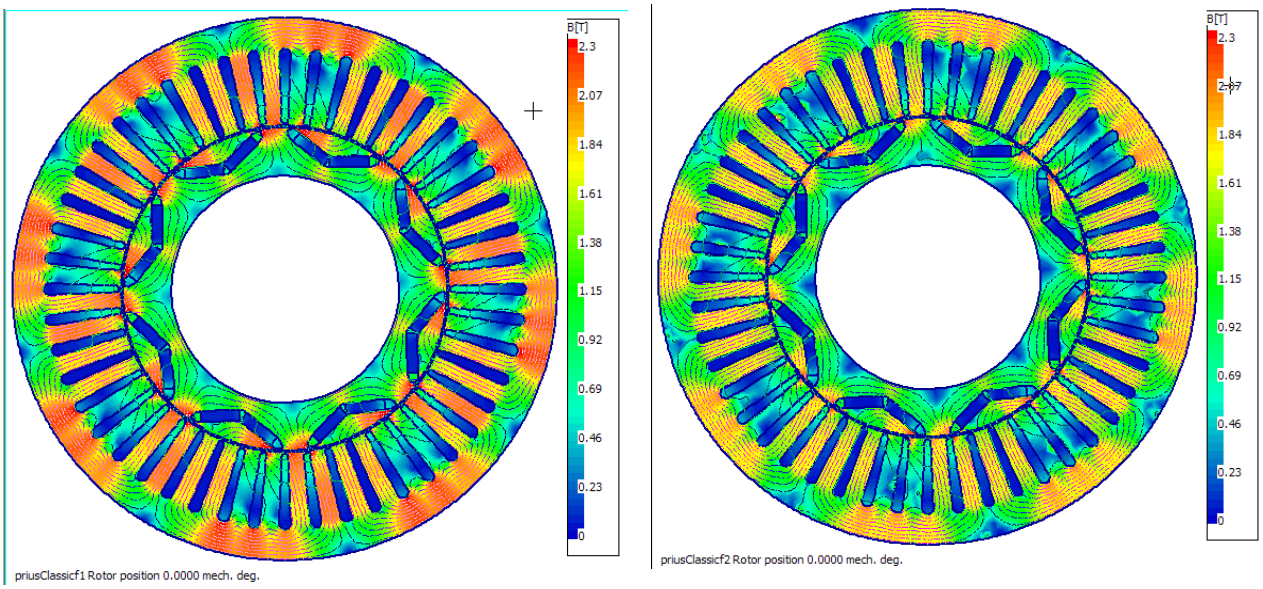

(a) Flux density in laminated M-19, 24 gauge core **(b) Flux density in Metglas 2605SA1 core**

Fig. 4. Increased flux density in M-19 core provides more flux linkages that produce more power in the motor with the M-19 core.

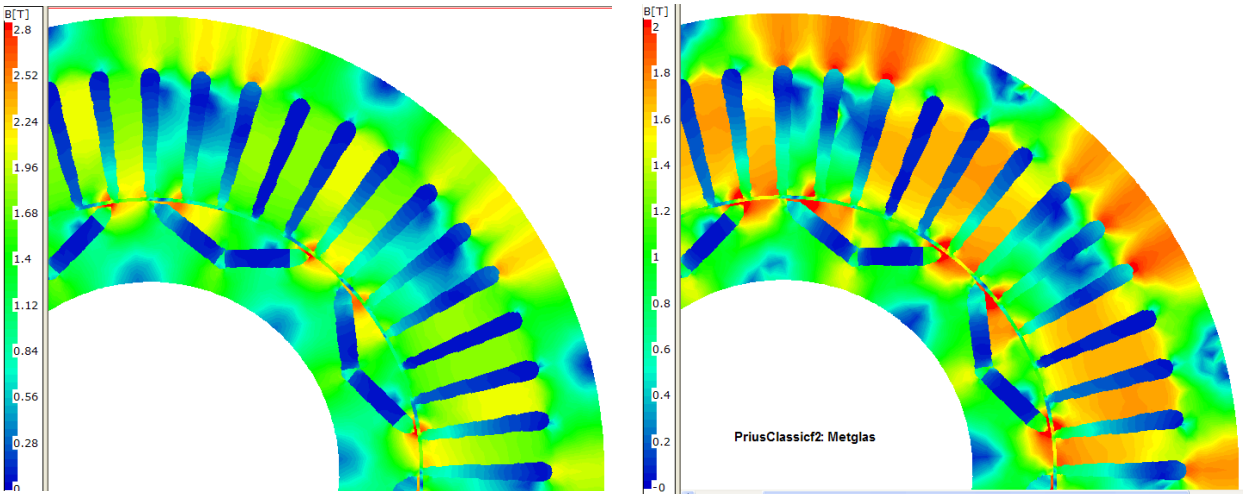

(a) Saturation in laminated M-19, 24 gauge core **(b) Saturation in Metglas 2605SA1 core.**

Fig. 5. Increased saturation in Metglas 2605SA1 core of baseline IPM.

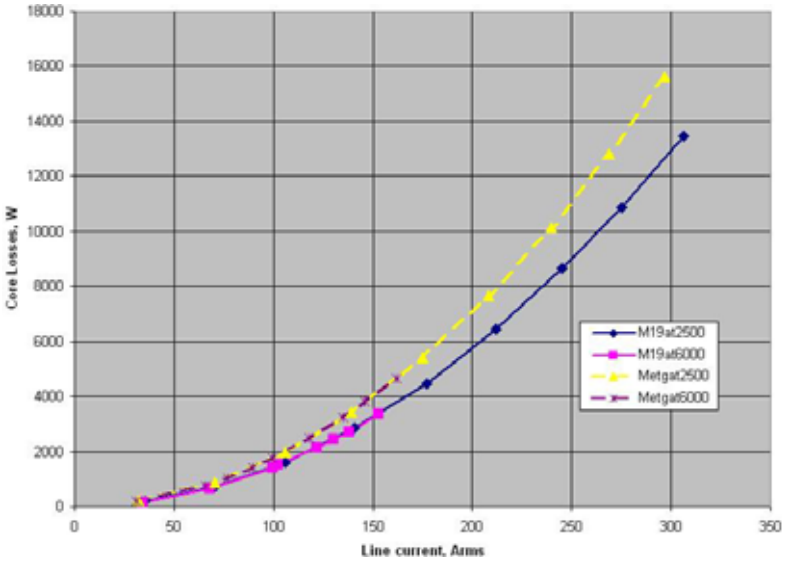

Fig. 6. Increased copper losses in baseline motor with Metglas core.

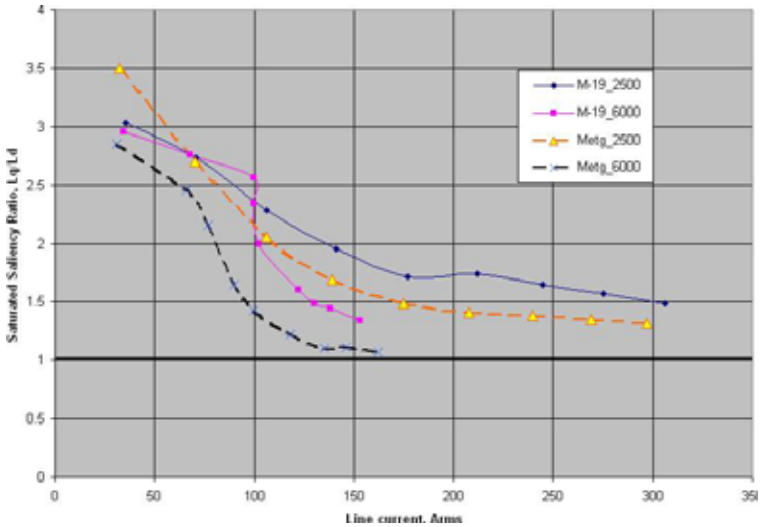

Fig. 7. Reduced saturated saliency ratio for Metglas.

Equation (2) shows the relation between power, saliency ratio, and Id:

$$P = 3p\left[Eq \times Iq - (\rho - 1) \times Xd \times Id \times Iq\right], \qquad (2)$$

where p is the number of pole pairs
Eq is the back-emf, V
Iq is the direct current, which produces torque, A
Id is the direct current, A, which is negative and weakens the magnets' flux density
Xd = $\omega_e L_d$, which is the direct reactance, ohms
Xq = $\omega_e L_q$, which is the quadrature reactance, ohms
ρ is the saliency ratio of the saturated core, which equals Xq/Xd or Lq/Ld

The first term may be considered to be a magnetic power and the second term to be a reluctance power. Inductances are corrected in SPEED's finite element analysis for saturation. Since the Metglas saliency ratio of the inductances falls below the M-19 saliency ratio, the direct current, which is negative, must increase to try to maintain maximum power. This makes the total current larger, thereby increasing the copper losses.

A representative for Metglas in the United States provided three cost estimates for purchases of 50 kg, 100 kg, and 1000 kg quantities. These estimates were $15.75/kg, $12.30/kg, and $9.20/kg respectively. These three points determine the coefficients of an equation to extrapolate the cost of 10,000 lb, or 4536 kg, the quantity for which AK Steel estimated a cost of $0.90/lb ($1.98/kg). The Metglas cost projection equation is

$$\$/kg = 8.85 + 337.58e^{-0.9948*\ln(\text{kg purchased})}, \quad (3)$$

which is $8.93 for 10,000 lb; therefore, material costs for Metglas 2605SA1 are 4.5 times higher than for M-19 laminated silicon steel.

Representatives for Metglas and Hitachi discussed the feasibility of applying Powerlite technology, which Hitachi uses to produce small amounts of material for use in chokes, to produce larger chunks of material for use in stator segments and rotors of radial-gap IPM motors. Their Powerlite production facility on the outskirts of Deli, India, is very labor-intensive because the 0.001 in. thick pieces of tape are layered and bonded; 750 layers must be stacked to produce a ¾ in. thick chunk. There are further problems if the layers have complicated shapes that require punching, because the hard tape has a wearing effect on a punch. A new tool is required for about every 1000 punches, further increasing the production costs. There is now no known way to produce Metglas for use in a radial-gap motor at a reasonable cost. Metglas's challenge was to design a radial-gap motor that can use the tape as produced.

A design for such an axial-gap motor produced by wrapping the tape to form an axial core was proposed by Lipo et al. in 1990 [3]. A Hitachi representative referred us to Light Engineering, which developed a line of axial-gap motors of this type. It markets the M3202L2 SmartTorq Axial-gap PM motor, which can deliver torque and power that meet FreedomCAR targets. Upon request, Light Engineering provided a nonbinding cost estimate of about $6743, excluding cabling, for this motor with its inverter drive in lots of 100,000. The company also sent an efficiency map. It appeared that the motor's efficiencies were insufficient to warrant the additional cost, but further simulations and lab measurements would be necessary if FreedomCAR interest in axial-gap PMs were rekindled.

Conclusion

Because of the problems associated with obtaining bulk Metglas and the high material costs, there is low probability that a radial-gap motor could be built to meet the FreedomCAR cost target. The low saturation flux density of Metglas prevented the baseline motor from achieving improved efficiency, showing the importance of considering the motor design when using amorphous core material.

References

1. Michael E. McHenry, Matthew A. Willard, and David E. Laughlin, "Amorphous and nanocrystalline materials for applications as soft magnets," *Progress in Materials Science* **44,** 291–433 (1999).
2. M. A. Willard et al, "Structure and magnetic properties of $(Fe_{0.5}Co_{0.5})_{88}Zr_7B_4Cu_1$ nanocrystalline alloys," *Journal of Applied Physics* **84**(12) (December 15, 1998).
3. T. A. Lippo, C. C. Jensen, and F. Profumo, *A Low Loss Permanent Magnet Brushless DC Motor Utilizing Tape Wound Amorphous Iron,* WEMPEC Research Report 90-18, July 1990.

3.5 Development of Improved Powder for Bonded Permanent Magnets

Principal Investigator: Iver E. Anderson
Materials and Engineering Physics Program
Ames Laboratory, Iowa State University
Ames, IA 50011
Voice: 515- 294-9791; Fax: (515) 294-8727; E-mail: andersoni@ameslab.gov

DOE Technology Development Manager: Susan A. Rogers
Voice: 202-586-8997; Fax: 202-586-1600; E-mail: Susan.Rogers@ee.doe.gov

ORNL Program Manager: Mitch Olszewski
Voice: 865-946-1350; Fax: 865-946-1262; E-mail: olszewskim@ornl.gov

---

Objectives

- Increase the maximum operating temperature from about 125 to 200C and environmental stability of permanent magnet (PM) materials to enable high volume manufacturing of advanced electric drive motors with improved operating characteristics and lifetime.
- Reduce the overall manufacturing cost of traction motors and enable a new generation of machine designs by developing magnets that can be molded efficiently into net-shapes or in-place as motor component assemblies with high magnetic energy density to conserve valuable materials.

Approach

- Develop enhanced control of nucleation and growth of nano-crystalline structure in fine spherical magnet alloy powders to reduce processing cost and minimize annealing requirements.
- Attempt development of anisotropic (aligned cellular or single crystal) magnetic microstructures in particulate of MRE-Fe-B alloys to make large gains in bonded magnet properties.
- Pursue improved protective coating process for flake particulate and fine spherical gas atomized powders of MRE-Fe-B magnet alloys to simplify processing and increase bonded magnet durability.
- Explore prospects for anisotropic sintered permanent magnets from the MRE-Fe-B alloys using extrinsic additives for consolidation of aligned high strength (full density) magnets for high temperatures.
- Conduct detailed analysis of total manufacturing cost for advanced drive motors with both sintered and bonded permanent magnets to provide validation of current magnet development directions.

Major Accomplishments

- Contracted an industry expert to conduct an independent analysis of the total manufacturing cost for an advanced electric drive motor with either sintered or bonded permanent magnets in appropriately designed interior PM rotor electric machines.
- Received report from industry expert on contracted study and placed into Ames Laboratory report system to permit broad dissemination.
- Participated in assembling a proposal entitled "Integrated Traction Drive System" to form a CRADA partnership with General Motors and Arnold Magnetic Technologies that successfully competed in a recent RFP issued by the PEEM office and may provide an industrial test of the isotropic (nano-crystalline) bonded magnet technology that was developed in this project for such IPM motors.
- Demonstrated successful oxidation resistance at 300C for flake particulate (WT-096) from fluorination process that was adapted to fully scalable rotating kiln coating system.

- Compression molded a full set of bonded magnet samples from coated magnet flake particulate (MQP-11HTP) from an enhanced Ames magnet alloy design (WT-096) and completed the second stage of industrial environmental testing.
- Discovered WT184 alloy for isotropic nano-crystalline bonded magnets that has 5.3 at% Y (Y:Dy of 6:1) and superior $(BH)_{max}$ above 75C, compared to the commercial MPQ-14-12, resulting from an unexplained peak in magnetic properties. This new alloy for melt spun flake particulate exhibits excellent properties at both ambient temperature and 200C with an unexpectedly small content of expensive Dy.
- Demonstrated further improvement in the room temperature and high temperature maximum magnetic energy product in fine spherical powder of the MRE-(Fe,Co)-B-ZrC magnet alloy with in situ coating, where it was determined that the temperature coefficients of M_r and H_c are 0.084 and 0.4%/°C in the temperature range of 27 to 100°C, respectively, with $(BH)_{max}$ at room temperature and 200°C of 10.1 and 5.6 MGOe, respectively.
- Performed initial experiments that showed progress on processing of anisotropic micro-crystalline sintered magnets from high temperature alloy that was processed by chill casting and mechanical comminution. Initial success was also achieved on processing of anisotropic nano-crystalline bonded magnets from high temperature magnet alloy by melt spinning with reduced wheel speed.

Future Directions

- To radically increase the energy product of polymer-bonded magnets without sacrificing high temperature performance or net-shape molding, development of an anisotropic, nano-crystalline magnetic microstructure will be explored extensively in particulate of MRE-Fe-B alloys. This task will involve hybrid rapid solidification processes derived from melt spinning and gas atomization and innovative post-solidification treatments. To accommodate decreased funding and scope, the initial trials for producing anisotropic highly loaded polymer bonded magnets will be delayed.
- To enable the maximum energy product to be realized in high temperature MRE-Fe-B alloys, development of sintered (full density) aligned permanent magnets will be pursued in depth. This task will involve further magnet alloy design and processing of micron-sized (single crystal) particulate, along with further magnet consolidation experiments and development of an extrinsic alloy for liquid phase sintering of the aligned magnetic particle assembly.
- To enhance the protective coating capability of the in situ fluorination process for fine spherical magnetic particles, the atomization chamber sensor system will be upgraded and the post-anneal fluidized bed coating process must be fully developed in the rotating kiln vessel for flake and spherical particulate. This task will use the fully developed MRE-Fe-B alloy for gas atomized powders and will involve gas atomization, melt spinning, annealing, and rotating kiln experiments.
- To further explore the application of in-situ protective coating, the mechanical milling process chamber also will be fitted with fluorination capability to attempt coating of the micro-crystalline MRE-Fe-B alloys during comminution to improve their durability and processing characteristics.
- For continued melt spun alloy improvement, additional reduction in the cost of the magnet alloy components will also be pursued, e.g., by substitution of less expensive RE (i.e., Y for Dy, La for Y, etc.) and by minimizing the Co content, while maintaining acceptable energy product and temperature coefficients.

Technical Discussion

Executive Summary

The efficient use of energy for personal transportation is of prime concern for the Department of Energy. In addition, the Clean Air Act requires the implementation of the best available technology to reduce automotive emissions while promoting efficient use of non-renewable liquid transportation fuels. The

work outlined here is aimed at the rapid introduction of internal combustion/electric hybrids, plug-in hybrids, and full electric vehicles through improvements in the efficiency and durability of electric drive systems, which will also be employed by future fuel cell powered vehicles with electric drive. By this means, the use of non-renewable liquid transportation fuels will be greatly diminished or, eventually, completely eliminated.

To meet performance and cost goals for advanced electric drive motors, it is essential to improve the alloy design and processing of permanent magnet (PM) powders. This project is expected to develop the materials and processes needed to fabricate high performance, bonded permanent magnets (PM) that can be used for traction motors with an internal PM rotor design. It should be noted that the starting alloy cost will be about the same as current alloys, but the total magnet material used per motor could be less, if motor design is optimized for the precise arc shapes, full rotor length, and curved magnetization patterns that are possible with bonded magnets. The fully developed PM material must be suitable for elevated temperature (180-200˚C) operation to minimize motor cooling needs, where increased high temperature magnetic performance is a critical advantage over current commercial magnetic material. Such a magnetic alloy design for high temperature operation may be implemented at a first level of advantage with nano-crystalline isotropic flake particulate using conventional isotropic bonded magnet processing methods and a high temperature polymer. A second level of advantage may be realized if this high temperature magnet alloy flake particulate is protected with an oxidation resistant surface coating by a batch process that is being developed in this project. A third level of advantage may be realized for isotropic bonded magnets, if the high temperature magnet alloy can be translated successfully to a fine spherical isotropic powder production process based on inert gas atomization with capability for in situ protective powder coating. This third level of manufacturing advantage is derived from reduced molding pressures and enhanced performance and reliability for isotropic bonded magnets, through increased magnetic powder loading and reduced irreversible magnetic losses from oxidation and corrosion.

A fourth (much higher) level of advantage may be achieved if nano-crystalline anisotropic fine particulate can be produced so that a bonded magnet (insert) molding process can be accompanied by the application of an external magnetization field sufficient for full alignment (and locking) of the particulate in the desired field pattern within the complex cavities of an advanced rotor. This fourth level of advantage comes from the possible 4X multiplication of the magnetic torque available from such anisotropic bonded magnets with a shaped field direction, compared to isotropic bonded magnets of the same loading. The project will be transitioning beyond the third level of advantage in the new plan, with the implication that a significant reduction in the total manufacturing cost of PM traction motors is likely. An expert was engaged in a study to test this prediction and to develop other specific findings about the directions of our project plan. In one of the most recent innovative directions, sintered aligned permanent magnets also are being pursued with micron-sized single crystal particles of the high temperature magnet alloy and an extrinsic alloy phase for liquid phase sintering. These advantages should all accelerate the widespread introduction of fuel-saving hybrids and could be claimed by the AEEPM program as a clear beneficial outcome.

Introduction

Permanent magnets based on $RE_2Fe_{14}B$ intermetallic compounds, with $Nd_2Fe_{14}B$ as a prototype, have had a large technological impact because of their unsurpassed (theoretical) magnetic energy density. Over the past 30 years, extensive research has been performed to develop and improve the technological properties of these magnetic compounds. Commercially, two classes, aligned-sintered (microcrystalline) and isotropic nano-crystalline, $Nd_2Fe_{14}B$ magnets have been successfully developed. It should be noted that aligned-sintered $Nd_2Fe_{14}B$ magnets are used in current hybrid vehicle systems with interior PM motor designs that require high magnetic torque, but this magnet class and magnetic torque-dominated motor design have been judged (by at least one of the OEM partners) to be impractical for very large scale mass production at reduced cost. Alternatively, the opportunity exists to use a new motor designs that utilize

increased reluctance torque, and, as such, are well suited to the reduced magnetic flux available from bonded magnets. Because there is some uncertainty about the total manufacturing cost advantage for the new type of drive motor system from this revolutionary shift in magnet type and motor design, a cost analysis of this situation by an "industry expert" was commissioned by this project and was completed recently.

Based on knowledge of the magnetic behavior of the 2-14-1 compound, it is likely that the ability to produce a fine particulate, where each particle is a highly aligned cellular (nano-crystalline) structure or a single crystal (microcrystalline) 2-14-1 phase, can result in a very large gain (about 4X) in magnetic properties (fourth level of advantage). This is possible if an ensemble of particulate can be aligned and locked in a polymer matrix to form a bonded magnet or can be aligned and secured in a partially fused (extrinsic) inter-particle phase to form a fully dense sintered magnet. Both types of aligned or anisotropic magnets will be formulated from the high temperature magnet alloy base that was developed in this project to retain the ability to operate at temperatures up to 200C. The large gains in magnetic strength come from the change in project focus from isotropic magnets with isotropically oriented magnetic domains to anisotropic magnets with uni-directional (fully or partially aligned) magnetic domains. It should also be noted that the nano-crystalline anisotropic magnets also benefit from multiple domain coupling (across cell boundaries) to increase their coercivity. However, the micro-crystalline anisotropic magnets must have each single crystal/single domain particle separated by a non-magnetic phase with each particle surrounded by a smooth grain boundary to permit maximum magnetic strength.

Approach

Surface passivation methods for enhanced oxidation resistance of MRE-Fe-B isotropic magnet alloy particulate continued in development by further improvement of the in situ method during the gas atomization process and by completing fabrication and testing of up-scaled fluidized-bed batch processing for both spherical powder and flake particulate. A fluorination (gas reaction) process was developed for in situ treatment during the high-pressure gas atomization process to reduce the hazard and oxidation losses that are typical for powders with high surface area of this type of RE alloy. This process built on the results of our post-atomization fluidized bed coating experiments and used the atomization spray chamber as a reaction vessel with the dispersed, high temperature particulate spray as a natural fluidized (turbulent) state. The reaction was stimulated by the downstream addition of an NF^3-Ar gas mixture during He (and later Ar) atomization, where the downstream location was determined by process chamber temperature analysis and by consideration of the spray chamber flow patterns and dynamic thermal conditions. The powder surface film effects were investigated by bulk oxygen measurements on the powder, by air oxidation tests in a thermo-gravimetric analyzer (TGA), and by explosivity testing at an independent laboratory. Since the current hazard reduction measurement (to a "moderate" explosivity level) was confirmed, both the larger scale and research scale atomization systems can be employed to produce prototype spherical powder batches for experimental injection molding trials. Resulting surface film structure and composition also was characterized by x-ray photoelectron spectroscopy (XPS), by Auger electron spectroscopy, and by microstructural analysis for both spherical powder and flake particulate.

Efficient screening of magnet alloy design modifications was accomplished by melt spinning methods, primarily using parameters that simulate the quenching rates accessible during gas atomization, the desired spherical powder processing method. The alloy approach for MRE-Fe-B magnetic alloys (MRE = mixed rare earth, e.g., Y, Dy, Nd) was refined to increase the remanence and energy product at ambient temperatures for isotropic PM material while maintaining superior temperature coefficient values to 200˚C. The magnetic properties of commercial spherical atomized powder and isotropic flake particulate were benchmarks. For gas atomized spherical powders the design target favored direct solidification to a nano-crystalline 2-14-1 phase, without annealing. An alloy additive of ZrC+Zr was developed to enhance the crystallization potency for 2-14-1 phase and was gas atomized successfully during this year.

Comprehensive characterization of closely related gas-atomized and melt-spun samples of a variety of promising MRE-Fe-B compositions continued as a strong emphasis in both as-solidified and annealed states. The initial magnetic characterization at both ambient and elevated temperatures was accompanied by x-ray diffraction and calorimetric characterization on all new samples. In addition, microstructural analysis with SEM and TEM added critical understanding about the product phase morphologies and spatial distributions that give rise to differences in as-solidified properties and in annealing response. Our overall goal remained exploration of the generality of MRE-Fe-B alloy rapid solidification behavior during gas atomization that minimizes glass formation and allows annealing to be avoided, because of the potential processing simplification advantage that could lead to reduced costs for bonded magnet production.

Industrial partnerships were continued to compare experimental bonded magnets against equivalent commercial magnets in extended motor trials at elevated temperatures. This was aided by formation of a CRADA partnership for this type of work with support from EERE. Our existing resources and network of contacts also were utilized to contract with a qualified outside expert with significant experience and expertise both in electric motor design and testing and in permanent magnet (PM) manufacturing for a detailed cost analysis of the choice between bonded and sintered magnets for interior permanent magnet motors. The critical criteria for these recommendations was a comparison to robust industrial manufacturing processes using both existing commercial magnets and the expected performance of experimental magnet material in conventional and experimental motor designs to characterize expected performance and temperature tolerance, measuring progress against accepted APEEM goals.

Results

System Cost Analysis for an Interior Permanent Magnet Motor

A major milestone for this year was the completion of a consultant's report, "System Cost Analysis for an Interior Permanent Magnet Motor" from an independent expert, Peter Campbell. Dr. Campbell was Vice President of Technology and Sales for Magnequench, Inc., the dominant global producer of rare earth-iron-boron powder for high energy bonded permanent magnets from 1999 until December of 2005. He was a consultant in electrical machines for 18 years prior to that and was a faculty member at USC where he specialized in electrical machines. Dr. Campbell was contracted to provide an assessment of the cost structure for an *interior permanent magnet* ("IPM") motor, which is designed to meet the 2010 FreedomCAR specification. The report evaluated the range of viable permanent magnet materials for an IPM motor. The report considered existing permanent magnet materials and the effects of possible future developments in this area. Motor costs were estimated for an annual production run of 200,000 units. The analysis considered key processing steps and evaluated alternative magnet shapes. Costs associated with magnetic raw materials, processing and manufacturing assembly methods were estimated. Mechanical stresses and thermal requirements were considered in the evaluation. The report found that there are two viable alternatives for IPM motors, which meet the FreedomCar goals. Both of these involve anisotropic magnets. The first uses conventional anisotropic sintered magnets while the second uses anisotropic bonded magnets. The bonded magnet evaluation was made using the only anisotropic powder currently commercially available. The report concluded that, with existing materials, the anisotropic bonded material enjoys a small price advantage. However, the successful development of an anisotropic magnet powder with the properties expected from the Ames composition would result in very significant improvements over the properties using existing anisotropic powder. The full report is included in the appendix. It also is available on the Ames Laboratory web site and on a U.S. Government sponsored website from the Office of Scientific and Technical Information (OSTI) (http://www.osti.gov/bridge/product.biblio.jsp?query_id=0&page=0&osti_id=940187).

Surface passivation

The development of a rotating kiln surface passivation apparatus, which represents a fully scalable process suitable for industrial applications, has been completed and tests to determine the optimum operation have been performed. The rotating kiln uses the same gas handling system as the fluidized bed system so that all of the systems modifications previously developed for minimizing oxygen content could be utilized in the larger apparatus. This apparatus allows the passivation of 100-200 g batches of flake material. This capability also allowed us to make test runs for an industrial requester interested in evaluating the process for possible commercial applications through the Materials Preparation Center (MPC) of Ames Laboratory.

Following repair of the RGA portion of the fluidized bed coating apparatus that became inoperable at mid-year of FY2007, the previous magnetically stirred reaction chamber was used to generate additional fluorinated flake samples of the MQP-11HTP particulate, made from the WT096 alloy by Magnequench. The new fluorinated flake samples were loaded to 60 vol.% in PPS polymer and compression molded into the remaining 6 samples that were needed by AMT for the second stage of industrial environmental testing. Compression molding utilized the same heated die sets that were used in FY2007. The results of the second stage STILT (short term irreversible loss testing) evaluation by AMT revealed that the bonded magnets made from fluorinated (-11HTP) flake essentially duplicated the mild decrease in flux of the control sample made from MQP-14-12 flake for increased exposure temperature. However, at the completion of the STILT measurements at 200C, the re-magnetized sample gained back essentially all of the original flux, an excellent result.

Alloy development, cost optimization.

An alloy termed WT147, ($\{[Nd_{0.45}(Y_2Dy_1)_{1/3*0.55}]_{2/17.3}Zr_{0.3/17.3}Co_{1.0/17.3}Fe_{13/17.3}B_{1/17.3}\}_{1-2x}+Zr_xC_x$, x=0.01), with Zr substitution and ZrC addition exhibited very good magnetic properties as melt spun ribbons and as gas atomized powder in previous work. However, the magnet alloys that are the eventual output of this project are to be used in cost sensitive applications and raw materials costs are an important factor in the magnet optimization. Thus, a continuing focus of the project has been on alloy component cost reduction. In alloy WT147, Co and Dy are the primary components impacting the material cost, although recent cost increases in Nd have raised concern. In 2-14-1 magnets, Co additions enhance the Curie temperature and reduce the temperature dependence of the remnant magnetization, although Co tends to reduce the coercivity. Additions of Dy increase the magneto-crystalline anisotropy, which increases the coercivity and decreases the temperature dependence of the coercivity. However, Dy decreases the remnant magnetization. Previously, we worked on minimizing the Co content, reducing by 1/3 the amount required. This year, we focused on the effect of the Y:Dy ratio on magnetic properties at room temperature. The Y addition is considerably less expensive than Dy and somewhat less expensive than Nd, so significant cost reductions are possible with an increased Y:Dy ratio. However, elemental Y does not have a magnetic moment and does not contribute directly to the anisotropy of a 2-14-1 compound, which may result in degradation of the coercivity.

The alloys studied were based on WT147 that has both Zr substitution for Fe and ZrC additions as a grain size stabilizer, i.e., ($\{[Nd_{0.45}(Y_yDy_z)_{1/3*0.55}]_{2/17.3}Zr_{0.3/17.3}Co_{1.0/17.3}Fe_{13/17.3}B_{1/17.3}\}_{1-2x}+Zr_xC_x$, x=0.01), where the Y:Dy ratio (y/z in the base alloy formula) was investigated at levels of 1:1, 2:1, 3:1, 4:1, 5:1, 6:1 and no Dy. In these trials, the atomic percentage of Y was 3.1, 4.2, 4.6, 5, 5.2, 5.3, and 6.2, respectively. Ingots of the alloys were arc melted and chill cast. The castings were melt spun at a wheel speed of 25 m/s. The as-spun ribbons were annealed at 750C for 15 minutes. When increasing Y from 3.1 to 6.2 at.%, the remanence was increased from 6.7 to 7.5 kGs and the coercivity was decreased from 15 to 6 kOe. The maximum energy product, $(BH)_{max}$, was increased from 10 MGOe at 3.1Y(at.%) to 12.7 MGOe at 5.3Y, and to the maximum of 13.6 MGOe at 5.5Y, before decreasing to about 12.9 MGOe at 6.2Y.

The hysteresis loops, of the three highest Y alloys exhibited good "squareness" of the demagnetization curve, similar to the WT147 results.

It also was a concern that increasing the Y:Dy ratio may result in a change of high temperature stability for the resulting alloys. The experimental results revealed that for increasing Y content, the temperature coefficient of M_r monotonically decreases, while the temperature coefficient of H_c first increases and then tends to decrease. Compared to the magnetic properties for the other alloys studied, it was found that WT184 with 5.3Y (Y:Dy=6:1) exhibits the best compromise of low temperature coefficients for both coercivity and remanence, predicting the best magnetic properties at high temperature.

As an overall "figure of merit" comparison, the $(BH)_{max}$ was measured for samples with different Y content as a function of temperature and compared to Magnequench MQP-14-12, the best commercial particulate for high temperature bonded isotropic magnets. In general, the $(BH)_{max}$ at room temperature is increased with increasing Y content, but $(BH)_{max}$ decreases more rapidly with rising temperature for increased Y. Fortunately, the temperature dependent behavior of $(BH)_{max}$ for WT184 (5.3 at.%Y) is anomalous. Although as yet unexplained, a sharp peak in $(BH)_{max}$ with Y content was observed for 5.3Y at 200C and it is near the top of a broader peak in $(BH)_{max}$ for ambient temperature. Therefore, we have discovered that WT184 is a "sweet spot" alloy with 93% of the energy product of MQP-14-12 at ambient, but clearly superior to this benchmark for any temperature above about 75C. Furthermore, WT184 has equivalent $(BH)_{max}$ to WT147 (previous best) at 200C, but contains 58% less of the costly Dy.

Using alloy WT184 as a new base, a reinvestigation of the effect of Co on magnetic properties also was studied. Since the role of Co is to enhance the high temperature performance of the magnets, the hysteresis loops of the annealed ribbons were measured from room temperature to 275°C using our high temperature vibrating sample magnetometer (VSM). The resulting $(BH)_{max}$ values with varying Co content as a function of temperature were compared to the $(BH)_{max}$ of the commercial magnet alloy flake, MQP-14-12. While room temperature performance of all the alloys is largely independent of Co content (with the exception of WT184), the $(BH)_{max}$ vs. T curves exhibited increasing slopes with decreasing Co content. In other words, at high temperature the reduction of $(BH)_{max}$ is accelerated with decreasing Co content, where the high temperature magnetic energy product is influenced directly by the decrease of T_c that results from diminished Co, In fact, the high temperature portion of the $(BH)_{max}$ curve of the Co-free alloy overlaps that of the commercial MQP-14-12. With the exception of the alloy without any Co, all of the alloys still exceed the performance of MQP-14-12 above about 125C.

Influenced by previous work on MQP-14-12 alloy for high temperatures, the effect was studied of a Nb substitution for Fe on the magnetic properties of the WT196 sample without Co. A small amount of Nb was substituted for Fe according to the formula: $(\{[Nd_{0.45}(Y_6Dy_1)_{1/7*0.55}]_2Zr_{0.3}Nb_xFe_{14-x}B_1\}_{0.98}+Zr_{0.01}C_{0.01})$, where x=0.05, 0.1 and 0.2. Unfortunately, it was seen that a minor substitution of Nb for Fe doesn't cause significant changes in room temperature magnetic properties. With increasing Nb content, the coercivity of samples slightly increases at the cost of a slightly higher temperature coefficient of M_r. In general, the studies on Nb substitutions and NbC additions show that the substitution of Nb for Fe in the alloys with Zr+ZrC doesn't significantly improve the magnetic properties, especially at higher temperatures

Gas Atomization

The development of spherical powders produced by high-pressure gas atomization focused on optimizing the isotropic magnetic properties and minimizing processing costs. As part of processing cost reduction, replacing He with Ar as the atomizing gas was investigated, since the cost of Ar is at least 3X lower than He, with the most recent trend for even higher He gas cost. The alloy studied was based on the WT147 with composition $(\{[Nd_{0.45}(Y_2Dy_1)_{1/3*0.55}]_{2/17.3}Zr_{0.3/17.3}Co_{1.0/17.3}Fe_{13/17.3}B_{1/17.3}\}_{1-2x}+Zr_xC_x$, x=0.01). Several atomization runs based on this composition were performed. The GA-1-114 batch was produced using Ar

gas and the size distribution of the atomized powders was determined by automated laser light scattering (Microtrac). Sieving and air classification was used to divide the yield into size fractions. The largest fraction of powder was in the highly desirable 20-25 μm range. This was confirmed by loose powder SEM analysis. The SEM micrographs revealed very spherical powders in the smaller size fractions, below about 32μm. At larger size cuts, more satellites were present and a large number of hollow particles were viewed. However, the majority of the particles appeared to be solid spheres of the appropriate size.

Magnetization was measured initially as a function of temperature (M vs. T) for as-atomized and for annealed powder with a particle size less than 20μm. Careful analysis revealed the existence of two ferromagnetic ordering transformations around 280 and 400C for as-atomized powder. These two transformations coincide with the Curie transformations of the 2:17 and 2:14:1 phases, respectively. After annealing at 700C for 15 min., the M vs. T curve exhibited only the 2:14:1 phase transition at 410°C, confirming that the phase composition had evolved from a majority 2:14:1 plus a small amount of 2:17 phases to a single 2:14:1 phase during the annealing process. From initial hysteresis measurements on as-atomized 20-25μm powder, the demagnetization curve exhibited a feature consistent with an amorphous phase (or magnetically soft phase), which verifies the results revealed by the M vs. T and subsequent DTA studies. Annealing at 700C for 15 min. resulted in a smoother demagnetization curve and increased squareness in the shape of the hysteresis loop, a clear indication of full crystallization and transformation to a single phase 2:14:1 structure from the 2:14:1 and 2:17 phase mixture. Further analysis of the detailed results of SEM and TEM microstructure observations and those of XRD and DTA measurements on size fractioned (5μm increments) powders in as-atomized and annealed conditions revealed in more detail that partial substitutions of Zr and the ZrC additions promoted the formation of a uniform and fine nano-crystalline microstructure with enhanced magnetic properties after annealing.

Extensive magnetic property measurements on all of the powder size fractions demonstrated that these microstructure and phase structure changes on annealing are critical to the final magnetic properties of the powder. First, it appeared that the sub-5μm powder, having greater surface area, was more readily oxidized during annealing, resulting in degraded magnetic properties. Next, the $(BH)_{max}$ increased with increasing powder size from 9.1MGOe for 5-10μm, reached the peak value of 9.8MGOe at the size range of 15-20μm and decreased gradually with larger powder size to about 32μm. Thus, these specific size classified powders exhibited 9MGOe or better from 5-32μm after annealing. With particle screen size fractions greater than 32μm, a coarser crystalline microstructure was observed in annealed powders that reduced the magnetic properties by weakening reversal field strength (coercivity). The highest energy product of 10.1MGOe was observed for a less specific particle size range of sub-20μm. The temperature dependence of the magnetic strength of the annealed sub-20μm powder was also measured, revealing temperature coefficients of M_r and H_c are 0.084 and 0.4%/°C, respectively, in the temperature range of 27 to 127C, with an energy product of 5.6MGOe at 200C. For this sub-20μm powder, the $(BH)_{max}$ is 92% of the best commercial spherical powder, MQP-S-11-9, at room temperature and superior to this baseline powder for all temperatures above 75C.

Anisotropic Alloy Development

As noted in the consultant's report (see appendix), isotropic bonded magnets are limited in their remanence and magnetic energy product. It is therefore highly desirable to develop anisotropic magnets, both bonded and sintered, with good high temperature performance. In order to build on the properties of the isotropic rapidly solidified (nano-crystalline) YDy-based $MRE_2(Fe, Co)_{14}B$ (MRE=Nd+Y+Dy) ribbons and powders which have been produced by melt spinning (MS) and gas atomization (GA) techniques, respectively, we have begun investigating the production of anisotropic magnets based on these compositions. We are employing a two-stage approach to anisotropic magnets. First, we are pursuing the most direct approach to anisotropic sintered (micro-crystalline) magnets through crushing

and sintering. Then we will attack the more difficult task of producing anisotropic nano-crystalline powders for bonded magnets.

Part A. Anisotropic sintered magnets

1. Alloy design for sintered micro-crystalline magnets

There are several techniques to make anisotropic magnets. For sintered micro-crystalline magnets, densification is realized by liquid phase sintering (LPS) techniques. Traditional $Nd_2Fe_{14}B$ magnets are consolidated by means of LPS because there exists a low-melting Nd-rich phase in addition to $Nd_2Fe_{14}B$ and $Nd_{1+\mu}Fe_4B_4$ phases. In other words, they form a ternary eutectic that makes liquid phase sintering possible, enabling rapid (essentially complete) densification without significant grain growth. In addition, the Nd-rich phase is non-magnetic to decouple domain reversal between adjacent grains that also are single crystal particles. It locates at grain boundaries and isolates the $Nd_2Fe_{14}B$ grains (typically 1-3μm dia.), forming a discrete magnetic structure with high coercivity. While the $MRE_2Fe_{14}B$ magnet alloy system under study (dominated by "heavy" rare earth elements like Y and Dy, not the "light" rare earths like Nd and Pr) has enhanced high temperature magnetic properties, these improved magnet alloys unfortunately have a different phase diagram that has no such Nd-rich liquid phase at lower temperature. Therefore, in order to make possible the LPS technique for consolidating grains of the $MRE_2Fe_{14}B$ magnet alloys, a higher melting reaction must be utilized to form an alternative intrinsic alloy liquid fraction or some suitable extrinsic sintering aid (metal or alloy powder) must added to generate a sufficient fraction of wettable liquid phase during low temperature LPS processing.

In the design of alloys and LPS processes for sintered high temperature magnets, a simplified (without Co, Zr, or ZrC) $MRE_2Fe_{14}B$ base alloy, primarily $[Nd_{0.45}(Y_6Dy_1)_{1/7*0.55}]_{16.6}Fe_{76.7}B_{6.7}$ (WT212), was used to provide thin chill castings or "under-quenched" melt spun ribbon with large (> 5μm) grains of 2:14:1 phase that could be mechanically ground to produce "phase-pure" 1-3μm particulate without segregation or grain boundaries. In preliminary extrinsic sintering aid tests, flake particulate of WT212 magnet alloy was blended with flake particulate of $(Cu_{0.4}Ag_{0.6})_{1-x}Nd_x$ alloys with x=2, 4, 6, 8 at. %, as a 10 vol.% addition. Each blended sample was uni-axially pressed in a high magnetic field (using a special non-magnetic punch and die set) and sintered above the melting point of the Cu-Ag-Nd particulate in a preliminary attempt at LPS magnet fabrication. The moderate degree of magnetic property enhancement that was measured on these samples encouraged more systematic studies of extrinsic sintering aids. Alternative extrinsic sintering aid alloys, including Fe-78 at.%Nd (eutectic melting at 685C), Cu-35.5 at.%Zr (liquidus of about 975C), and Al-13 at.%Si (eutectic melting at 577C) were designed and initial tests were conducted in a model melting and wetting configuration with cast disks of WT212 magnet alloy. Analysis of these tests is underway to guide improvements in this concept with the goals of adding a minimal amount of sintering aid, of maximizing wettability during LPS, and of minimizing LPS reaction zone consumption of the 2:14:1 particulate. In a companion effort to use higher melting intrinsic sintering reactions, adjusted high temperature magnet alloy compositions have been tried that are expected to form sufficient RE-rich liquid phase at higher temperatures, such as $[Nd_{0.45}(Y_6Dy_1)_{1/7*0.55}]_{3.2}Fe_{14}B_{1.2}$ (WT213). Extra MRE content was added in these alloys to compensate for oxidation losses during mechanical milling and sintering processes and to form adequate liquid phase for sintering densification. With such MRE-enriched magnet alloys, it may be possible to obtain strong sintered anisotropic magnets without adding extrinsic sintering aids.

2. Powder preparation methods for sintered magnets

In order to obtain more uniform (near-perfect) magnetic domain alignment of 2:14:1 magnet alloy powder and, thus, higher M_r and $(BH)_{max}$, it is critical to produce fine (1-3μm, from experience with $Nd_2Fe_{14}B$) and uniform sized particulate by a mechanical grinding (comminution) process in a controlled atmosphere, which is challenging due to the reactivity of the $MRE_2Fe_{14}B$ material. In contrast to typical experimental situations, comminution of large (kg) quantities of magnet material is much easier than making small (< 25g) batches, since in a large batch a small fraction of the sample may be sacrificed (to

consumption by oxidation) to clean up the atmosphere in the sealed milling container without detriment to the remaining material. In addition, it is necessary to optimize many factors in a high energy ball milling process to obtain fine particles. We have already set up or are establishing three different methods to perform particulate comminution. These methods include: a) SPEX mill with high energy; b) common ball mill, and c) autogenous jet mill. We also set up a motorized mortar and pestle in an inert atmosphere (N_2) glove box. For preliminary comminution experiments, chill cast ingots of WT212 and WT213 were ground into 75μm coarsen powder and loaded into SPEX mill or ball mill containers under nitrogen gas.

3. Initial test results

Table 3 is a summary of milling and sintering parameters. A different "Ball mill-x" or "SPEX-x" designation under the mill method column represents a different ratio of balls (grinding media)-to-powder (starting coarse particulate). For example, in Ball-mill-1, the grinding media was balls with diameter larger than 3mm. After 50h of milling, the powder of WT212 obtains an average particle size of 8.3μm, from laser light scattering (Microtrac) measurements. If the milling time was increased to 70 hrs, the average particle size of the resulting powder was reduced to 7.2μm. Both powders were aligned under 1.8 T field and pre-compacted in a uni-axial die. After the magnet was de-energized, each compact was carefully removed from the die and further compacted in a hydraulic press. The resulting samples were sintered in a high vacuum at 1120°C for 2h and (slowly) cooled in the vacuum furnace. The sintered sample densities were 7.1 and 7.3g/cm^3, respectively, similar to the full density of the alloy (about 7.4g/cm^3). Unfortunately, magnetic measurements of the resulting samples confirmed the absence of 2:14:1 phase in both. Subsequent analysis found that the 2:14:1 phase was lost due to a loss of rare earth content (most likely from oxidation) after extended milling.

Table 3. Summary of milling and sintering properties

Alloy	Mill method	Mill time (hr.)	Average powder size (μm)	Sintered T (°C)	Density (g/cm^3)	2-14-1 phase?
WT212	Ball-mill-1	50	8.3	1120	7.1	No
WT212	Ball-mill-1	70	7.2	1120	7.3	No
WT213	Ball-mill-2	40	18.4	1120	6.7	Yes
WT213	Ball-mill-3	18	5.0	1120	6.7	Yes
WT213	Ball-mill-3	25	3.5	1120	6.9	Partial
WT213	SPEX-1	3	14.7	1120	7.0	Partial
WT213	SPEX-1	5	15.4	-	-	No
WT213	SPEX-2	1.5	Unavailable	1110	6.8	Yes
WT213	SPEX-2	3.0	10.4	-	-	Partial

To minimize exposure to oxygen contamination, shortening the milling time was investigated by optimizing the grinding media sizes and the ratio of balls-to-powder. For example, small (1mm) grinding balls are expected to yield a narrower size distribution with a smaller average particle size, while larger size (3 mm and above) grinding balls are expected to effectively break larger particulates down in the early stages of milling. Thus, experiments were initiated on a combination of ball sizes to speed the comminution process, attempting to retain the magnetic phase. In these results, WT213 alloy particles that were milled for 40h (see Ball-mill-2) and for 18h with the Ball-mill-3 parameters were sintered and their hysteresis behavior was measured along both the aligned direction and along the direction perpendicular to the aligned direction. Both samples exhibited stark differences in the hysteresis loops for different alignment directions indicating that some significant particulate orientation and locking has been achieved with only the intrinsic sintering method, as described in the procedure for Ball-mill-1. The coercivity and $(BH)_{max}$ of these samples were 2-2.5 kOe, 5.7-7.7 MGOe, respectively, but had a reduced density for the sintered

samples (only 6.7 g/cm^3), indicating clearly that powder preparation and sintering parameters need to be further optimized.

In addition, we started study of a higher energy ball milling process, i.e., a SPEX mill. Preliminary results (SPEX-1) showed that the apparent particle size after milling for 3 and 5h was 14.7 and 15.4μm, respectively, from automated size analysis. Longer milling time appeared to result in a slightly larger average size in this case, indicating either that finer particles start to become cold-welded together or that powder clumping (fragile agglomeration) occurred during the automated size analysis studies. SEM analysis is needed to help clarify this issue. After increasing the ball-to-powder ratio (run SPEX-2), the milling time was greatly reduced and retention of the 2:14:1 phase was enhanced for apparently finer powder. Although these magnetic properties are not optimum, these preliminary results show that the WT213 alloy may be promising to develop into anisotropic sintered magnets.

Part B. Anisotropic ribbons for anisotropic bonded magnets

Theoretically, the most direct way to produce a bonded magnet with greatly enhanced performance is to achieve anisotropic nano-crystalline powders that can be used in the bonding process. The energy product of a bonded anisotropic magnet can, in principal, be three to four times that of a bonded isotropic magnet for the same volumetric loading. To date, two processes have been used to produce (Nd-rich) $RE_2Fe_{14}B$ based bonded anisotropic magnets. The "HDDR" process has been the most successful recently; however it produces powders with poor environmental stability and a reduced operating temperature limit (excessive negative temperature coefficients). On the other hand, Magnequench produced a respectable anisotropic nano-crystalline magnet powder for bonded magnets by grinding of scrap anisotropic nano-crystalline magnets, i.e., recycled MQIII magnets. However, this process was only viable when their solid state production process (open die hot forging) yielded large numbers of scrap MQIII magnets, a highly undesirable situation. The approach we are taking is to control the alloy composition and cooling conditions so that a nano-crystalline texture parallel to the easy axis of tetragonal $MRE_2Fe_{14}B$ phase is formed directly on solidification. While previous work has shown that this type of alignment is possible, the resulting material has always been magnetically soft due to large grains.

In this work, we studied new MRE magnet alloys, WT186, $[Nd_{0.45}(Y_2Dy_1)_{1/3*0.55}]_{2/17.33}Co_{1/17.3}Fe_{13/17.3}B_{1/17.3}$ and $[Nd_{0.45}(Y_2Dy_1)_{1/3*0.55}]_{2/17.33}Co_{1/17.3}Fe_{13/17.3}B_{1/17.3}$, which were melt spun at wheel speeds of 5-7m/s under 0.5 atm. of Ar. The orientation of the grain structure with respect to the ribbon surface was studied by XRD and magnetic property measurements. XRD measurements of both sides of ribbon samples (wheel side and free side) with different wheel show that it is possible to produce a textured structure going through the cross section of ribbons by controlling wheel speed.
The ribbons melt spun at 7 m/s were ground into sub-30μm powders and aligned in epoxy under a magnetic field of 1.5T. The resulting hysteresis loops exhibit a high degree of anisotropy. It should be noted that unlike the particles used in anisotropic sintered magnets, these powder particles contain thousands of nano-metric columnar grains. Interestingly, the coercivity observed in the hysteresis loops is at least two orders of magnitude larger than we expect for the microstructure we have observed. In addition, it is noted that sample WT201 still exhibited a coercivity of 2 kOe even though the sample was annealed at a high temperature of 1000°C for four days. These results are very promising for the successful development of anisotropic powders for bonded magnets.

Industrial Partnerships

Through the years of this project (FY2001 to present), research collaborations have developed with ORNL and Arnold Magnetic Technologies (AMT), an industrial producer of bonded permanent magnets. We have collaborative research relationships and on-going technical discussions with several other

industrial partners, including General Motors, Magnequench International, Unique Mobility, and Reliance Electric. Specifically, this year in March we started a 10-month CRADA project (recent no-cost extension through FY2009) entitled "Integrated Traction Drive System" with General Motors and Arnold Magnetic Technologies as direct partners. These on-going relationships and others should be beneficial to eventual transfer of the powder making and magnet fabrication technologies developed in this project, the ultimate objective of this work.

Conclusion

The current FY2008 progress can be viewed in several main areas, including contracting for a comprehensive magnet cost analysis, up-scaled surface passivation methods and completion of isotropic bonded magnet fabrication, magnet alloy improvements for isotropic nano-crystalline permanent magnets, magnet alloy and process design for anisotropic micro-crystalline sintered magnets, magnet alloy and process design for anisotropic nano-crystalline bonded magnets, and continued industrial partnership growth. The new efforts for FY2009 will include extending the investigation of anisotropic micro-crystalline sintered magnets and, especially, anisotropic nano-crystalline bonded magnets. The potential large gains in magnetic energy product per mass of magnet alloy, without loss in complex shape forming for the latter, serve as the primary drivers for this work.

References

1. J. F. Herbst, Reviews of Modern Physics, Vol. 63(1991), p. 819 and reference therein.
2. R. Grössinger, R. Krewenka, X. K. Sun, R. Eibler, H. R. Kirchmayr, and K. H. J. Buschow, J. Less-Common Met., Vol. 124 (1986), p. 165.
3. S. Hirosawa, Y. Matsuura, H. Yamamoto, S. Fujimura, M. Sagawa, and H. Yamauchi, J. Appl. Phys. Vol. 59 (1986), p. 873.
4. W. Tang, K. W. Dennis, M. J. Kramer, I. E. Anderson, and R. W. McCallum, Materials Science Forum **475,** (2005) p. 2155.
5. W. Tang, Y. Q. Wu, K. W. Dennis, M. J. Kramer, I. E. Anderson, and R. W. McCallum, Journal of Applied Physics **97,** 10H106 (2005).

Publications

1. N. T. Oster, I. E. Anderson, W. Tang, Y. Wu, K. W. Dennis, M. J. Kramer, and R. W. McCallum, "Alternative Approaches for Reactive Surface Coating on Rare Earth Magnet Alloy Particulate," Advances in Powder Metallurgy & Particulate Materials, Washington, D.C., 2008, pp. 6-131 - 6-141.
2. P.K. Sokolowski, I.E. Anderson, W. Tang, Y.Q. Wu, K.W. Dennis, M.J. Kramer, and R.W. McCallum, "Gas Atomized $MRE_2Fe_{14}B$ Permanent Magnet Particulate with Enhanced High Temperature Performance," in *Advances in Powder Metallurgy and Particulate Materials-2007*, compiled by J. Engquist and T.F. Murphy, (Metal Powder Industries Federation, Princeton, NJ, 2007), part 9, pp. 119-132.

Patents

R. W. McCallum, Y-W. Xu, I. E. Anderson, K. W. Dennis, and M. J. Kramer, U.S. Patent Application (PCT) filed November 18, 2002, "Permanent Magnet Alloy with Improved High Temperature Performance," under examination.

4. Power Electronics Research and Technology Development

4.1 Wide Bandgap Materials

Principal Investigator: Madhu Chinthavali
Oak Ridge National Laboratory
National Transportation Research Center
2360 Cherahala Boulevard
Knoxville, TN 37932
Voice: 865-946-1411; Fax: 865-946-1262; E-mail:chinthavalim@ornl.gov

DOE Technology Development Manager: Susan A. Rogers
Voice: 202-586-8997; Fax: 202-586-1600; E-mail: Susan.Rogers@ee.doe.gov

ORNL Program Manager: Mitch Olszewski
Voice: 865-946-1350; Fax: 865-946-1262; E-mail: olszewskim@ornl.gov

---

Objectives

- Keep up to date with state-of-the-art SiC power devices by acquiring, testing, and characterizing new-technology silicon carbide (SiC) power devices.
- Utilize new wide-bandgap (WBG) devices in vehicle power electronics simulations to ascertain system level benefits.
- Study conceptual changes to inverters/ converters and their packaging and thermal management designs that are uniquely possibly through the use of WBG devices.

Approach

- Acquire, test, and characterize new-technology WBG power devices
  - — Static characteristic tests
  - — Dynamic characteristic tests
  - — Behavioral modeling
  - — As appropriate, utilize characterization results in simulations to determine device benefits for power electronics.

- Determine converter concepts that make the best use of the attributes of WBG-based power devices
  - — Survey literature
  - — Design and develop circuits
  - — Model and simulate novel converter designs and thermal control concepts
  - — Research new packaging techniques

Major Accomplishments

- Acquired several SiC junction field effect transistors (JFETs). Tested, characterized, and modeled SiC JFETs and their body diodes.
- Developed several concepts to take advantage of SiC device attributes and completed three new air-cooled traction drive inverter designs.

Future Direction

- The inverter designs developed in FY 2008 will be evaluated to build an air-cooled inverter prototype based on the results of the thermomechanical analysis.

- An electrical design that includes gate drivers, a device layout, and the component inter-connects will also be analyzed.

Technical Discussion

1. Device Testing

The new WBG devices acquired this year were normally-on SiC JFETs, normally-off SiC JFETs, and a high-temperature-packaged normally-on SiC JFET. These devices were tested, characterized, and modeled. The body diode of a normally-on SiC JFET was also tested. All the devices obtained were experimental samples.

2. Normally-on SiC JFET

Static characteristics

Static characteristics of the 600 V, 5 A SiC JFET received this year are shown in Fig. 1 for different operating temperatures. SiC JFETs have a positive temperature coefficient, which means that, as in SiC Schottky diodes, their conduction losses will be higher at higher temperatures. However, the positive temperature coefficient makes it easier to parallel these devices and reduce the overall on-resistance. The on-resistance of the JFET increases from 0.25 Ω at 25°C to 1.07 Ω at 200°C, as shown in Fig. 2.

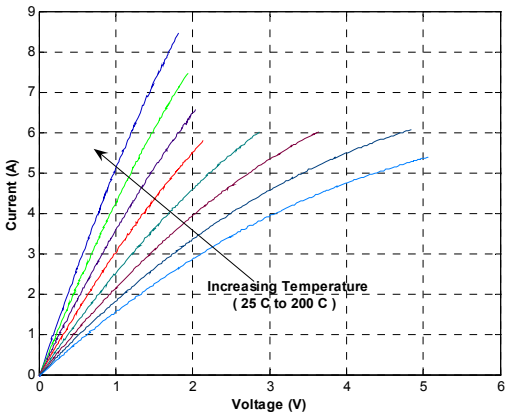

Fig. 1. VI curves of a normally-on SiC JFET at different operating temperatures.

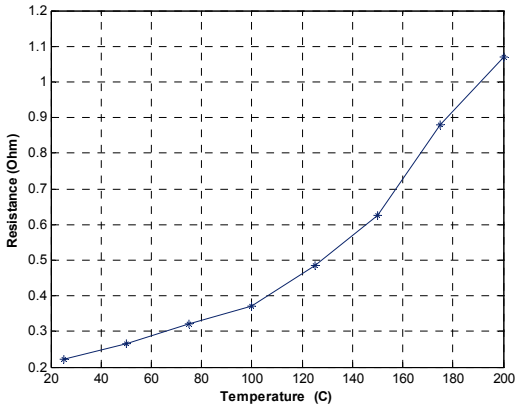

Fig. 2. On-resistance of a normally-on SiC JFET at different temperatures.

Dynamic characteristics

The SiC JFET was tested in a chopper circuit with double pulse switching to observe its dynamic characteristics. The double pulse circuit enables the use of an inductive load instead of a resistive and inductive load together. The current through the inductor builds up during the first pulse, and the peak forward current is adjusted by changing the width of the first pulse. The switch is turned off and turned on for short periods after the first pulse. The turn-on and turn-off energy losses can be obtained during the short pulse intervals.

The turn-on and turn-off energy losses of the JFET during switching are shown in Fig. 3. The turn-on losses do not change significantly with temperature, but the turn-off losses decrease with increasing temperature.

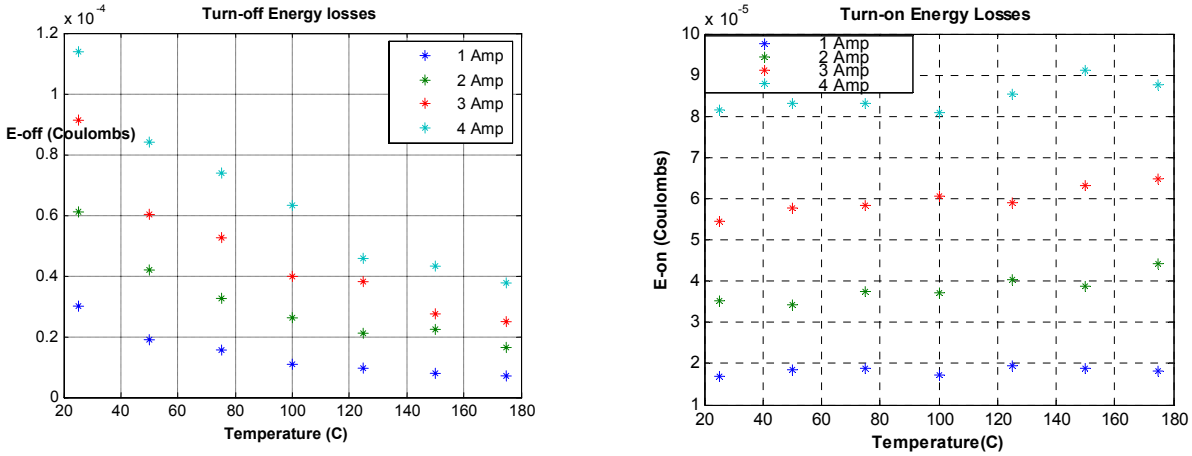

(a) Turn –off energy losses **(b) Turn–on energy losses**

Fig. 3. Switching energy losses of a normally-on SiC JFET for different currents and temperatures.

2. Normally-off SiC JFET

Static characteristics

The static characteristics of an 800 V, 5 A normally-off SiC JFET received this year are shown in Fig. 4 for different operating temperatures. This was the first normally-off SiC JFET tested. Normally-off devices are the preferred type of device in power converters for a fail-safe mode of operation. This could be a revolutionary device, which could have a significant impact on the choice of SiC devices for automotive inverters. Testing of the device determined that the on-resistance of the JFET increases from 0.15 Ω at 25°C to 0.88 Ω at 200°C as shown in Fig. 4.

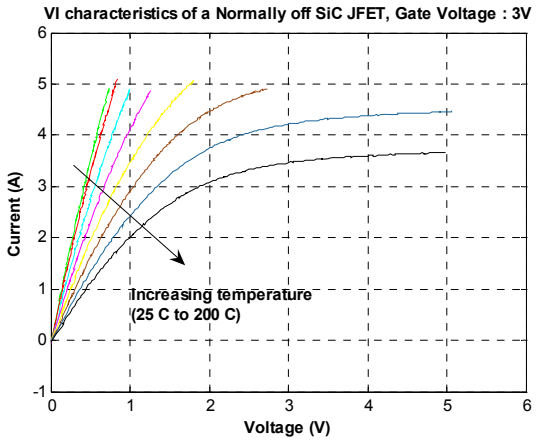

Fig. 4. VI curves of a normally-off SiC JFET at different operating temperatures.

Dynamic characteristics

The turn-on and turn-off energy losses of the JFET during switching are shown in Fig. 5. The turn-on losses do not change significantly with temperature, but the turn-off losses decrease with increasing temperature. The energy losses are not much different from those of the normally-on SiC JFET.

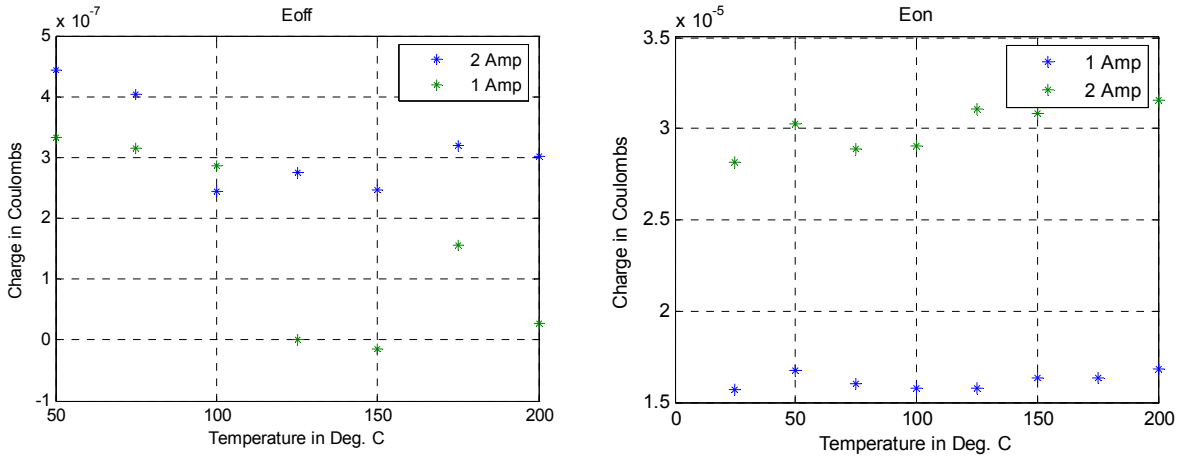

(a) Turn –off energy losses **(b) Turn –on energy losses**

Fig. 5. Switching energy losses of normally-off SiC JFET for different currents and temperatures.

3. High-temperature normally-on SiC JFET

Static characteristics

A high-temperature packaged 600 V, 5 A normally-on SiC JFET prototype device was tested. The tests demonstrated the operation of the SiC JFET at 400°C. On-state resistance increased from 0.25 Ω at 25°C to 2.5 Ω at 400°C. The static characteristics of the JFET are shown in Fig. 6 for different operating temperatures.

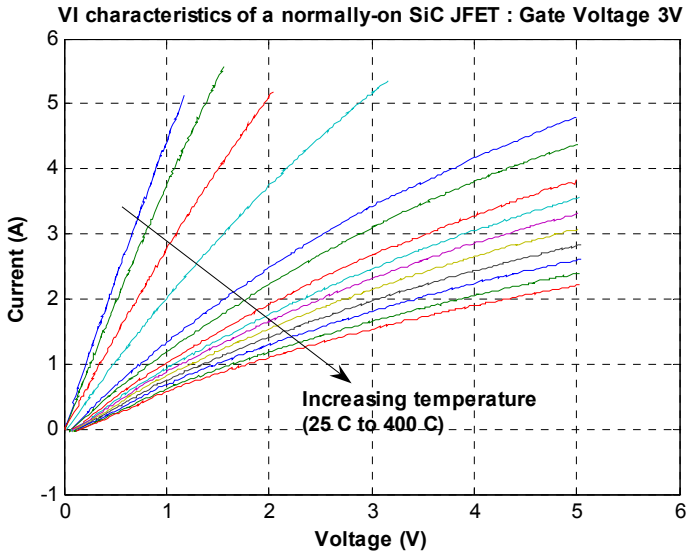

Fig. 6. VI curves for a high-temperature packaged normally -on SiC JFET at different operating temperatures.

4. Body diode of a normally-on SiC JFET

Static characteristics

The body diode in a normally-on JFET can be used as a free-wheeling diode in a voltage source inverter for automotive applications. Using this diode can reduce the number of devices necessary in an inverter by eliminating the anti-parallel diodes. The body diode is available only in normally-on devices with a combined lateral and vertical channel design from SiCED. This particular device is a pn diode formed as a consequence of the specific device design. Static characteristics of the body diode in a 1200 V, 5 A SiC JFET are shown in Fig. 7 for different operating temperatures.

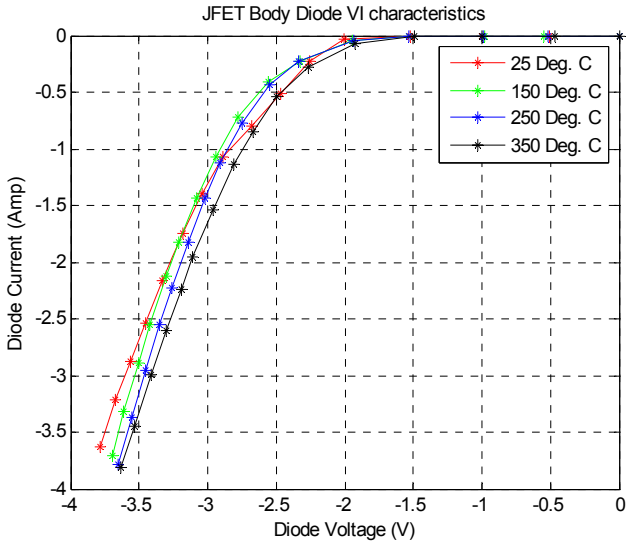

Fig. 7. VI curves of a body diode of a normally-on SiC JFET at different operating temperatures.

Dynamic characteristics

The pn body diode has a longer reverse recovery time than a Schottky diode. This increased recovery time results in switching losses in an inverter. The reverse recovery characteristics of the body diode at different temperatures are shown in Fig. 8. The peak reverse recovery current increases along with temperature. However, the change in current is small, resulting in a minimal increase in reverse recovery losses at higher temperatures.

5. Study of Concepts

Technical areas in which new concepts can be developed were identified during FY 2008. The impact of SiC device attributes on inverters was analyzed, and specific problems were identified that need to be addressed in developing a high-temperature inverter. This analysis resulted in several novel air-cooled SiC-based inverter designs. The main objective of these designs is to enable cooling with air, eliminating the need for the liquid-cooled thermal management systems that are currently used. These designs are expected to increase the power density and decrease the volume and weight for electric-based vehicle traction drive inverters. This design concept will enable the development of an integrated motor/inverter drive system during the next fiscal year.

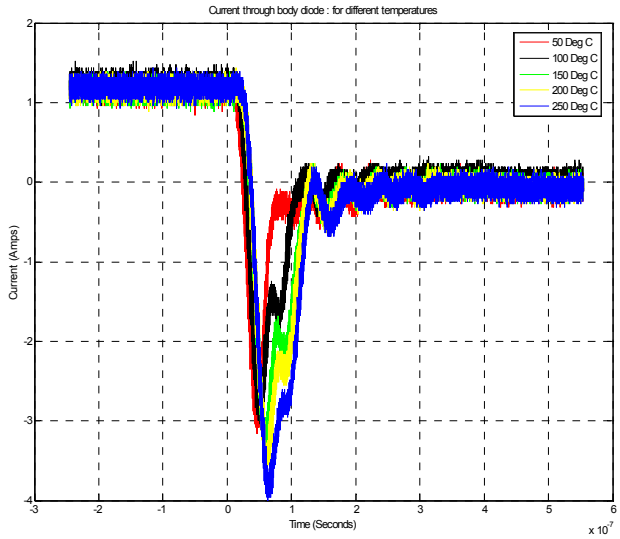

Fig. 8. Reverse recovery characteristics of a body diode in a normally-on SiC JFET.

The selected design will realize the following benefit to achieve high-temperature operation:

- The low-temperature electronics and capacitors (dc-link/filter) will be separated from the high-temperature components, creating both low- and high-temperature zones.

This concept enables the use of low-temperature electronics in close proximity with high-temperature power devices.

- Thermal interface material is eliminated, thereby increasing the thermal efficiency.
- Active cooling of the buss bars will increase the reliability of the inverter.
- The design can be modified for current source, voltage source, or a Z-source inverter.
- Direct-bonded copper material with low thermal conductivity can be used in the thermal design. The design enables the use of cheaper materials.
- The buss bar design will result in fewer problems related to electromagnetic interference.
- The inverter design concept will enable integration with a motor, which will reduce costs through the reduction in the number of connectors and interconnects.
- The number of solder joints will be substantially reduced, increasing reliability and reducing manufacturing costs.
- The capacitor design will enable better cooling of the capacitor and hence increased ripple current handling capability.
- Wire bonds will be eliminated with a novel packaging concept, increasing reliability and reducing manufacturing costs
- Normally-on JFETs can be used if a current-source inverter topology is used.
- The design may allow the elimination of anti-parallel diodes.

Conclusion

Several new SiC JFETs, including a high-temperature packaged SiC JFET, were acquired, tested and, modeled. The body diode in a SiC JFET was tested to evaluate the feasibility of using the diode to

eliminate anti-parallel diodes. Several concepts to take advantage of SiC device attributes were studied and were used to develop air-cooled inverter designs.

Publications

1. L. M. Tolbert, H. Zhang, B. Ozpineci, and M. Chinthavali, "SiC-based power converters," Materials Research Society Spring Meeting, Symposium D, San Francisco, March 24–27, 2008.
2. B. Ozpineci, M. Chinthavali, L. M. Tolbert, and H. Zhang, "SiC power electronics research at ORNL," GOMACTech, Las Vegas, March 17–20, 2008.
3. B. Ozpineci, M. Chinthavali, A. Kashyap, L. M. Tolbert, and A. Mantooth, "A 55 kW three-phase inverter with Si IGBTs and SiC Schottky diodes," I*EEE Transactions on Industry Applications*, **44** (2008).

4.2 An Active Filter Approach to the Reduction of the dc Link Filter

Principal Investigator: Burak Ozpineci
Oak Ridge National Laboratory
National Transportation Research Center
2360 Cherahala Boulevard
Knoxville, TN 37932
Voice: 865-946-1329; Fax: 865-946-1262; E-mail:ozpinecib@ornl.gov

DOE Technology Development Manager: Susan A. Rogers
Voice: 202-586-8997; Fax: 202-586-1600; E-mail: Susan.Rogers@ee.doe.gov

ORNL Program Manager: Mitch Olszewski
Voice: 865-946-1350; Fax: 865-946-1262; E-mail: olszewskim@ornl.gov

---

Objectives

- To replace the bulky dc link capacitor in a traction inverter with a much smaller active power filter (APF) that imitates what a dc link capacitor does.
- The weight and volume of the traction inverter will be reduced while the reliability and lifetime of the inverter will be increased.
- The active filter is expected to weigh half as much as the dc link capacitor and occupy less than half the space.

Approach

- A current source APF with a small capacitor and inductor can be used in the dc link together with semiconductor switches to replace the dc link capacitor.
- The impacts of this approach are reduced size and cost and possibly a more cost-effective solution for high-temperature operation.

Major Accomplishments

- Performance requirements have been established for an active filter.
- An APF has been developed to replace the dc link capacitor.
- A traction drive system has been simulated using both a dc link capacitor model and an APF model replacing the dc link capacitor.
- The practical feasibility of the active filter replacing a dc link capacitor has been assessed. With the current approach, there are efficiency and size concerns that can be solved by using different devices and new designs.

Future Direction

- Develop other circuitry and control algorithms to reduce the APF inductance, inductor current, and switching frequency.
- Develop adaptive controls to automatically update the inductor current depending on the load current.
- Design and build an APF benchtop module. Test the module in a 55 kW inverter, replacing the dc link capacitor.
- Build a 105°C compatible version.

Technical Discussion

Operation principle

The block diagram of the active filter is shown in Fig. 1 connected to the dc link of the traction system. The traction system is composed of a dc source, a three-phase inverter, and a traction motor. The sinusoidal pulse-width modulation (PWM) technique typically used in an inverter introduces high-frequency-current harmonic content in the dc link. Figure 2 shows the typical input current of an inverter. The purpose of the active filter is to absorb ripple current, as a traditional passive filter capacitor does, and leave only the dc component to be drawn from the dc source.

To compensate for the dc link ripple current, a current source active filter topology is used. As shown in Fig. 1, the active filter is composed of an inductor, a full bridge inverter, and a relatively small capacitor for voltage smoothing. The active filter works as a current source inverter without a dc power supply. The inductor current is kept constant and should be larger than the peak value of the ripple current. The filter current injected to the dc link can be positive, negative, or zero depending on the operation mode of the active filter (Fig. 3).

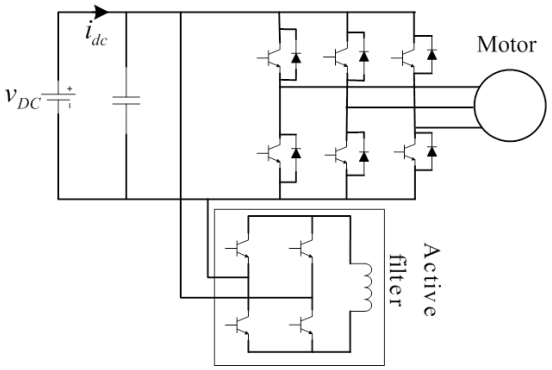

Fig. 1. Traction system with active filter.

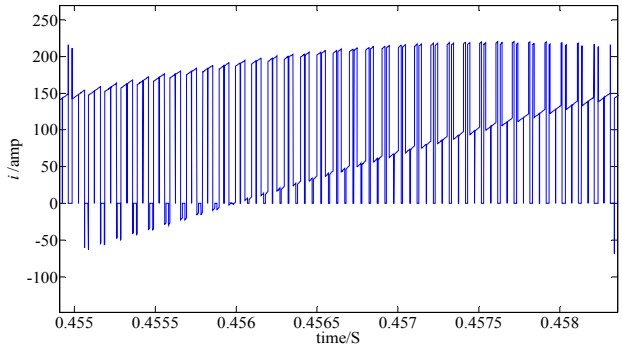

Fig. 2. Input current of inverter.

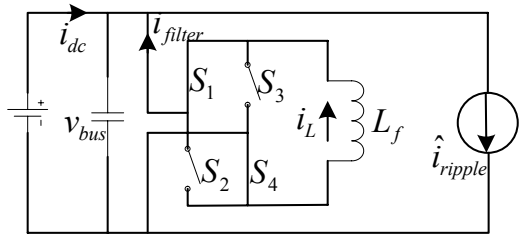

(a) Mode 1

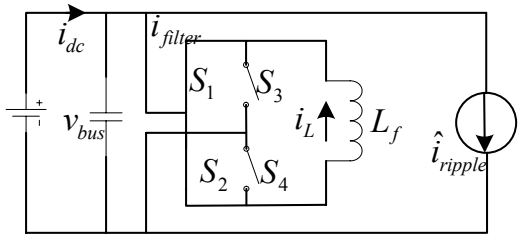

(b) Mode 2

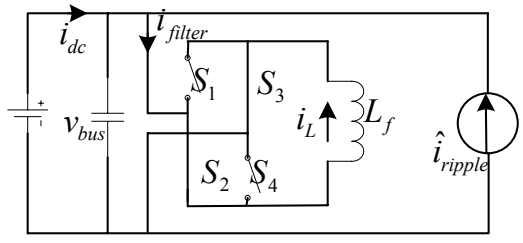

(c) Mode 3

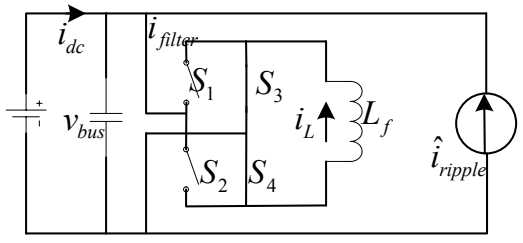

(d) Mode 4

Fig. 3. Equivalent circuit.

To illustrate the operation principle, the equivalent circuit in Fig. 3 is used. In the equivalent circuit, a ripple current source i_{ripple} is used to imitate the effect of the three-phase inverter and the motor. Figure 3 shows the equivalent circuit working in different modes, according to the direction of the filter current. Figure 4 illustrates the operating current and voltage waveforms: the load ripple current, the dc bus voltage, and the injected filter current.

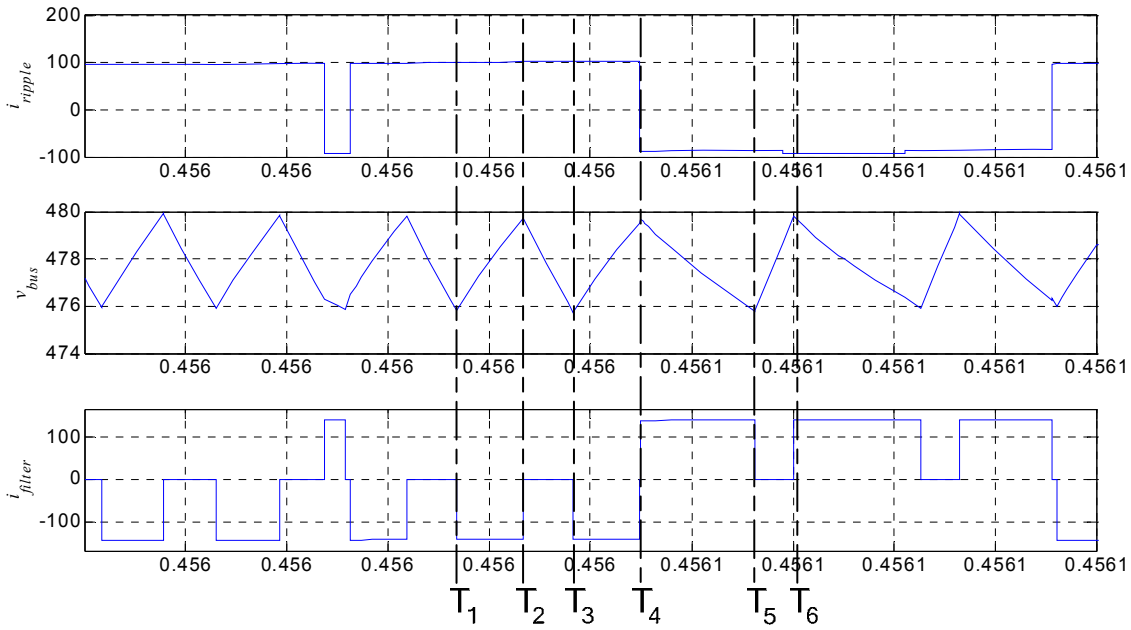

Fig. 4 Waveforms for load ripple current, dc bus voltage, and filter current.

Mode 1: When the ripple current goes into the inverter, which we define as positive, S1 and S4 of the active filter close and the current of the inductor is injected into the dc link; this direction is defined as negative. This mode is also illustrated in Fig. 4 from T_1 to T_2. Since i_{filter} is larger than i_{ripple}, i_{filter} supports i_{ripple} and at the same time charges the capacitor; the voltage, v_{bus}, increases. There is a hysteresis-band for v_{bus}; when it reaches the upper boundary, Mode 2 starts.

Mode 2: In this mode, ripple current is still positive, S1 and S2 close, inductor current i_L freewheels through S1 and S2, and the filter current i_{filter} is zero. The ripple current discharges the capacitor. This mode corresponds to the interval between T_2 and T_3. v_{bus} decreases as a result of the discharge. When it reaches the lower bound, this mode ends.

Mode 3: When the ripple current is negative, S2 and S3 close and filter current i_{filter} is positive. Ripple current i_{ripple} goes into the filter, since the filter current is larger than the ripple current. The current difference $i_L - i_{ripple}$ discharges the capacitor and the dc bus voltage decreases as shown in interval T_4 to T_5 in Fig. 4. When v_{bus} reaches the lower bound, the active filter will change and enter mode 4.

Mode 4: In this mode, S3 and S4 close and the inductor current freewheels. The filter current i_{filter} is zero. Ripple current i_{ripple} charges the capacitor; therefore, the dc bus voltage increases. This mode corresponds to the interval between T_5 and T_6.

From another point of view, the function of this APF is to further increase the frequency of the dc link current so that a small dc link capacitor can filter the ripple current.

Simulation results

According to the operation principle described, a simulation was conducted using Simulink. Some system parameters used in the simulation are listed in Table1. A traction drive system was simulated with a conventional dc link capacitor and with an APF that was designed to match the functions of the dc link capacitor.

Table 1. System parameters

Parameter	Value
dc input voltage	500 V
Power of IM	30 kW
Peak current	200 A
Capacitor	100 μF
Filter inductor	5 mH

Figure 5 shows the filtered and unfiltered dc link currents. Figure 5a is the conventional case with a dc link capacitor and Fig. 5b is the case using the active filter. The dc input current ripple is 10 A in both cases. For the conventional case, the current ripple varies, but the maximum value is around 10 A. Figures 6 and 7 show expanded views of the dc input current and dc bus voltage, respectively. For both cases, the ripple voltage is around 2 V.

For easier comparison, some important system parameters and simulation results are listed in Table 2. As can be seen in the table, only a 100 μF capacitor is needed for the active filter case, compared with a 2,200 μF capacitor in the conventional case to achieve the same filtering results. Although the active filter solution can match the conventional case, note also that four extra insulated-gate bipolar transistors (IGBTs), two extra diodes, and an extra inductor are required for the active filter.

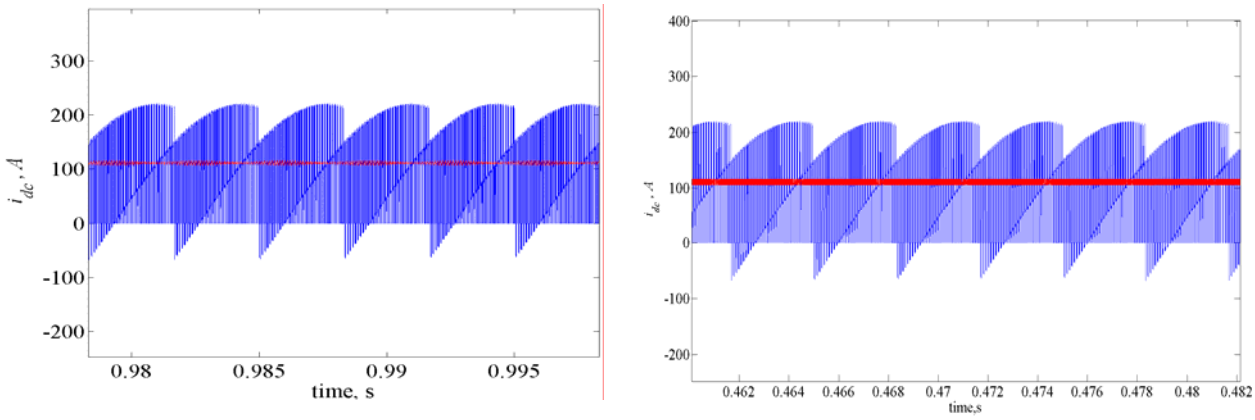

(a) **(b)**

Fig. 5. Inverter input current and dc input current: (a) for capacitor case and (b) for APF case

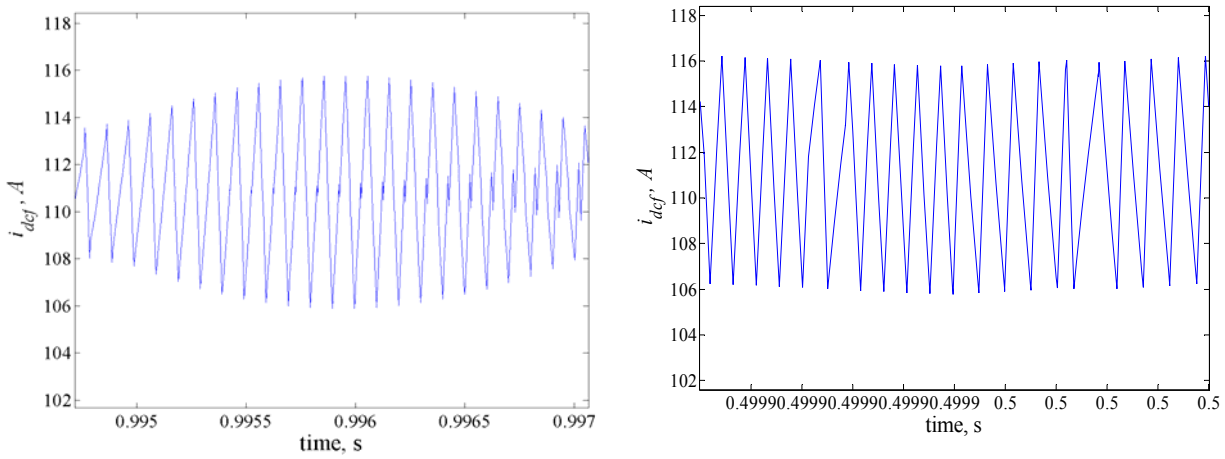

Fig. 6. dc input current

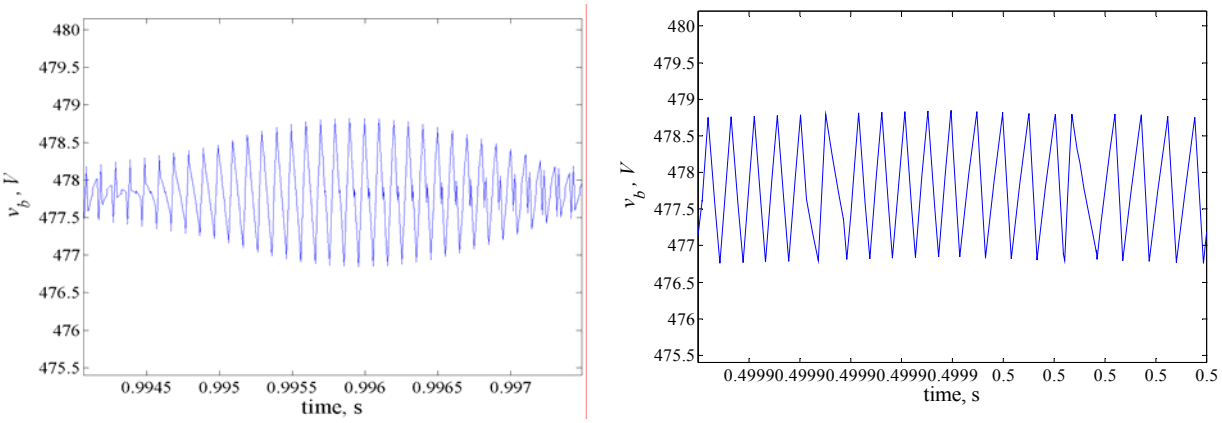

Fig. 7. dc bus voltage

Table 2. Parameter comparison

	Case 1 (capacitor)	Case 2 (APF)
dc link capacitor	2200 μF	100 μF
APF inductor		5 mH
APF frequency		100 kHz
Extra components		4 IGBTs and 2 diodes
APF inductor current		140 A
dc link voltage ripple	2 V	2 V
Input current ripple	10 A	10 A
Current ripple before filtering	220 A	220 A
dc link voltage	500 V	500 V
Output power	30 kW	30 kW

Analysis of parameter dependence

To get better filtering results and reduce the losses associated with the active filter, the performance of the active filter was studied further. Research indicates that the dc bus voltage ripple, with a preset hysteresis band, can affect the dc input current ripple. Figure 8(a) shows the relationship between the two. The current ripple increases along with the increase of the voltage ripple. When the hysteresis band is set to 2 V, the current ripple is 10 A. When the hysteresis band increases to 5 V, the current ripple is 25 A.

The switching losses in power switches are directly proportional to the switching frequency; therefore, to reduce active filter losses, the switching frequency should be lower, too. According to the simulation results, two parameters can affect the active filter frequency: the dc bus voltage ripple hysteresis band and the smoothing capacitor size. An increase in the bus ripple voltage can decrease the switching frequency. However, since the bus ripple voltage is also proportionally related to the current ripple, there are limits on how much it can be increased. A tradeoff is needed. A 2~3 V ripple was assumed for the simulation studies in this project. The capacitor size is inversely proportional to the switching frequency when the capacitor is 1 per-unit (pu), which was 100 μF in this simulation; the maximum active filter switching frequency was 160 kHz. However, when the capacitor size was increased to 2 pu, the switching frequency decreased to 60 kHz.

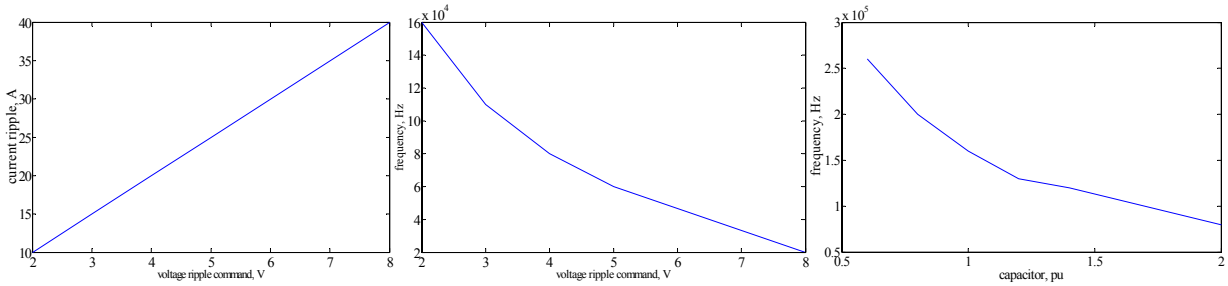

Fig. 8. Parameter dependence.

These parameter dependence relations can be explained by the basic equation

$$\Delta V_{bus} \times C = \Delta Q \quad (1)$$

where ΔV_{bus} is the dc bus voltage ripple, C is the capacitor, and $\Delta Q = I \times \Delta t$ is the change in the capacitor charge. The charging or discharging current I is affected by ΔV_{bus} or C. Therefore, if C is not changed, Δt which is the charge or discharge time, is proportional to ΔV_{bus}, and the average switching frequency is inversely proportional to the voltage ripple. If ΔV_{bus} is kept constant, then the switching frequency is inversely proportional to the capacitor value.

The active filter inductor affects the filtering of the low-frequency components. Figure 9 shows the comparison for 5 mH and 1 mH inductance cases. The upper waveforms (from left to right) are the i_{dc}, v_{bus}, and i_L waveforms with a 5 mH inductor; the lower ones are the corresponding waveforms with 1mH inductance. With a lower inductance, all the current and voltage waveforms show increased low-frequency ripple. The frequency of oscillation is three times the inverter line frequency. This is because the inductance is too small to absorb the low-frequency energy fluctuation generated by the three-phase inverter.

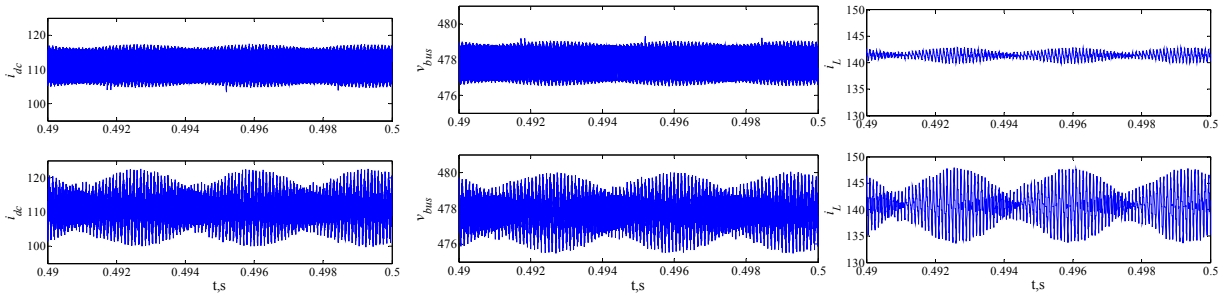

Fig. 9. Effects of filter inductance.

The inductor current should always be designed to be higher than the peak ripple current, since in operation mode 1, the inductor current supports the ripple current and charges the capacitor. However, this inductor current cannot be too large, because it charges or discharges the capacitor. If the charge or discharge is very fast, it will increase the active filter switching frequency.

Conclusion

An APF was developed to replace a dc link capacitor. The simulation of the active filter showed that it functioned as expected, filtering the current ripple in the dc link. The assessment of the simulation and design results can be summarized as follows:

- The APF switching frequency is inversely proportional to the smoothing capacitor size and the dc link voltage ripple hysteresis band limits.
- The dc link voltage ripple hysteresis band limits are directly proportional to the amount of dc current ripple.
- Barriers for practical application and possible solutions include the following:
  - Device losses can be reduced by
    - Using fewer switches and diodes or using a different topology.
    - Reducing the inductor current.
    - Reducing switching frequency.
  - Inductance value and associated inductor size:
    - Inductance value determines how stiff the filter dc current is.
    - Low inductance causes low-frequency voltage ripple. An optimum inductance value is required.

References

1. Bhim Singh, et al., "A review of active filters for power quality improvement," *IEEE Transactions on Industrial Electronics*, **46**(5), 960–972 (October 1999).
2. Fang Z. Peng, "Harmonic sources and filtering approaches," *IEEE Industry Applications Magazine*, 18–25 (July/August 2001).
3. Bimal K. Bose, et al., "Electrolytic capacitor elimination in power electronic system by high frequency active filter," presented at IEEE Industry Applications Society Annual Meeting.

4.3 Advanced Converter Systems for High-Temperature Hybrid Electric Vehicle Environments

Principal Investigator: Leon M. Tolbert
Oak Ridge National Laboratory
National Transportation Research Center
2360 Cherahala Boulevard
Knoxville, TN 37932
Voice: 865-946-1332; Fax: 865-946-1262; E-mail:tolbertlm@ornl.gov

DOE Technology Development Manager: Susan A. Rogers
Voice: 202-586-8997; Fax: 202-586-1600; E-mail: Susan.Rogers@ee.doe.gov

ORNL Program Manager: Mitch Olszewski
Voice: 865-946-1350; Fax: 865-946-1262; E-mail: olszewskim@ornl.gov

---

Objectives

- Develop a high-efficiency bidirectional dc-dc power converter.
- Incorporate high-temperature power devices and capacitors with a high-temperature packaging technology and gate drives that will enable the converters to operate in high-ambient-temperature conditions.

Approach

- Utilize new high-temperature silicon carbide (SiC) power electronics devices with high-temperature capacitors and new high-temperature packaging concepts.
- Develop and incorporate an integrated, silicon-on-insulator (SOI) high-temperature gate drive into the design of the module.

Major Accomplishments

- An SOI gate drive chip with dimensions of 2.2 mm^2 was fabricated and tested at temperatures of up to 225°C.
- A 55 kW, 200 V/600 V multilevel dc-dc converter was fabricated and tested at low temperatures. Efficiency was in the 96 – 98% range.
- High-temperature packaging of SiC junction gate field effect transistors (JFETs) was demonstrated and tested at up to 175°C.

Future Direction

- This project ended September 30, 2008.
- A new project to concentrate on the gate drive design will start October 1, 2008. It will use the results of this project to build a highly integrated SOI gate drive chip that also incorporates protection features.
- High-temperature packaging of SiC power electronic devices will continue under the wide-bandgap project.

Technical Discussion

3X dc–dc Converter Development

The 3X dc–dc converter employs the topology shown in Fig. 1. With proper control, it can provide three different input/output voltage ratios, e.g., 1, 2, or 3 in steady state. Because of its bi-directional nature, the converter can act as a voltage multiplier or a divider based on the definition of source and load.

30 kW Prototype

A 30 kW prototype was fabricated and tested. The film capacitors are mounted on the insulated gate bipolar transistor (IGBT) modules via a 9-layer printed circuit board. Underneath the capacitor board is the gate drive circuit. Control and power supply circuits share the same board with the gate drive circuit. For the controller, the complex logic for duty ratio and frequency control was implemented in one complex programmable logic device (CPLD), Xilinx part number XC9572XLPC44. In addition, a novel clamping circuit represented in Fig. 2 was developed to address the voltage spikes caused by the diode reverse recovery.

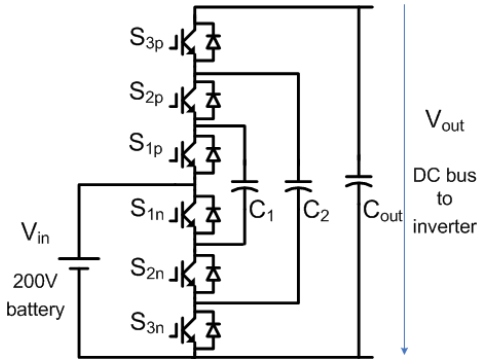

Fig. 1. 3X dc–dc converter topology.

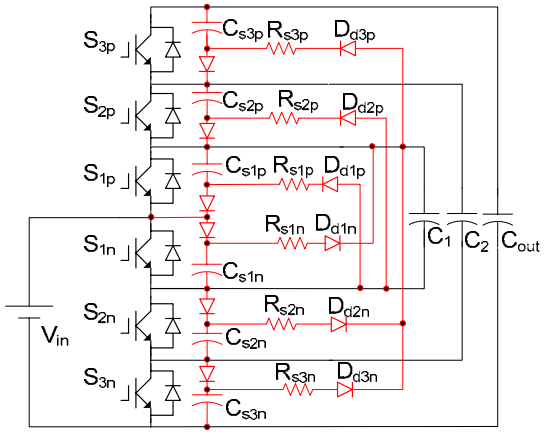

Fig. 2. Topology of the clamping circuit.

System specification and parameters for the 30 kW prototype is as follows:

1. The input voltage range at the low-voltage battery side is 100~200 V. The maximum input voltage under a no-load condition is 200 V.
2. Output power: 30 kW output at the nominal operation voltage of 180 V.
3. Power switching devices: three 250 V, 600 A Powerex CM600DU5F IGBT modules.

Some typical experimental results during steady state operation are shown in Figs. 3 to 6. The capacitors for C_1 and C_2 in Fig. 1 are 500 µF and 160 µF film capacitors. The output capacitor C_{out} consists of a 20 uF capacitor from the 3X dc–dc converter, a 390 uF capacitive load and 0.09 Ω resistor to simulate an inverter load. In the boost mode steady state test, a 1 kHz buck converter is used as an electronic load, which generates 1 kHz load current ripple as seen in Fig. 3(a). The output voltage of the converter is very stable despite the load current ripple. Figure 4 indicates the effectiveness of the clamping circuit. Without the clamping circuit, the converter, restricted by the rated voltage of the IGBT, could handle only around

10 kW output power at 170 V. Figure 5 shows the input and output voltage and current waveforms in 3X buck mode. The efficiency measured by the Yokogawa power meter WT1600 is shown in Fig. 6. The efficiency at 30 kW output in 3X boost mode is 96.8% with a 178 V input voltage and 6.9 kHz switching frequency.

During the transitions when the output voltage ratio changes (such as 2X to 3X or vice versa), the capacitor voltage differences can lead to high transient current through the devices and capacitors. Therefore, a variable pulse width modulation (PWM) duty ratio with high switching frequency is used during transition from one mode to another. Furthermore, a small air-core inductor (3.4 uH) is added when parasitic inductance is not enough for the large voltage difference, and when the adopted devices cannot achieve sufficiently high switching frequency. The converter performance during voltage ratio change transition is shown in Fig. 7. In all cases the transient current is well limited. The periodic peak current in Fig. 7 (a) and (c) is caused by the discrete increment of the duty cycle generated by the CPLD.

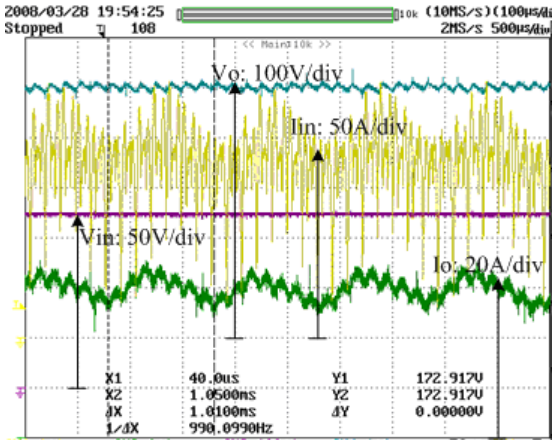

(a) Input and output waveforms

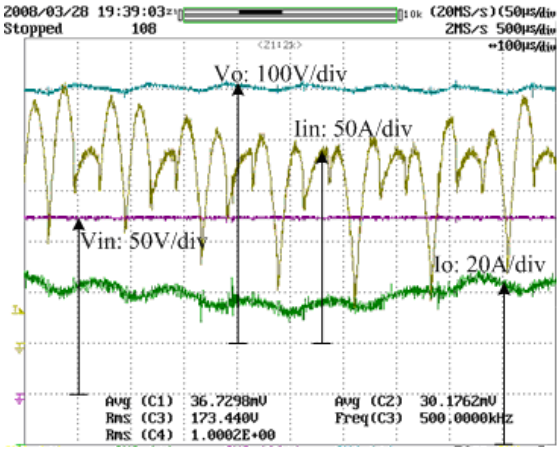

(b) Zoom-in detail

Fig. 3. Input and output voltage and current waveforms of 30 kW output in 3X boost mode.

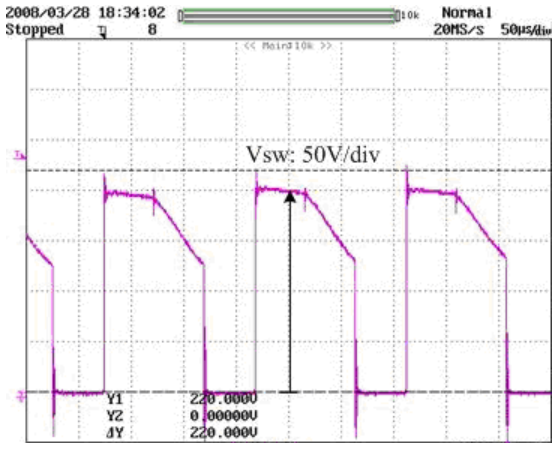

Fig. 4. Highest spike across switch in 30 kW boost mode.

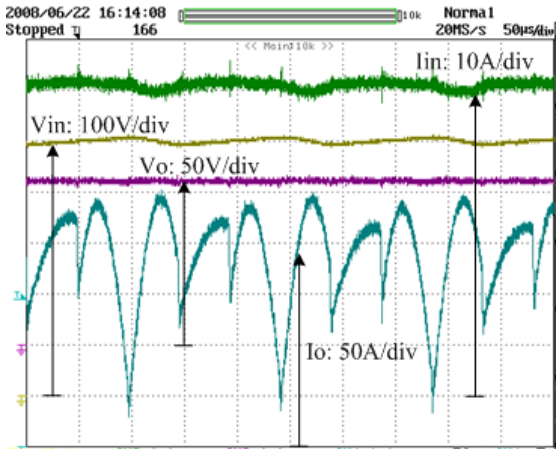

Fig. 5. Input and output voltage and current waveforms for 30 kW output in 3X buck mode.

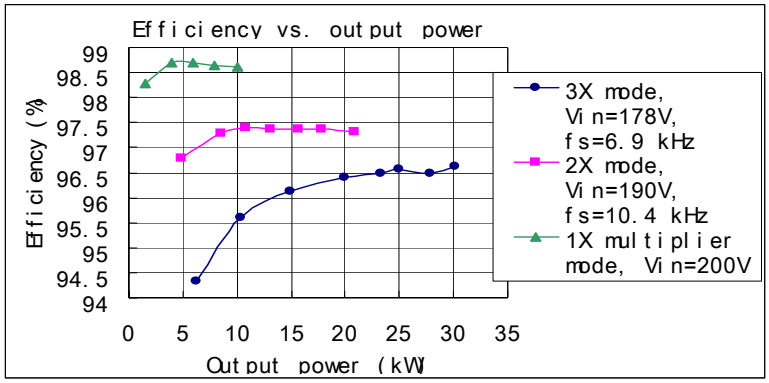

Fig. 6. Efficiency testing results of nX boost mode.

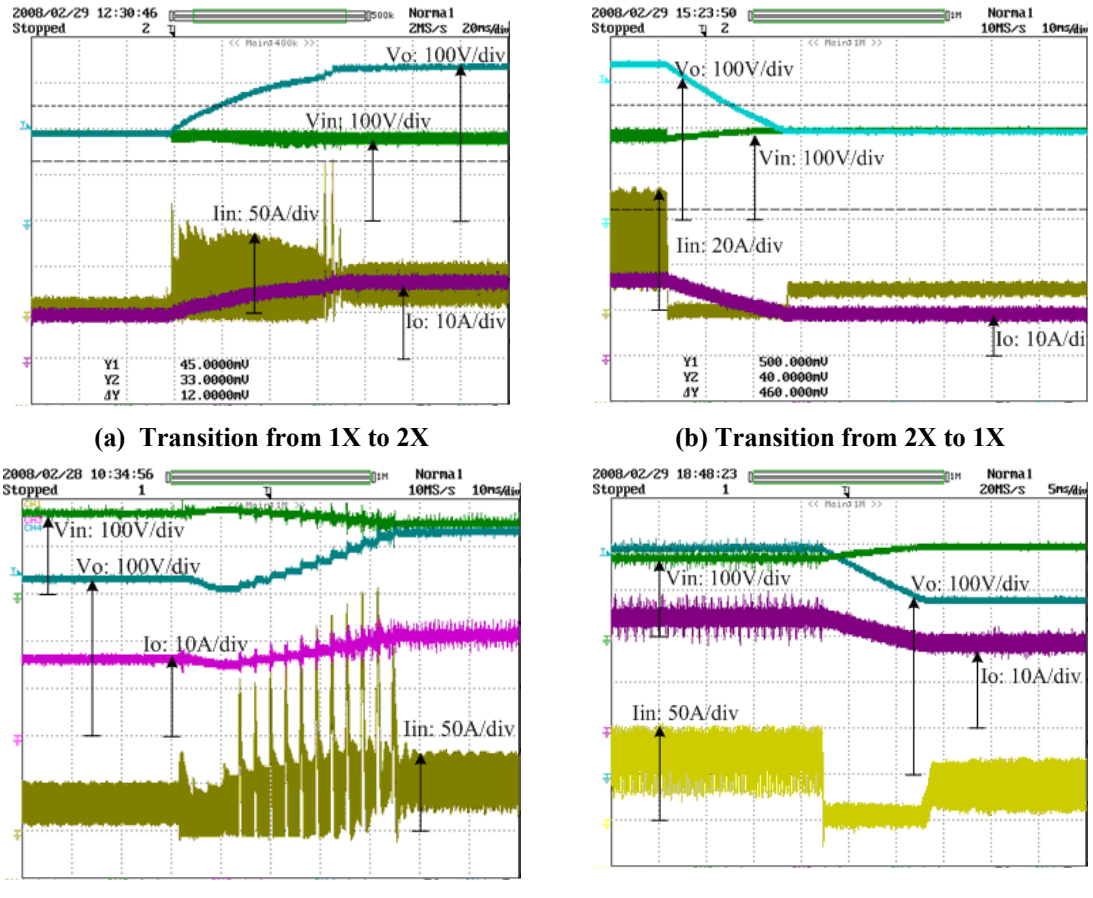

(a) Transition from 1X to 2X

(b) Transition from 2X to 1X

(c) Transition from 2X to 3X

(d) Transition from 3X to 2X

Fig. 7. Experimental results of transient performance test.

55 kW Prototype

A second-generation prototype was built with a wider operating voltage range and higher output power capability. In this prototype, the film capacitors were connected to the intelligent power module by bus bars, as shown in Fig. 8.

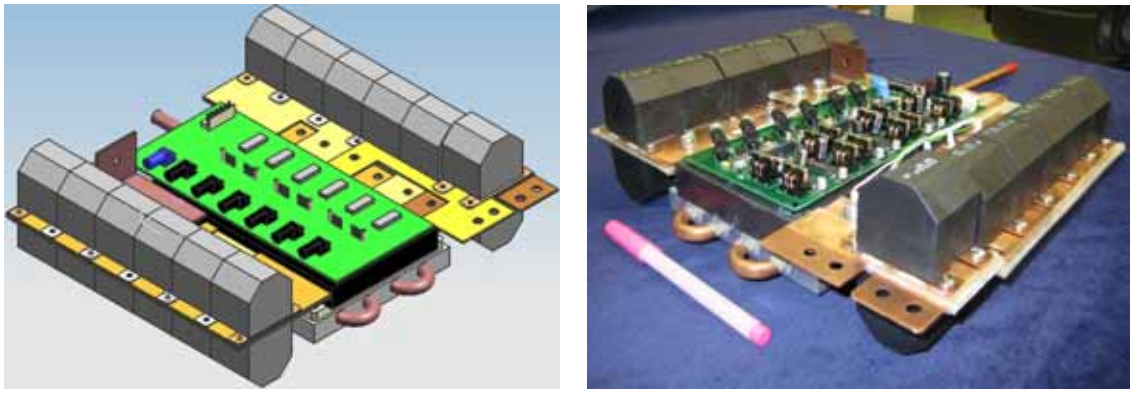

(a) 3-dimensional model **(b) 55 kW prototype.**

Fig. 8. 55 kW prototype.

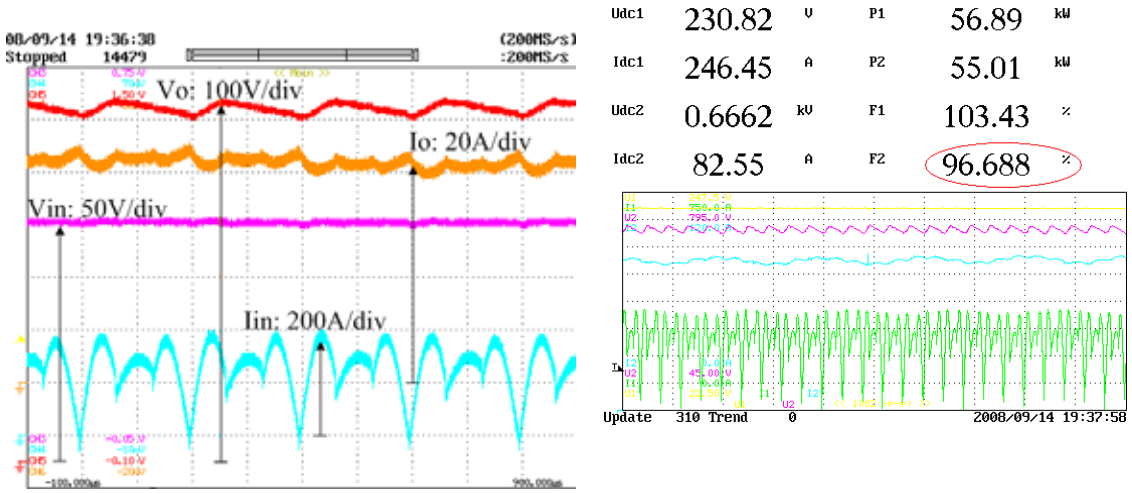

(a) Input and output waveforms **(b) Efficiency data**

Fig. 9. Experimental results at 55 kW output power for second-generation prototype.

The operation condition is specified as follows:

1. Battery side input voltage range: 100~230 V
2. Output power: 30 kW continuous power and 55 kW peak power for 18 s
3. Devices: one 6-pack
4. 600 V, 600 A intelligent power module, Powerex PM600CLA060

The nX boost mode steady state operation was tested on the 55 kW prototype. The waveforms and efficiency at rated power are shown in Fig. 9. The capacitance of C_1 in Fig. 1 is 500 uF, and C_2 is 240 uF. The lumped output capacitor C_{out} in the test is 430 uF. At 5 kHz switching frequency, the measured efficiency is 97.3% at 30 kW continuous power and 96.7% at 55 kW peak power. The optimum switching frequency for this prototype has yet to be determined. For this topology, a higher switching frequency does not necessarily lead to the lower efficiency. At higher frequency, the input current ripple will be lower so that the capacitor charging/discharging loss and the equivalent series resistance (ESR) conduction loss will be reduced. This reduction in loss might be greater than the increase in switching loss at higher switching frequency.

High-temperature gate drive integrated circuit

Figure 10 shows the schematic of the second-generation integrated, high-temperature gate driver circuit designed and fabricated using the Bipolar-complementary metal-oxide semiconductor (CMOS)-double diffused metal-oxide semiconductor (DMOS), or BCD, on-SOI process from Atmel. Compared with the first generation, this version has the additional circuitry of a dead zone generator, a pulse shaper, and an on-chip voltage regulator. A 1.25 nF bootstrap capacitor was also made on-chip. Sizes of the high-voltage negative-channel metal oxide semiconductors (NMOSs) in the half-bridge output stage were increased further to boost the current drive of the circuit. The purpose of these additions and modifications was to achieve higher reliability and to make the driver circuit more integrated.

The high-side and low-side buffers drive the gates of the high-side and low-side high voltage laterally diffused MOSs (M_H and M_L) in the half-bridge output stage, respectively. The bootstrap capacitor (C_B) based charge pump establishes a voltage above the available highest rail voltage (V_{DDH}), which works as a floating battery for the level shifter, SR latch, and high-side buffer. The level shifter converts the incoming digital input signal from the low-side voltage level (V_{DD}) to the high-side voltage level (V_{DDH}). The latch controller generates the appropriate timing pulses (S and R) for the level shifter. *SET* and *RESET* signals from the level shifter controls the SR latch, whose output is passed through the high-side buffer before being applied to the gate of the high-side transistor.

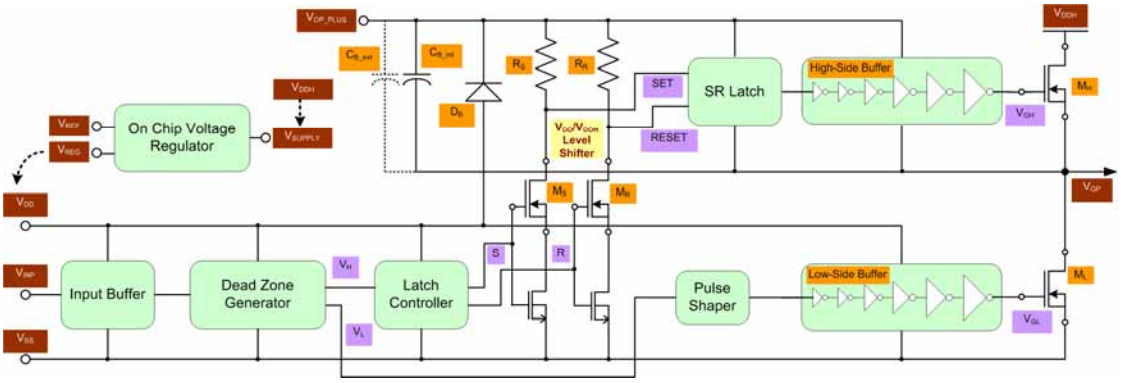

Fig. 10. Schematic of the high-voltage, high-temperature integrated circuit gate driver.

The newly added dead zone generator generates two non-overlapping copies (V_H and V_L) of the incoming logic level input signal. The dead time provided between these two copies ensures the complementary turning ON and OFF of the transistors in the output stage. Since the pulse trains generated by this circuit pass through different circuit paths, an additional pulse shaper circuit is also introduced to further modify the low-side gate signal to ensure complementary switching of the M_H and M_L transistors. Figure 11 shows the schematic of the dead zone generator that uses a circuit topology similar to that of a complementary clock generator with the addition of delay components.

The high-voltage, high-temperature gate driver integrated circuit (IC) was fabricated using 0.8 micron, 3-metal, and 2-poly bipolar complementary MOS and double-diffused MOS (BCD) in an SOI process from Atmel. Figure 12 shows the fabricated chip's microphotograph compared with a dime. This circuit occupies an area of 5 mm^2 (2,240 µm × 2,240 µm) including an on-chip bootstrap capacitor, a voltage regulator, bonding pads, and electrostatic discharge protections. The two high-voltage NMOS devices of the half-bridge output stage occupy a major portion of the chip area. They are sized (W/L = 28,000 µm/1.6 µm) to provide large peak current to obtain shorter rise and fall times. Each of these NMOS transistors comprises seven hundred 45 V NMOS devices (each with W = 40 µm) connected in parallel.

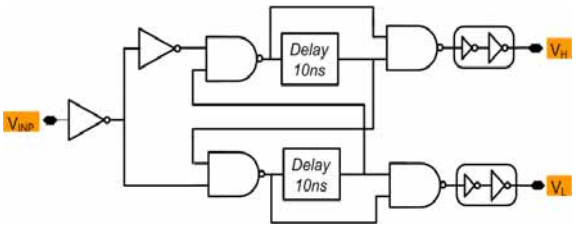

Fig. 11. Dead zone generator circuit.

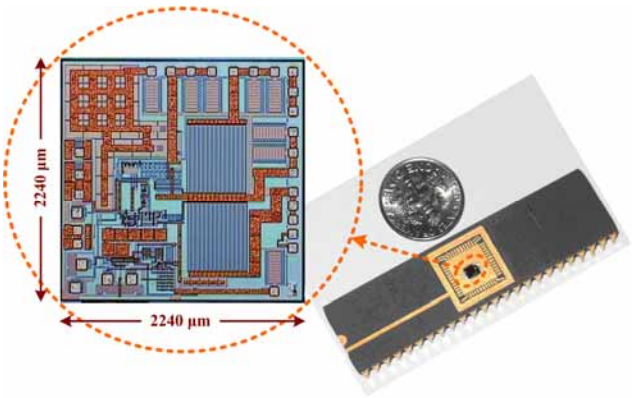

Fig. 12. Microphotograph of the gate driver integrated circuit.

Multiple pad connections are used for the power supply and output nodes to minimize the bond wire's parasitic inductances. All critical metal interconnects are made thick to avoid electromigration, which is a potential failure mechanism at higher temperatures.

High-temperature packaging of the bare dies was developed by both Atmel and Promex; 48-pin dual in-line ceramic packages were used for high-temperature testing. A double-layer PCB was designed to mount the chip and power supply filter networks. These boards were fabricated by Sierra Proto using polyimide material, which can withstand temperatures higher than 200°C. Figure 13 shows one of the test boards used for high-temperature testing of the prototype circuit. High-melting-point solder was used to connect all the components to the PCB. All the connection wires to the PCB used during testing have insulation made of Teflon so that they can safely operate at 200°C. Tantalum capacitors from Kemet (rated for 175°C and 50 V) were used in the test board for power supply filtering. For more reliable testing of the gate driver circuit, capacitors with even higher voltage and temperature ratings are needed.

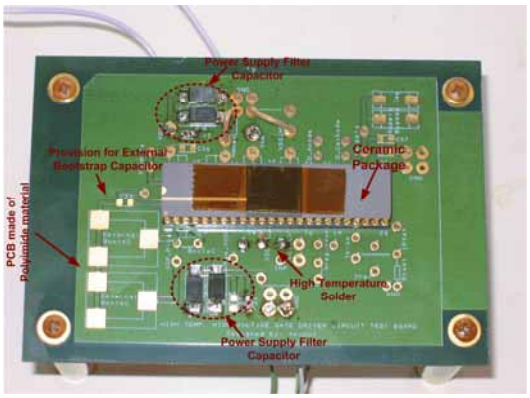

Fig. 13. High temperature test board.

A SiC power metal-oxide semiconductor field-effect transistor (MOSFET) prototype, developed by Cree, was tested with this gate driver chip. An 80 Ω load was used with the SiC MOSFET in a common-source configuration, and the bus voltage was set at 320 V. A 4 A peak load current was passing through the MOSFET when it was turned ON by the gate driver circuit. The test board was placed inside the temperature chamber and the SiC MOSFET kept outside the chamber, as it was not packaged for high-temperature applications. Starting from room temperature, the chip was tested at up to 200°C. Switching frequency was set at 20 kHz and the duty cycle was 10%.

Figure 14 shows the gate voltage (pink), gate drive current (green), and MOSFET drain terminal voltage (blue) and load current (cyan) waveforms at 200°C. The temperature of the chamber was raised from room temperature to 200°C in five steps (85°, 125°, 150°, 175° and 200°C). Figure 14 also shows the time-scale magnified version of the MOSFET switching edges. The ringing effect observed in the wave shapes was due to the added parasitic inductances of the connecting wires that ran from inside the

temperature chamber to the outside. Table 1 records the 10 to 90% rise-time and 90 to 10% fall-time for both the gate drive voltage signal and MOSFET drain voltage at each temperature level. These readings showed that this high-temperature gate driver circuit maintains a fairly constant driving strength over the entire test temperature range.

Table 6. Rise-time and fall-time at different ambient temperatures

Ambient temperature (°C)	Drain voltage (V_{DS})		Gate voltage (V_{GS})	
	t_{rise} (ns)	t_{fall} (ns)	t_{rise} (ns)	t_{fall} (ns)
25	24.1	40.9	42.3	55.6
85	20.9	39.3	42.8	55.6
125	24.8	41.2	43.5	61.1
150	23.5	39.2	43.9	63.7
175	25.2	41.9	43.7	65.5
200	25.1	41.5	43.5	63.3

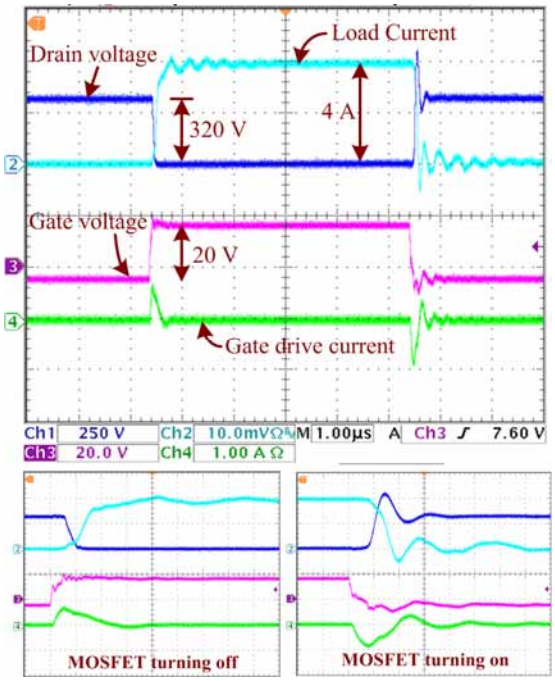

Fig. 14. Prototype circuit's test results at 200°C when driving SiC MOSFET.

This gate driver circuit was also tested with a SiC normally-on JFET from SemiSouth. The prototype gate driver circuit was used to generate a 35 V peak-to-peak (–31.6 V to 3.4 V) gate signal to control the JFET, which was connected to a 160 V bus through a 40 Ω load resistor. Figure 15 shows this test result at room temperature. This driver IC was also tested at up to 200°C with the JFET with the bus voltage set to a relatively low voltage (50 V) and the load resistor at 10 Ω. In both MOSFET and JFET testing, the duty cycle of the logic signal and hence the gate drive signal were also varied from 1 to 99%.

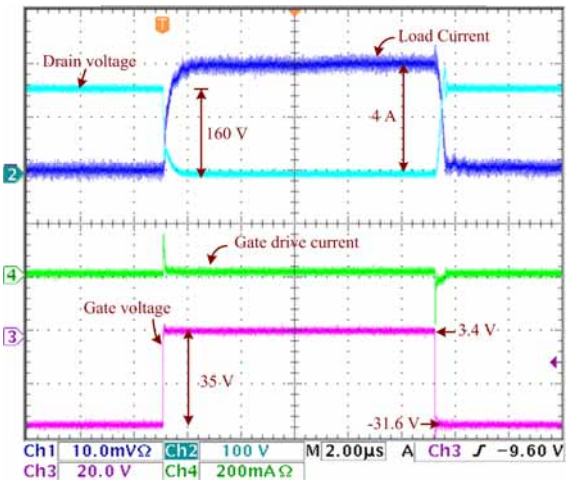

Fig. 15. Prototype circuit's test results at room temperature when driving SiC normally ON JFET.

In this prototype an on-chip voltage regulator (first generation) was included to generate the low bias voltage (V_{DD}) from the high supply voltage (V_{DDH}) to the chip. Depending on the required gate voltage of the SiC power switch that this driver is driving, the V_{DDH} can be set to any value between 15 and 30 V. Hence this regulator needs to work over a wide range of input voltage in addition to maintaining a stable output voltage over a wide temperature range (−50 to 200°C).

A schematic of the low-dropout type of voltage regulator topology used in this work is shown in Fig. 16. This circuit has two distinct building blocks. The first is a bandgap reference (BGR) circuit that generates a constant reference voltage over a wide temperature variation. The second is a single-stage differential amplifier that forms a negative feedback loop with a positive-channel metal-oxide semiconductor (PMOS) pass transistor. A compensation circuit has been added to improve the phase margin of the voltage regulator. The temperature-compensated reference voltage generated by the BGR circuit is used as the reference voltage for the differential input amplifier. The temperature coefficient (TC) of the BGR is minimized by proper weighting of the positive TC of the thermal voltage with the negative TC of the diode forward voltage in the circuit.

Figure 17 shows the regulator output voltage in response to a 15 and 30 V input signal while 4.16 mA peak current is supplied to the load. Figure 17 (inset) also shows the reference voltage generated by the BGR circuit in this test condition. The regulator worked at up to 150°C without any heat sink or cooling. Although the BGR circuit, while tested independently, generated fairly constant voltage up to 200°C, the regulator failed above 150°C. The current driving capability of the regulator circuit needs to be increased to use it with the gate driver circuit. The regulator circuit also needs to be revised and improved to make it work with the gate driver circuit at ambient temperatures of 200°C or more.

A second generation of the high–voltage, high-temperature IC gate driver has been fabricated in the SOI process. This circuit has been tested at high temperatures (≥ 200°C) for several cycles without any cooling. So far no failure or any significant performance deterioration has been observed. This driver circuit has been successfully tested with a SiC MOSFET from Cree and a SiC normally-on JFET from SemiSouth. The duty cycle of the gate drive signal was also varied from 1 to 99%. The bandgap voltage reference (BGR) circuit part of the voltage regulator generated a near constant reference voltage up to 200°C.

However, the complete voltage regulator circuit could not generate 5 V above 150°C. (Note that the voltage regulator circuit was a first generation circuit on the second generation chip—the first generation chip did not have a voltage regulator circuit).
Knowledge learned from this design will be used to design a newer version of the regulator circuit.

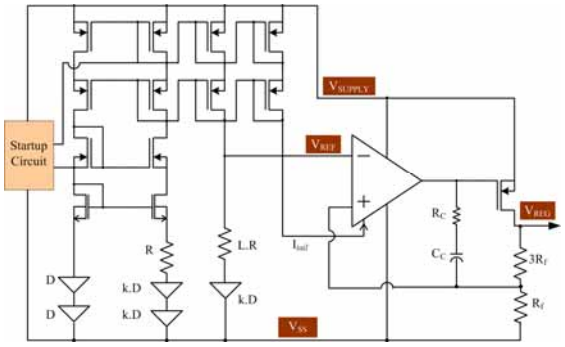

Fig. 16. Schematic of the first-generation on-chip voltage regulator circuit.

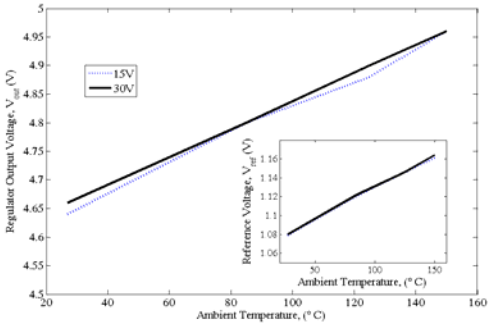

Fig. 17. Regulator test result (up to 150°C) with 4.26 mA peak load current.

This SOI-based driver IC can be used for both SiC MOSFETs and JFETs and in any power electronics modules in which ambient temperature is higher than 125°C, which is the typical maximum operating range of bulk Si-based gate drivers. The SOI-based high temperature-gate driver IC will extend to the system level the advantages of high-temperature capabilities provided by wide-bandgap power devices such as SiC-based power FETs.

Some of the features of the integrated SOI gate drive are:

- Built using the advantages of BCD on SOI processes
- High source and sink current capability: peak 2.3 A @ 27°C and 1.7 A @ 200°C ambient
- Gate drive supply range from 10 to 40 V p-p
- High operating temperature: 200°C ambient without any cooling mechanism
- High capacitive load drive capability: 10 nF in <100ns @ 200°C
- Integrated bootstrap diode and capacitor
- Low supply current
- Built-in dead-time control function
- Output in phase with the input

High-temperature packaging

Several SiC JFET samples packaged for operation in ambient temperatures of up to 175°C ambient were obtained from SiCED (Germany), tested, and characterized. The SiCED SiC JFET had a voltage rating of 1200 V and an on resistance of 150 mΩ@1A.

The devices were placed in an environmental chamber to raise the ambient temperature from 25°C up to 175°C in 25°C increments. The static characteristics of the SiC JFET are shown in Fig. 18. The on-state resistance of the SiC JFET increased with temperature, while the transfer characteristic changed only slightly for the temperatures used in the tests.

The switching energy losses at different temperatures and current levels are shown in Fig. 19; they increased with current and did not change much with temperature. A custom gate drive PCB for double

pulse switching was designed, fabricated, and populated. The commercial gate driver IC HCNW3120 was used to drive the SiC JFET. The gate voltage was 0 V for "turn on" and −15 V for "turn off".
Figure 19 shows that the switching loss in the SiC JFET is almost independent of temperature for the 25 to 175°C region. It also shows that the transfer characteristic (gate voltage requirement) is nearly independent of temperature. However, the on-state resistance does increase with temperature, but this will allow the devices to be paralleled.

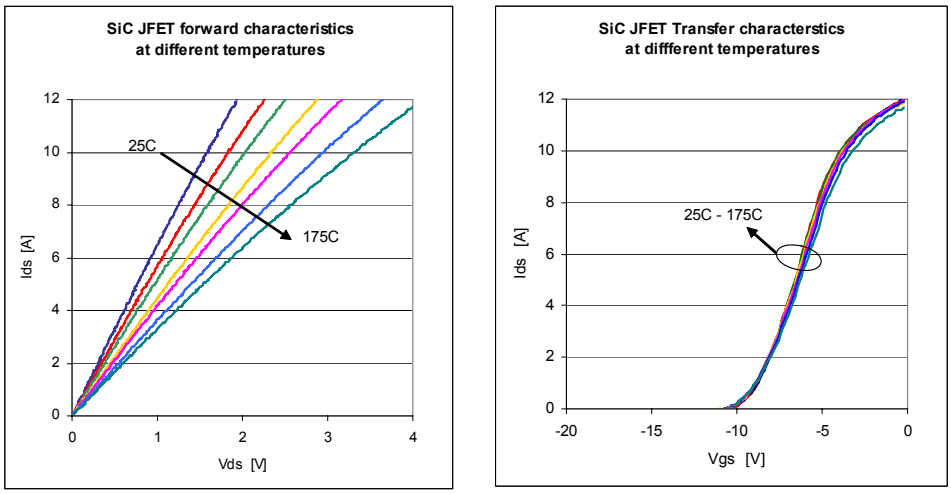

(a) Forward characteristics (I-V curve) **(b) Transfer characteristics**

Fig. 18. Static characteristics of the SiC JFET (SiCED, 1200 V, 150 mΩ).

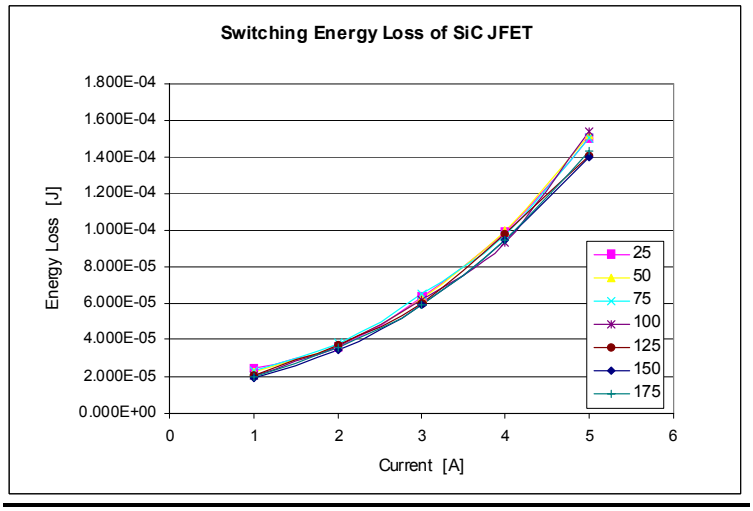

Fig. 19. Switching loss of the SiC JFET vs. current at different temperatures.

Conclusion

This challenging project involves the development and demonstration of several novel technologies in order to achieve a converter that can operate at high ambient temperatures. Novel magnet-less or small

magnetic dc-dc converter topologies will result in reduced volume and weight compared with conventional topologies. The multilevel design of these converters will also allow segregation of the battery pack into multiple modules. This will allow replacement of only a portion of the battery pack in case of failure. It may also result in an increase in reliability and availability of the battery power, as the converter designs will allow for a damaged or failed battery module or power electronics module to be bypassed.

A high-temperature gate drive has been fabricated in SOI and tested at high temperatures. This design shows great promise for allowing the gate drive to be located near high-temperature power electronics with no cooling. SiC JFETS show switching loss and transfer characteristics to be independent of temperature and the ability to operate at high ambient temperatures. Slow progress in SiC switching transistors (JFETs) and high-temperature capacitors has hampered this project, but it has nonetheless demonstrated several valuable technologies for future hybrid electric vehicles. Gains made from this project will likely impact other power electronics projects that need high-temperature packaging, gate drives, or modular conceptual designs.

Publications

1. M. A Huque, S. K. Islam, B. J. Blalock, C. Su, R. Vijayaraghavan, and L. M. Tolbert, "Silicon-on-insulator based high-temperature electronics for automotive applications," in *IEEE International Symposium on Industrial Electronics*, Cambridge, England, June 30–July 2, 2008.
2. M. A Huque, B. J. Blalock, C. Su, R. Vijayaraghavan, S. K. Islam, and L. M. Tolbert, "SOI-based integrated circuits for high-temperature applications," in *IMAPS International Conference on High Temperature Electronics*, Albuquerque, New Mexico, May 12–15, 2008.
3. M. Shen, F. Z. Peng, and L. M. Tolbert, "Multilevel DC-DC power conversion system with multiple DC sources," *IEEE Transactions on Power Electronics* **23**(1), 420–426 (January 2008).
4. F. Khan and L. M. Tolbert, "A multilevel modular capacitor clamped DC-DC converter," *IEEE Transactions on Industry Applications* **43**, 1628–1638 (November/December 2007).
5. F. H. Khan and L. M. Tolbert, "Generating isolated outputs in a multilevel modular capacitor clamped DC-DC converter (MMCCC) for hybrid electric and fuel cell automotives," pp. 967–973 in *IEEE Power Electronics Specialists Conference*, Rhodes, Greece, June 15–19, 2008.
6. F. H. Khan and L. M. Tolbert, "A universal multilevel DC-DC converter with variable conversion ratio and high component utilization," pp. 17–23 in *IEEE Applied Power Electronics Conference*, Austin, Texas, February 24–28, 2008.
7. L. M. Tolbert, H. Zhang, M. S. Chinthavali, and B. Ozpineci, "SiC-based power converters for high temperature applications," *Materials Science Forum* **556–557**, 965–970 (2007).

4.4 Current Source Inverter

Principal Investigator: Gui-Jia Su
Oak Ridge National Laboratory
National Transportation Research Center
2360 Cherahala Boulevard
Knoxville, TN 37932
Voice: 865-946-1330; Fax: 865-946-1262; E-mail: sugj@ornl.gov

DOE Technology Development Manager: Susan A. Rogers
Voice: 202-586-8997; Fax: 202-586-1600; E-mail: Susan.Rogers@ee.doe.gov

ORNL Program Manager: Mitch Olszewski
Voice: 865-946-1350; Fax: 865-946-1262; E-mail: olszewskim@ornl.gov

---

Objectives

- Overall project objectives
  - — Eliminate the drawbacks of the voltage source inverter (VSI) by switching to a current-source–based topology.
  - — Reduce inverter cost and volume by 25% compared with the Toyota Prius inverter.
  - — Improve inverter and motor lifetime.
  - — Increase motor efficiency (10% loss reduction).
  - — Increase constant-power speed range.
  - — Reduce the cost and size of batteries in plug-in hybrid electric vehicles (HEVs).
  - — Enable silicon carbide (SiC) -based inverters to operate in elevated-temperature environments.
- Objectives for FY 2008 effort
  - — Design, fabricate and test a 55 kW prototype with a voltage boost ratio of 3, a reduction in motor voltage harmonic distortion and bearing leakage current of 90%, and a reduction in capacitor requirements from 2,000 to 200 μF.

Approach

- Finalize the inverter design developed in FY 2007.
- Fabricate a prototype of a 55 kW current source inverter (CSI) based on the design specifications.
- Develop digital signal processing (DSP) code to implement the control algorithms.
- Test and evaluate the prototype against the technical performance goals.

Major Accomplishments

- A 55 kW prototype was designed, fabricated and successfully tested.
- Total capacitance was reduced to 195 μF.
- Test results confirmed a voltage boost ratio of up to 3.47.
- An output voltage total harmonic distortion factor lower than 12.5% was achieved.
- Measured motor leakage current at each motor terminal voltage was as low as 1.146 mA/V.

Future Direction

- Design, fabricate, and test a 55 kW prototype that can operate with a 105°C coolant.

Technical Discussion

Background

Current electric and hybrid electric vehicles (EVs/HEVs) use inverters that operate off a voltage source. They are called VSIs (Fig. 1a) because the most readily available and efficient energy storage devices, batteries, are inherently voltage sources. The VSI, however, possesses several drawbacks that make it difficult for it to meet FreedomCAR goals for volume, lifetime, and cost for an inverter operating with a high-temperature (105°C) coolant. A VSI requires a very-high-performance dc bus capacitor to maintain a near-ideal voltage source. Also, currently available capacitors that can meet the demanding requirements are costly and bulky, taking up one-third of the inverter volume and cost. The reliability of the inverter is also limited by the capacitors and further hampered by the possible shoot-throughs of the phase legs making up a VSI (S_1-S_2, S_3-S_4, and S_5-S_6 in Fig. 1a). In addition, steep rising and falling edges of the output voltage in the form of pulse trains generate high electromagnetic-interference (EMI) noises, impose high stress on the motor insulation, and produce high-frequency losses in the copper windings and iron cores of the motor, as well as generate bearing-leakage currents that erode the bearings over time.

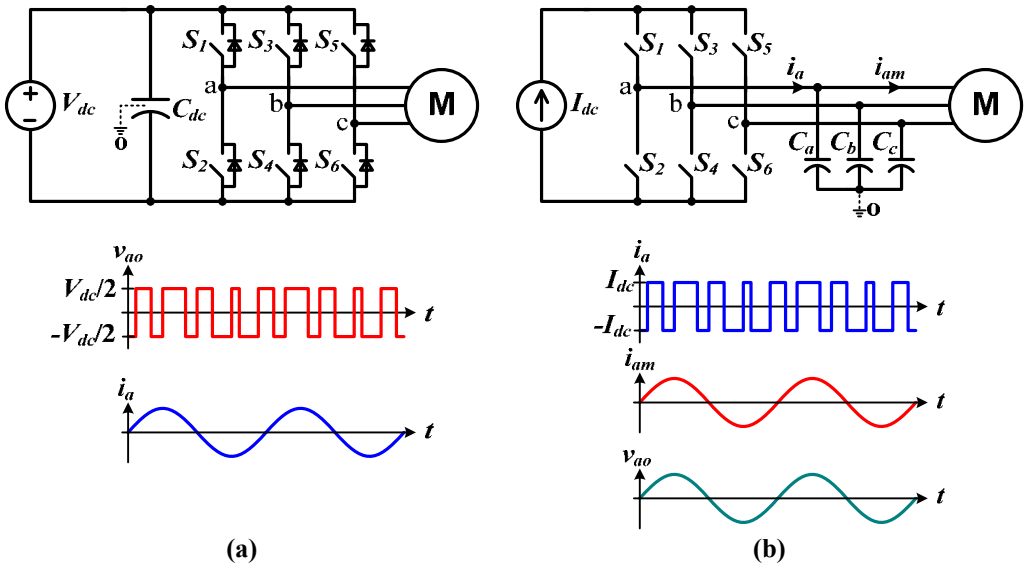

Fig. 1. Schematics of the two types of inverters and typical output voltage and current waveforms: (a) the voltage source inverter and (b) the current source inverter.

As the maximum operating junction temperature of the latest silicon insulated gate bipolar transistors (IGBTs) increases, the capacitor, in fact, presents the most difficult hurdle to operating a VSI in automotive high-temperature environments. The function of the dc bus capacitor is twofold: (1) to maintain a near-ideal voltage source and (2) to absorb the ripple current generated by the switching actions of the inverter.

The root mean square value of the ripple current is proportional to the motor current with a maximum ratio of 50~60%, depending on the pulse-width modulation (PWM) scheme. Currently, two types of dielectrics, polymer film and ceramics, are being pursued for use in high-temperature environments. The polymer-film capacitor is the choice of capacitor technology for HEVs currently on the market because of its benign failure mode and adequate ripple-current handling capability at a lower coolant temperature (about 70°C); however, its ripple-current handling capability rapidly diminishes as the temperature increases. As a result, a significantly larger capacitor would be required in the higher operating temperature environment. On the other hand, although ceramic capacitors can still provide adequate

ripple-current capability even at higher temperatures, their tendency to produce catastrophic failures and their higher cost have made them unacceptable for HEV applications.

In addition, for the VSI to operate from a low-voltage battery, a bidirectional dc-dc converter is needed. Figure 2 shows a widely used inverter topology with such a converter, where two additional IGBTs and an inductor are used for interface with a low-voltage battery.

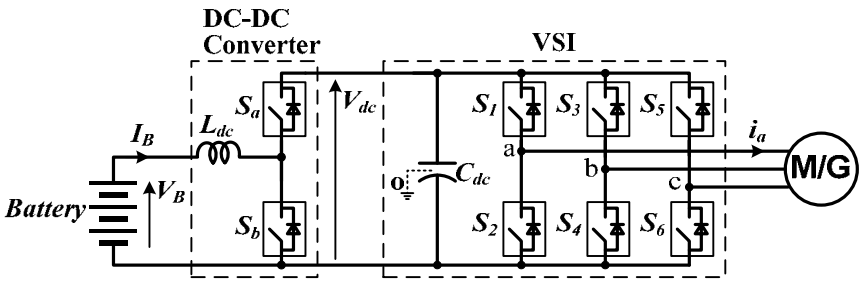

Fig. 2. A voltage source inverter with a bidirectional dc-dc converter for interfacing with a low-voltage battery.

All these problems can be eliminated or significantly reduced by the use of another type of inverter, the current source inverter (CSI) (Fig. 1b). The CSI requires no dc bus capacitors and uses only three alternating-current (ac) filter capacitors of a much smaller capacitance. The total capacitance of the ac filter capacitors is estimated at approximately one-fifth that of the dc bus capacitance in the VSI. In addition, the CSI offers many other advantages important for EV applications: (1) it does not need antiparallel diodes in the switches, (2) it can tolerate phase-leg shoot-throughs, (3) it provides sinusoid-shaped voltage output to the motor, and (4) it can boost the output voltage to a higher level than the source voltage to enable the motor to operate at higher speeds. These advantages could translate into a significant reduction in inverter cost and volume with increased reliability, a much higher constant-power speed range, and improved motor efficiency and lifetime.

Two factors, however, have so far prevented the application of CSIs in HEVs. The first is the difficulty of incorporating batteries into a CSI as energy-storage devices; the second is the limited availability of power switches that can block voltages in both forward and reverse directions. IGBTs with reverse-blocking capability are being offered as engineering samples, and the technology is rapidly reaching the maturity needed for commercial production. This research aims to remove the remaining hurdles and bring the advantageous CSI to HEV applications by offering a new inverter topology based on the CSI but with a novel scheme to incorporate energy-storage devices. By significantly reducing the amount of capacitance required, the CSI-based inverter with silicon IGBTs will be able to substantially decrease the requirements for cooling systems and, further, could enable air-cooled power inverters in the future when SiC-based switches become commercially viable.

The overall objective of the research is to design, fabricate, test, and evaluate a 55 kW inverter prototype based on the novel CSI topology to replace the VSI for EV and HEV applications. Three major tasks will be carried out over a 3-year period: (1) modeling and simulation, (2) design and fabrication of a 55 kW prototype, and (3) testing and evaluation. In FY 2007, computer modeling and simulation was conducted to down-select an optimal interfacing circuit, followed by production of a conceptual design of a 55 kW inverter system. Building on the FY 2007 activities, a 55 kW prototype was be designed, fabricated, and tested in FY 2008 to provide data for performance analysis.

Description of the proposed current source inverter

Figure 3 shows a schematic of the proposed CSI with a battery-interfacing circuit. The interfacing

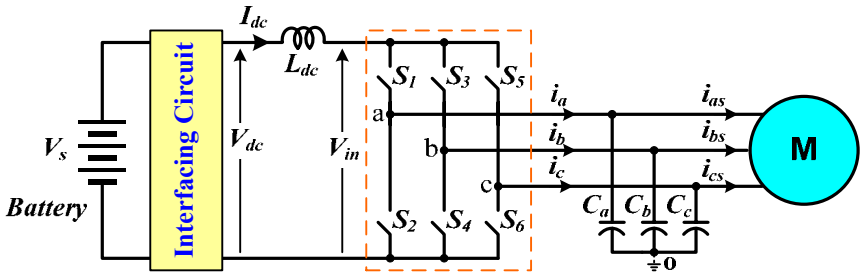

Fig. 3. Schematic of the proposed current source based inverter.

circuit—with the help of the dc choke, L_{dc}—transforms the voltage source of the battery into a current source to the inverter bridge by providing the capability to control and maintain a constant dc bus current, I_{dc}. More important, the interfacing circuit also enables the inverter to charge the battery during dynamic breaking without the need for reversing the direction of the dc bus current.

Whereas the VSI produces a voltage pulse train, the CSI generates a current pulse train in each phase output by turning on and off the switches, S_1-S_6, in the bridge according to a PWM strategy. The pulsed phase currents are then filtered by a simple filter network of the three capacitors, C_a, C_b, and C_c, leaving near sinusoidal currents as well as sinusoidal voltages to the electrical motor. The sinusoidal voltages are desirable for the motor because they eliminate problems with the VSI output voltages. These include pulse trains with steep rising and falling edges, which generate high EMI noises imposing high stresses on the motor insulation, and producing high-frequency losses in the copper windings and iron cores of the motor as well as generating bearing-leakage currents.

An ac generator driven by an internal combustion engine could also be incorporated into the inverter system for hybrid vehicles.

Generally, modulation schemes can be categorized into two main groups: carrier-based and space vector schemes. Because of the duality between the VSI and CSI, it is possible to translate the modulation schemes between the two types of inverters. Switching tables of the VSI and the CSI are given in Table 1 and Table 2, respectively. The space vector diagrams are given in Fig. 4.

Table 1. Switching table of the VSI

	Top devices			Bottom devices			Phase voltages		
	S_1	S_3	S_5	S_2	S_4	S_6	V_{ao}	V_{bo}	V_{co}
V_0	0	0	0	1	1	1	0	0	0
V_1	1	0	0	0	1	1	V_{dc}	0	0
V_2	1	1	0	0	0	1	V_{dc}	V_{dc}	0
V_3	0	1	0	1	0	1	0	V_{dc}	0
V_4	0	1	1	1	0	0	0	V_{dc}	V_{dc}
V_5	0	0	1	1	1	0	0	0	V_{dc}
V_6	1	0	1	0	1	0	V_{dc}	0	V_{dc}
V_7	1	1	1	0	0	0	V_{dc}	V_{dc}	V_{dc}

Table 2. Switching table of the CSI

	Top devices			Bottom devices			Phase currents		
	S_1	**S_3**	**S_5**	**S_2**	**S_4**	**S_6**	i_a	i_b	i_c
I_1	1	0	0	0	0	1	I_{dc}	0	$-I_{dc}$
I_2	0	1	0	0	0	1	0	I_{dc}	$-I_{dc}$
I_3	0	1	0	1	0	0	$-I_{dc}$	I_{dc}	0
I_4	0	0	1	1	0	0	$-I_{dc}$	0	I_{dc}
I_5	0	0	1	0	1	0	0	$-I_{dc}$	I_{dc}
I_6	1	0	0	0	1	0	I_{dc}	$-I_{dc}$	0
I_7	1	0	0	1	0	0	0	0	0
I_8	0	1	0	0	1	0	0	0	0
I_9	0	0	1	0	0	1	0	0	0

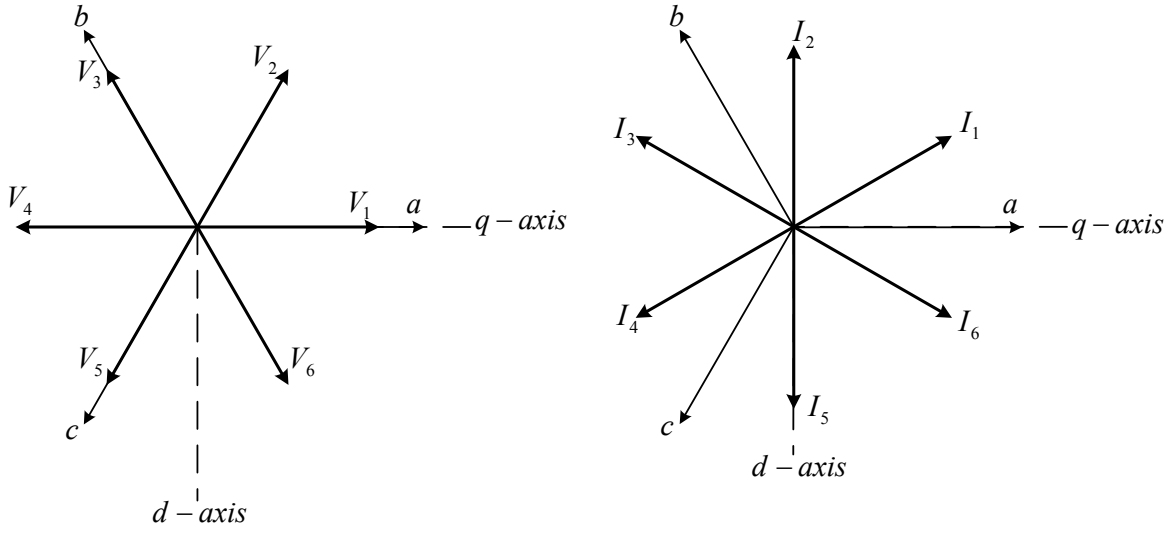

Fig. 4. Space vector diagrams for the VSI (left) and CSI (right).

The voltage vector of the VSI is mapped to the current vector of the CSI according to the following rules:

$$\begin{aligned} &V_1 \to I_6 \qquad V_2 \to I_1 \\ &V_3 \to I_2 \qquad V_4 \to I_3 \\ &V_5 \to I_4 \qquad V_6 \to I_5 \end{aligned} \tag{1}$$

The switching functions of the CSI can then be mapped from that of the VSI by

$$\begin{aligned} &S_{1i} = S_{1v} \cdot S_{6v} + S_{0i} \qquad S_{3i} = S_{3v} \cdot S_{2v} + S_{0i} \\ &S_{5i} = S_{5v} \cdot S_{4v} + S_{0i} \qquad S_{2i} = S_{2v} \cdot S_{5v} + S_{0i} \\ &S_{4i} = S_{4v} \cdot S_{1v} + S_{0i} \qquad S_{6i} = S_{6v} \cdot S_{3v} + S_{0i} \end{aligned} \tag{2}$$

where the subscript "*v*" represents the switching function of the VSI and the subscript "*i*" represents that of the CSI; S_{0i} represents the zero sequence states of the CSI, I_7, I_8 and I_9. The zero sequence signals are there to balance the on time intervals for the switches and will not affect the fundamental component; however, they can be used to minimize the switching losses. Table 3 gives the optimal zero sequence for each switching state.

Table 3. Optimal zero sequence

Current active vector	Next active vector	Sector	Optimal zero sequence
I_6	I_1	I	I_7
I_1	I_2	II	I_9
I_2	I_3	III	I_8
I_3	I_4	IV	I_7
I_4	I_5	V	I_9
I_5	I_6	VI	I_8

It should be noted that because of the phase angle difference between the voltage vectors and the current vectors, the direct mapping of the space vectors of the VSI to those of the CSI produces a 30° phase shift between the output current and the reference current.

The triangle carrier-based modulation produces two active zones, each composed of two active states arranged with different sequences. Zero states are located at both the beginning and the end of each active zone. The sawtooth carrier-based modulation, on the other hand, removes the zero state between the two active zones and combines the two active zones into one. Therefore, the latter may further reduce the amount of device switching over a switching cycle.

Space vector PWM is another attractive method for digital control because of its inherent advantage of enabling direct calculations in the *qd* reference frame and straightforward implementation in digital controllers. The space vector modulation methodology of a VSI can also be adapted to a CSI. The goal is to optimally use the three variables—two active vectors "a" and "b" and a zero vector—to generate the desired current vector. The process of implementation can be divided into three steps: (1) transformation of the commands from the abc stationary reference frame to the q-d stationary reference frame, (2) calculation of the time intervals of the vectors "a" and "b", and (3) generation of modulation signals based on the time intervals. Table 4 gives the normalized time interval for the two active and zero vectors for each sector.

The carrier-based PWM scheme can be realized by direct mapping from VSI counterparts and is thus simple and easy to implement with analog circuits. The active state intervals are calculated indirectly, and the sequence and ordering of the active states are implicit for the carrier-based PWM schemes; however, with the space vector PWM algorithm, the sequence, the ordering, and the period of the active states are all explicitly computed. Moreover, the sequence of the active states and null state can be arranged arbitrarily as long as the total time period for each switching cycle meets the desired value. The space vector PWM algorithm is therefore good for digital control and will be used in prototype development.

Table 4. Normalized time intervals for the two active and zero vectors for each sector

Sector	First active vector (t_α)	Second active vector (t_β)	Zero vector (t_0)
I	$-\frac{i_c}{I_{dc}}$	$-\frac{i_b}{I_{dc}}$	$1-\frac{i_a}{I_{dc}}$
II	$\frac{i_b}{I_{dc}}$	$\frac{i_a}{I_{dc}}$	$1+\frac{i_c}{I_{dc}}$
III	$-\frac{i_a}{I_{dc}}$	$-\frac{i_c}{I_{dc}}$	$1-\frac{i_b}{I_{dc}}$
IV	$\frac{i_c}{I_{dc}}$	$\frac{i_b}{I_{dc}}$	$1+\frac{i_a}{I_{dc}}$
V	$-\frac{i_b}{I_{dc}}$	$-\frac{i_a}{I_{dc}}$	$1-\frac{i_c}{I_{dc}}$
VI	$\frac{i_a}{I_{dc}}$	$\frac{i_c}{I_{dc}}$	$1+\frac{i_b}{I_{dc}}$

Modeling and control of the current source inverter

Assume the interface circuit generates the output voltage, V_{dc}, proportional to the input voltage, V_s, i.e.,

$$V_{dc} = M_{dc} \cdot V_s , \tag{3}$$

where M_{dc} is a control signal. The CSI switch network can be modeled by

$$i_a = S_1 \cdot I_{dc} - S_2 \cdot I_{dc}, \quad i_b = S_3 \cdot I_{dc} - S_4 \cdot I_{dc}, \quad i_c = S_5 \cdot I_{dc} - S_6 \cdot I_{dc} . \tag{4}$$

The ac filter capacitors and dc link inductor can be described by Eqs. (5) and (6), respectively.

$$Cdv_{ao} / dt = i_a - i_{as}, \quad Cdv_{bo} / dt = i_b - i_{bs}, \quad Cdv_{co} / dt = i_c - i_{cs} ; \tag{5}$$

$$L_{dc} pI_{dc} = V_{dc} - V_{in} . \tag{6}$$

The input voltage, V_{in} can be calculated from the switching functions and the ac capacitor voltages as

$$V_{in} = v_{ao}(S_1 - S_2) + v_{bo}(S_3 - S_4) + v_{co}(S_5 - S_6) . \tag{7}$$

The equivalent circuit of the CSI, which is essentially a boost converter, is shown in Fig. 5, in which the switching device *G* represents the switches of the CSI while the RL load represents a motor.

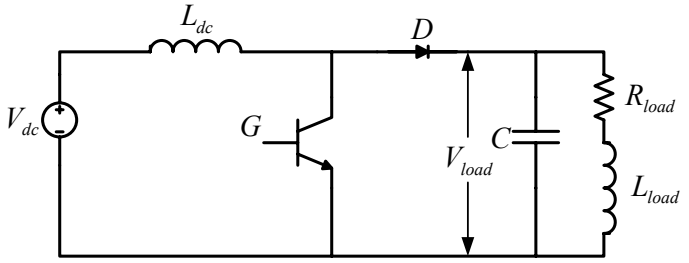

Fig. 5. Equivalent circuit of the CSI for voltage boosting.

The input and output voltages of the boost converter are related by

$$\frac{V_{load}}{V_{dc}} = \frac{1}{1 - D_{on}}, \quad (8)$$

where D_{on} is the duty ratio of the switching device G. The duty ratio is equal to the shoot-through ratio and can be found for balanced three-phase stator currents by

$$D_{on} = 1 - \frac{3}{\pi} M, \quad (9)$$

where M is the modulation index for the CSI. Equation (8) can be expressed as

$$V_{load} = \frac{\pi}{3M} V_{dc}. \quad (10)$$

It is now apparent from Eq. (10) that the load voltage increases when the magnitude of the modulation index decreases. When the desired output currents are given, the multiplication of the dc link current and the modulation signals is fixed. Hence, if the modulation signals decrease, the dc link current needs to be increased to track the desired output phase current.

Prototype and experimental results

A conceptual design of a 55 kW current source inverter was carried out in FY 2007 based on the simulation study. The design was finalized in FY 2008 and a prototype was fabricated according to the design specifications. Since the CSI requires IGBTs that can block voltages in both forward and reverse directions, and since those IGBTs were not available at the required voltage and current ratings, we designed custom modules comprised of an IGBT and a diode connected in series. We contracted with a power device manufacturer to produce the quantities needed for prototype development. Figure 6 shows photos of the prototype. The total amount of capacitance is 195 μF, compared with the 2000 μF required in a typical 55 kW VSI.

The prototype was tested with a resistive load to measure the voltage boost factor and output voltage harmonic distortion. Figure 7 plots the measured voltage boost ratio vs inverter duty cycle. The boost ratio increases as the duty cycle decreases. The measured ratio at a duty cycle of 0.35 is 3.47. Figures 8 and 9 illustrate waveforms in boost mode at voltage ratios of 2.67 and 1.35, respectively. With the help of the interfacing circuit, the CSI can also operate in buck mode to decrease the output voltage. Figure 10 shows waveforms in the buck mode at a voltage ratio of 0.67. Table 5 gives measured output voltage total harmonic distortion factor (THD) at several load power points.

The prototype was then tested with an induction motor to assess the motor bearing leakage current. Figure 11 shows test waveforms acquired during testing. The measured leakage current is 0.319A, resulting in a line-to-line motor terminal voltage value of 1.146 mA/V.

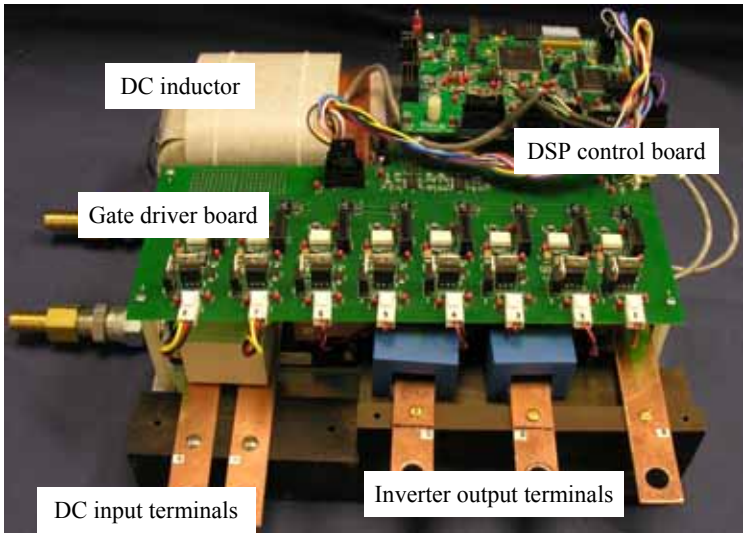

(a) Front view

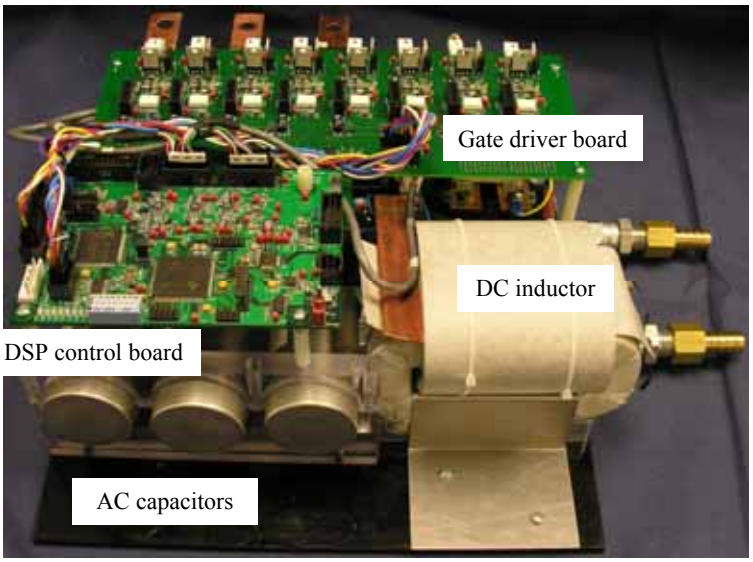

(b) Rear view

Fig. 6. A photo of the 55 kW prototype. Heat sink footprint: 8 in. width × 11 in. depth.

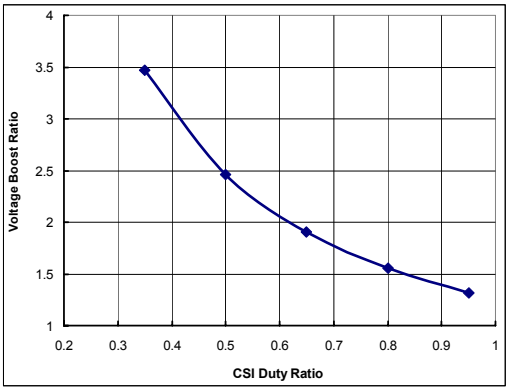

Fig. 7. Measured voltage boost ratio vs inverter duty cycle.

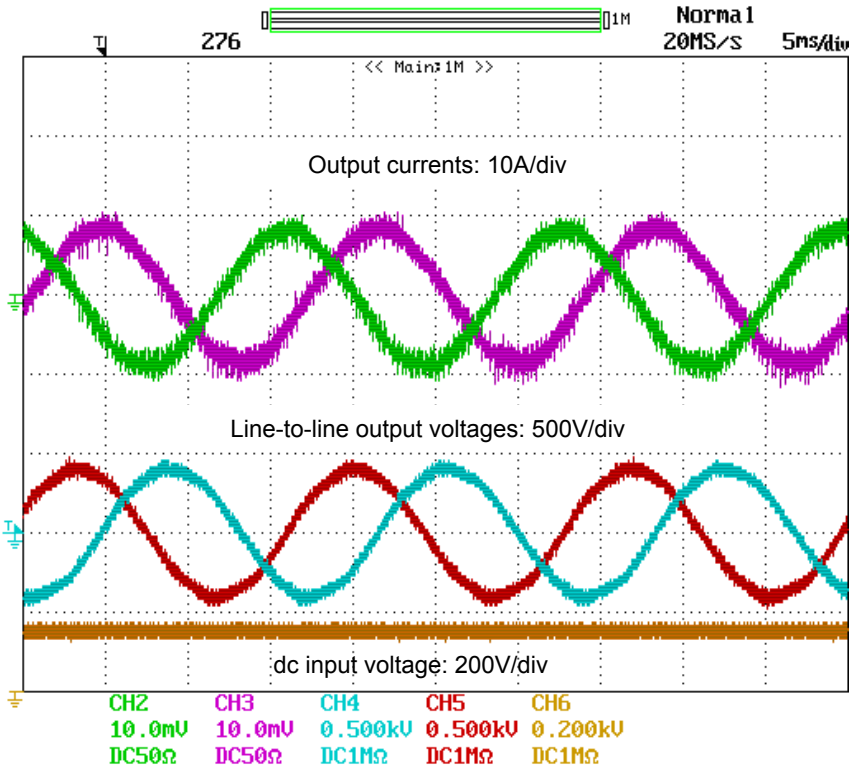

Fig. 8. Waveforms in boost mode at a voltage ratio of 2.67.

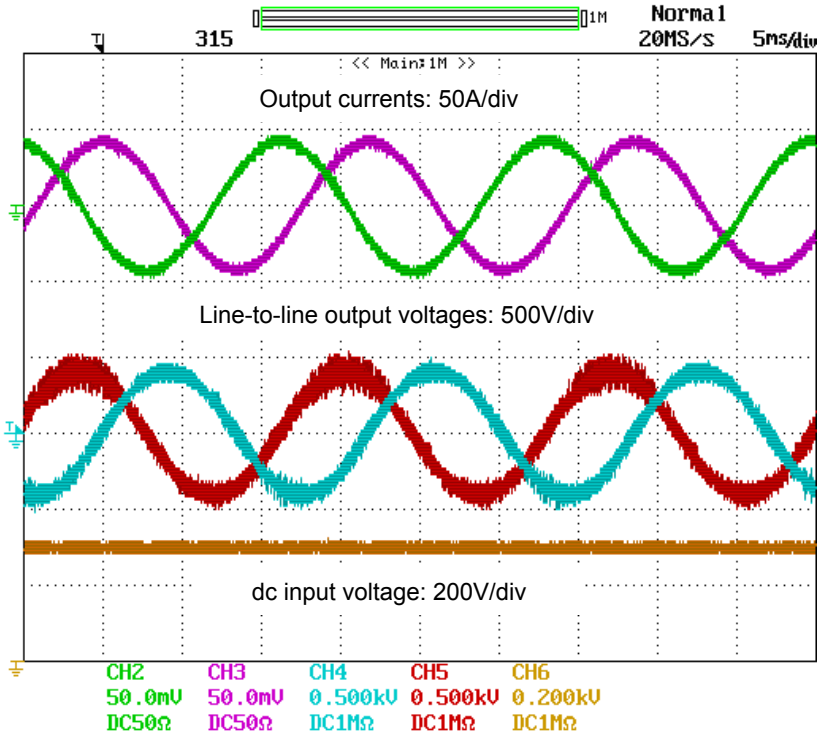

Fig. 9. Waveforms in boost mode at a voltage ratio of 1.35.

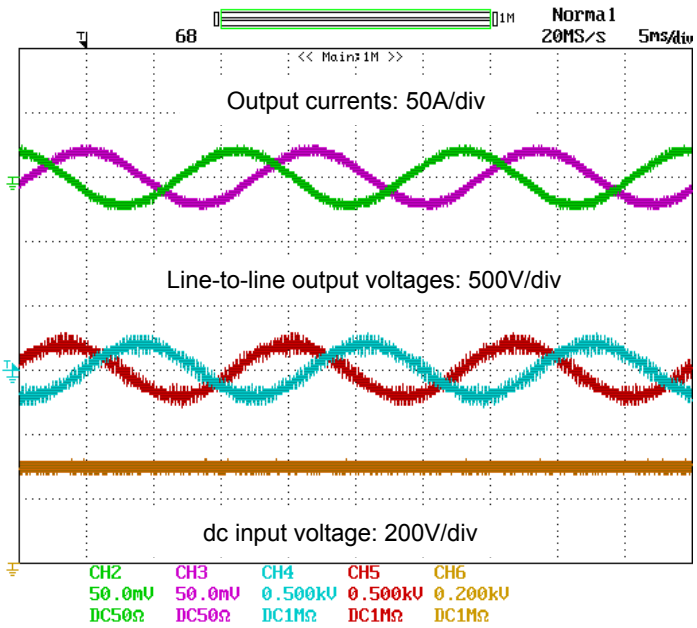

Fig. 10. Waveforms in buck mode at a voltage ratio of 0.67.

Table 5. Measured output voltage distortion factor

Load Power [kW]	Voltage THD [%]
11.31	12.20%
14.78	10.80%
20.24	11.55%

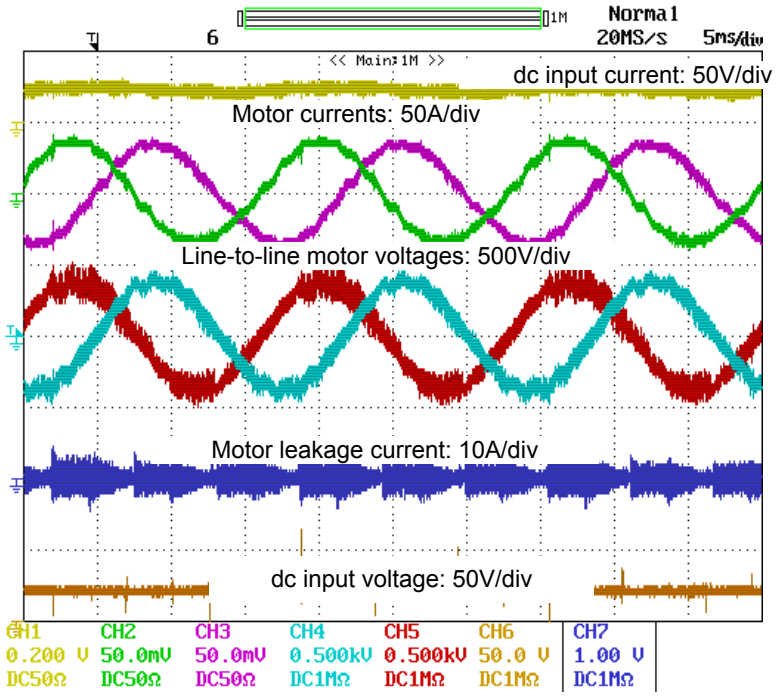

Fig. 11. Test waveforms for measuring motor bearing leakage current, 0.319A.

Conclusion

A high-performance motor drive using a current-source–based inverter has been proposed for HEV applications. The CSI offers many advantages, including (1) high reliability as a result of eliminating dc bus capacitors and the ability to endure phase-leg shoot-through, (2) improved motor efficiency and lifetime as a result of sinusoid-shaped voltage and current to the motor, (3) an increased constant-power speed range owing to the voltage boosting capability, and (4) reduced requirements for battery storage capacity in plug-in HEVs.

A 55 kW CSI was designed, fabricated, and tested. Test results confirmed the following:

- Total capacitance can be reduced to 195 μF from 2000 μF in a VSI.
- Voltage boost ratio can be achieved up to 3.47.
- Output voltage total harmonic distortion factor of less than 12.5%.
- Motor leakage current per motor terminal voltage of: 1.146 mA/V.

References

1. B. Wu, G. R. Slemon, and S. B. Dewan, "PWM-CIS induction motor drive with phase angle control," *IEEE Transactions on Industry Applications* **27**(5), 970–976 (September/October 1991).
2. B. Wu, S. B. Dewan, and G. R. Slemon, "PWM-CIS inverter for induction motor drives," *IEEE Transactions on Industry Applications* **28**(1), 64–71 (January/February 1992).
3. G. Joos, G. Moschopoulos, and P. D. Ziogas, "A high performance current source inverter," *IEEE Transactions on Power Electronics* **8**(4), 571–579 (October 1993).
4. M. Takei, Y. Harada, and K. Ueno, "600V-IGBT with reverse blocking capability," pp.413–416 in *Proceedings of IEEE ISPSD'2001*, 2001.
5. E. R. Motto, J. F. Donlon, M. Tabata, H. Takahashi, Y. Yu, and G. Majumdar, "Application characteristics of an experimental RB-IGBT (reverse blocking IGBT) module," pp. 1504–1544 in *Proceedings of IEEE IAS 2004 Annual Meeting*, 2004.

Patents

Gui-Jia Su, "Power Conversion Apparatus and Method," Provisional application LNG 64117.PV.

4.5 Using the Traction Drive Power Electronics System to Provide Plug-in Capability for Hybrid Electric Vehicles (HEVs)

Principal Investigator: Gui-Jia Su
Oak Ridge National Laboratory
National Transportation Research Center
2360 Cherahala Boulevard
Knoxville, TN 37932
Voice: 865-946-1330; Fax: 865-946-1262; E-mail: sugj@ornl.gov

DOE Technology Development Manager: Susan A. Rogers
Voice: 202-586-8997; Fax: 202-586-1600; E-mail: Susan.Rogers@ee.doe.gov

ORNL Program Manager: Mitch Olszewski
Voice: 865-946-1350; Fax: 865-946-1262; E-mail: olszewskim@ornl.gov

---

Objectives

- Overall project objectives
  - Reduce cost and volume by 90% compared with stand-alone battery chargers.
  - Provide rapid charging capability for use at high-power charging stations.
  - Enable plug-in hybrid electric vehicles (PHEVs) as mobile power generators.
  - Investigate hardware and software requirements for implementing smart charging and vehicle-to-grid capabilities.
- Objectives for FY 2008 effort
  - Design, fabricate, and test an HEV power electronics system prototype comprised of a 55 kW motor inverter and a 30 kW generator inverter to evaluate its battery charging capability.
  - Characterize charging performance in terms of efficiency, power factor, and grid current harmonic distortion factor.

Approach

- Finalize the design developed in FY 2007.
- Fabricate a prototype of a 55 kW motor inverter and a 30 kW generator inverter based on the design specifications.
- Develop digital signal processing code to implement the battery charging control algorithms for both slow and rapid charging.
- Test and evaluate the prototype's charging capability and performance.

Major Accomplishments

- Designed, fabricated, and successfully tested an HEV power electronics system prototype consisting of a 55 kW motor inverter and a 30 kW generator inverter for operation as a battery charger.
- Attained a maximum efficiency of >95% with a 120 V input and >98% with a 240 V input.
- Attained a grid current harmonic distortion factor at rated power of <9% at 120 V input and < 7% at 240 V input

Future Direction

- Modify the prototype to implement and demonstrate mobile power generator capability.
- Assess thermal control requirements for mobile generation and rapid charging operations.
- Implement smart charging capabilities.

Technical Discussion

Background

PHEVs are emerging as a pre–fuel cell technology that offers greater potential than hybrid vehicles currently on the market to reduce oil consumption and carbon dioxide emissions. In PHEVs, the energy storage capacity of the battery needs to be increased significantly to enable a driving distance of at least 40 miles in an all-electric mode, the distance needed to substantially reduce oil consumption for daily commuting. A charger is also required to replenish the battery after it is depleted, typically done overnight to leverage energy costs by taking advantage of off-peak electricity rates.

Stand-alone battery chargers, however, impose an extra cost on already expensive HEVs and have other limitations. A typical stand-alone battery charger for PHEVs consists of a diode rectifier and a unidirectional dc-dc converter (i.e., it can only charge the battery) that uses power semiconductor switches, diodes, inductors, and capacitors, as shown in Fig. 1. A charger with a low charging capability of 1~3 kW can cost almost 30% as much as the electric traction system for a mid-size PHEV-20 car ($690) [1]. The limited charging capability results in a long charging time (6~8 hours), which could negatively impact the acceptance of PHEVs.

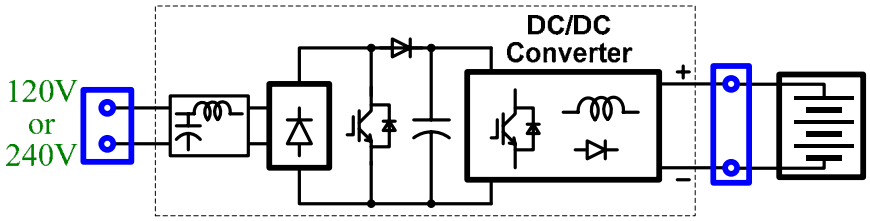

Fig. 1. A schematic showing major components in a stand-alone battery charger.

To minimize the cost of the charger, this project is investigating the use of the power electronics and motors already aboard the vehicle to fulfill the charging requirements. It is expected that, compared with a stand-alone battery charger, the proposed approach will impose virtually no additional cost or will significantly reduce the cost, depending on the configuration of the onboard traction drive system. The proposed approach is to integrate the battery charging function into the traction drive system and eliminate or minimize the number of additional components. Because traction power inverters have a greater current-carrying capability, the integrated charger can reduce the charging time significantly. Another benefit of this approach is that it enables PHEVs to function as mobile generators at little or no additional cost. Another objective is to investigate hardware and software requirements for implementing smart charging and vehicle-to-grid capabilities.

Description of the reduced-part dc-dc converter

Figure 2 shows topologies for using the onboard electrical drive system to provide plug-in charging and mobile generation capabilities for HEVs. The onboard electrical drive system may consist of one or more electrical motor drive units, all connected to a common dc bus. Each motor drive unit typically employs a three-phase inverter/converter (INV/CONV) and a three-phase motor/generator (MG) with a Y-connection with a neutral point (N_{MG}). At least one drive unit is coupled to the engine shaft through a mechanical transmission device. The basic idea is to use the MGs as inductors by connecting their neutral points to an external charging source to charge the battery, or to external loads to supply power to them. The external charging source can be a dc or single-phase or multiphase ac power supply, depending on the number of onboard drive units. Figure 2a illustrates an arrangement for a series HEV in which two

INV/CONVs and two MGs are employed. For such vehicles, virtually no additional components except some wiring and connectors are required. An ac filter capacitor may also be needed to meet grid interface

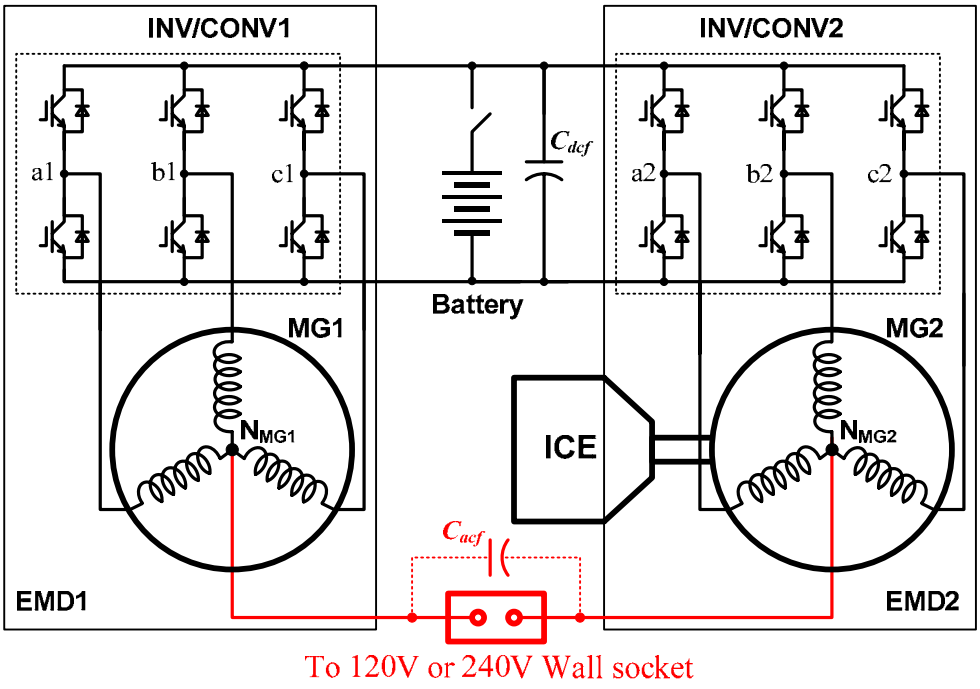

(a) For HEVs using two inverters and motors

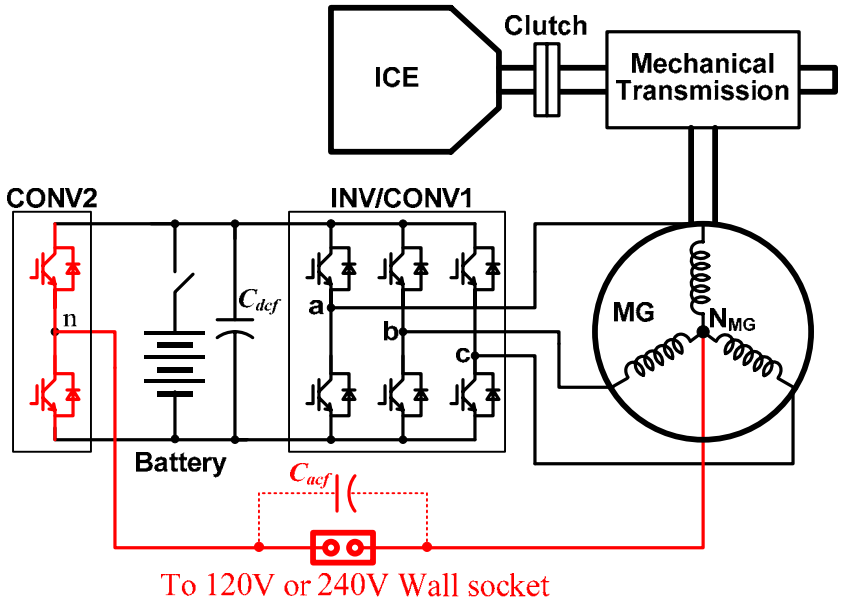

(b) For HEVs using a single inverter and motor

Fig. 2. Topologies for using the onboard electrical drive system to provide plug-in charging and mobile generation capabilities for HEVs. (Red denotes added components).

power quality requirements. For parallel HEVs, in which only one INV/CONV and MG are used, two switches must be added, as shown in Fig. 2b.

All the switch legs in each INV/CONV collectively function as a single switch leg and the MG as an inductor. Together, the drive units form a single-phase or multiphase converter, operating in the charging mode, to regulate the dc bus voltage. In the generation mode, the drive units form a single-phase or multiphase inverter to supply external loads. In this mode, the MG of the drive unit coupled to the engine shaft is driven by an engine to generate power to supply the dc bus and ultimately the external loads. Or power can be drawn from the battery for short operating intervals.

Figure 3 shows an equivalent circuit of Fig. 2a during operation in charging mode. All three switch legs (a1, b1, c1 and a2, b2, c2) in INV/CONV1 and INV/CONV2 collectively function as a single switch leg and the MGs function as two impedance networks—their stator zero sequence impedance networks (ZSIN1 and ZSIN2). Each ZSIN consists of three branches and each branch comprises the stator winding phase resistance (R_{ms1} or R_{ms2}) and the stator phase leakage inductance (l_{m0s1} or l_{m0s2}). Together, the two drive units form a single-phase converter to regulate the battery voltage, V_{bat}, or the charging current, I_{bat}. Normally, the single-phase converter is controlled so as to maintain a unity power factor by keeping the source current, i_s, in phase with the source voltage, v_s. An additional benefit of operating the three-phase converters as single leg converters is the reduction in harmonic current components resulting from interleaving the gating signals of the three legs.

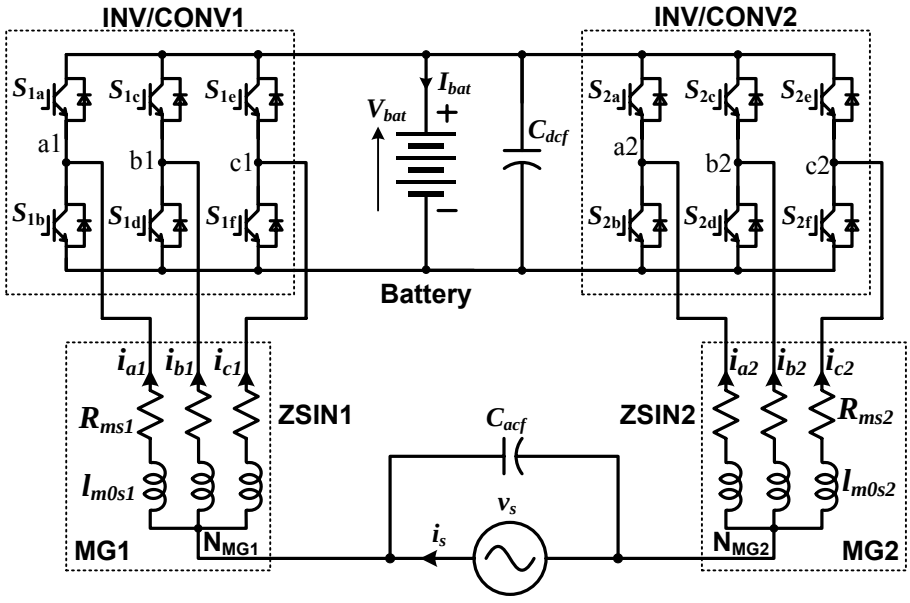

Fig. 3. An equivalent circuit for battery charging mode.

Figure 4 shows equivalent circuits of Fig. 2a during operation in mobile generation mode. There are two available power sources, the battery and the engine. Figure 4a illustrates the case in which the battery is the source. In this case, all three switch legs in each of the two INV/CONVs collectively function as a single switch leg and the MGs as two impedance networks. Together the two drive units form a single-phase inverter to regulate the load voltage, v_{Load}.

Figure 4(b) illustrates the case in which power is generated by the MG2 driven by the engine. In this case, the three switch legs in INV/CONV1 collectively function as the first single switch leg of a single-phase

inverter and the MG1 functions as an impedance network. INV/CONV2 has dual functions. It first operates as a three-phase converter to regulate the dc bus voltage, V_{dc}, by drawing power from the generator; at the same time, its three phase legs collectively form the second switch leg of the single-phase inverter to regulate the load voltage, v_{Load}.

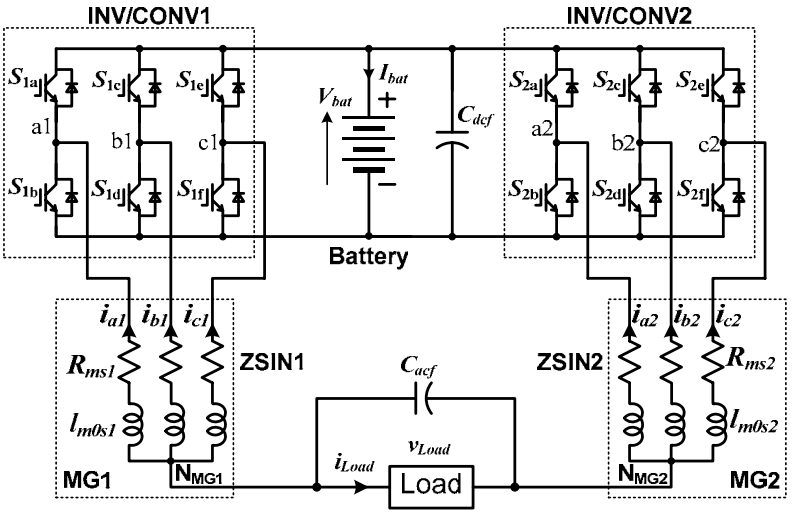

(a) Using the battery as the power source

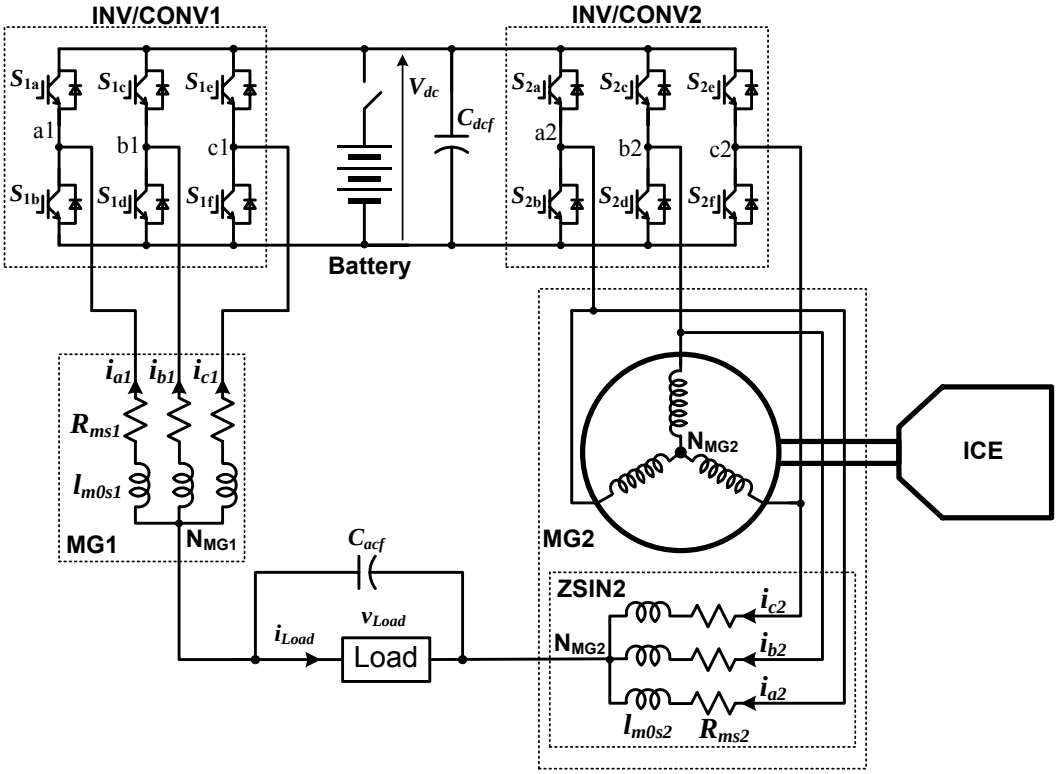

(b) Using the motor MG2 driven by the engine as the power source

Fig. 4. Equivalent circuits for mobile generator mode.

Prototype fabrication and testing

Based on the simulation results, a conceptual design of a drive inverter system consisting of a 55 kW and a 30 kW inverter with plug-in charging and mobile generation capabilities was completed in FY 2007. The design was finalized and a prototype was fabricated. Figure 5 is a photo of the prototype. The 55 kW inverter was implemented with a six-pack insulated gate bipolar transistor (IGBT) module rated at 600 V and 600 A, part number PM600CLA060 from Powerex; and the 30 kW inverter was implemented with a six-pack IGBT module rated at 600 V and 300 A, part number PM300CLA060 from the same vendor. The bus capacitor bank is constructed using four film capacitors, part numbers UP33BC0375, rated at 600 Vdc and 375 μF. These components are mounted on a 12 × 7 in. cold plate.

A 10.9 kW induction motor and a permanent magnet motor rated at 8.2 kW were used in the testing. Table 1 gives their zero sequence resistances. The resistance values of Toyota Camry motors are also given for comparison. Notice the combined resistance of the two test motors is more than 5 times larger than that of the Camry motor owing to the large resistance of the induction motor. This had a significant impact on efficiency.

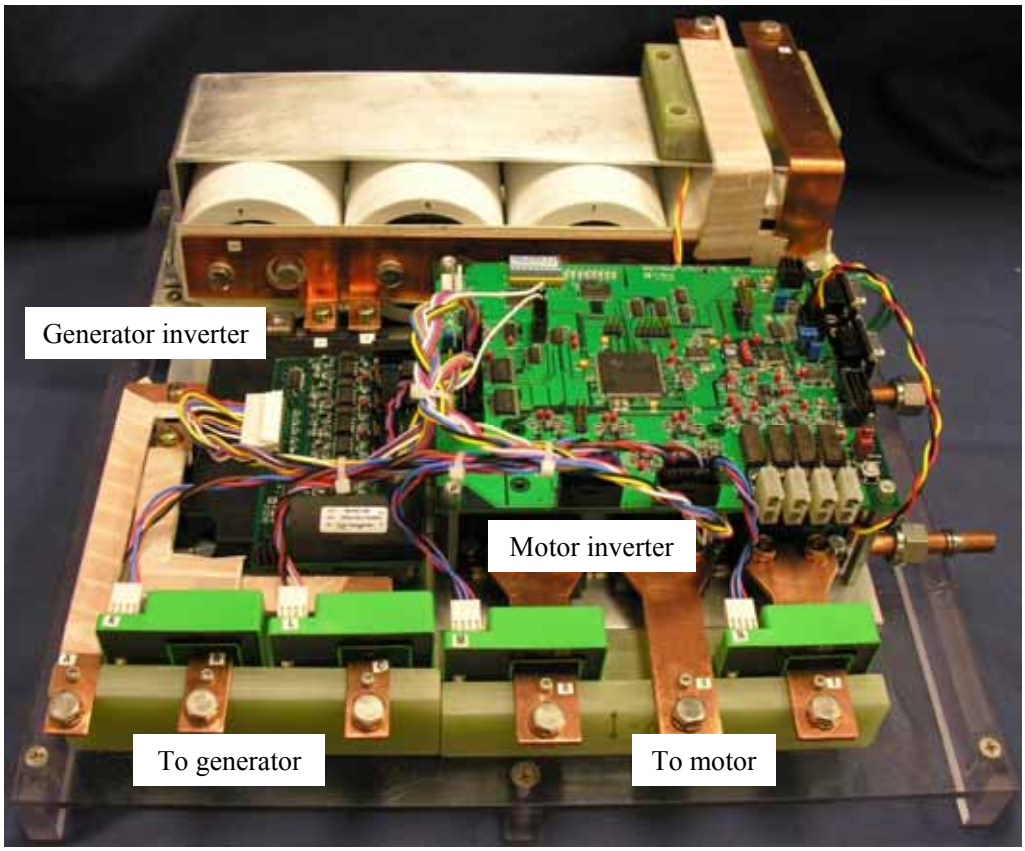

Fig. 5. A photo of a prototype consisting of a 55 kW motor inverter and a 30 kW generator inverter with plug-in charging capability. The heat sink footprint is 12 in. width by 7 in. depth.

Table 1. Motor zero sequence resistance

Test motor 1	165.74 mΩ	Camry generator	21.58 mΩ
Test motor 2	23.8 mΩ	Camry motor	10.75 mΩ
Combined	189.54 mΩ	Combined	32.32 mΩ

The prototype was tested with 120 V and 240 V input sources for varying dc charging power. Figure 6 illustrates test results showing operating waveforms in the charging mode at 12.4 kW from a 240 V source. Figure 7 shows waveforms operating at 2.13 kW from a 120 V source. In both cases, the charger was operating at a near-unity power factor, as indicated by the fact that the source currents were in phase with the source voltages.

Figure 8 plots measured efficiency against dc charging power. The maximum efficiency was 92.6% with a 120 V input and 97.0% with a 240 V input. The large resistance of the test motors significantly lowered the efficiency numbers as the output power increased. For comparison purposes estimated charging efficiencies for the Toyota Camry motor are also shown. The Camry estimations are 95.3% with a 120V input and 98.2% with a 240 V input. Although the prototype was designed to provide a maximum charging power of greater than 20 kW, the tests were limited to 14.5 kW by the 240 V source capability.

Figure 9 plots measured power factor and Fig. 10 plots measured total harmonic distortion (THD) of the grid current against dc charging power. The power factor is over 99% over a wide range of dc charging power. Grid current THD at rated power is less than 9% with a 120 V input and less than 7% with a 240 V input.

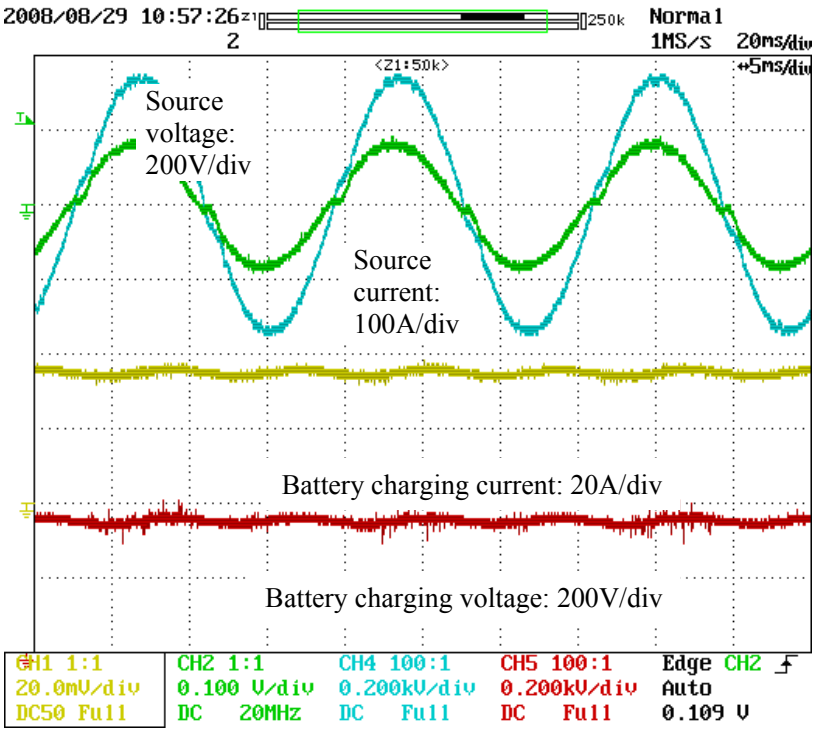

Fig. 6. Test results showing operation in charging mode at 12.4 kW from a 240 V source.

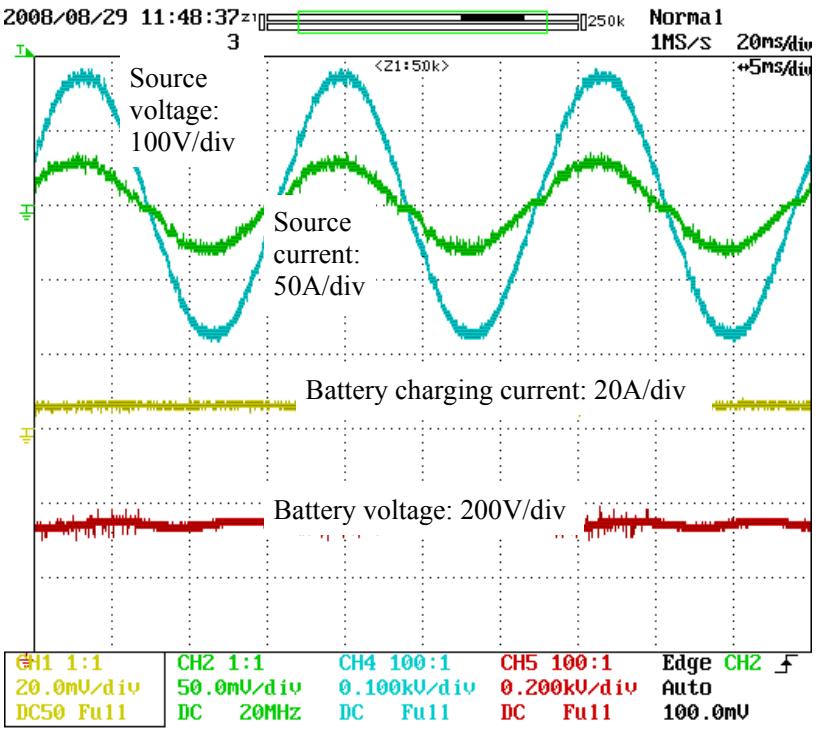

Fig. 7. Test results showing operation in charging mode at 2.13 kW from a 120 V source.

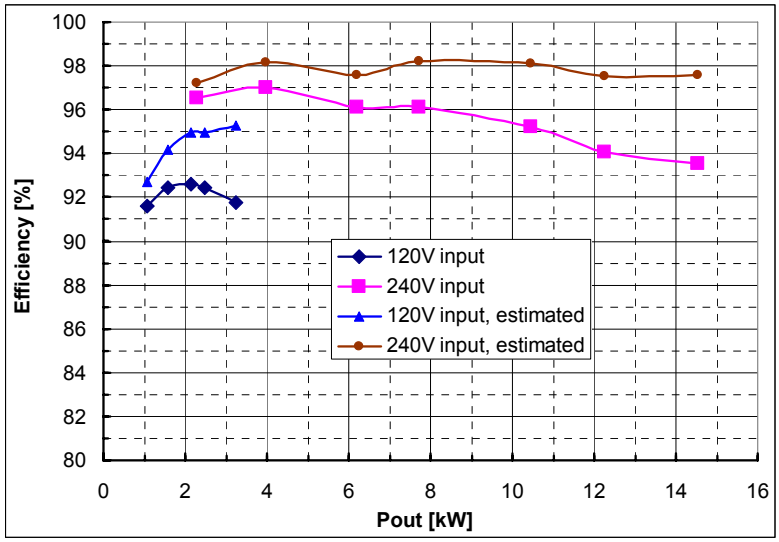

Fig. 8. Measured and estimated efficiency.

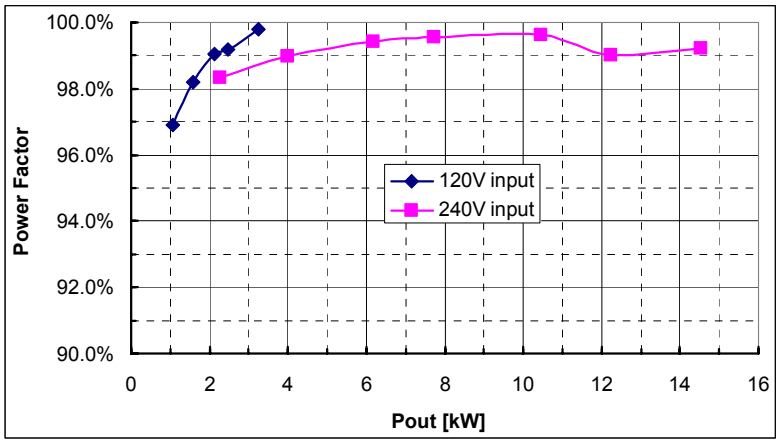

Fig. 9. Measured power factor.

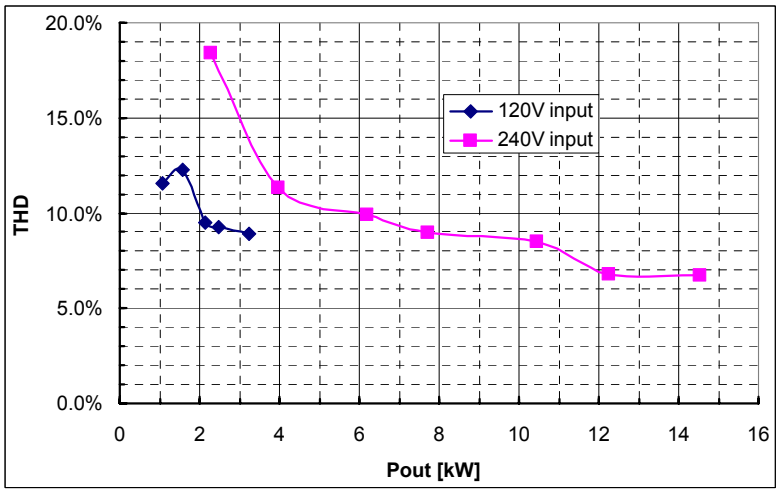

Fig. 10. Measured total harmonic distortion (THD) of the grid current.

Conclusion

This project explored ways of using the onboard electrical drive system in different HEV configurations to provide plug-in charging capability. The proposed charging schemes offers many benefits, including (1) significantly reducing the cost and volume of battery chargers in PHEVs, (2) providing rapid charging capability, and (3) enabling the use of PHEVs as mobile generators. Detailed circuit simulations were carried out, and the simulation results proved the concepts and validated the rapid charging capability.

An HEV power electronics system prototype made up of a 55 kW motor inverter and a 30 kW generator inverter was designed, fabricated, and successfully tested for operation as a battery charger. Test results confirmed high efficiency, high power factor, and low harmonic distortion:

- Maximum efficiency: >95% with a 120 V input and >98% with a 240 V input
- Grid current harmonic distortion factor at rated power: < 9% with a 120 V input and < 7% with a 240 V input

References

1. *Advanced Batteries for Electric-Drive Vehicles*, Report 1009299, Electric Power Research Institute, May 2004.

Patents

Gui-Jia Su, "Electric Vehicle System for Charging and Supplying Electrical Power," Patent No. US2008/0094013A1, pending.

4.6 High Dielectric Constant Capacitors for Power Electronic Systems

U. (Balu) Balachandran, B. Ma, M. Narayanan, and S. E. Dorris
Energy Systems Division
Argonne National Laboratory
9700 S. Cass Avenue
Argonne, IL 60439
Voice: 630-252-4250; Fax: 630-252-3604; E-mail: balu@anl.gov

DOE Technology Development Managers: Susan A. Rogers and Steven Boyd
Voice: 202-586-8997; Fax: 202-586-1600; E-mail: susan.rogers@ee.doe.gov; steven.boyd@ee.doe.gov

Argonne Program Manager: U. (Balu) Balachandran
Voice: 630-252-4250; Fax: 630-252-3604; E-mail: balu@anl.gov

Objectives

The goal of this R&D program is to develop high performance and economical DC bus capacitor technology that will meet the APEEM specifications for HEV, PHEV, and FCV power electronic systems. Current DC bus capacitors occupy a large fraction of the volume and weight of the inverter module, cannot tolerate temperatures >120°C, and suffer from poor packaging, inadequate reliability, and deleterious failure modes. Traditional capacitor architectures with conventional dielectrics cannot adequately meet all of the performance goals for capacitance density, weight, volume, and cost. Meeting these goals requires a dielectric with high permittivity and breakdown field that tolerates operating at high temperature, is packaged in architecture with high volumetric efficiency, and exhibits benign failure features.

Approach

Argonne National Laboratory's (Argonne) capacitor R&D program addresses the technology gap in an innovative manner. We are developing high performance, low cost capacitors that are either stacked on printed wire board (PWB) or embedded directly into the PWB. In these "film-on-foil capacitors", a base-metal foil (nickel or copper) is coated with a high permittivity ferroelectric material, $(Pb,La)(Zr,Ti)O_3$ (abbreviated as PLZT). Ferroelectrics possess high permittivity, breakdown electric fields, and insulation resistance. They can withstand high temperatures such that high ripple currents can be tolerated at under-the-hood temperatures. Use of base-metals and solution-based deposition techniques reduce the cost. The stacked and embedded capacitors approaches significantly reduces component footprint, improves device performance, provides greater design flexibility, and offers an economic advantage for commercialization. This technology will achieve the high degree of packaging volumetric efficiency with less weight. Device reliability is improved because the number and size of interconnections are reduced.

Our R&D efforts focus on examining the issues that underpin the performance of film-on-foil capacitors, establishing fabrication protocols that are commercially robust and economically viable, and transferring the technology to industry for manufacturing.

Major Accomplishments

- Demonstrated film-on-foil PLZT dielectrics with dielectric constant (relative permittivity), k >1100, breakdown field >6 MV/cm, and leakage current $<10^{-8}$ A/cm^2 at room temperature.
- Measured an increase in k of ≈50% as temperature increased from 25°C to 150°C.
- Measured k ≈70 at 300 V applied bias on a ≈1.15 μm-thick PLZT film at room temperature.

- Refined processing conditions to fabricate PLZT on copper foils.
- PLZT film-on-foil capacitors were thermally cycled ≈1000 times between -50°C and 150°C with no measurable degradation in k.
- Preliminary high temperature measurement predicted mean time-to-failure of ≈4000 h at 100°C under 260 kV/cm steady-state DC field.
- Evaluated mechanical properties of film-on-foil capacitors (measured at ORNL).
- PLZT films with breakdown field >9 MV/cm and energy density ≈170 J/cm^3 have been measured.
- Demonstrated graceful failure mode in single-layer film-on-foil dielectrics.
- Established a CRADA with Delphi Electronics to build a high temperature inverter using film-on-foil PLZT dielectrics.
- Presented program status and future direction to EE Tech Team, DOE APEEM projects kickoff, and Annual Merit Review meetings.
- Published three papers in peer reviewed international journals.
- Submitted three manuscripts for publication in peer reviewed international journals and seven manuscripts for publication in conference proceedings.
- Presented the results at eight scientific conferences.

Future Direction

Using small area (250–750 μm diameter) top electrodes, the R&D effort has demonstrated that the properties of PLZT film-on-foils are suitable for power electronics operating at under-the-hood temperatures. The next step is to optimize the processing and fabrication conditions to make large area capacitors with the desired dielectric properties. Important processing issues such as substrate polishing, defects in the films, clean room processing, pyrolysis and crystallization temperatures have been identified during the R&D effort in FY 2008. Focusing our effort on these already identified issues, we will establish the processing science and technology needed to fabricate high voltage-capable, large area, film-on-foil capacitors. Building upon our current success with PLZT film-on-foil capacitors, we will investigate the issues that underpin dielectric performance, and use that knowledge to refine processing conditions. We will perform experiments to determine capacitor reliability, lifetime, and high-temperature behaviors. Electrode architectures will be investigated to achieve benign failure in stacked film-on-foil capacitors. This will set the stage to begin the development of prototype PLZT film-on-foil capacitors for high temperature inverters. This will require our technology to be refined and aligned with PWB fabrication routines. Currently the film-on-foils are fabricated by a spin coating technique. In this technique, a thin layer of PLZT material is deposited on the base metal substrate from a solution and heat treated at high temperature to form the desired crystalline phase. The spin coating and heat treatment steps are repeated to obtain the desired thickness for the PLZT layer. This current process is time consuming; therefore, our future effort will be to develop methods to reduce the processing steps and the cost of making high voltage-capable capacitors for power electronic applications. We will also investigate other compositions in the PLZT system to increase breakdown field and capacitance density and decrease the loss factor. These improvements will reduce the volume of dielectrics and, therefore, the cost of capacitors for inverter applications.

The PLZT film-on-foil sheets will be integrated into a PWB manufacturing process. Working with our industrial partner, we will address the challenges posed by stacking, embedding, imaging the inner-layers, metallization, and circuit design. We will build prototype multilayer capacitor components, test the device's performance and benchmark it against APEEM goals. These initial prototypes will be evaluated by ORNL as well as other research institutions.

Technical Discussion

The replacement of bulky inefficient discreet capacitors with film-on-foil capacitors either stacked on PWB or embedded directly into the PWB is an innovative and highly desirable solution for applications that require high capacitance density and volumetric efficiency. Embedded capacitors can be located directly underneath the active devices, significantly reducing component footprint and greatly improving reliability. While this technology has primarily received attention for low voltage, high frequency decoupling capacitors, it can potentially be extended to the higher voltages of hybrid electric vehicle systems. The vision of embedded DC bus capacitors is compelling and offers US automotive companies a substantial technological advantage over their foreign counterparts. The bulky coke-can-like banks of capacitors can be replaced by lengths of capacitors tucked flat and neatly underneath the active components and bus structure. Reducing the number of solder joints and decreasing the length of electrical leads will improve reliability. While embedding the film-on-foil capacitors into the PWB is the ultimate goal, the short-term practical approach is to target high voltage, high temperature, stacked capacitors for the inverter demonstration using film-on-foil dielectric layers. The short-term target will address the important issues, namely, weight, volume, and cost advantages of the film-on-foils compared to the conventional, bulky, wound polymer capacitors.

The key provision is the integration of high-k PLZT ceramic layers within a PWB. Because high temperature (≈650°C) processing is required to obtain dense crystalline PLZT materials with high-k, direct deposition on a polymeric printed wire board is not possible. Instead, a pre-fabricated 'film-on-foil' approach is adopted, whereby the ferroelectrics are first deposited via chemical solution deposition (CSD) on a thin base metal foil, and then crystallized at high temperatures, and the coated foils subsequently integrated into the PWBs.

Due to the high-temperature processing condition required for the fabrication of 'film-on-foil' capacitors, a principal concern is eliminating deleterious effects from the formation of a low-k parasitic oxide at the metal-ceramic interface. This low-k oxide would act as a series capacitor and reduce the overall capacitance. To negate the influence of an interfacial oxide, two approaches have been investigated: (1) a conductive oxide buffer layer is interposed between the PLZT and the metal foil, and acts as an effective bottom electrode. Any discontinuous secondary oxide that may form below the buffer layer at the metal interface is inconsequential to the parallel plate capacitor. (2) Crystallization of the PLZT ceramic layer is conducted in a controlled atmosphere whose pO_2 is low enough to prevent formation of an interfacial oxide but not so low that the dielectric decomposes.

1 – PLZT/LNO/Ni Capacitors

We have developed a core technology for fabricating CSD PLZT on Ni film-on-foil capacitors with $LaNiO_3$ (LNO) buffer layers. CSD solutions were synthesized at Argonne, and films were deposited by spin coating. All pyrolyses and crystallizations were done in air and repeated to build up layers of sufficient thickness.

The conductive LNO can obviate the parasitic influence of any interfacial NiO formation during the high temperature processing that is required for crystallization of PLZT on a Ni substrate in air. We have deposited PLZT on LNO-buffered 1 in. x 1 in. Ni foils. Platinum (Pt) top electrodes of ≈250 μm – 750 μm diameter and ≈100 nm thickness were deposited on PLZT films by electron-beam evaporation. The film-on-foil capacitor samples were analyzed by several methods. A Bruker AXS diffractometer with General Area Detector Diffraction System was used for X-ray diffraction (XRD) analysis. An HP 4192A impedance analyzer was employed for measuring the capacitance and dissipation factor with a 0.1-V oscillating signal at 10 kHz; a Keithley 237 high-voltage source meter for leakage current and breakdown field strength; and a Radiant Technologies' Premier II dielectric testing system for hysteresis loops. The samples were immersed in silicon oil during the dielectric breakdown measurements. Figure 1 shows the

relative permittivity and dielectric loss of a PLZT/LNO/Ni sample measured at room temperature using ≈250 µm Pt top electrode as a function of applied bias field. The thickness of the PLZT was ≈1.15 µm, deposited on top of a ≈0.4-µm-thick LNO buffer. A relative permittivity of ≈1300 and dielectric loss (tan δ) ≈0.05 were measured at room temperature. Capacitance density of 1.0 microfarads/cm^2 was achieved on a ≈1.15 µm-thick PLZT/LNO/Ni capacitor. A relative permittivity of ≈1150 and dielectric loss (tan δ) ≈0.07 were measured using a 750 µm-diameter top electrode. Defects in the substrate and film contributed to the decrease in relative permittivity and increase in dielectric loss. Attempts are being made to reduce the defects and make PLZT films with uniform properties over larger areas.

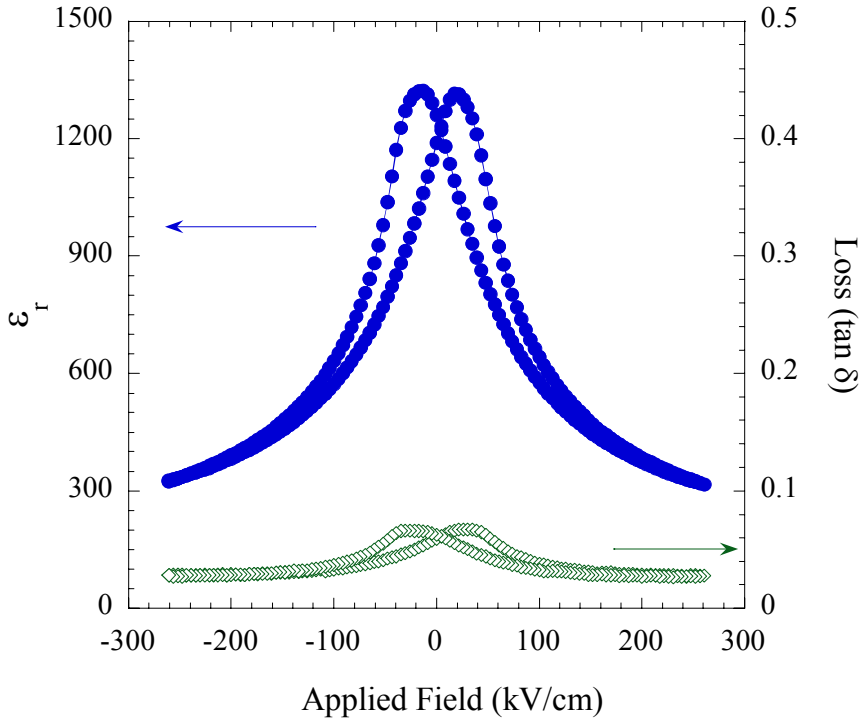

Fig. 1. Relative permittivity and dielectric loss measured at room temperature as a function of applied bias field for a 1 in. x 1 in. PLZT/LNO/Ni film-on-foil capacitor (measured on a ≈250 µm Pt top electrode).

The breakdown field strength was measured with a "top-to-bottom" electrode configuration. The applied voltage was increased by 5 V per second, soaking time was 1 second, and the breakdown voltage was determined by using a 1-µA criterion. Weibull statistics were employed for failure behavior analysis. Figure 2 shows a Weibull plot of breakdown field strength obtained from 20 measurements (made on ≈250 µm Pt top electrode) with PLZT/LNO/Ni capacitors (with ≈1.15-µm-thick PLZT). The solid straight line is a fitting to the two-parameter distribution function and led to the mean breakdown field strength of 6.7 MV/cm. The dashed curve is a fitting to the three-parameter distribution and resulted in smaller mean breakdown field strength of 6.3 MV/cm. When an electric field of 3.3 MV/cm is applied on the film-on-foil capacitor, the probability of failure is <1% based on the three-parameter Weibull analysis.

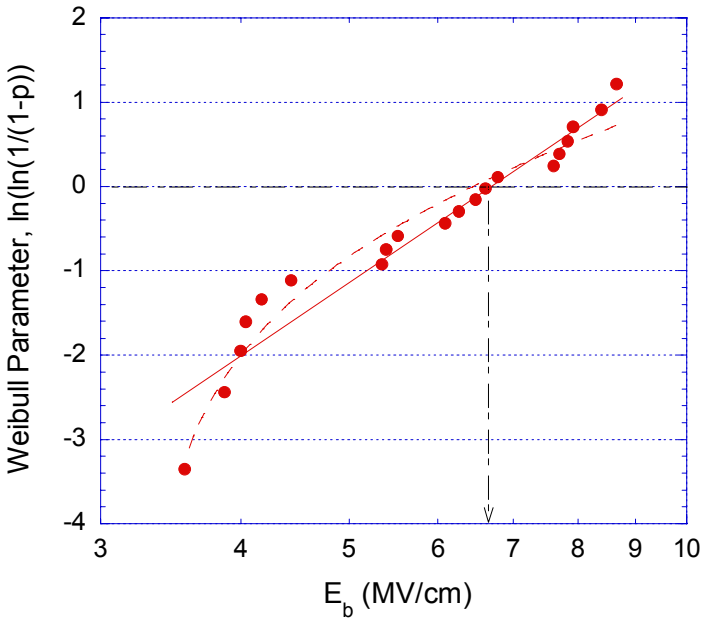

Fig. 2. Weibull plot for breakdown field strength of PLZT/LNO/Ni film-on-foil capacitors with ≈1.15-µm PLZT layer (measured on a ≈250 µm Pt top electrode). The straight solid line and curved dotted line are fittings to two- and three-parameter functions for failure probability.

Figure 3 shows the histogram of breakdown fields measured at 25 spots with ≈250 µm Pt top electrode on a ≈1.15 µm-thick x 1 in. x 1 in. PLZT/LNO/Ni sample. As seen from Fig. 3, twelve measurements showed breakdown fields exceeding 8 MV/cm. These measurements show that there is potential for further increase in breakdown field strength of the PLZT film-on-foil capacitors.

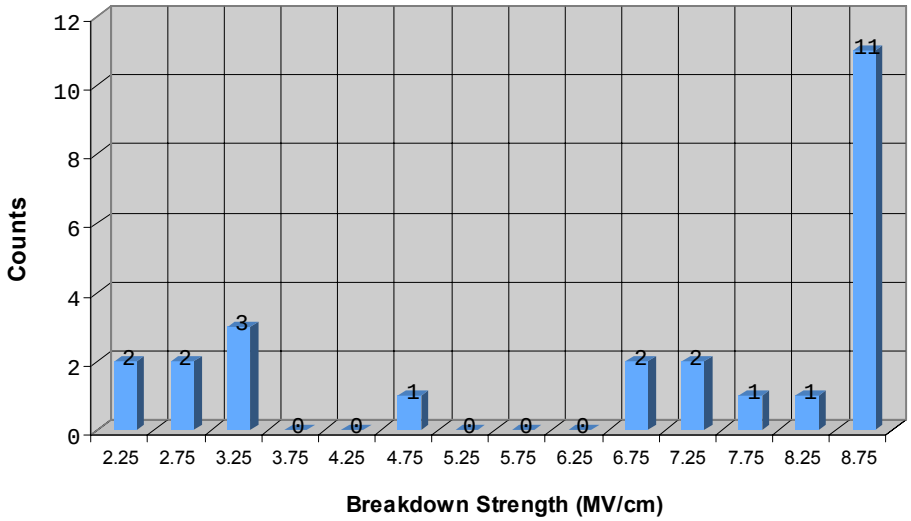

Fig. 3. Breakdown field histogram of 25 measurements made on a ≈1 µm-thick PLZT/LNO/Ni film-on-foil capacitor using ≈250 µm diameter Pt top electrodes.

2 – PLZT/Cu Capacitors

Cu is the primary material for PWB interconnects and metallization. We have initiated development of PLZT on bare Cu foils. In this process, a controlled environment with reduced pO_2 is used to prevent formation of a parasitic interfacial oxide layer. The pO_2 must be low enough to prevent oxidation of the Cu-PLZT interface, yet not too low to induce decomposition of the PLZT film. Thermodynamic models aid in determining the appropriate pO_2 for the heating, crystallization, and cooling cycles. Figure 4 shows the relative permittivity and dielectric loss of a 0.5 in. x 0.5 in. PLZT/Cu sample measured at room temperature as a function of applied bias field (measurements were made using ≈250 μm diameter Pt top electrode). The thickness of the PLZT was ≈1 μm, deposited on polished copper substrate. A relative permittivity of ≈1100 and dielectric loss (tan δ) ≈0.06 were measured at room temperature.

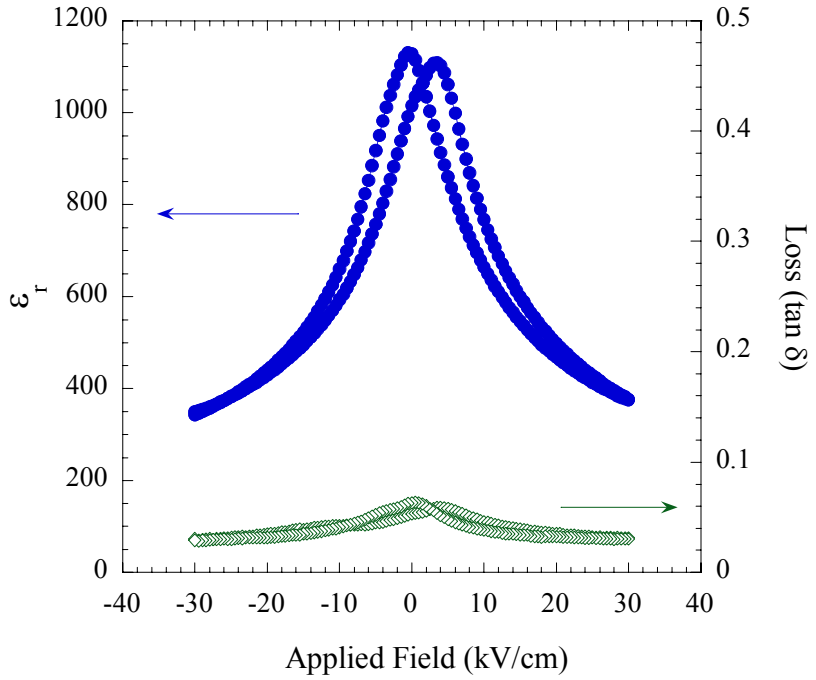

Fig. 4. Relative permittivity and dielectric loss measured as a function of applied field on a Pt/PLZT/Cu capacitor.

3 – Temperature Dependent Characterization of Dielectric Properties

With the newly constructed dielectric testing system, we tested film-on-foil capacitor samples as a function of temperature. Figure 5 shows the dielectric constant and dielectric loss measured with zero bias for PLZT grown on LNO-buffered Ni foil in the temperature range 25 - 200°C. The dielectric constant increases by ≈50% and loss decreases by ≈25% as temperature is increased from 25 to 140°C. The ripple current capability of the capacitor is improved as the operating temperature is increased to 140°C.

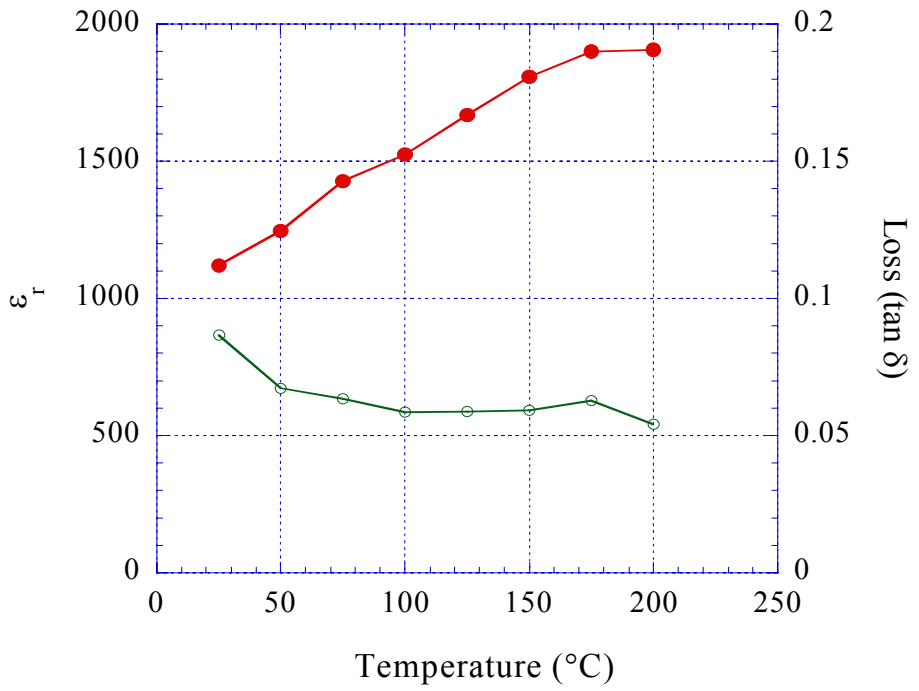

Fig. 5. Temperature dependent dielectric constant and dielectric loss of a 1 in. x 1 in. PLZT/LNO/Ni film-on-foil capacitor (measured using ≈250 µm diameter Pt top electrode)

A PLZT/LNO/Ni film-on-foil capacitor with platinum top electrode has been thermally cycled at temperature between -50°C and 150°C for ≈1000 times at Delphi Electronics and Safety. Dielectric properties of the PLZT/LNO/Ni film-on-foil capacitor were measured before and after the thermal cycling experiments. No measurable degradation in dielectric properties or aging effect was detected after thermal cycling.

4 – Polarization-field (P-E) Hysteresis Measurement

Figure 6 shows the P-E loop measured at room temperature on a PLZT/LNO/Ni film-on-foil capacitor with ≈2.0 µm-thick PLZT. Electric field up to ≈5 MV/cm (1000 V) was applied during the test. Remnant polarization (P_r) ≈60 µC/cm^2 and coercive field (E_c) ≈83 kV/cm were measured. Fitting the high electric field P-E loop curve, we estimated that the energy density is ≈170 J/cm^3 (as illustrated by the shaded area in Fig. 6) when the dielectric film is subjected to an electric field of ≈5 MV/cm (corresponding to 1000 V for a ≈2 µm-thick PLZT film).

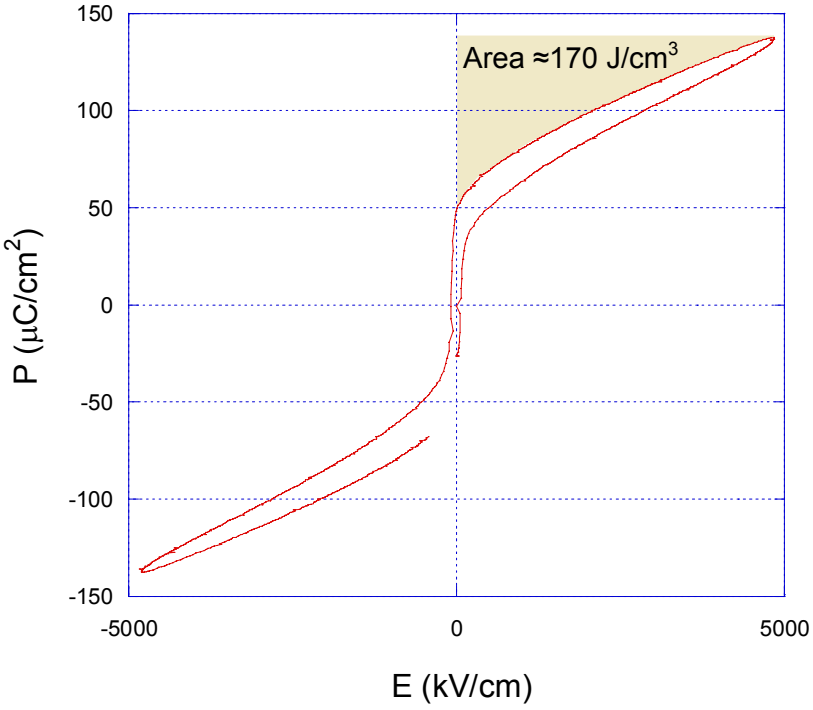

Fig. 6. Polarization vs. field (P-E hysteresis loop) measured at room temperature with ≈250 μm Pt top electrode on ≈2 μm thick PLZT on Ni foil. The calculated energy density is shown in the shaded area of the hysteresis loop.

5 – Graceful Failure

We have developed film-on-foil capacitors that exhibit graceful failure – a gradual loss in capacitance during localized breakdown events. Following a breakdown occurrence, the capacitor continues to function and is considered to have failed only after a defined leakage current or dielectric loss is reached.

At sufficiently high voltages, dielectric breakdown occurs at a discrete faulted area. This discharges the stored energy of the dielectric in that localized spot. In a matter of microseconds the discharge heats the immediate area, which physically "clears" away the dielectric from the defect site, and vaporizes the metal top electrode in a small region surrounding the defect. By this process the breakdown site becomes electrically isolated and removed from the remainder of the capacitor structure. The capacitor continues to operate to even higher voltages. Capacitors can sustain many breakdown events during their lifetime and can tolerate higher voltages. A small loss in capacitance is observed only after several breakdown/clearing events occur. Indeed, it usually takes hundred to thousands of such clearings to cause a few percent losses in capacitance. In such a manner, instead of shorting, the capacitor effectively fails gracefully. Such graceful failure modes are the same as those in metalized polymer capacitors. A U.S. Patent has been issued to Argonne for developing graceful failure in film-on-foil capacitors.

6 – Prototype Development

We have demonstrated a proof-of-concept for film-on-foil capacitors. Preliminary measurements on capacitor reliability (i.e., mean-time to failure) have been made. To proceed towards the next step of prototype capacitors, we have teamed with Delphi Electronics and Safety, a leading automotive

electronics supplier. The challenge now is to fabricate larger area film-on-foil capacitors with uniform properties for inverter applications. Together with our partner, we will begin to develop technologies for integrating film-on-foils into PWB fabrication. This will include stacking, embedding, imaging and etching, and interconnects and terminations. Novel PWB circuit designs will be conceived to maximize the capacitance and voltage in the smallest possible volume. The film-on-foil capacitors will be assembled and analyzed under hybrid electric vehicle inverter conditions.

Conclusion

We have developed a core technology for fabricating high capacitance density PLZT film capacitors on base metal foils. PLZT film-on-foil capacitors have been fabricated with LNO buffer layers atop Ni foils, allowing the capacitors to be processed in air. Low pO_2 processing has been used to fabricate PLZT capacitors on Cu foils without the need for a buffer layer. An alliance with an automotive electronics company was established to stack/embed our film-on-foil dielectric elements and fabricate capacitor prototypes for hybrid electric vehicle inverters. Top electrode metallization design and connection layout for a prototype capacitor were studied. This film-on-foil technology will be used to fabricate DC bus capacitors for high temperature inverters with significantly reduced size and weight, and improved performance and reliability.

Selected Publications

1. B. Ma, D. K. Kwon, M. Narayanan, U. Balachandran, *Chemical Solution Deposition of Ferroelectric Lead Lanthanum Zirconate Titanate Films on Base-Metal Foils*, Journal of Electroceramics, (in press,2008; available online, doi:10.1007/S10832-007-9410-1).
2. B. Ma, D. K. Kwon, M. Narayanan, and U. Balachandran, Leakage Current Characteristics and Dielectric Breakdown in Antiferroelectric $Pb_{0.92}La_{0.008}Zr_{0.95}Ti_{0.05}O_3$ Film Capacitors Grown on Metal Foils, J. Phys D: Appl. Phys., **41**, No. 20, 205003, 2008.
3. B. Ma, D. K. Kwon, M. Narayanan, and U. Balachandran, *Dielectric Properties of PLZT Film-on-Foil Capacitors*, Materials Letters, **62**, 3573, 2008.
4. M. Narayanan, D. K. Kwon, B. Ma, and U. Balachandran, Deposition of Sol-gel Derived PLZT Thin Films on Copper Substrate, Appl. Phys. Lett., **92**, 252905, 2008.
5. U. Balachandran, B. Ma, D. K. Kwon, and M. Narayanan, Fabrication of Ceramic Dielectric on Base-Metal Foils for Embedded Capacitors, Published in the Proc. of the 4th Int. Conf. on Ceramic Interconnect and Ceramic Microsystems Technologies, April 21-24, 2008.
6. B. Ma, D. K. Kwon, M. Narayanan, and U. Balachandran, *Ferroelectric Thin Films on Base-Metal Foils for Embedded Passives*, Mater. Res. Soc. 2007 Fall Meeting Symp. Proc., Boston, MA, Nov. 25 – 30, 2007.

Patents

1. D. K. Kaufman, S. Saha, Ceramic capacitor exhibiting graceful failure by self-clearing method for fabricating self-clearing capacitor, US Patent #7,009,141, August, 2006.

4.7 Glass Ceramic Dielectrics for DC Bus Capacitors

Principal Investigator: Michael Lanagan
Penn State University
278 Materials Research Laboratory
University Park, PA 16802
Voice: 814-865-6992 ; Fax: 814-865-2326; E-mail: mlanagan@psu.edu

DOE Technology Development Managers: Steven Boyd and Susan A. Rogers
Voice: 202-586-8997; Fax: 202-586-1600; E-mail: Steven.Boyd@ee.doe.gov, Susan.Rogers@ee.doe.gov

---

Objectives

Commercial capacitors for hybrid electric vehicles (HEVs) and plug-in hybrid electric vehicles (PHEVs) do not meet US automaker's specifications for high temperature operation, cost and reliability. The goals of this project are to develop high temperature capacitors that go beyond what is commercially available and to minimize the need for costly coolant systems within the HEVs and PHEVs. In addition, the project will leverage promising new glass materials that were previously developed for consumer electronics. This project provides an integrated development effort that involves materials, capacitor, and power electronic companies. Specific technical objectives include:

- Increase energy density beyond 1 J/cm^3 in a fully packaged capacitor (related to overall power electronic converter volume).
- Demonstrate graceful failure mechanisms in glass ceramic capacitors (related to long-term power converter performance).
- Characterize the electrical properties of commercial materials that are fabricated from large-scale production processes (i.e. flat panel displays) which is related to converter cost.

Approach

- Adapt low-cost production methods and materials, already developed for flat panel displays, to high temperature capacitors.
- Characterize glass materials at high temperature to project reliability.
- Develop benign failure modes in glass capacitors to avoid catastrophic failure.
- Manufacture prototype capacitors in collaboration with industrial partners.

Major Accomplishments

- Collaborated with commercial glass manufacturers (Schott Glass USA and Corning) to establish flat panel display glass as a viable capacitor material.
- Developed conducting coatings to enhance benign failure in glass capacitors and to increase reliability.
- Demonstrated through highly accelerated life testing of commercial glass that glass materials will withstand 600 V at 140ºC for 10,000 hrs.
- Developed a stacking concept with a capacitor manufacturer for glass capacitors.

Future Direction

- Scale-up glass capacitors to 10 μF 1,000 V levels
- Establish coating technologies for electrodes and graceful failure mechanisms in glass capacitors.

- Develop a portfolio of invention disclosures around glass coatings for enhanced capacitor performance.

Technical Discussion

Collaboration with Commercial Glass Manufacturers:

There is general agreement within the automotive and power electronic communities that revolutionary approaches, drawing on diverse disciplines, will be necessary to develop the next generation of power systems for electric vehicles. New active and passive components need to be manufactured which can operate at high temperature for long periods of time. In addition, component miniaturization is important to reduce the total volume of the power electronic circuitry on board an electric vehicle. A summary of the results of this study is shown in Figure 1.

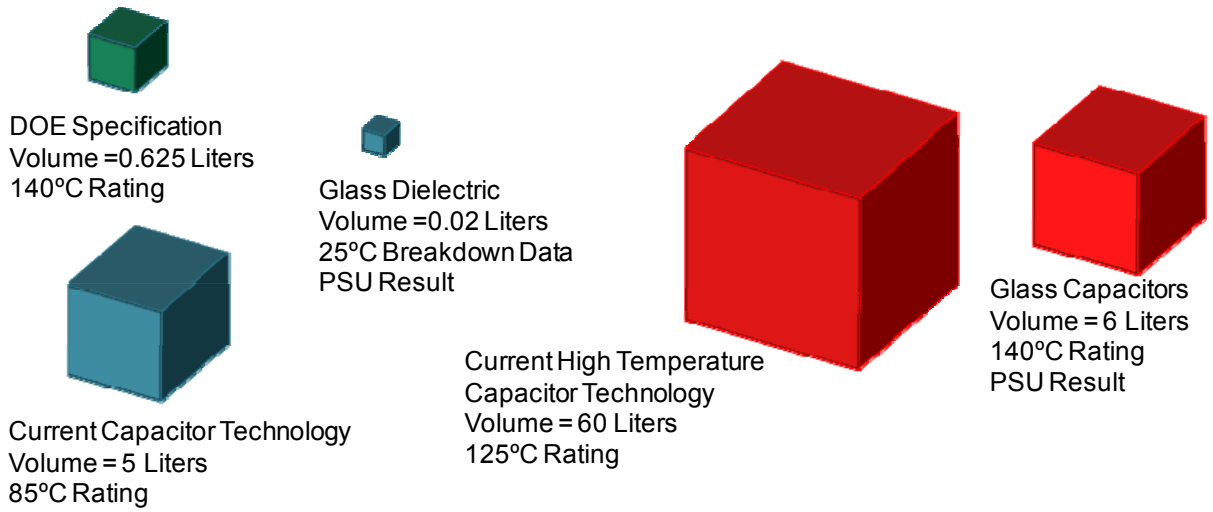

Figure 1: Volumetric comparison between DOE capacitor specifications, commercial capacitors and the projected capacitor volumes from the research at Penn State. All volumes shown are for a 1000 µF 1000 V capacitor.

The DOE specifications (Figure 1 upper left corner) were derived from discussions with the EE tech team and component manufacturers. Presently, polypropylene film capacitors (Figure 1 lower left corner) are used in hybrid electric vehicles which have eight times the volume of the DOE specification and the temperature rating is only 85ºC. The glass dielectrics explored in this study have the potential to operate above 140ºC and the volume is much smaller than commercial high temperature capacitors (Figure 1 right side).

Recent developments in the flat panel display industry and a $30 Billion investment in new production plants have made thin glass sheets a commodity material and a potential low cost dielectric for high temperature power capacitors [1]. Penn State is working with Schott Glass, Nippon Electric Glass and Corning Inc. who are developing new processes for making continuous sheets of glass less that 30 µm in thickness. Glass sheets are common in various consumer electronic and domestic appliances and the processes for manufacturing these dielectrics operate at the megaton level. Recently, alkali free glass has been developed in thin sheets (< 50 µm) for flat panel displays and process provides for near-pristine surfaces. Penn State has characterized the insulating performance of these glass materials and projected the capacitor performance.

Graceful Failure of Glass Capacitors and Accelerated Life Testing:

A primary concern for power electronic capacitor operation is the failure mode. Commercial polymer capacitors are designed to breakdown as an open circuit mode in which there is a loss of capacitance over time. Ceramic capacitors fail catastrophically as a short circuit, which is unacceptable for a power circuit. The primary challenge of this research is in the transition of new glass materials to capacitors for power electronic systems. Risk is mitigated by creating innovative graceful failure architectures on the component level in which only part of the component fails, leaving the remainder of the component operational. Graceful failure mechanisms involve new electrode designs and materials that will be integrated into prototype parts and tested for performance and reliability.

Penn State has successfully deposited alumimum coatings to glass sheet which is the first step in creating a graceful failure mechanisms in glass capacitors (Figure 3).

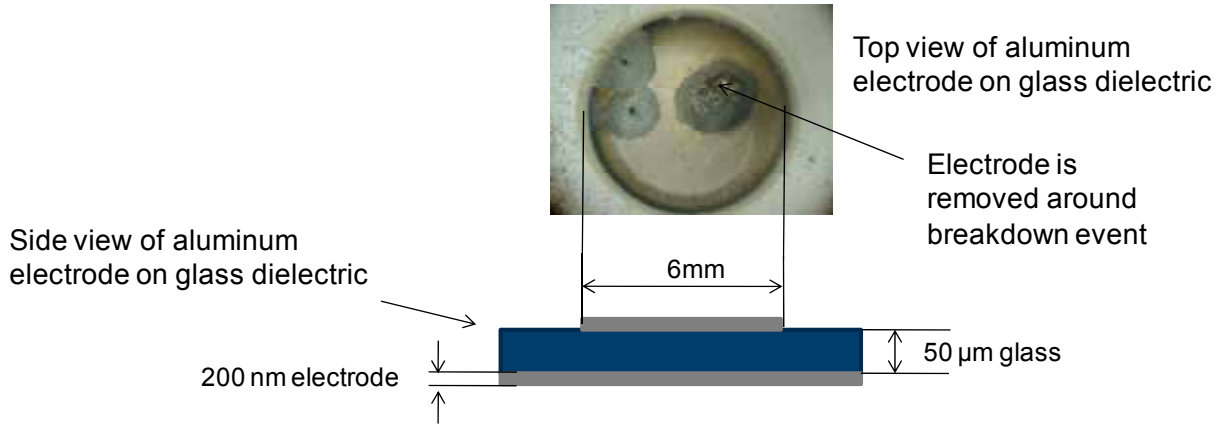

Fig. 3. Graceful failure mode in a prototype glass capacitor that was held at 450ºC at 1kV. The glass was AF45 material from Schott Glass. Top: the failure modes the hot spot is shown as a red region on a blue background. The hot spot is generally a weak spot in the dielectric that conducts and heats. Bottom: Schematic cross section of prototype capacitor.

A complex and serious issue is the lifetime prediction. Fundamentally, the voltage de-rating of a capacitor is required to ensure adequate lifetimes under normal operating conditions for an HEV so the factors that control the lifetime of these prototyped capacitors will be investigated. Highly accelerated lifetime testing (HALT), in which capacitors are DC voltage stressed at high temperature, will elucidate the origins of the failure. A traditional HALT is conducted with a dc-voltage applied to the dielectric at elevated temperatures and the leakage current is monitored as a function of time to a critical condition, such as an order of magnitude increase in leakage current. On the basis of a series of tests, the median-time-to-failure (MTTF), τ, can be related to the voltage stresses and the operating temperature: Using Equation 1,

$$\frac{\tau_1}{\tau_2} = \left(\frac{V_2}{V_1}\right)^n \exp\frac{E_A}{K_B}\left(\frac{1}{T_1} - \frac{1}{T_2}\right) \qquad \text{(Equation 1)}$$

where E_A is the activation process controlling the degradation process, n is voltage acceleration factor, and V_1 and V_2 are the voltage conditions for two conditions corresponding to the isothermal temperatures T_1 and T_2. Accurate predictions of capacitor lifetime are possible by varying the temperature and voltage. Penn State has developed a HALT test system which operates from 25 to 500ºC (Figure 4).

Fig. 4. Highly accelerated life test (HALT) system developed at Penn State University. Over 20 samples can be tested at time so that the failure mechanisms can be statistically determined.

The result for HALT testing the Schott AF45, 50 micron thick glass is shown in Figure 5 and the goal is to have a capacitor life greater than 10,000 hours. Note from Figure 5 that the glass sheet is predicted to survive a temperature of 200 C, 1000V for 10,000 hours.

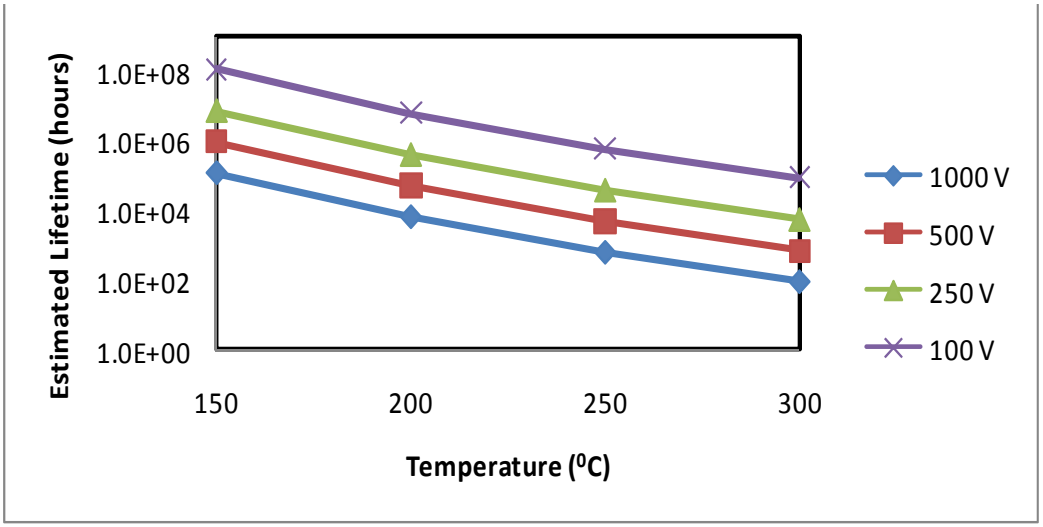

Fig. 5. Estimated life prediction for AF45 glass from Schott using Equation 1 and HALT data accumulated from apparatus shown in Figure 4.

To properly estimate capacitor life, capacitors will require further testing. The projected life in Figure 5 was the result of DC testing and power capacitors generally operate under AC conditions. Penn State will explore the potential of setting up an AC test system for predicting component life under more realistic conditions.

Scale up Glass Capacitor Manufacturing with TRS Technologies:

Penn State researchers are also exploring new production methods with small capacitor manufacturers to fabricate high temperature capacitors. A prototype 1 µF capacitor is shown in Figure 6 which shows the dimensions for a stacked array of individual glass sheets. In the future, large capacitor sheets (10 cm x 10 cm) will be coated with aluminum metal electrodes and the electrical properties will be tested under a variety of voltage and temperature conditions.

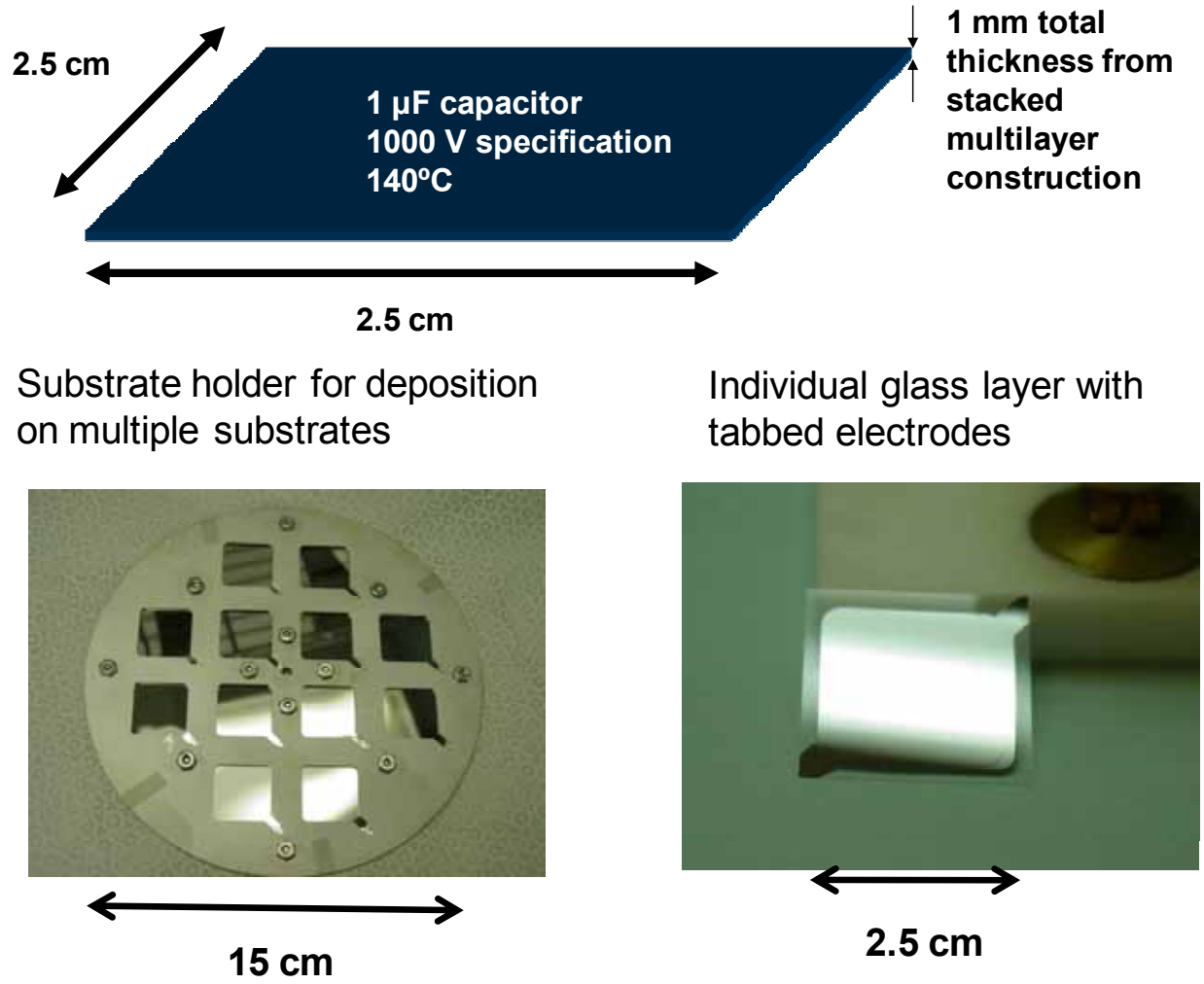

Fig. 6. Production of prototype power capacitors from commercial flat panel display glass. Top: schematic of the final capacitor geometry and specifications. Bottom Left: Fixture for coating the glass sheet with aluminum metal to form the internal capacitor electrodes. Bottom Right: Electrode configuration for a single sheet, including the end terminations connecting the individual layers within the capacitor structure.

Conclusion

The outcome of this project is a cost effective manufacturing process for high temperature capacitors that will meet the US automaker specifications for HEV and PHEV applications. Penn State has collaborated with several industrial partners including large raw materials manufacturers (Corning Inc. and Schott Glass USA) and small capacitor manufacturers (TRS Technologies) to investigate reliable prototype capacitors from glass-ceramic materials.

References

1. http://investintaiwan.nat.gov.tw/en/news/200601/2006010401.html
2. Y Matasumoto, "Ultrathin Glass" presented at the Solar Energy Workshop, Pittsburgh, Nov. 17 (2008).

Publications and Presentations Resulting from this DOE Sponsored Program

1. M.T. Lanagan, T. Shrout, B. Rangarajan, C. Pantano, and S. Conzone, "Glass Based Dielectrics for High Temperature Capacitors," Proc. of the IMAPS High Temperature Electronics Conf., 6 pages, Albuquerque, New Mexico, May 13-15, 2008.
2. M. Lanagan, E. Furman, R. Rajagopalan and P. Tewari Glass and Glass Ceramics as High Energy Materials, US-Japan Winter School on New Functionality in Glass, February 4 - 17, 2008, Kyoto Japan.
3. M. Lanagan, "High Power Capacitors and Energy Storage," Materials Day, April 14, 2008, State College, PA.
4. M. Lanagan, C. Pantano, S. Perini, B. Rangarajan, S. Conzone, "High Temperature Glass-based Dielectrics for Capacitors," presented at IMAPS HiTec Conference , May 13, 2008.
5. M. Lanagan, "High Field Conduction and Space Charge Distribution, and Polarization in Composites," Sandia Pulsed Power Breakout Session, Sandia National Laboratory February 27, 2008, Albuquerque, NM
6. M. Lanagan, "Dielectric Behavior for High Field and High Power over Broad Time Ranges," CDS fall meeting, State College, PA. October 13, 2008.
   M. Lanagan, "An Update on High Energy Storage Capacitors," CDS spring meeting, State College, PA., April 9-10, 2007.
7. M. Lanagan, T. Shrout, B. Rangarajan*, C. Pantano, and S. Conzone, "Glass Based Dielectrics for High Temperature Capacitors," Proc. of the IMAPS High Temperature Electronics Conf., 6 pages, Primary Author, 2008.
8. D. Kwon, T. Akiyoshi, H. Lee and M. Lanagan, "Synthesis and Electrical Properties of Stabilized Manganese Dioxide (a-MnO2) Thin Film Electrodes," J. Amer. Ceram. Soc., 91: 906-909, First Author Supervised by Candidate, 2008.
9. B. Rangarajan, B. Jones, T. Shrout and M.T. Lanagan, "Barium/Lead Based Invert Glasses for High Energy Density Capacitor Applications," J. Amer. Ceram. Soc., 90(3):784-788, 2007.
10. D. Kwon, T. Akiyoshi and M.T. Lanagan, "(ICACC-S10-049-2007) Synthesis of Manganese Oxice Thin Films for Capacitor Electrodes," 31st International Cocoa Beach Conference & Exposition on Advanced Ceramics & Composites, Daytona Beach, Florida. January, 2007.
11. M.T. Lanagan (Primary Presenter), D. Kwon and E. Semouchkina, "(ICACC-S10-056-2007) Dielectric Materials Development for Low Temperature Co-Fired Ceramics ," 31st International Cocoa Beach Conference & Exposition on Advanced Ceramics & Composites, Daytona Beach, Florida. January, 2007. (Invited Presentation).
12. M. T. Lanagan, Workshop Organizer, "High Energy and Temperature Capacitor for Advanced Power Systems (HEATCAPS) Workshop," State College, PA October, 2007.
13. M. T. Lanagan, "Electronic Applications of Glass," 1st International Workshop on Scientific Challenges of New Functionalities in Glass, Washington DC, April 2007 (Invited Presentation).
14. B. Rangarajan, B. Jones, T. Shrout and M. Lanagan, "Glass ceramics from invert glasses for high energy density capacitor applications, GOMD Meeting, Greenville, SC, May 15-19, 2006.
15. B. Rangarajan, "Glass capacitors with high energy densities as energy sources in hybrid vehicles," Global Roadmap for Ceramics, International Congress on Ceramics, Toronto, June 25-29, 2006
16. B. Rangarajan, B. Jones, C. Wang, T. Shrout and M.T. Lanagan, "Barium/Lead Based Invert Glasses for High Energy Density Capacitor Applications," 8th International Symposium on Crystallization in Glasses and Liquids, Jackson Hole, Wyoming. September, 2006.

4.8 High Temperature Thin Film Polymer Dielectric Based Capacitors for HEV Power Electronic Systems

Shawn M. Dirk,[†] Patti Sawyer,[†] Jill Wheeler,[‡] Mark Stavig,[†] Bruce Tuttle[‡] and Joseph Bond[±]
[†]Organic Materials Department and
[‡]Electronic & Nanostructured Materials Department
Sandia National Laboratories
P.O. Box 5800
Albuquerque, NM 87185
Voice: 505-844-7835; Fax: 505-844-9624; E-mail: smdirk@sandia.gov

[±]Electronic Concepts Inc. (ECI)
P.O. Box 1278
526 Industrial Way
Eatontown,
New Jersey 07724

DOE Technology Development Manager: Susan A. Rogers and Steven Boyd
Voice: 202-586-8997; Fax: 202-586-1600; E-mail: susan.rogers@ee.doe.gov; steven.boyd@ee.doe.gov

Sandia Program Manager: Shawn M. Dirk
Voice: 505-844-7835; Fax: 505-844-9624; E-mail: smdirk@sandia.gov

---

Objectives

Currently, DC bus capacitors are currently the largest and the lowest reliability component of fuel cell and electric hybrid vehicle inverters. Furthermore, current DC bus capacitors cannot tolerate temperatures greater than 120°C. Our project goal is to develop a replacement high energy densisty, high temperature dielectric for DC bus capacitors for use in electric hybrid and fuel cell vehicles. The improved capacitors will be based on novel high temperature polymer thin film dielectrics. Our technical goal is to enhance high temperature performance and volumetric efficiency compared to present dielectrics. Specific metrics include the development of polymer film dielectrics with dissiaption factors of 0.01 or less at 150 ºC. Synthesis, fabrication, and high temperature (100 to 150 ºC) characterization of these dielectric materials is an integral part of the material development program. In addition, work will focus on transitioning the material to industry to produce rolls of the novel high temperature polymer dielectric film will lead directly to the production of a prototype capacitor.

Approach

Sandia National Laboratory's (Sandia) capacitor R&D program addresses the technology gap in an innovative manner. We are developing high performance, high temperature, low cost capacitors that are based on novel Sandia developed polymer chemistry. Capacitors fabricated using this polymer technology will achieve the high degree of packaging volumetric efficiency with less weight. Our R&D efforts focus on 1) determining the optimum polymer stoichiometry for high temperature dielectric performance as well as 2) producing polymer film in an appropriate quantity to fabricate prototype capacitors.

Major Accomplishments

- Completely characterized copolymer stoichiometry and the effect on high temperature dielectric performance.

- Identified an industrial partner (ECI) to produce rolls of polymer film (>100 m length) and then fabricate prototype capacitors.
- Started the first large scale run of polymer film formation.

Future Direction

The R&D effort has demonstrated feasibility of using high temperature dielectrics for power electronics operating at high temperatures (150 ºC). Progress achieved thus far sets the stage to begin fabrication of prototype high temperature capacitors. This will require the development of polymer casting conditions that allow the production of large rolls (>100 m length) of polymer dielectric films. We will continue to work with our industrial partner (ECI) to produce a desired amount of material capable of prototype capacitor formation. We will further work with ECI to produce several prototype capacitors. These prototype capacitors will be evaluated and benchmark it against APEEM goals. These initial prototypes will be evaluated by ORNL as well as other research institutions. We will continue our effort in developing dielectric materials with improved performance focusing on the incorporation of nanoparticle fillers to increase the energy density further.

Technical Discussion

1.0. Materials Development

Recently much research has focused on the development of new polymer dielectric materials for next generation capacitors that may find use in the inverters of next generation hybrid electric vehicles (HEV). Capacitors used in HEVs inverters will be required to operate at 150 °C, 600V, and have an energy density of 0.9 J/cm^3. Polymer based thin film capacitors are ideal for this application due to their relatively high energy density, low cost, and high dielectric breakdown field. Perhaps one of the most beneficial attributes of thin polymer film based capacitors is their propensity to fail gracefully open rather than short. The best metric for comparison of polymeric thin film materials is the energy density (Ue) which is given by $U_e = 1/2\varepsilon_r\varepsilon_0 E^2$, where ε_r is the dielectric permittivity, ε_0 is the vacuum permittivity (ε_0 = 8 × 10-12 F/m), and E is the applied electric field. Accordingly, both a large dielectric constant and a large breakdown strength are required to increase energy density.

Currently polymer film capacitors rely on polymers with dielectric constants ranging from 2-3.5, however, several fluoropolymers have demonstrated much greater dielectric constants.[1] An example of one of the polymers currently in use is biaxially oriented polypropylene (BOPP) which has a low dielectric constant (~2.2).[2] The current polymer based capacitors have ceiling operational temperatures of between 105 °C and 120 °C. This limitation is because as the polymer dielectric temperature rises typically the dissipation factor increases above a usable value.

In this communication we have evaluated free standing thin films of N-Phenyl-7-oxanorbornene-5,6-dicarboximide (**1**, PhONDI) and several of its copolymers with norbornene for possible use as next generation polymer dielectrics in thin film capacitors. The 7-oxanorbornene monomers can be easily synthesized and modified in order to add diverse chemical functionality.[3-5] 7-oxanorbornenes can be polymerized using ring opening metathesis polymerization (ROMP), a living polymerization that allows very good control over the final polymer molecular weights.

The monomer (**1**) was initially evaluated because its chemical structure contains a large heteroatorm content and contains an imide functional group. We have observed that the dielectric constant typically increases with increased heteroatom content. The imide functional group was appealing because of the superior high temperature performance of Kapton materials.[6] The N-Phenyl-7-oxabicyclo[2.2.1]5-heptene-2,3-dicarboximide (PhONDI) was synthesized from the Diels Alder reaction of furan (2) and N-

phenyl maleimide (**3**). Polymerization of PhONDI to produce polymer **4** was accomplished with the use Grubbs 1st generation[7] ruthenium carbene catalyst as shown in Scheme 1.

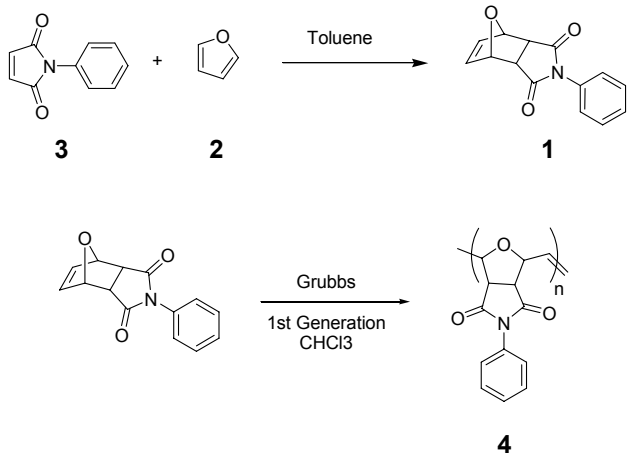

3 **2** **1** **4**

Scheme 1. Synthesis of PhONDI and the homopolymer of PhONDI.

Polymer **4** produced in this manner was evaluated as a next generation polymer capacitor dielectric. In order for a polymer to be useful as a dielectric the polymer needed to have a relatively high dielectric constant (when compared to other carbon based polymers), a low dissipation factor, and have a high breakdown strength. In addition the polymer dielectric needs to be processed into thin flexible films that allow for the production of rolled capacitiors.

The homopolymer of PhONDI exhibited very good electrical properties, with a $k > 6.0$ and a low dissipation factor at 1 kHz. However, the homopolymer did not enable the fabrication of the needed thin free standing thin films. The polymer was very brittle as a result of the high T_g. The T_g of the homopoymer was found to be 172 °C.[8] In order to lower the Tg of the polymer we copolymerized PhONDI with norbornylene ($\varepsilon_r = 2.2$).[9] It has previously been reported that the Tg of a 50/50 molar blend was 125 °C.[10] In our lab we found the 50/50 blend to lower the Tg of the resulting material to 72 °C.

Several molecular weights were initially evaluated in order to produce thin flexible films. A molecular weight of 150,000 was chosen as the target in order to make a flexible thin film that exhibited some yield and would be capable of being wound into rolled capacitors.

Initial polymer films were formed by spin casting onto silicon wafers. Electrical characterization of the spuncast 50:50 blend is shown in Figure 1.

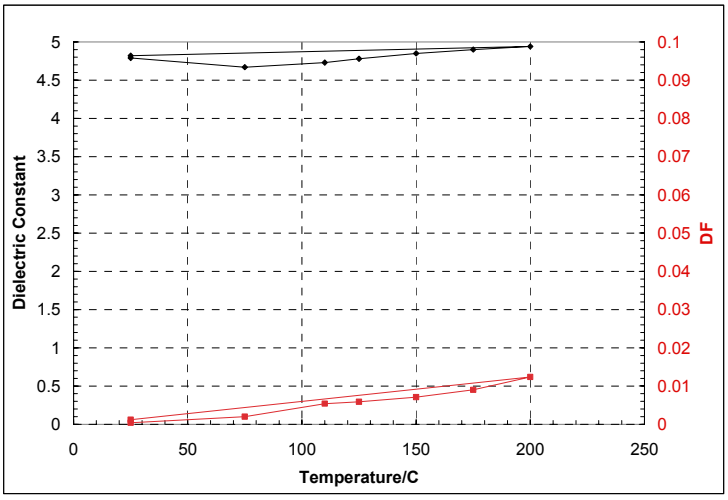

Fig. 15. Dielectric characteristics of a 50:50 random copolymer of norbornylene andPhONDI spuncast onto a silicon wafer.

Several other copolymer formulations were synthesized. Once the copolymer was synthesized it was redissolved in chloroform and cast using a drawdown machine. The polymer solution was placed on a Teflon substrate in order to allow for easy removal of the formed film. Using this method we have been able to produce large (8.5" x 11") area polymer films. The thickness of the polymeric material was controlled by using different metering rods on the drawdown machine. Using this technique we have been able to produce polymer films ranging in thickness from 2 - 40 um.

The polymer was removed from the teflon substrate as one single continuous film. The resulting polymer film was cut in order to place the polymer film in an evaporator. The polymer film was coated with Au on one side to produce 2.5 um^2 Au electrodes with 2.5 um pitch.

The electroded polymers were placed on a copper plate and contact was made via a probe tip to the top Au electrode and the copper plate. A Hewlett Packard 4284A Precision LCR meter was used to measure the capacitance of the small test capacitors and the dielectric constant of the polymer film was calculated based on the thickness and area of the polymer dielectric. Both the dielectric constant and the dissipation factor were measured initially at 25 °C as shown in Fig. 16.

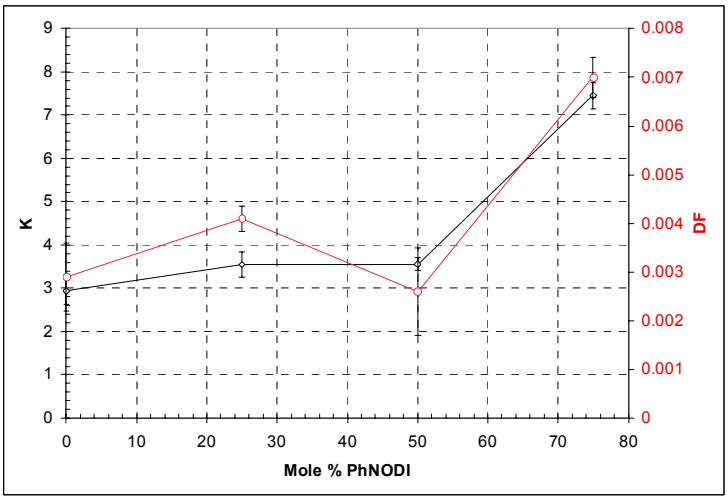

Fig. 16. Electronic characterization of solvent cast films including K and DF as a function of PhONDI concentration measured at 25C.

and then as a function of temperature up to 200 °C as shown in Fig. 17. Films produced using the solvent cast drawdown method did not electricially perform as well as spuncast films. Solvent cast films had more surface defects than the spuncast films as noted by visual observation.

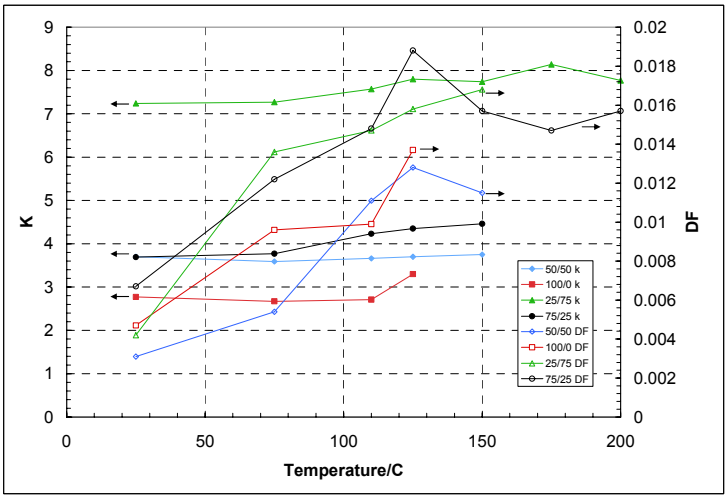

Fig. 17. Electronic characterization of solvent cast films including K and DF as a function of temperature.

The breakdown strengths of the polymers as a function of PhONDI concentration is shown in Figure 18.

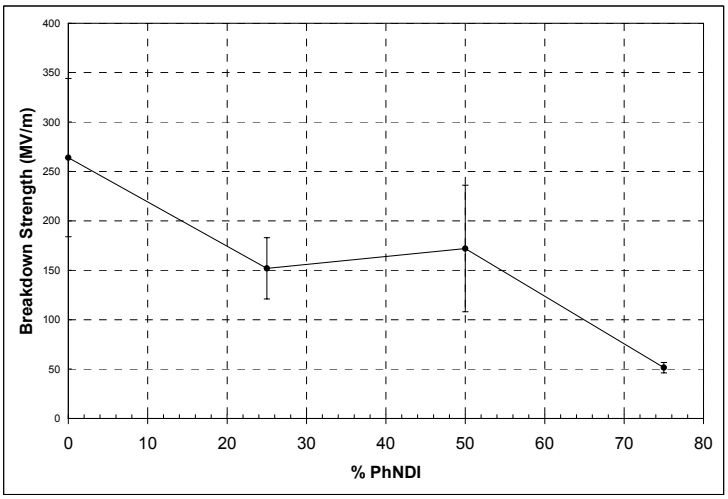

Figure 18. Breakdown strength of the solvent cast polymers as a function of PhONDI concentration.

2.0.Polymer Film Production

An industrial partner (ECI) was identified in January 2008 to begin the fabrication of large rolls (>100 m length) of polymer film. A purchase order was placed to begin the production of polymer films. In order to facilitate thin film production ~1 kg of the identified polymer was sent to ECI where several solvents and solvent combinations were evaluated in order to produce the required rolls of polymer film. To date only small amounts of polymer films have been produced at ECI. Process development will continue in order to produce the required amount of polymer dielectric film.

Conclusion

We have developed a novel polymeric material that has superior high temperature dielectric properties. Furthermore we have electrically characterized various copolymer stoichiometries to identify the optimal high temperature dielectric. We have begun working with and industrial partner (ECI) to fabricate large rolls (> 100 m length) of polymer dielectric film leading to prototype capacitor fabrication. This high temperature polymer film technology will be used to fabricate high temperature DC bus capacitors with significantly reduced size and weight, and improved performance and reliability.

References

1. Zhang, Z.; Chung, T. C. M., The Structure-Property Relationship of Poly(vinylidene difluoride)-Based Polymers with Energy Storage and Loss under Applied Electric Fields. *Macromolecules (Washington, DC, U. S.)* **2007,** 40, (26), 9391-9397.
2. Claude, J.; Lu, Y.; Li, K.; Wang, Q., Electrical Storage in Poly(vinylidene fluoride) based Ferroelectric Polymers: Correlating Polymer Structure to Electrical Breakdown Strength. *Chem. Mater.* **2008,** 20, (6), 2078-2080.
3. Gangadhara, I. C.; Thomas, M.; Reyx, D., Synthesis and characterization of 4-cyanobiphenyl-4'-yloxy-functionalized poly(7-oxanorbornene-5,6-exo-dicarboximide)s via ring opening metathesis polymerization (ROMP). *J. Polym. Sci., Part A: Polym. Chem.* **1998,** 36, (15), 2807-2821.
4. Santiago, A. A.; Vargas, J.; Gavino, R.; Cerda, A. M.; Tlenkopatchev, M. A., Synthesis and ring-opening metathesis polymerization of new oxanorbornene dicarboximides with fluorine pendant groups. *Macromol. Chem. Phys.* **2007,** 208, (10), 1085-1092.
5. Arjona, O.; Csaky, A. G.; Plumet, J., Sequential metathesis in oxa- and azanorbornene derivatives. *Eur. J. Org. Chem.* **2003**, (4), 611-622.

6. Critchley, J. P.; White, M. A., Perfluoroalkylene-linked aromatic polyimides. II. Further property studies. *J. Polym. Sci., Part A-1: Polym. Chem.* **1972,** 10, (6), 1809-25.
7. Trnka, T. M.; Grubbs, R. H., The Development of L2X2Ru:CHR Olefin Metathesis Catalysts: An Organometallic Success Story. *Acc. Chem. Res.* **2001,** 34, (1), 18-29.
8. Vargas, J.; Colin, E. S.; Tlenkopatchev, M. A., Ring-opening metathesis polymerization (ROMP) of N-cycloalkyl-7-oxanorbornene dicarboximides by well-defined ruthenium initiators. *Eur. Polym. J.* **2004,** 40, (7), 1325-1335.
9. Grove, N. R.; Kohl, P. A.; Bidstrup Allen, S. A.; Jayaraman, S.; Shick, R., Functionalized polynorbornene dielectric polymers: adhesion and mechanical properties. *J. Polym. Sci., Part B: Polym. Phys.* **1999,** 37, (21), 3003-3010.
10. Tlenkopatchev, M. A.; Vargas, J.; Lopez-Gonzalez, M. d. M.; Riande, E., Gas Transport in Polymers Prepared via Metathesis Copolymerization of exo-N-Phenyl-7-oxanorbornene-5,6-dicarboximide and Norbornene. *Macromolecules* **2003,** 36, (22), 8483-8488.

5. Systems Research and Technology Development

5.1 Benchmarking of Competitive Technologies

Principal Investigator: Tim Burress
Oak Ridge National Laboratory
National Transportation Research Center
2360 Cherahala Boulevard
Knoxville, TN 37932
Voice: 865-946-1216; Fax: 865-946-1262; E-mail: burressta@ornl.gov

DOE Technology Development Manager: Susan A. Rogers
Voice: 202-586-8997; Fax: 202-586-1600; E-mail: Susan.Rogers@ee.doe.gov

ORNL Program Manager: Mitch Olszewski
Voice: 865-946-1350; Fax: 865-946-1262; E-mail: olszewskim@ornl.gov

---

Objectives

- Determine the status of nondomestic hybrid electric vehicle (HEV) technologies through assessment of design, packaging, fabrication, and performance during comprehensive evaluations
  - — Compare results with those from other HEV technologies
  - — Distribute findings in the open literature
- Support FreedomCAR program planning and assist in guiding research efforts
  - — Confirm the validity of the program technology targets
  - — Provide insight for program direction
- Produce a technical basis that aids in modeling/designing
- Foster collaborations with the Electrical and Electronics Technical Team (EETT) and Vehicle Systems Analysis Technical Team (VSATT)
  - — Identify unique motor/inverter/converter/drive-train technologies
  - — Ascertain what additional testing is needed to support research and development

Approach

- Choose a vehicle subsystem
  - — Evaluate the potential benchmarking value of various HEVs
  - — Consult with original equipment manufacturers as to which system is most beneficial
- Tear down a power converter unit (PCU) and an electronically-controlled continuously variable transmission (ECVT)
  - — Determine volume, weight, specific power, and power density
  - — Assess design and packaging improvements
  - — Test magnets and capacitors
- Prepare components for experimental evaluation
  - — Develop interface and control algorithm
  - — Design and fabricate hardware necessary to conduct tests
  - — Instrument subsystems with measurement devices
- Evaluate hybrid subsystems
  - — Determine peak and continuous operation capabilities
  - — Evaluate efficiencies of subsystems
  - — Analyze thermal data to determine assorted characteristics

Major Accomplishments

- Selected the 2008 Lexus LS600h system to benchmark based on anticipated automotive manufacturer interest due to the novel double-sided cooling technique that accompanies the most powerful HEV drivetrain currently on the market.
- Conducted design/packaging studies of the LS600h PCU and ECVT, revealing significant improvements over Toyota Prius and Camry designs.
- Bypassed the LS600h PCU motor inverter controls to allow full control over testing conditions.
- Disassembled and evaluated key components within the PCU/ECVT.
- Assessed mass, volume, power density, and specific power of various PCU/ECVT components.
- Evaluated efficiency, performance, and continuous operational capabilities of the LS600h subsystems.
- Communicated effectively with EETT and VSATT to aid in discerning project direction, test plan, and test results.

Future Direction

- Discussions will be conducted with EETT and VSATT to determine the appropriate system to study in FY 2009.
- Approaches similar to those of previous benchmarking studies will be taken while working to meet the universal need for standardized testing conditions.

Technical Discussion

The subsystems of the 2008 Lexus LS600h Synergy Drive were obtained in order to conduct thorough studies of design, packaging, efficiency, performance, and operational characteristics. The LS600h hybrid drive system is similar to those of the Toyota Prius and hybrid Camry in terms of overall function. However, there are significant differences between the designs in both the PCU and ECVT subsystems. The primary discrepancy between the LS600h PCU and previous PCU designs is the introduction of a double-sided cooling technique that incorporates a power electronics module with cooling plates for both the collector and emitter sides of the insulated gate bipolar transistor (IGBT), as opposed to a cooling plate for only the collector side of the IGBT. The double-sided cooling method greatly increases the capability to remove heat from the IGBTs and diodes and thereby reduces the constraints placed upon these high-power semiconductors.

The LS600h ECVT has an elongated transmission housing to supplement all-wheel drive capability in contrast to the front-wheel-drive transaxle configurations previously benchmarked. Consequently, the primary interior permanent magnet motor of the LS600h has a smaller diameter but is more elongated than its front-wheel-drive counterparts. This geometrical reformation is suited to the constraints associated with the undercarriage location of the ECVT. Published specifications indicate that the primary drive motor is rated at 165 kW, can produce 300 Nm up to 5,250 rpm, and has a maximum motor speed of 10,230 rpm. The motor is connected to the primary drive shaft through a gear ratio much like that of the Camry; however, the gear ratio of the Lexus can be selected to be high or low by means of a Ravigneaux gear system with a clutch and brake system.

An important product of the benchmarking efforts is not only validation of specifications published by the manufacturer, but also a detailed understanding of requirements and characteristics corresponding with operation points throughout the entire operation range, including peak regions. For example, the LS600h motor can produce 300Nm only for very short periods of time, and the extent of the time varies with parameters such as speed and ambient temperature. These requirements and characteristics are essential in making comparisons with other drive system designs and are particularly useful for comparisons of motor/power converter design, motor modeling, and thermal modeling. The results from these efforts are detailed in [1].

Teardown—power converter unit

The PCU shown in Fig. 1 includes a cooling infrastructure for the double-sided power modules, boost converter, motor inverter, generator inverter, and their associated components such as capacitors, drivers, and controllers. Although the overall function and appearance of the LS600h PCU is similar to that of the Camry PCU, there is a significant difference between the two in terms of architecture. As shown in Ref [1], the Camry PCU has a separate compartment for the boost converter. To accommodate the move to the double-sided cooling technique, all power electronics are located adjacent to one another in the LS600h PCU. Additionally, the control and driver electronics for the boost converter and inverters are grouped together on the same boards, as opposed to the Camry design. The bus architecture and cooling infrastructure have also been significantly redesigned. There are many subtle differences between the Camry and Lexus PCU, such as a larger dc link capacitor, and boost converter inductor, and the side housing for motor and generator connectivity.

Fig. 1. The LS600h power converter unit.

The PCU was completely disassembled; its primary components are indicated in Fig. 2. Shown in the upper portion of Fig. 2 is the entire PCU with two ~288 V connectors as well as the control and driver boards. A battery voltage of ~288 V is applied to the boost converter input and is also fed to the secondary ~288 V connector through a fusible link in order to supply energy to the air-conditioning compressor inverter. Under the lid covering the driver and controller circuits, the topologies appear to be generally similar to that of the Camry, yet further analysis reveals several design changes.

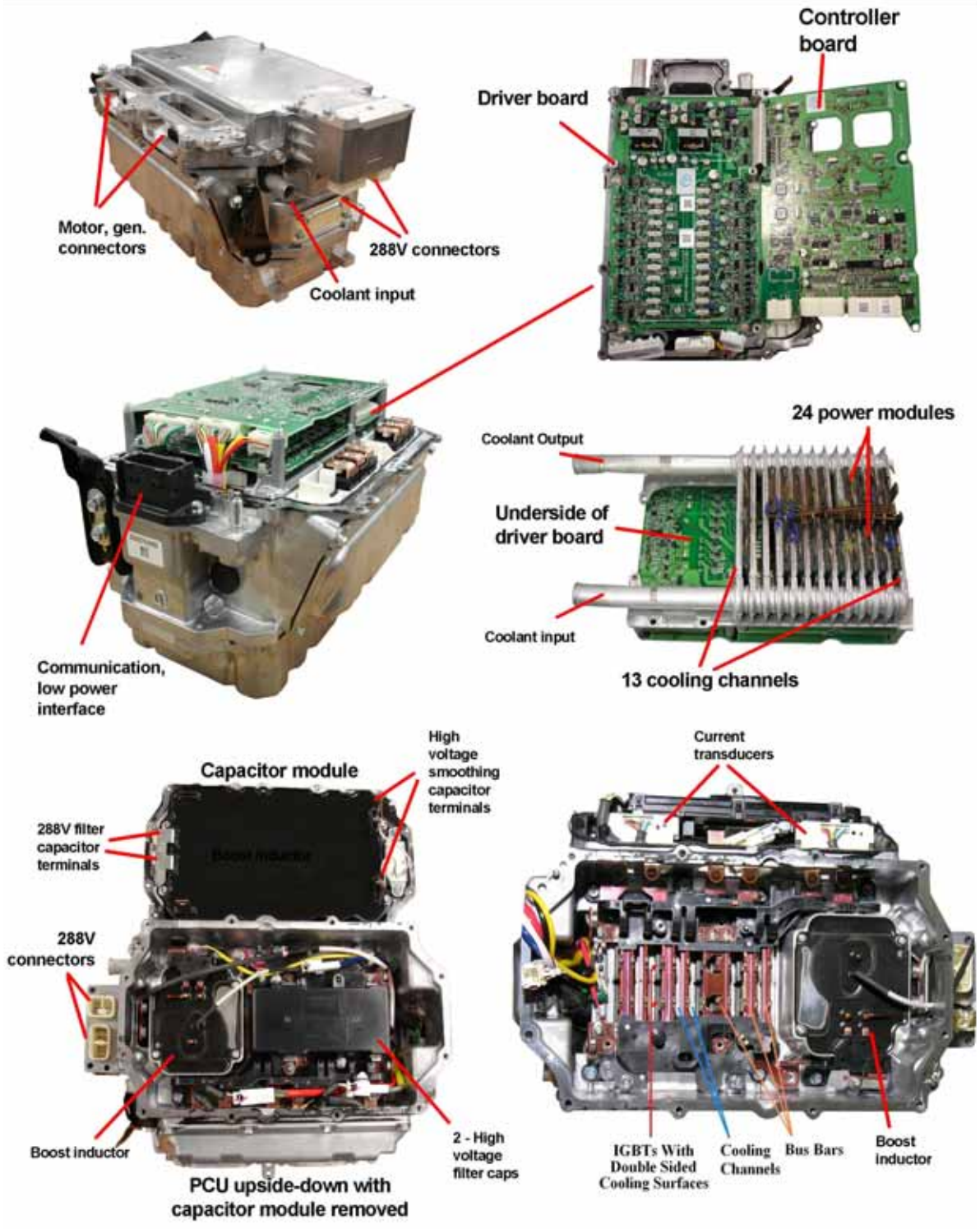

Fig. 2. LS600h PCU teardown.

In the lower-left portion of Fig. 2, the PCU sits upside-down with the capacitor module removed and placed adjacent to the PCU. The size of the capacitor module has increased significantly compared with the Camry, as it now houses both the low-voltage filter capacitor and the high-voltage smoothing capacitor. Capacitance values increased for the high-voltage capacitor from 2.098 to 2.61 mF and

decreased for the low-voltage capacitor from 378 to 365 μF in moving to the Lexus design. Terminals of the low-voltage capacitor section of the module connect to terminals at the boost converter input, which is supplied directly from the 288 V battery. The high-voltage capacitor terminals connect directly to the dc link, which reaches up to 650 V and is shared by the motor and generator inverters. A bus bar inside the capacitor module serves as the common to the low and high sides of the boost converter. Just as in the in the Camry PCU, a 54 kΩ resistor is used and is located next to and attaches directly to the high-voltage terminals, thereby bleeding off the dc-link during inactivity. Located in the middle compartment next to the boost converter inductor are two additional high-voltage filter capacitors, which are combined into a small capacitor module. After the small capacitor module is removed, the bus bars, power modules, and cooling channels are visible, as shown in the lower-right hand corner of Fig. 2.

Shown in the middle portion of Fig. 2 is the entire PCU cooling infrastructure for the 24 double-sided power electronics modules. Just as in previous designs, an ethylene glycol and water mixture is circulated through the PCU and ECVT to a radiator that is on a separate loop from the internal combustion engine. However, the LS600h cooling system does not incorporate a conventional heat sink but instead uses 13 cooling channels to straddle the 12 sets of upper and lower power electronics modules. With a total of 24 modules, 12 are used in the motor inverter, 6 in the generator inverter, and 6 in the boost converter. Each module contains a diode and an IGBT with five drive/sensing pins as well as collector and emitter bus bars protruding from the module, as indicated in the upper-left segment of Fig. 3.

The LS600h power module detailed in Fig. 3 incorporates a collector plate/bus and an emitter plate/bus, both of which transfer heat to the nearest cooling channel through thermal grease, and an insulator. A black high-density, high-temperature plastic retains and supports all components of the power module. The IGBT collector and diode cathode are soldered directly to the collector plate, and the IGBT emitter and diode anode are soldered to spacers, which are soldered to the emitter plate. With the PCU sitting upright, collector and emitter bus bars extend downward to the converter/inverter bus bars, while the drive/sense pins extend upward to the driver board. A large metal strip applies pressure to the entire stack of modules and cooling channels to ensure mating surfaces are complementary to heat transfer. Although the output power rating of the motor inverter is increased considerably from that of the Camry, the number of IGBTs and diodes used for the motor inverter decreased from 18 to 12, as the semiconductor ratings are greatly affected by the capabilities of the thermal management system.

Teardown—ECVT

The overall functionality of the 2008 LS600h ECVT, shown in Fig. 4, is similar to that of the Camry and Prius, yet there are significant differences between the subsystem designs. All systems use the sun gear of a planetary gear set to receive input from the generator with a hollow rotor shaft, through which a shaft connected to the internal combustion engine passes and connects to the planetary carrier. The ring of the planetary gear is connected directly to the motor output in the Prius and to the motor through a high-speed reduction gear in the Camry. The Prius and Camry planetary rings drive the differential output through a series of drive gears. Similar to the Camry design, the LS600h ring gear connects to the motor output through a gear system. However, the LS600h uses a Ravigneaux gear configuration to facilitate a high and low gear selection through a clutch, brake, and pressure plate mechanism similar to what is found in many conventional automatic transmissions. A Ravigneaux gear system consists of two planetary gear sets, and its operation can be manipulated depending on which clutch set has pressure applied to it, thereby locking the ring of the corresponding planetary gear set to the chassis. A long shaft passes through the center of the drive motor rotor and connects the power split planetary ring to the output of the Ravigneux gear system, and the two are unified into one spline. This spline mates with the input of the transfer case, which also uses a small planetary gear to distribute power to the front and rear wheels appropriately.

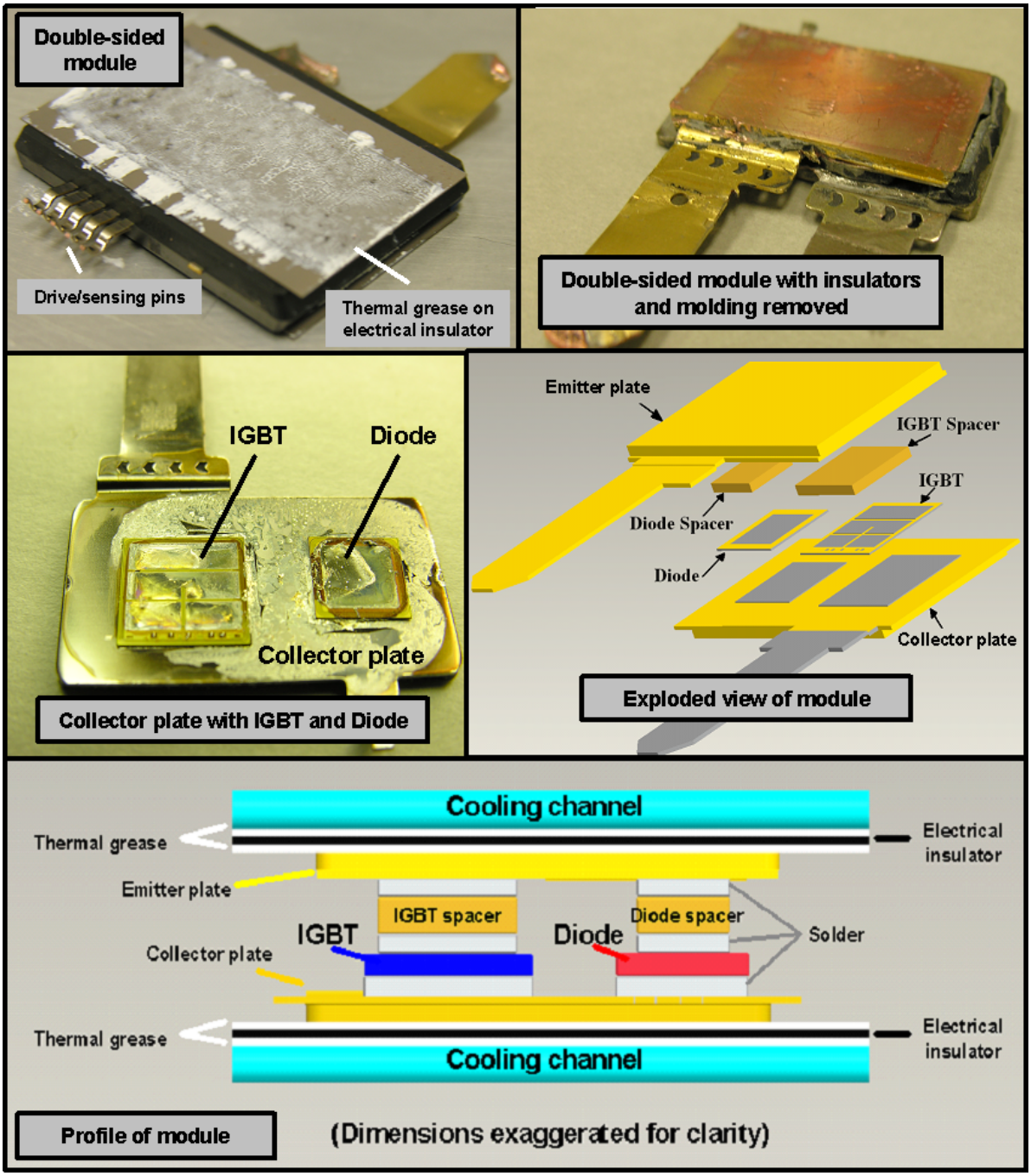

Fig. 3. LS600h power module with double-sided cooling.

One of the most noticeable features of the electric machines in Fig. 4 is the elongated shape of the motor rotor. Figure 5 provides details of the LS600h motor design, as well as a comparison of the motor stator laminations of the LS600h and 2007 Camry. Table 1 lists various LS600h and Camry motor parameters. The outer diameters of the LS600h motor and Camry motor stator laminations are 7.88 and 10.395 in., respectively. Stator lamination stack lengths for the LS600h and Camry motor are 5.33 and 2.4 in., respectively. Although the lamination outer diameter of the LS600h is only 76% that of the Camry, the lamination stack is more than twice the length. The entire stator mass is relatively the same, but the LS600h rotor is about 6.5 lbs heavier than the Camry rotor.

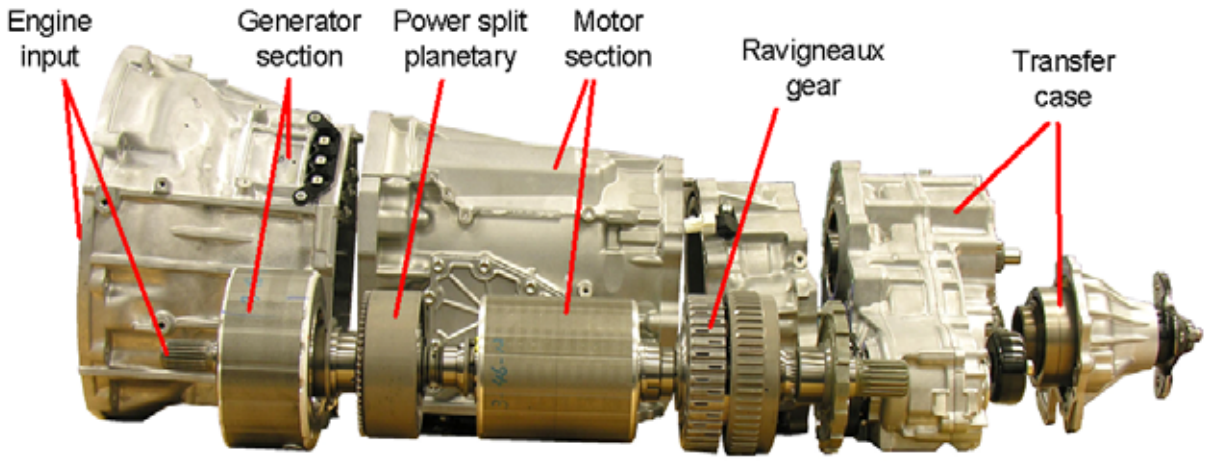

Fig. 4. Various sections of 2008 Lexus LS600h ECVT.

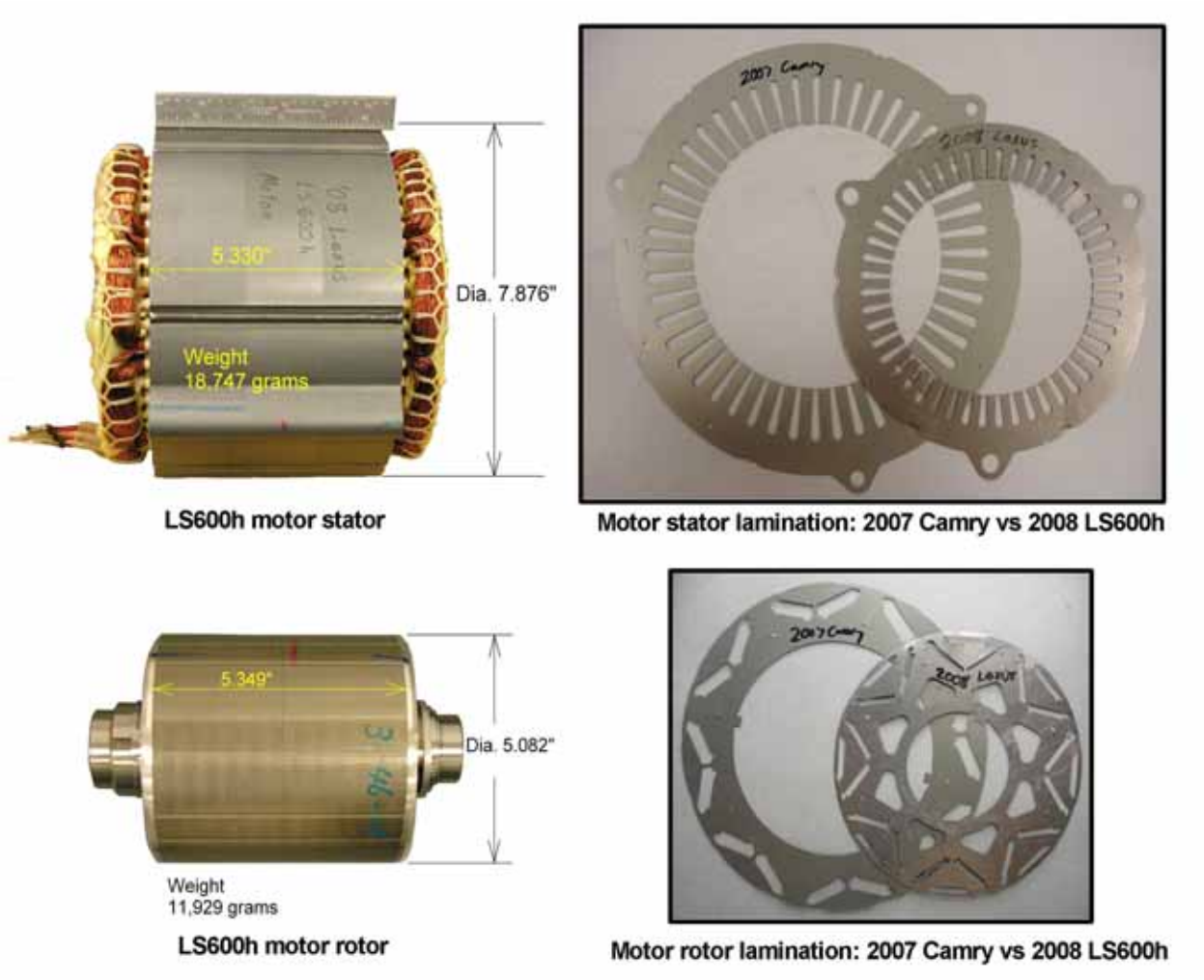

Fig. 5. LS600h vs Camry: motor stator (upper) and motor rotor (lower).

Table 1. Comparison of 2008 LS600h and 2007 Camry motor parameters

	LS600h	Camry
Motor stator outer diameter	7.88 in.	10.395 in.
Motor stator stack length	5.33 in.	2.4 in.
Motor stator mass	41.3 lb	39.7 kg
Motor rotor mass	26.2 lb	19.8 lb
Magnet mass	2.97 lb	2.05 lb
Copper mass	7.92 lb	12.5 lb
Peak air-gap flux measurement	8.53 kG	8.2 kG

A closer look at the LS600h and Camry rotor laminations in Fig. 5 reveals that the LS600h magnet slots are much thinner, and there is also an additional slot. Beginning with the 2004 Prius, all Toyota permanent magnet motors have had the "inverted V" magnet orientation. Although the additional magnet in the LS600h adds to the peak magnet strength, as verified in air-gap flux measurements, the location of the magnet effectively hinders the reluctance torque component. The length of each magnet was increased from 2.387 to 2.62 in. and the thickness reduced from 0.26 to 0.12 in. Two sets of these magnets are installed into the LS600h rotor, giving a total of 48 magnets. Overall, the magnet mass increased from ~2 to ~3 lb. It is possible that the low maximum-speed rating of 10,230 rpm is due to the mechanical stresses associated with the retention of the additional extra magnet. It is not set as deeply into the lamination as the "inverted V" magnets. Although the elongated design has a higher magnet mass, the amount of copper used in the stator was reduced from 12.5 to 7.92 lb, even though the peak power capability was increased considerably. Although the motor underwent significant design changes, the LS600h generator stator laminations have the same outer diameter and inner diameter as the stator laminations of the Camry motor and generator.

Table 2 provides a comparison of the specific power and power density of three HEV systems, the Prius, Camry, and LS600h. The results indicate that the peak power density and peak specific power of the inverter improved by ~50% from the Camry to the LS600h. Note that peak power capabilities were used in these calculations, and the use of continuous ratings may yield closer results for the motor assessments. However, it is difficult to generalize continuous power ratings as they are based upon a variety of conditions, such as coolant temperature, stator temperature limit, and motor speed. Nonetheless, the double-sided cooling technique has an apparent advantage over previous designs.

Table 2. Comparison of specific power and power densities for various HEV components

Component and parameter	Lexus (110 kW)	Camry (70 kW)	Prius (50 kW)
Motor			
Peak power density, kW/L	6.6	5.9	3.3
Peak specific power, kW/kg	2.5	1.7	1.11
Inverter (excluding generator inverter and buck/boost converter)			
Peak power density, kW/L	17.1	11.7	5.7
Peak specific power, kW/kg	14.8	9.3	5.7

Experimental evaluation

Various evaluations were conducted of the PCU and ECVT to determine operational characteristics such as efficiency, continuous capability, and performance. Initial tests include measurement of back-emf (electromotive force) voltage, no-load losses, and locked rotor torque. These tests provide parameters and characteristics of the motor that are useful for approximating its capabilities. Secondary evaluations include efficiency, performance, and continuous analyses of the subsystems. Before any tests could be conducted, the ECVT was modified to provide access to the motor shaft. The only shafts externally accessible are the engine input and Ravigneaux gear output shafts. Although the Ravigneaux gear is indirectly connected to the motor, power measurements through these gears would not be accurate enough to make precise motor efficiency calculations. A shaft was designed and fabricated in order to provide external access to the motor rotor. The fabricated shaft was fed directly to a speed and torque transducer. The other side of the torque transducer was coupled to a speed reduction gear box. The gear box is capable of handling speeds of up to 18,000 rpm, and the dynamometer can operate at power levels of up to 400 hp. All hardware on the high-speed portion of the shaft was designed to have face-mount couplings, which provide extra safety since the shafts are shorter and are not exposed. Additionally, shaft alignment issues are avoided with this approach.

Extensive efforts were made to ensure that the ECVT modification did not impact cooling or lubrication characteristics by inadvertently hindering or enhancing oil flow. The system depends greatly on proper oil circulation for heat conduction and lubrication. Oil is circulated with a mechanically driven trochoid oil pump and an electrically driven trochoid oil pump. Consideration of proper shaft support was also an important part of the process to ensure that no bearings were overloaded. A heat exchanger located off the side of the ECVT is in series with the inverter. Thermocouples were strategically placed to monitor stator, inner/outer case, and oil temperatures both near and far from the heat exchanger.

Additional instrumentation was added to the ECVT and PCU and a data acquisition system was developed to collect thermal, mechanical, and electrical data such as coolant temperatures, heat sink temperatures, torque, speed, currents, and voltages. These data were collected, fed into an immense spreadsheet, and saved for future use. An optimal control scheme was developed to ensure the most efficient operation of the motor throughout the entire operation range. The controller used speed, position, and current feedback to regulate the output conditions supplied by the inverter. The original equipment manufacturer motor inverter controls were bypassed to allow full control over the inverter, enabling uninhibited testing of the system over various operation conditions.

Back- emf tests were conducted by spinning the permanent magnet synchronous motor rotor with a secondary motor as the voltages across the open motor leads were measured. These tests provided information about the air gap flux due to the permanent magnets, as the induced back-emf voltage is proportional to speed and permanent magnet flux. Locked rotor torques were measured as a positive dc current was fed to phase “a” and returned through phases “b” and “c” connected in parallel, and the rotor position was swept through an entire electrical cycle. The torque measurements for stator currents of 50, 100, 150, and 200 A are shown in Fig. 6. To avoid extreme stator temperatures and possible stator damage, measurements were taken only during the peak torque region for the higher dc currents of 250, 300, 350, and 400 A. Compared with the Camry, the LS600h has a considerably lower torque per current ratio for currents of up to about 250 A. Beyond this dc current level, Camry locked rotor test results revealed substantial effects of saturation; the LS600h did not sustain such detriments and had a much higher torque per current ratio at currents near 400 A. Although the LS600h motor has a smaller diameter, its increased stack length leads to a greater air-gap surface area than that of the Camry. Therefore, even though fewer turns can be fit into the small slots and thereby the torque per current ratio decreases, the larger surface area is less susceptible to saturation.

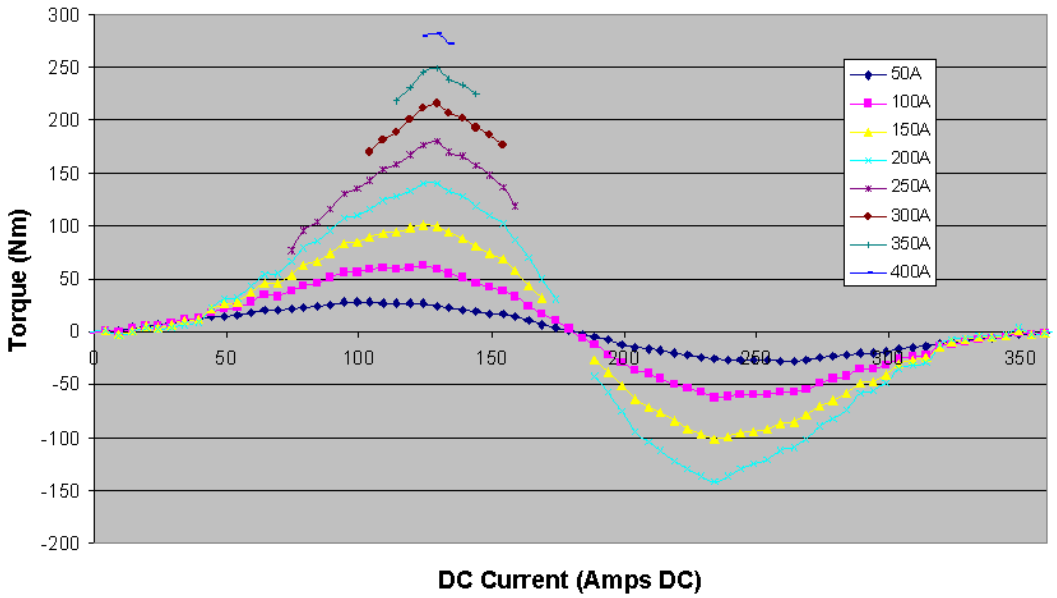

Fig. 6. 2008 Lexus LS600h locked rotor test results.

Efficiency measurements of the motor and inverter were taken over the entire operation range of the motor. The efficiency contour map in Fig. 7 represents the steady state efficiency characteristics of the motor for efficiencies above 50%. Compared with the efficiency map of the Camry, the advantages of the Lexus motor become apparent. The peak efficiency of 95% as well as efficiencies above 88% are spread out over a much a larger area of the operation region. Note that for much of the high-torque regions, a coolant temperature of ~0°C was used to permit extensive testing in this region. Otherwise, the torque levels nearing 300 Nm could be maintained only for extremely short periods of time before reaching stator temperature limits. Although the published peak power was verified with ~0°C coolant, operation could not be held at this power level for an 18 second duty. Further testing revealed that the motor is capable of producing 110 kW for 18 seconds before reaching a stator temperature of 180°C. However, in practice, the stator temperature limit is likely set to be much lower, and normal stator temperatures are near 100°C. Thus, only a very short duration of high-current operation is possible in most cases. Note that it appears the motor is capable of operating above its rated speed, as the torque was not reduced significantly at 10,000 rpm. However, the speed limitation was likely due to the mechanical stress of retaining the additional magnet.

Continuous tests were conducted at 25kW and 50 kW at 3,000, 5,000, and 7,000 rpm with a constant coolant temperature of 50°C. Stator winding, internal/external case, inverter, and coolant temperatures were measured throughout the tests. Shown in Fig. 8 are the results from a test conducted at 50 kW and 3,000 rpm. The hottest location in the motor is near the upper portion of the stator, which is farthest from the heat exchanger, as indicated by the light blue line. This particular test condition was maintained for about 3.3 minutes, at which time a stator temperature of 150°C was reached. For the same conditions, 50 kW was maintained at 5,000 rpm for about 14.2 minutes and at 7,000 rpm for about 18.5 minutes until a stator temperature of 150°C was reached. The duration of operation at a specific power level was significantly affected by speed, coolant temperature, and temperature restraints placed on the stator.

Additional data, further analyses, and more elaborate documentation of the findings and results from the FY 2008 benchmarking efforts can be found in [1].

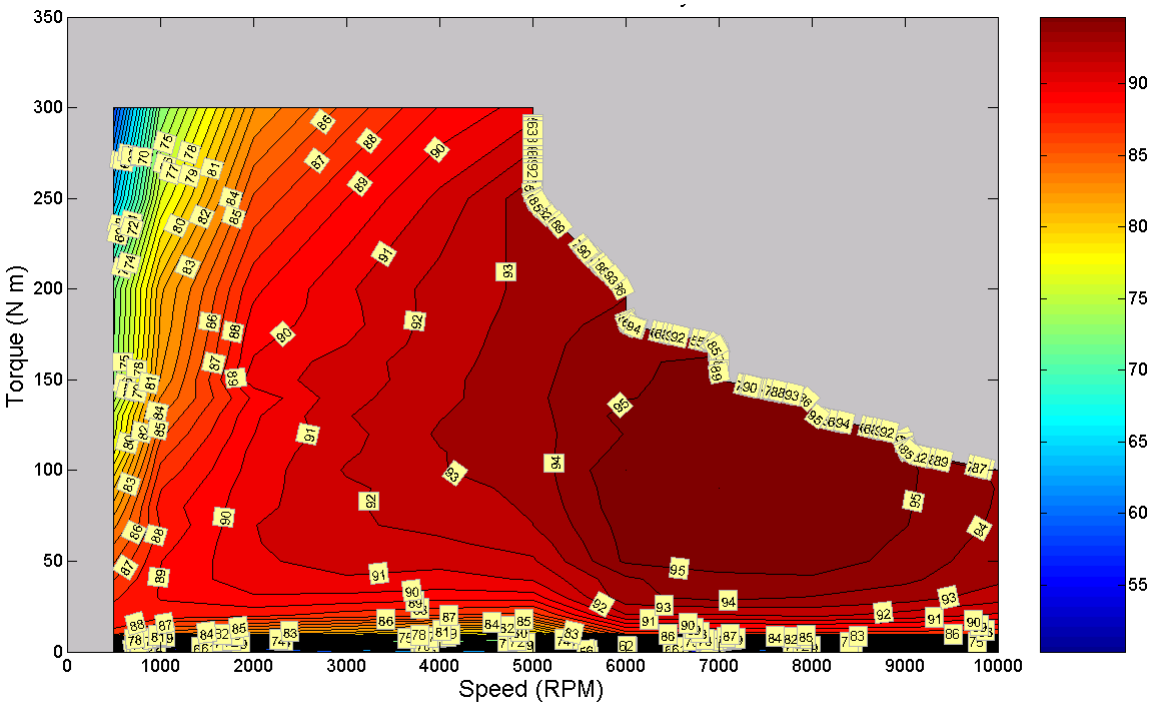

Fig. 7. 2008 Lexus LS600h motor efficiency map.

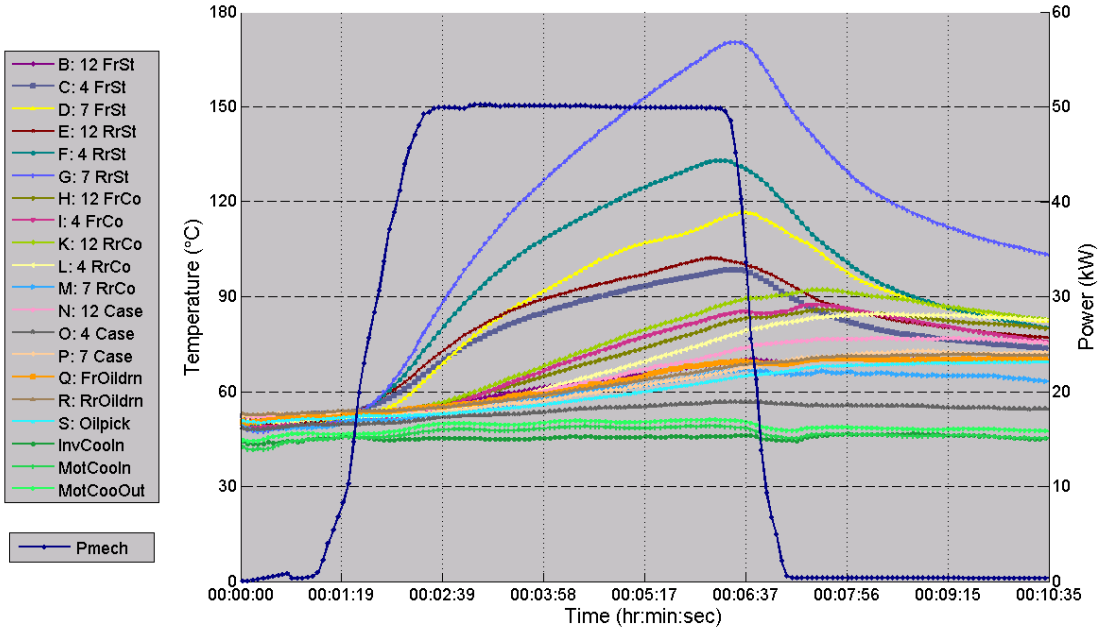

Fig. 8. 2008 LS600h continuous tests at 50 kW and 3,000 rpm.

Conclusions

- Benefits of the double-sided cooling technique lead to immense advances in inverter specific power and power density (about a 50% increase)
- The IGBT and diode count is reduced, even though the LS600h has a higher power rating than the Camry.
- Cost of some PCU components may not be advantageous.
- Motor stator outer diameter is reduced to 76% that of the Camry.
- Motor lamination stack length is more than doubled.
- Air-gap surface area is significantly larger than in the Camry but uses only 7.92 lb of copper vs 12.5 lb in the Camry.
- Motor magnet mass increased from ~2 to ~3lb.
- Power density of the Lexus motor has been improved to 2.5 kW/kg from 1.7 kW/kg in the Camry.
- Specific power of the Lexus motor has been improved to 6.6 kW/L from 5.9 kW/L in the Camry.
- Torque per current suffers at low currents but is superior at high currents.
- Motor efficiencies are above 90% for a great portion of the operation range, even better than the Camry.
- The 18 second peak power capability of the primary Lexus motor is about 110 kW at 5,000 rpm.
- Continuous duration varies significantly with speed and specified stator temperature limit. A power level of 50 kW was maintained at 7,000 rpm for about 18.5 minutes, at which a stator temperature of 150°C was reached.

Publications

1. T. A. Burress, et al., *Evaluation of the 2008 Lexus LS600h Hybrid Synergy Drive System*, ORNL/TM-2008/185, Oak Ridge National Laboratory, 2008.

T. A. Burress
C. L. Coomer
S. L. Campbell
L. E. Seiber
L. D. Marlino
J. P. Cunningham
A. A. Wereszczak

References

1. T. A. Burress, C. L. Coomer, S. L. Campbell, L. E. Seiber, L. D. Marlino, R. H. Staunton, and J. P. Cunningham, *Evaluation of the 2007 Toyota Camry Hybrid Synergy Drive System*, ORNL/TM-2007/190, Oak Ridge National Laboratory, 2007.

DISTRIBUTION

Internal

1. D. J. Adams
2. K. P. Gambrell
3. J. B. Green, Jr.
4. L. D. Marlino
5. M. Olszewski
6. Laboratory Records
   Authors
   Co-Authors

External

7. R. Al-Attar, DCX, raa9@chrysler.com.
8. S. J. Boyd, U.S. Department of Energy, EE-2G/Forrestal Building, 1000 Independence Avenue, S.W., Washington, D.C. 20585.
9. J. Czubay, General Motors Corporation, GM Powertrain Headquarters, Mail Code: 483-710-270, 895 Joslyn Avenue, Pontiac, Michigan 48340.
10. H. Dadkhah, Chrysler, LLC, CIMS 526-00-00, 1960 Technology Drive, Building D, Troy, Michigan 48083.
11. P. B. Davis, U.S. Department of Energy, EE-2G/Forrestal Building, 1000 Independence Avenue, S.W., Washington, D.C. 20585.
12. R. R. Fessler, BIZTEK Consulting, Inc., 820 Roslyn Place, Evanston, Illinois 60201-1724.
13. S. Gopalakrishnan, General Motors Corporation, RMB-356, Mail Code 480-106-390, 30500 Mound Road, Warren, Michigan 48090.
14. G. Hagey, 501 Randolph St., Williamsburg, Virginia 23185.
15. E. Jih, Ford Motor Company, Scientific Research Laboratory, 2101 Village Road, MD-1170, Rm. 2331, Dearborn, Michigan 48121.
16. K. J. Kelly, National Renewable Energy Laboratory, 1617 Cole Boulevard, Golden, Colorado 80401.
17. F. Leonardi, Ford Motor Company, 15050 Commerce Drive, North, Dearborn, Michigan 48120-1261.
18. F. Liang, Ford Motor Company, Scientific Research Laboratory, 2101 Village Road, MD1170, Rm. 2331/SRL, Dearborn, Michigan 48121.
19. M. W. Lloyd, Energetics, Inc., 7164 Columbia Gateway Drive, Columbia, Maryland 21046.
20. M. Mehall, Ford Motor Company, Scientific Research Laboratory, 2101 Village Road, MD-2247, Rm. 3317, Dearborn, Michigan 48124-2053.
21. N. Olds, United States Council for Automotive Research (USCAR), nolds@uscar.org
22. S. A. Rogers, U.S. Department of Energy, EE-2G/Forrestal Building, 1000 Independence Avenue, S.W., Washington, D.C. 20585.
23. G. S. Smith, General Motors Advanced Technology Center, 3050 Lomita Boulevard, Torrance, California 90505.
24. R. A. Sullivan, U.S. Department of Energy, EE-2G/Forrestal Building, 1000 Independence Avenue, S.W., Washington, D.C. 20585.

A Strong Energy Portfolio for a Strong America

Energy efficiency and clean, renewable energy will mean a stronger economy, a cleaner environment, and greater energy independence for America. Working with a wide array of state, community, industry, and university partners, the U.S. Department of Energy's Office of Energy Efficiency and Renewable Energy invests in a diverse portfolio of energy technologies.

For more information contact:
EERE Information Center
1-877-EERE-INF (1-877-337-3463)
www.eere.energy.gov